UNIVERSITY OF SOUTHAMPTON
Faculty of Engineering, Science and Mathematics
Institute of Sound and Vibration Research

AN INVESTIGATION INTO INCONSISTENCIES BETWEEN THEORETICAL PREDICTIONS AND MICROPHONE ARRAY MEASUREMENTS OF RAILWAY ROLLING NOISE

by

TOSHIKI KITAGAWA

Thesis submitted for the degree of Doctor of Philosophy

December 2007

DECLARATION OF AUTHORSHIP

I, **Toshiki Kitagawa**

declare that the thesis entitled

An investigation into inconsistencies between theoretical predictions and microphone array measurements of railway rolling noise

and the work presented in the thesis are both my own, and have been generated by me as the result of my own original research. I confirm that:

- this work was done wholly or mainly while in candidature for a research degree at this University;
- no part of this thesis has previously been submitted for a degree or any other qualification at this University or any other institution;
- where I have consulted the published work of others, this is always clearly attributed;
- where I have quoted from the work of others, the source is always given. With the exception of such quotations, this thesis is entirely my own work;
- I have acknowledged all main sources of help;
- where the thesis is based on work done by myself jointly with others, I have made clear exactly what was done by others and what I have contributed myself;
- parts of this work have been published as:

  T. Kitagawa and D.J. Thompson, Comparison of wheel/rail noise radiation on Japanese railways using the TWINS model and microphone array measurements, *Journal of Sound and Vibration* **293**, 496-509, 2006.

Signed: 北川敏樹

Date: 12/12/07

UNIVERSITY OF SOUTHAMPTON

ABSTRACT

FACULTY OF ENGINEERING, SCIENCE AND MATHEMATICS

INSTITUTE OF SOUND AND VIBRATION RESEARCH

Doctor of Philosophy

AN INVESTIGATION INTO INCONSISTENCIES BETWEEN THEORETICAL PREDICTIONS AND MICROPHONE ARRAY MEASUREMENTS OF RAILWAY ROLLING NOISE

By

Toshiki Kitagawa

Theoretical models, such as TWINS, and microphone array measurements have been widely used to gain better understanding of rolling noise. However, the array measurements are often inconsistent with the TWINS predictions and give less prominence to the rail than the theoretical models. The objectives of this thesis are to make validation work of the TWINS model for Japanese railway lines, and to explore the reason why the microphone array gives a correct estimate of sound power radiated by the rail.

A comparison in terms of noise and rail vibration has been carried out for six wheel/rail conditions of Japanese railways. The TWINS predictions show good agreement with the measurements. After confirming the applicability of the TWINS model, the effects of wheel load on noise and rail vibration are investigated, and the predictions show similar trends to the measurements. The acoustic properties of a rail as measured with a microphone array have been investigated through simulations and field tests. In the simulation the rail is modelled as an array of multiple sources. Results are given for two situations: (a) the multiple sources are incoherent, which is assumed in determining sound power from a microphone array, (b) the sources are coherent, which is more representative of the rail radiation. It is found that the microphone array cannot detect a large part of the noise generated by the rail in the frequency range where free wave propagation occurs. Sound measurements were carried out to validate the radiation model of the rail by using a shaker excitation of a track. It is found that the noise is radiated from the rail at an angle to the normal when free wave propagation occurs in the rail, and that the predictions based on coherent sources show good agreement with the measurements. Sound measurements for a moving train were also performed with a microphone array. It is shown that the microphone array misses a large part of noise generated by the rail, when directed normal to the rail. This leads to an underestimation of the rail component of the noise in the array measurements.

LIST OF CONTENTS

LIST OF SYMBOLS

$A(x)$	transfer accelerance at position x
A_x	vertical accelerance
A_y	horizontal accelerance
A_{xy}	cross-accelerance
D	spacing between two sources arranged in a line
D_{total}	total span length of a microphone array
I	normal intensity
$I_{1n,coh,di}$	normal intensity on the surface of the first sphere of the n^{th} dipole of an array of coherent dipoles
$I_{doublet,1}$	normal intensity of the first monopole of a dipole
$I_{n,coh,mono}$	normal intensity on the surface of the n^{th} monopole of an array of coherent monopoles
M	number of microphones
N	number of sources
N_d	number of measurement positions
P_0	sound pressure of an incident plane wave
P_m	output of the m^{th} microphone
Q	volume velocity of a source
Q_n	volume velocity of the n^{th} monopole
$S_{coh,di,pl}$	total output of the microphone array, appropriate for a plane wave, for the line array of coherent dipoles
$\tilde{S}_{coh,di,pl}$	normalized output of the microphone array, designed for a plane wave, for the line array of coherent dipoles
$S_{coh,di,sp}$	total output of the microphone array, appropriate for a spherical wave, for the line array of coherent dipoles
$\tilde{S}_{coh,di,sp}$	normalized output of the microphone array, designed for a spherical wave, for the line array of coherent dipoles

$S_{coh,mono,pl}$	total output of the microphone array, appropriate for a plane wave, for the line array of coherent monopoles
$\tilde{S}_{coh,mono,pl}$	normalized output of the microphone array, designed for a plane wave, for the line array of coherent monopoles
$S_{coh,mono,sp}$	total output of the microphone array, appropriate for a spherical wave, for the line array of coherent monopoles
$\tilde{S}_{coh,mono,sp}$	normalized output of the microphone array, designed for a spherical wave, for the line array of coherent monopoles
$S_{dipole,pl}$	output of the microphone array, appropriate for a plane wave, due to an incident wave of a dipole
$\tilde{S}_{dipole,pl}$	normalized output of the microphone array, appropriate for a plane wave due to an incident wave of a dipole
$S_{dipole,sp}$	output of the microphone array, appropriate for a spherical wave, due to an incident wave of a dipole
$\tilde{S}_{dipole,sp}$	normalized output of the microphone array, appropriate for a spherical wave, due to an incident wave of a dipole
$S_{inc,di,pl}$	total output of the microphone array, appropriate for a plane wave, for the line array of incoherent dipoles
$\tilde{S}_{inc,di,pl}$	normalized output of the microphone array, designed for a plane wave, for the line array of incoherent dipoles
$S_{inc,di,sp}$	total output of the microphone array, appropriate for a spherical wave, for the line array of incoherent dipoles
$\tilde{S}_{inc,di,sp}$	normalized output of the microphone array, designed for a spherical wave, for the line array of incoherent dipoles
$S_{inc,mono,pl}$	total output of the microphone array, appropriate for a plane wave, for the line array of incoherent monopoles
$\tilde{S}_{inc,mono,pl}$	normalized output of the microphone array, designed for a plane wave,

	for the line array of incoherent monopoles
$S_{inc,mono,sp}$	total output of the microphone array, appropriate for a spherical wave, for the line array of incoherent monopoles
$\tilde{S}_{inc,mono,sp}$	normalized output of the microphone array, designed for a spherical wave, for the line array of incoherent monopoles
$S_{mono,pl}$	output of the microphone array, appropriate for a plane wave, due to an incident wave of a monopole
$\tilde{S}_{mono,pl}$	normalized output of the microphone array, appropriate for a plane wave, due to an incident wave of a monopole.
$S_{mono,sp}$	output of the microphone array, appropriate for a spherical wave, due to an incident wave of a monopole
$\tilde{S}_{mono,sp}$	normalized output of the microphone array, appropriate for a spherical wave, due to an incident wave of a monopole
$S_{n,dipole,pl}$	output of the microphone array, appropriate for a plane wave, for the n^{th} dipole
$S_{n,mono,pl}$	output of the microphone array, appropriate for a plane wave, for the n^{th} monopole
$S_{n,dipole,sp}$	output of the microphone array, appropriate for a spherical wave, for the n^{th} dipole
U	surface normal vibration
U_1	surface normal velocity of the first monopole of a dipole
U_2	surface normal velocity of the other monopole of a dipole
$U_{1n,coh,di}$	surface normal velocity on the first monopole of the n^{th} dipole
$U_{n,coh,mono}$	surface normal velocity on the n^{th} monopole
W	bean pattern of a microphone array
$W_{1n,coh,di}$	time-averaged sound power of one source of the nth dipole
$W_{coh,di}$	time-averaged sound power of an array of coherent dipoles
$W_{coh,mono}$	time-averaged sound power of an array of coherent monopoles

W_{dipole}	time-averaged sound power of a monopole
$W_{doublet}$	time-averaged sound power of a dipole
$W_{doublet,1}$	time-averaged sound power of the first monopole of a dipole
$W_{inc,di}$	time-averaged sound power of an array of incoherent dipoles
$W_{inc,mono}$	time-averaged sound power of an array of incoherent monopoles
W_{mono}	time-averaged sound power of a monopole
X	coupling effect between vertical and lateral directions
a	radius of a pulsating sphere
c_0	speed of sound in air
d	distance between two neighbouring monopoles
$\overrightarrow{e_r}$	unit vector along array axis
$\overrightarrow{e_\phi}$	unit vector in the preferred direction, ϕ, of a microphone array
$\overrightarrow{e_{\phi m}}$	unit vector of m^{th} microphone in the preferred direction, ϕ, of a microphone array
i	i=1 near-field wave, i=2 bending wave
k	wavenumber
k_i	imaginary part of wavenumber in structure
$\overrightarrow{k_\theta}$	wavenumber vector for a wave arriving from an angle, θ, which is different from the preferred direction of a microphone array
$\overrightarrow{k_{\theta m}}$	wavenumber vector on m^{th} microphone for a wave arriving from an angle, θ
$\overrightarrow{k_\phi}$	wavenumber vector for a wave arriving from an angle, ϕ, which is the preferred direction of a microphone array
$\overrightarrow{k_{1\theta m}}$	wavenumber vector on m^{th} microphone for a wave of the first monopole of a dipole arriving from an angle, θ
$\overrightarrow{k_{2\theta m}}$	wavenumber vector on m^{th} microphone for a wave of the other monopole arriving from an angle, θ

p	complex sound pressure
$\tilde{p}$	normalized sound pressure
p_1	complex sound pressure of the first monopole of a dipole
p_2	complex sound pressure of the other monopole of a dipole
$p_{1n,coh,di}$	complex sound pressure at the surface of one of the spheres of the n^{th} dipole
$p_{coh,di}$	complex sound pressure of an array of coherent dipoles
$\tilde{p}_{coh,di}$	normalized sound pressure of an array of coherent dipoles
$\tilde{p}_{coh,mono}$	normalized sound pressure of an array of coherent monopoles
$p_{inc,di}$	complex sound pressure of an array of incoherent dipoles
$\tilde{p}_{inc,di}$	normalized sound pressure of an array of incoherent dipoles
$p_{inc,mono}$	complex sound pressure of an array of incoherent monopoles
$\tilde{p}_{inc,mono}$	normalized sound pressure of an array of incoherent monopoles
p_m	sound pressure of the m^{th} microphone
$p_{n,coh,mono}$	complex sound pressure of the n^{th} monopole
r	distance between a source and a microphone
r_0	distance between a microphone array and a track
r_1	distance between the first monopole of a dipole and a microphone
r_2	distance between the other monopole of a dipole and a microphone
r_{1n}	distance between the first monopole of the n^{th} dipole and a microphone
r_{2n}	distance between the other monopole of the n^{th} dipole and a microphone
r_{1ni}	distance between the first monopole of the i^{th} dipole and a point at the surface of the first monopole of the n^{th} dipole
r_{2ni}	distance between the other monopole of the i^{th} dipole and a point at the surface of the first monopole of the n^{th} dipole
r_n	distance between the n^{th} monopole and a microphone
r_{ni}	distance between the i^{th} monopole and the surface of the n^{th} monopole
$\overrightarrow{r_m}$	position vector of the m^{th} microphone

$\overrightarrow{r_{2\theta m}}$	position vector of m^{th} microphone for a wave of the other monopole of a dipole arriving from an angle, θ
$\overrightarrow{r_{\theta m}}$	position vector of m^{th} microphone for a wave arriving from an angle, θ
$\overrightarrow{r_{\theta mn}}$	position vector of the m^{th} microphone for a wave of the n^{th} monopole arriving from an angle, θ
$\overrightarrow{r_{1\theta m}}$	position vector of m^{th} microphone for a wave of the first monopole of a dipole arriving from an angle, θ
$\overrightarrow{r_{\phi m}}$	position vector of m^{th} microphone for a wave arriving from an angle, ϕ
s	output of a microphone array
s_i	wavenumber in structure
t	time
u	total response of near-field and bending waves
u_i	point response in wave i
w_m	weighting factor
$\mathit{\Delta}$	decay rate
$\mathit{\Delta}_m$	time delay of individual microphone
Δx_i	the distance between adjacent measurement positions
β	imaginary part of wavenumber
β_i	real part of wavenumber in structure
δ	microphone spacing between two neighbouring microphones
θ	angle between the x-axis and a line joining the origin to a observation point
λ λ_{air}	wavelength in air
λ_{rail}	wavelength in a rail
ρ	density of air
ϕ	preferred angle of a microphone array
ψ	angle determined by the supersonic structural radiation
ω	angular frequency

ACKNOWLEDGEMENTS

I wish to express my gratitude to my supervisor, Prof. D. J. Thompson, for his inspired instruction and discussions, encouragements and patience throughout my project. I would also like to thank Dr. C. J. C. Jones and Dr. N. S. Ferguson for their useful suggestions.

In addition, I am grateful for the time I spent at Institute of Sound and Vibration Research, University of Southampton, which enabled me to grow professionally and personally. I would like to deeply thank my company, Railway Technical Research Institute, for the financial support to me in 2002 and 2003. I also express my appreciation to my colleagues in Noise Analysis group, RTRI, who encouraged me during the finalising of this study.

Finally, I wish to thank my wife, Eri, for supporting me to make this study in England.

1 INTRODUCTION

1.1 Background

In Japan, serious problems due to the wayside noise of the conventional narrow-gauge railway lines caused a strong social demand for environmental controls in the 1990s. After many studies were examined carefully, such as the methods for evaluation of noise and influence on people who live near the railways, the Environment Agency established the "Guidelines for Noise Measures with regard to Construction and/or Large-scale Improvement of Conventional Railways" in 1995 [1]. Table 1.1 shows the environmental guidelines for the noise of conventional railway lines. In the guidelines, the measuring point ("reference point") is defined, which is located at a distance of 12.5 m away from the centreline of the nearest track, and at a height of 1.2 m above the ground.

Table 1.1 Guidelines for Noise Measures with regard to Construction and/or Large-scale Improvement of Conventional Railways.

Newly constructed railway lines	Day time (07:00-22:00) $L_{\mathrm{Aeq}} \leq 60$ dB(A) Night time (22:00-07:00) $L_{\mathrm{Aeq}} \leq 55$ dB(A)
Large-scale improvement of existing railway lines	Noise exposure level shall be less than that before the improvement

The guidelines do not control the noise of the existing conventional railway lines. However, by social demand, the guidelines are also implicitly applied to the existing railway lines. Therefore, it is more important than ever to make effective reduction of railway noise. In order to apply appropriate countermeasures for railway noise, it is necessary to understand which noise source has the greatest contribution to the total.

Railway noise is radiated from various track and vehicle components, such as the rail, the wheel, the engine or traction motors and other components. For the conventional narrow-gauge lines in Japan, the noise generated by railway vehicles mainly consists of rolling noise and noise from the driving devices in the motor vehicles (traction-motor fan noise and gear noise). Rolling noise is generated by vertical vibration of the wheel and rail, which is induced by a relative displacement between them due to the roughnesses on the wheel and rail surfaces [2, 3]. Traction-motor fan noise is aerodynamic noise generated by the fan that cools the traction motor.

Figure 1.1 shows the contributions of the two noise components at the reference point, defined in the guidelines for the noise of conventional railway lines [4, 5, 6]. The mean-square sound pressure is shown on a linear scale, although the totals are stated in dB. The traction-motor fan noise was the most dominant source in the past (see Figure 1.1, Train A). However, in new vehicles, the traction-motor fan noise has been considerably reduced by the introduction of a newly developed traction-motor, and the relative contribution of rolling noise for the total noise is therefore larger than before (see Figure 1.1, Train C). Now, in order to reduce the noise at the reference point, a better understanding of rolling noise is required.

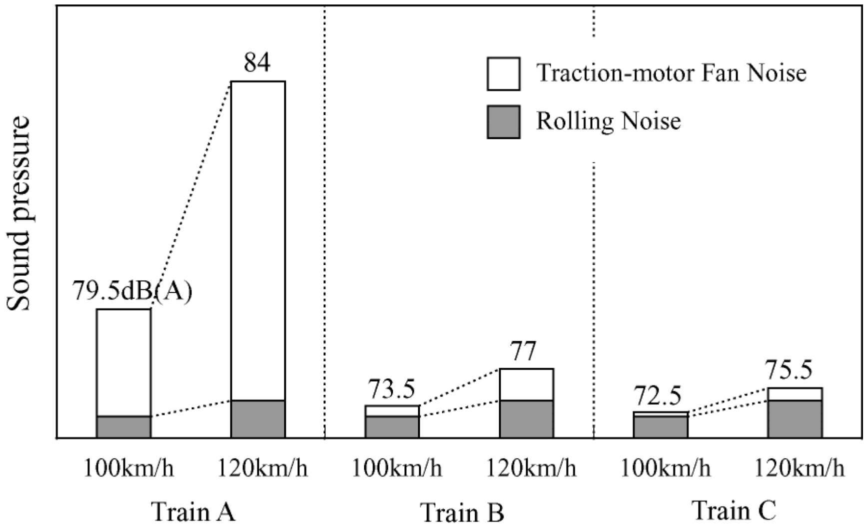

Figure 1.1 Noise of the conventional narrow-gauge lines in Japan [4, 5, 6]. Ground condition: embankment (1.5 m in height), ballast track, plain barrier (2 m in height). Car condition: 10 cars (motor vehicle: 6, trailer: 4), gear ratio: 6. Train A: motors with an outer fan. Train B: motors with an inner fan. Train C: motors with a high pressure inner fan).

Studies to develop understanding of the noise from both wheel and rail, which are the important components of rolling noise, have been performed by both theoretical models and measurements. The theoretical models, such as TWINS, have been developed in order to predict noise generated by wheel and rail [2, 3]. The TWINS model has been validated in terms of noise and vibration [7, 8, 9, 10, 11], and gives reliable predictions of rail and wheel contributions to the total noise for conventional and novel designs of wheels and tracks [12]. Meanwhile, in order to localize and identify noise sources along a train directly, measurements have been carried out with high performance microphone arrays [13, 14]. By using the measured data from the microphone arrays, methods have been developed to estimate how much acoustic power is generated by wheel and rail [15, 16, 17].

1.2 Description of TWINS

Theoretical models of wheel/rail rolling noise generation have mainly been developed by Thompson [18, 19, 20, 21, 22]. Subsequent research resulted in the implementation of the prediction model in a computer program, TWINS [3]. Figure 1.2 shows a schematic diagram of the theoretical model on which TWINS is based. This model is explained in the following sub-sections, summarised from [3].

1.2.1 Excitation

The excitation of the wheel-rail system is caused by the surface roughnesses of wheel and rail. In order to estimate the surface roughnesses, the spatial data on a series of multiple parallel lines on the surface of the rail and/or wheel are measured with a point sensor, and an equivalent roughness is calculated by the point-reacting spring model included in TWINS [23, 24]. In this model, the wheel and rail surfaces are represented by an array of non-linear springs to simulate dynamic properties in the contact patch. The following three features are effectively included in this method of analysis of the roughness:

(1) the removal of small holes in the surface,

(2) the attenuation for wavelengths shorter than the contact patch length,

(3) the correlation of the variations in the roughness across the width of the contact patch.

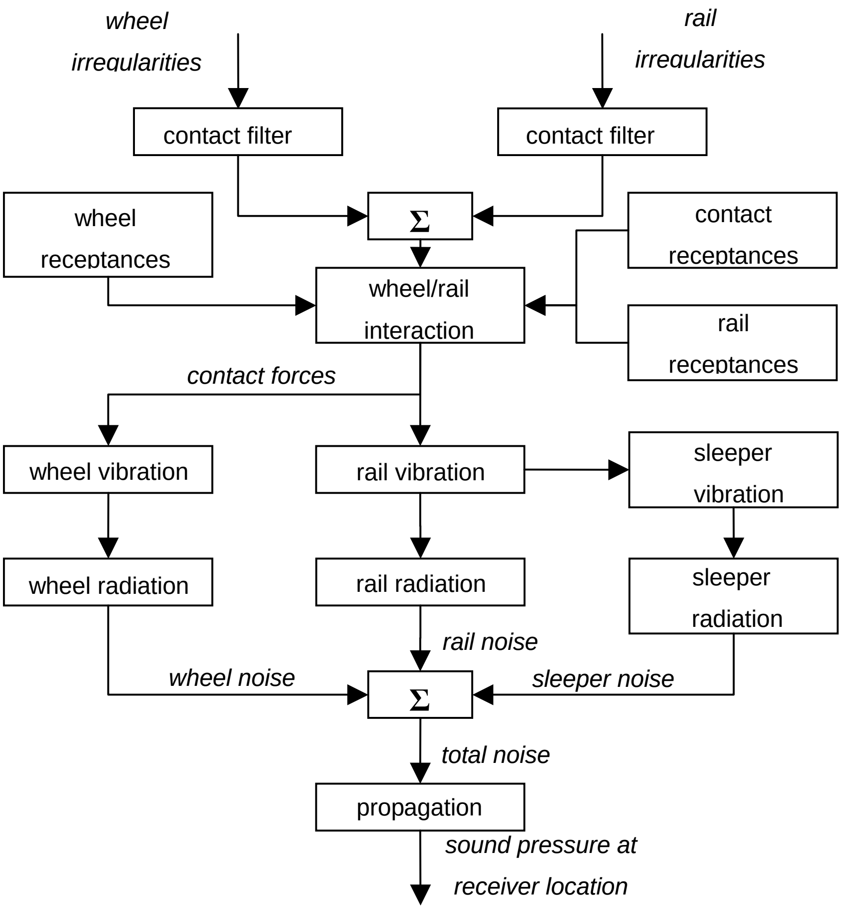

Figure 1.2 Flow diagram of TWINS calculation model [3].

However, TWINS can also be used to calculate the response to a unit roughness, and previously determined roughness spectra can be combined with these results to give the overall noise in a given situation [3].

1.2.2 Wheel-rail interaction

The wheel/rail interaction model [18] calculates the vertical and lateral displacements of the wheel and the rail using the roughness estimated by the excitation part of the model. In the model, contact elements linking wheel and rail are derived from

(1) a linearized Hertzian contact stiffness in the vertical direction, and

(2) a creep force element in the lateral direction, which is represented by a damper connected to a spring in series.

1.2.3 Wheel response

The modal characteristics of a railway wheel are derived from a finite element model, and the frequency responses of the wheel are predicted in TWINS by combining the modal characteristics using the modal summation theory [19, 25]. Modal damping should be defined either from measurements or based on experience of similar wheels. It is possible to neglect the axle, constraining the inner edge of the hub. However, for the modal damping ratio, experience has shown that the value for the radial mode with one nodal circle should then be set to 1 [12]. Wheel rotation effects are also included [22].

1.2.4 Rail response

Three theoretical models of the dynamic behaviour of railway track in the frequency range 50-6000 Hz are considered in TWINS [2, 7, 8, 9, 10, 20]. All models have two elastic layers, which correspond to rail pads and ballast. The characteristics of the three models may be stated, as follows.

(1) Continuously supported beam model (*rodel* model):

The track is considered as a Timoshenko beam on a continuous support, which is composed of a resilient layer (the rail pads), a mass layer (the sleepers) and a second resilient layer (the ballast). The two resilient layers are taken as springs with hysteretic damping. The same model is used for vertical and lateral directions with different parameter values, and the cross-coupling effect between vertical and lateral directions is estimated by using a parameter, X. The cross accelerance A_{xy} can be written as

$$A_{xy} = X\left(A_x A_y\right)^{\frac{1}{2}} \tag{1.1}$$

where A_x, A_y are vertical and lateral accelerances. The value of X (typically equivalent to -12 dB) is obtained from experimental data from tracks.

(2) Periodically supported beam model (*tinf* model):

The track is considered as a Timoshenko beam on periodic supports, which consist of spring-mass-spring systems as above. The location of the forcing point can be selected at any point within a sleeper span. The cross accelerance is again expressed by equation (1.1).

(3) Rail model including cross-section deformation (*perm* model):
The rail is modelled by using multiple finite elements, and the foundation is taken as a continuous support. The rail vibrations are analysed by combining the finite element method with periodic structure theory [20].

1.2.5 Sleeper response

In either of the first two track models described above, the sleeper vibration can be calculated using a beam model, which accounts for modal sleeper behaviour and frequency dependent ballast properties (stiffness and damping) [26, 27]. The results of the calculation are used as an alternative to the mass-spring description of sleeper and ballast.

1.2.6 Radiation

In TWINS, the sound power is calculated by combining the vibration spectra with radiation efficiencies in one-third octave bands. For the wheel, the radiation efficiencies for both axial and radial vibrations have been derived from boundary element analysis [28]. These have been used to derive simple analytical models that are used in TWINS. For the rail, an equivalent source model (*proluf* model) has been developed. This is a two-dimensional model, although the three-dimensional effects at low frequency and with high decay rate are included as correction terms [29]. For the sleeper, a model is based on a baffled rectangular piston, and the radiation efficiency obtained is close to 1.

The ground reflection effects that allow for a frequency-dependent complex ground impedance can also be introduced in the radiation models in the calculation of sound pressure at a receiver location.

1.2.7 Recent research on track vibration

Wu and Thompson have developed a methodology for studying rail vibration, allowing for effects not included in TWINS.

In order to develop a theoretical model for rail vibration, the rail is modelled by taking account of significant cross-sectional deformation of the rail in the vertical direction at high frequencies, which is caused by foot flapping [30]. In the model, the rail is considered as two infinite Timoshenko beams in the rail axis direction. The two Timoshenko beams correspond to the head and the foot of the rail, and are connected by continuously distributed springs to allow relative motion between the two beams. The cross-sectional deformation is represented by this double beam model. The results show good agreement with the measurement data in terms of point receptance and vibration decay rate along the rail.

A new model for studying the lateral vibration of a rail has also been developed [31, 32]. This model allows for all the essential cross-sectional deformations caused by the lateral vibration in the frequency range up to 6 kHz, including rail head bending and torsion, rail foot bending and torsion, and the relative motion between the rail head and foot. In this model, the whole rail is divided into three parts: the head and the foot are represented by two infinite Timoshenko beams which can be subjected to both bending and torsion, and the web is replaced by numerous beams connecting the head and foot. Using this, quite good agreement between the predictions and measurement data are obtained in terms of frequency response function.

The sleeper spacing and the ballast stiffness should be treated as random variables within certain limits. The effects of the random sleeper spacing and ballast stiffness on the track vibration have been investigated through numerical simulations [33]. Here, a railway track is simplified to an infinite Timoshenko beam with a finite number of discrete supports in order to represent the vertical vibration behaviour. It is shown that the point receptance and the vibration decay rate of the rail are distributed in a certain region, and that the phenomenon of the pinned-pinned resonance is suppressed by the random sleeper spacing.

Two effects of the presence of multiple wheels on the rail have been investigated [34, 35, 36, 37]. These effects are the influence of wave reflections in the rail induced by the multiple wheel/rail interactions, and the local stiffening of the track foundation due to the preload of the vehicle weight. It is shown that the preloading and wave reflections have significant effects on the rail receptance and the wheel/rail interaction force. However, the two effects are much smaller in the overall vibration and noise of the rail. This is due to the fact that the effects on the point receptance and wheel/rail interaction force largely cancel each other out.

These various effects have not yet been included in TWINS, although there are plans to include them in the future.

1.3 Microphone array systems

Microphone array systems with a highly directional character have been developed and used by a number of authors to study railway noise [38, 39, 40, 41, 42, 43, 44]. In the microphone array, a number of microphones are arranged in a precise geometrical pattern, and by combining the output signals from the microphones, the signals from one direction are produced [13, 14, 45]. Depending on the methods used in the systems, most microphone arrays can be categorised as a conventional array (additive antenna) [38, 39, 40, 41, 42]. An alternative approach is called the high resolution synthetic acoustic antenna (Syntacan) [43], which will be described separately.

In order to demonstrate the capabilities of the microphone array systems, the methods and their applications to measurements on trains with various configurations of microphone array will be described in the following sub-sections.

1.3.1 Conventional array

The methods of the conventional array are based on following two assumptions [13, 14, 45]:

(a) The source propagates a coherent wavefront to the microphones.

(b) The wavefront shape is known as a function of source position.

In the conventional array, multiple microphones are arranged in a geometrical design (e.g. a line), and the outputs of the microphones are summed using weighting factors. The mean square pressure in a given frequency band (e.g. one-third octave band) is calculated through filtering (e.g. one-third octave band filtering) or FFT methods. The directivity pattern of the array consists of a central main lobe and several side lobes of decreasing amplitude. The spatial resolution of the array depends on the source frequency, on the weighting factors, on the geometrical factors (e.g. distance from the source), on the microphone spacing and on the number of microphones.

For the weighting factors, the Hanning window function [45], Hamming window function [42, 46] and rectangular window function [16, 17, 41, 45, 47] are commonly used. In order to make a better beam pattern of the microphone array, the Dolph-Tschebyscheff method is also applied to determine the weighting factors of the microphones [38, 39, 40, 41, 48]. In this method, the narrowest possible beam width is produced for a desirable ratio of main beam to side lobe height when the microphone spacing is uniform.

In order to provide a reliable accuracy, attention should be given to the product of frequency bandwidth, B, and integration time, T, (BT product) [38, 40, 41]. This is due to the fact that the integration time for each frequency bandwidth must be large enough to provide a high statistical accuracy but not too large in order not to spoil the spatial accuracy. Therefore, it is desirable to ensure that the BT product is greater than 2.

For the measurements of sound emitted by a moving source (e.g. sources on a running train), it is also necessary to take account of the effect of source convection including the Doppler frequency shift [38, 49]. In order to eliminate the effect of the Doppler frequency shift, a technique has been developed in which the array beam is swept through a certain angle so as to follow the selected source on the train (i.e. de-dopplerisation technique). The array beam was directed through an angle from –7.5° to +7.5° relative to the array axis (for some spectra a wider angle of –20° to +20° was used) [38]. In the technique, the exact times for sound emitted from the focus point are computed for each microphone, and the data are sampled at the constant time intervals required at the computed arrival times. The calculation depends on the knowledge of the position of the emitting source relative to each microphone as a function of time; i.e. both the computed times and sampling frequencies would be a function of time. However, in many cases, it is implicitly assumed that the sources are 'stationary' (i.e. not time varying).

For the microphone spacing of the conventional array, in order to avoid spatial aliasing [13, 15, 45], it is necessary that the array operates at frequencies which satisfy

$$\frac{d}{\lambda} \le \frac{1}{2} \tag{1.2}$$

where d is the microphone spacing between two neighbouring microphones, and λ is the wavelength. The spatial resolution of the array is taken to be the array pattern's main lobe width [14]. The main lobe width, $\Delta\theta$, of the array is given by

$$\Delta\theta \propto \pm\sin^{-1}\left(\frac{\lambda}{md}\right) = \pm\sin^{-1}\left(\frac{\lambda}{D}\right) \tag{1.3}$$

where m is the number of microphones, and D is the total span length of the array. Equation (1.3) suggests that the main lobe width decreases as the number of microphones increases (for a constant microphone spacing) or as the microphone spacing increases (for the same number of microphones).

1.3.1.1 One-dimensional line array

For the one-dimensional line array, multiple omni-directional microphones are arranged in a line with an equal spacing for each frequency band [38, 39, 40]. The line array can localise sound sources in one dimension in the direction parallel to the line of the microphones. The horizontal array (WH array [38]) is located with its line of microphones parallel to the track, and gives useful information about the distribution of sound sources along the train. In order to determine the vertical extent of radiated sound sources, the vertical array (WV array [38]) is mounted with the line of microphones perpendicular to the plane of the track.

The WH and WV arrays can be arranged to have a directional character suitable for either a plane or spherical wave, since the wavefront shape of the incident wave could be either plane or spherical depending on the distance of a measuring point from the track. This means that the spatial resolution of the WH and WV arrays could depend on the geometrical factors, especially the relationship between the sound wavelength and the position of a measuring point. When the distance of a measuring position to the track is large (e.g. 25 m), it could be considered that the measuring point is located in the far-field of the source, and a microphone array designed for a plane wave can be used to measure source distributions on trains [39, 40, 46]. However, if the distance from the track is large, the view window of the microphone array is wide. If a measuring position closer to the track is used to improve the spatial resolution, the incident wavefront may be regarded as spherical, and it is necessary to design a microphone array suitable for a spherical wave [38, 48]. It can be effective to record the signal from each microphone, and then to use the appropriate post-processing method, in order to direct the focus of the array in any direction. To do this, suitable time delays are introduced electronically into the microphone signals when the data is processed.

(a) Horizontal array (WH array)

A horizontal array has been used to measure the spatial distributions on goods wagons and ICE trains during a pass-by. These show that, below 300 km/h, the local peak sound pressure levels occur at the positions corresponding to the wheels [38, 50]. For most of the wheel types studied, the measured sound powers have a speed exponent of about 3, and depend on the types of braking system installed on the wheels. The agreement between the spectrum of measured noise and the characteristic frequencies of the wheel indicated that the immediate sources of the measured noise are mainly due to the wheels above 1000 Hz [38]. Measurements on Shinkansen trains during a pass-by at speeds of 200 km/h and above show that aerodynamic noise is generated from each of the local parts of the car surface (e.g. pantographs, louvre intakes for air conditioning, front cars and gaps between adjacent cars) [39, 40].

(b) Vertical array (WV array)

Measurements on goods wagons and ICE trains using a vertical array show that the main noise sources are located in the region of the wheel and rail in the frequency range 1500-4500 Hz, and that the sound sources with maximum sound pressure level are located at a position between 0.1 and 0.25 m above the upper surface of the rail [38, 50, 51]. For the goods wagons, the locations do not depend on the type of braking system [51]. In a study focussing on the pantograph on ICE trains, the source distribution indicated that the noise sources are essentially concentrated in its head and foot region [50].

1.3.1.2 Two-dimensional arrays

Two types of two-dimensional microphone array have been developed in order to evaluate the two-dimensional distribution of noise sources on trains [15, 16, 41, 42, 44, 47]. These are cross or X-shaped arrays and planar arrays.

(a) Cross and X-shaped arrays

The cross and X-shaped arrays are formed by arranging two line arrays perpendicularly [41, 42, 46, 50, 51, 52]. The line arrays are one-dimensional conventional ones composed of multiple omni-directional microphones with an equal spacing along a line. The output signals from the microphones are combined by applying suitable time delay and sensitivity weighting to each microphone signal. The time delay appropriate for a spherical wave is used, since the array is located at a position close to the track (usually this is less than 10 m), so that the incident wave can be regarded as spherical [41, 42, 46, 50]. The directivity pattern of the array consists in a main lobe centred on the focused point and several side lobes of lower amplitude along the array axes. This suggests that the array leaves a strong ‘print’ of its own shape in the picture displaying source strength and positions at all frequencies [47, 53]. Furthermore, due to regular phased array geometries with a high degree of periodicity, grating lobes will appear in the visible region of the directivity pattern above a certain frequency ($d \geq \lambda$) [47]. A grating lobe is a side lobe with amplitude of the same size as the main lobe. These side lobes will introduce false sources in the measured source maps. To avoid the grating lobes in the directivity pattern, a method using multiple microphones arranged randomly in a plane has been developed [44]. In order to obtain two-dimensional source distributions projected on the car surfaces, the post-processing calculations for the measured results are carried out on the assumption that omni-directional uncorrelated point sources are located on the car surface, i.e. in a vertical plane at a pre-determined distance from the array.

The cross and X-shaped arrays are located in a vertical plane parallel to the track. Their use to determine a source distribution on goods wagons is reported in [51]. This indicates that the wheels are the principal locations of radiated sound in the frequency range 1500-4500 Hz, and that the principal locations do not depend on the brake type. Measurements performed on ICE, TGV-A and Shinkansen trains in the speed range 100-300 km/h show that the major sound sources are from the wheel/rail region as well as various aerodynamic sound sources [42, 46, 52]. Especially at the upper end of the speed range, aerodynamic sound sources, which are generated from the bogie region, the front car and the raised pantograph, appear to have a greater contribution.

(b) Planar arrays

In [41], a planar array is used with omni-directional microphones arranged in a square pattern. The output signal of this planar array was the simple average of the microphone signals (no weighting). As no time delay was introduced into each microphone signal, the incident wave was assumed to be planar. The frequency analysis is carried out through FFT methods. The directivity pattern of the planar array consists of a main lobe centred on the focused point, and the side lobes in the directivity pattern are considerably suppressed compared with those of the cross or X-shaped array. The spatial resolution of the planar array depends on the source frequency, on the microphone spacing and on the number of microphones. One way to increase the spatial resolution is to increase the microphone spacing (for a fixed number of microphones). This could serve to worsen the signal-to-noise ratio, since the finite number of microphones will cause the waves incident from unfocused directions to leak into the array [47]. With constant microphone spacing, the other way is to increase the number of microphones, at the same time increasing the array's spatial extent, particularly at low frequency. As for the cross and X-arrays, microphone arrangements with a high degree of periodicity in the planar array could yield grating lobes in the directivity pattern above a certain frequency ($d \geq \lambda$). The grating lobes cause ghost images to appear in the source map. In order to make the BT product suitable, a constant integration interval is used, and then the spatial selectivity of the planar array depends not only on the frequency but also on the train speed.

(c) Spiral array

Designs of two-dimensional microphone arrays with a higher resolution have been developed by selective arrangements of the locations of microphones, and include both a spiral array and a wheel array [15, 16, 44, 47, 53, 54]. As noted above, the two-dimensional microphone arrays composed of multiple microphones with a regular spacing yield grating lobes (i.e. ghost images) in their directivity pattern. In order to suppress the grating lobes, multiple omni-directional microphones may be irregularly distributed. The spiral array is designed to give a source distribution suitable for a spherical wave, and a rectangular window function is used for the array shading.

The spiral array is positioned close to the track (less than 10 m) in a vertical plane parallel to the track. Measurements on the Italian ETR 500 high-speed trains gave source distribution images in the frequency range 500-2500 Hz, and showed that the wheels have the greatest contribution to the total A-weighted level [15, 16]. Above 250 km/h, significant aerodynamic noise is generated from the pantographs and the cavities on the front and rear cars [15]. An attempt has been made to calculate the contribution of wheels and rail to the total sound power by using the resolution of the array determined numerically [16]. In the method, the radiation areas of wheels are isolated in the measured source image by cutting away the noise due to side-lobe effects, and the contribution of the wheels is obtained by integrating the radiation over the areas corresponding to the wheel. However, this method may not be reliable, due to the fact that the contribution in the area includes part of the radiation which comes from the rail. This may systematically lead to the underestimation of the rail contribution.

1.3.2 High resolution synthetic acoustic antenna

The theory of the high resolution synthetic acoustic antenna (Syntacan) is based on the two-dimensional Fourier technique of the space-time correlation functions applied to the microphone signals [13, 43]. By using the technique, the Syntacan decomposes the sound field into the frequency dependent contributions from different directions, which can be associated with sound sources. The benefit of the Syntacan is that a high directionality is obtained with many fewer microphones, compared with the conventional arrays.

The Syntacan was used as a one-dimensional array in a vertical orientation at 25 m from the track to measure the source strengths and the vertical source distribution of a French TGV [17]. A search on the source heights was made by reading the directions of the lobes measured with the Syntacan. The measurements with the Syntacan lead to the conclusion that the strongest sound source in the 2000 Hz octave band is seen in the direction of the rail, while in the 500 and 1000 Hz octave bands an apparent important source is seen at wheel height. This result is inconsistent with the conclusions found in the research on the wheel/rail noise radiation [2, 8], in which the rail dominates in the 500 and 1000 Hz octave bands and the wheel has a greater contribution at higher frequencies.

By using the Syntacan techniques, a T-shaped sparse array has been developed to identify the directions and to obtain a two-dimensional distribution of multiple uncorrelated noise sources [55]. The signal processing method is a two-dimensional extension of the one-dimensional Syntacan design, and is directly based on the two-dimensional cross-correlation function of the wave field. The benefit of the T-shaped array is that a relatively small number of microphones are needed, compared with conventional array techniques which require a full planar array of microphones, or even the cross or X arrays with regular spacing. However, for the beam patterns, the T-shaped array has a broader main lobe and less severe side lobes than the full planar array. Measurements with the T-shaped array on a passing train (InterCity) with a speed of 138 km/h were carried out by using the technique including corrections for the Doppler frequency shifts and travel time. The results give two-dimensional images with good spatial resolution, and show that the emitted noise is dominated by wheel/rail noise.

1.3.3 Acoustic mirror

An acoustic mirror consists of multiple microphones and a reflector, for which a portion of a paraboloid or ellipsoid is chosen [39, 56]. The acoustic mirror has a high spatial resolution at high frequencies, and gives useful information about two-dimensional source distributions. The directivity and sensitivity of the acoustic mirror depend on the frequency of the incident sound. To ensure sufficient spatial resolution above 500 Hz, the diameter of the acoustic mirror is 1.7 m (2.5 times the wavelength at 500 Hz).

Measurements on Shinkansen trains showed that aerodynamic noise is generated from windows, doors and gaps between adjacent cars at high frequencies [39]. An attempt was made to investigate the source distributions on the lower parts of cars by using the acoustic mirror [56]. The results indicated that the primary noise source is located in the wheel region at frequencies from 500 Hz to 4000 Hz, and that the wheel noise has a greater contribution than the rail noise. The conclusion is again not consistent with the results obtained from the TWINS model [2, 8].

1.3.4 Method of analysis for the array measurements

The mean square pressure measured with the microphone arrays corresponds to the acoustic energy composed of the contributions of the sources detected through the main lobe and side lobes of the microphone array. In some references [17, 39, 40, 41, 52], attempts have been made to quantify source levels generated by trains using the results measured with the microphone arrays.

A technique to estimate the contribution of each component of railway noise has been developed by using the spatial distributions measured with the WH array [39, 40]. In this technique, the railway noise is divided into continuous non-uniform line sources of a finite length, each of which is assumed to be composed of uncorrelated monopoles. The acoustic powers of the line sources are determined by using the readings from the measured spatial distributions and the directivity of the WH array. A hypothetical microphone array is considered that has a flat viewing window in the horizontal direction, and whose sensitivity is equivalent to that of the actual WH array. The directivity characteristic of the hypothetical array is arranged to be equal to the integration of the directivity pattern of the WH array from -90° to 90°, and then the hypothetical array can see the train only within the angle of ±6.7° horizontally. When the array is located parallel to the track at a distance of 25 m away from the track, the energy measured with the array is attributed to the radiation of the sources located within a length of about 6 m. By using the measured spatial distributions, the acoustic power level, PWL_A, radiated from a unit length (1 m) of each line source is given by

$$PWL_A = L_A + 28.2 \quad \text{dB(A)} \tag{1.4}$$

where L_A is the peak level in the spatial distribution measured. The level at troughs between wheels is also treated in the same way.

In order to determine the acoustic power levels of the sources on trains, the energy measured with the cross array is assumed to be attributed to the radiation of the sources located within the S_{-3dB} of the main lobe (S_{-3dB}: the area of the main lobe where the directivity is higher than -3dB) [41, 52]. In this assumption, the contributions of any side lobes are neglected implicitly. The S_{-3dB} of the main lobe is evaluated from the features of the array on the assumption that multiple uncorrelated monopoles are distributed over a vehicle surface. By using the S_{-3dB} values, an attempt has been made to estimate the average noise level radiated per unit area at the array position.

In [57], a technique to estimate the source power distribution on trains has been developed, in which the source characteristics are analysed by combining the outputs measured with the conventional arrays and a transfer matrix composed of Green's functions. The transfer matrix is derived on the assumption that uncorrelated discrete sources with spherical radiation characteristics (i.e. monopoles) are spread over a coach surface. Measurements were carried out for loudspeakers mounted on a TGV train's surface, and the calculated source strengths showed a good agreement with the true values.

The quantification of source levels has also been performed from the results measured with the Syntacan orientated vertically [17]. The Syntacan array composed of microphones with a selective directivity was designed to have a lateral window within the direction between -30° and 30°. In the method of analysis, railway coaches are modelled either as distributed monopole sources or as distributed dipole sources. The distributed sources are implicitly assumed to be uncorrelated. The relationship between the sound source strength and equivalent sound pressure level, L_{eq}, corresponding to a monopole and dipole during the passage of each source through the Syntacan's lateral window has been derived analytically at each source height. By combining the relationship with the results, L_{eq}, measured with the Syntacan, the source strength and the vertical source distribution of a TGV has been estimated.

In each case the basic assumption behind the use of a microphone array is that the sources to be identified consist of a distribution of uncorrelated point sources located in a plane at some known distance from the array. The outputs from each microphone are added together, allowing for some delay and a weighting function, to give the sound arriving from a particular direction. When the true sources are distributed in nature, such as the rail, this source model may not be appropriate and could lead to misleading results.

1.4 Aims and main contributions

The main aim of the thesis is to investigate the characteristics of the sound radiation generated particularly by the rail and to determine why a microphone array appears to give less prominence to the rail than theoretical models such as TWINS.

The thesis is composed of two main parts. In the first part, Chapters 2 and 3, the validation of the TWINS model for the Japanese railway situation will be carried out in terms of noise and vibration. After confirming the applicability of the TWINS model, an attempt will be made in Chapters 4 and 5 to investigate the characteristics of the noise radiated by the rail and to examine carefully the results that would be measured with a one-dimensional microphone array. Through experimental measurements using a one-dimensional microphone array, the validation of the radiation properties of a rail will be performed in Chapters 6 and 7.

The main contributions of the thesis are as follows:

- Through comparisons between predictions made using the TWINS model for rolling noise and measured data from RTRI, the TWINS model is shown to be applicable to a number of wheel types and a track typical of the Japanese situation (Chapter 2). The relative contributions of wheel, rail and sleeper to the total noise are also determined.
- The effects of wheel load on noise and rail vibration are quantified using the TWINS model and compared with measured data. These results show that rolling noise reduces slightly when the wheel load is increased (Chapter 3).

- A model for the sound radiation of the rail is produced on the basis of an array of simple sources, either monopoles or dipoles (Chapter 4). These are assigned source strengths according to the rail vibration (Chapter 5). This approach is extended to represent the response of a microphone array to single or multiple sources (Chapter 4).
- Measurements using a microphone array are simulated and used to show that the sound radiation from a rail can be greatly underestimated by the microphone array due to the distributed nature of the rail source (Chapter 5). The extent of this underestimation is quantified.
- Through experimental measurements using shaker excitation of a track, the radiation behaviour of a rail is quantitatively examined by directing a one-dimensional microphone array, and is found to agree closely to the predictions based on coherent sources (Chapter 6).
- Sound measurements for moving trains are used to show that, when a microphone array is directed normal to the rail, it does not detect a large part of the sound generated by the travelling waves in a rail (Chapter 7). This leads to an underestimate of the rail contribution.

2 VALIDATION OF THE TWINS MODEL FOR JAPANESE RAILWAYS

2.1 Measurement Description

A measurement campaign has been carried out for the evaluation and validation of the TWINS model for use in the Japanese situation [58]. The measurements were performed by Railway Technical Research Institute in 2000. In this section, the measurement campaign is described briefly.

2.1.1 Track and wheel conditions

Running measurements were carried out for a single track type [58], as listed in Table 2.1. This is located on a narrow-gauge line, with track gauge 1.067 m. The measurements were carried out for six wheel types, as listed in Table 2.2. Figures 2.1 and 2.2 show the cross-section details of the six wheels.

Table 2.1 Track conditions in Tokaido line (371K830M)

Track	Rail type	Rail-pad	Sleeper	Sleeper spacing (m)	Foundation
A	60	High stiffness “5N-type”	Concrete monobloc	0.6-0.65	Ballast

Table 2.2 Wheels which have been included in the measurements

Wheel	Description	Type of braking	Min. web thickness (mm)	Tyre width (mm)	Tyre height (mm)	Radius (mm)	Mass (kg)
A	Curved web	Tread (resin)	18	125	65	405	314
B	Curved web	Tread (sinter iron)	25	125	65	405	332
C	Straight web	Tread (cast iron)	28	125	65	430	314
D	Doubly curved web	Tread (resin)	10	125	65	430	292
E	Doubly curved web	Tread (sinter iron)	15	125	65	430	307
F	Doubly curved web	Tread (resin)	12	125	65	430	292

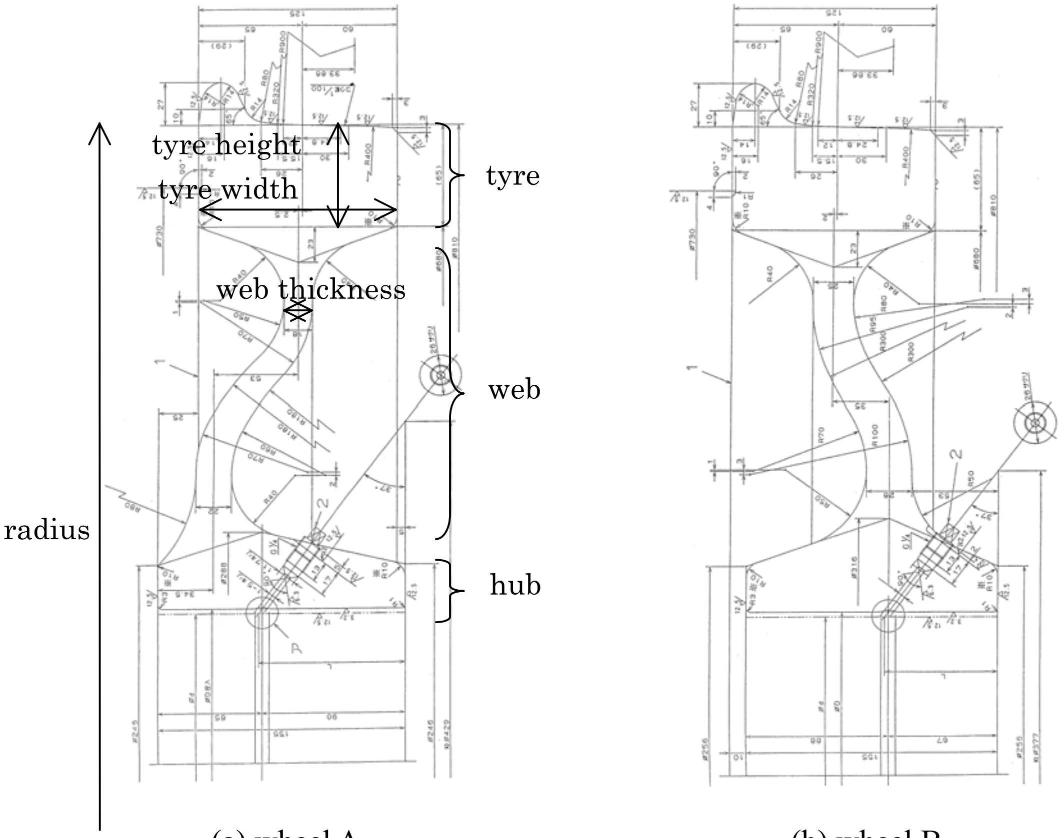

(a) wheel A (b) wheel B

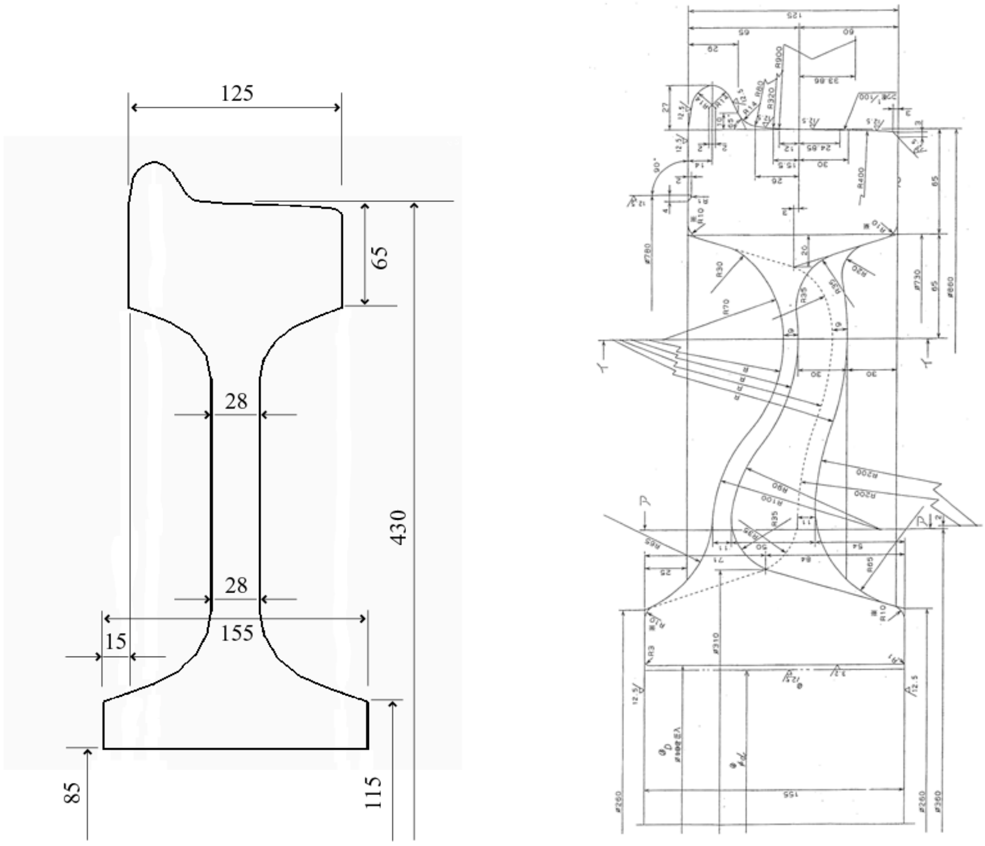

(c) wheel C (d) wheel D

Figure 2.1 Cross-section details of wheels A-D.

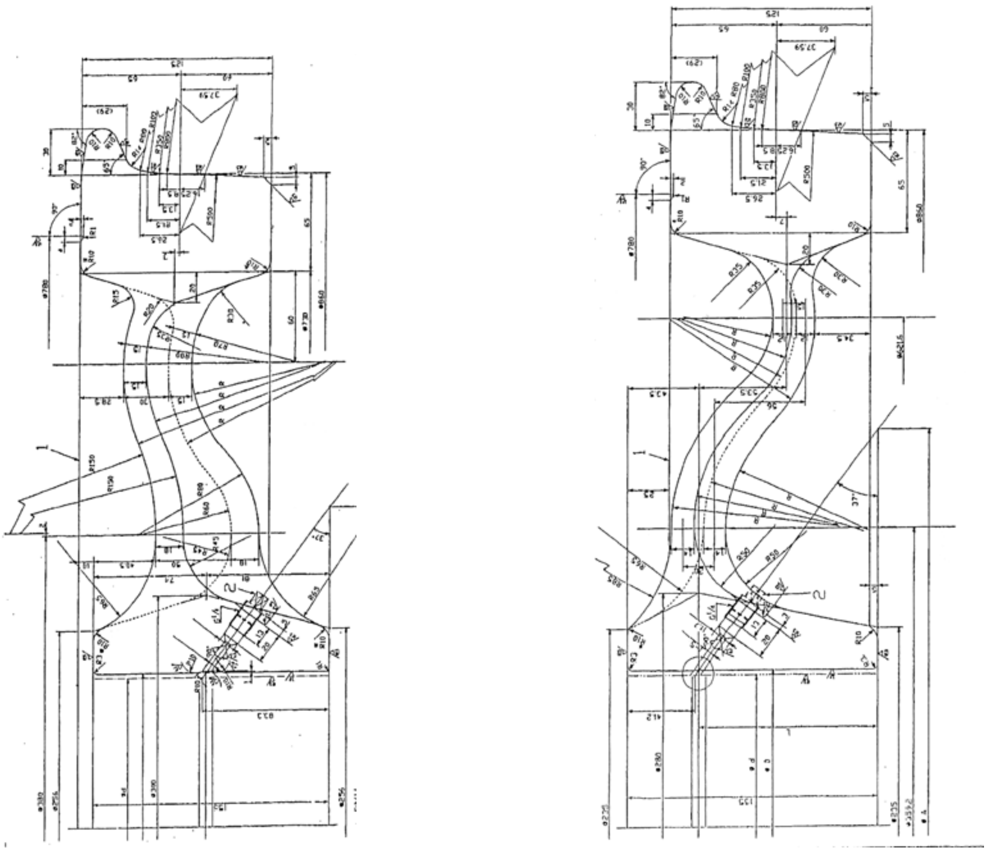
(a) wheel E (b) wheel F

Figure 2.2 Cross-section details of wheels E and F.

2.1.2 Measurements

At the trackside, measurements were made at the following positions during a train pass-by:

- an accelerometer on the rail (vertically on the rail foot)
- a microphone at 2 m from the centre of the track and 0.4 m above the railhead

These measurement locations are shown in Figure 2.3 and in the photographs of Figures 2.4-2.6. No measurements of wheel vibration were made during the campaign.

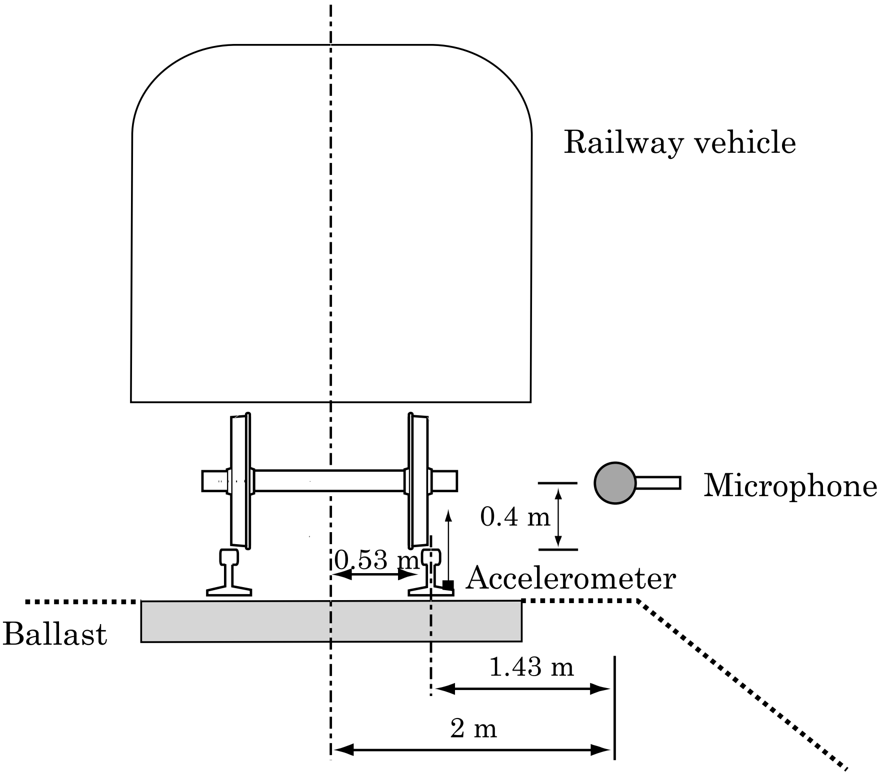

Figure 2.3 Diagram of measuring points.

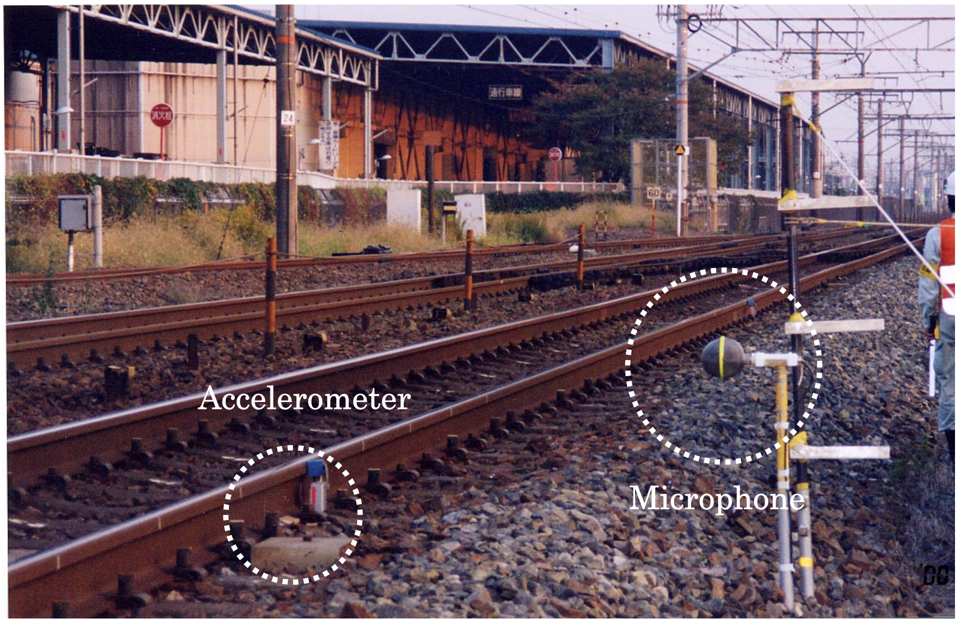

Figure 2.4 Full view of the measured section.

Figure 2.5 Photograph of the track and vehicles.

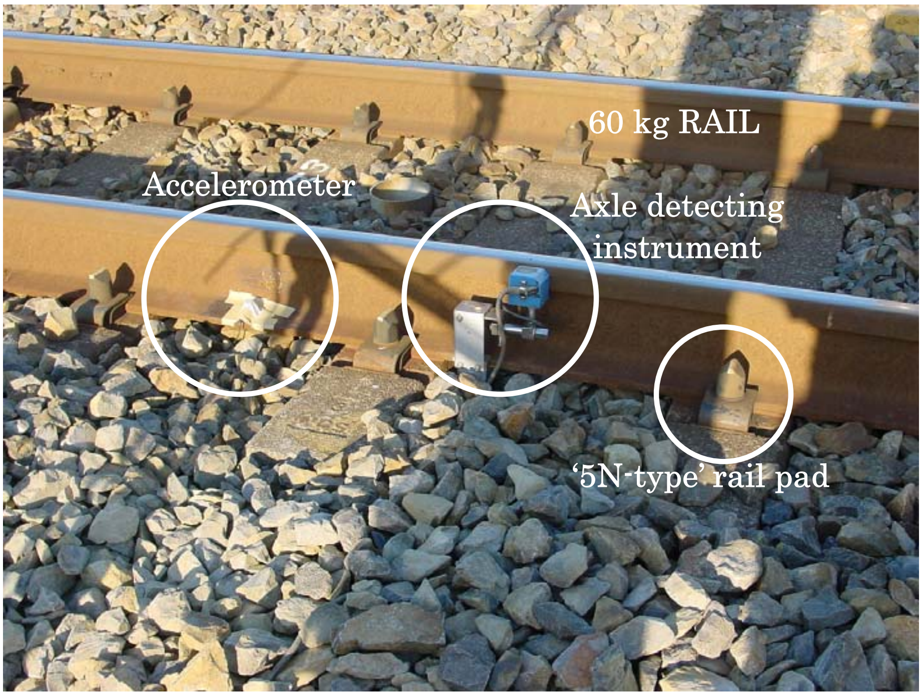

Figure 2.6 Setup of the accelerometer.

2.2 Calculation Parameters

2.2.1 Tuning of the track parameters

Static tests have been carried out at the Hino test site [59] in order to investigate the vibratory behaviour of track and determine appropriate calculation parameters. This is a different site from that used in the running measurements, but is fitted with the same track type. In the measurements, frequency response functions (e.g. accelerance) of a rail in both vertical and lateral directions have been obtained on unloaded tracks by hitting the railhead with an instrumented impact hammer, and measuring the response using accelerometers on the railhead, railfoot and sleeper. As the track behaviour in the lower frequency range is of most interest, the measurements were limited to frequencies below 2000 Hz [59]. This frequency range allows most of the resonant behaviour of the track to be seen.

These measurements are compared with predictions using the TWINS model. In the TWINS calculation, the “bi-bloc” sleeper model is used, in which the sleeper is regarded as a rigid mass. The parameters used for the TWINS model are presented in Table 2.3. In the table, the values of the stiffness and damping of the rail-pad and ballast have been chosen to obtain a good tuning for the track resonance behaviour between measurements and predictions in two directions.

Figure 2.7 shows the predicted and measured accelerances in the vertical direction. A comparison of the measured results with the predictions of two models available in TWINS (*rodel*: continuously supported beam model, *tinf*: periodically supported beam model) shows good agreement. In Figure 2.7, the following resonance behaviour can be seen, which is responsible for the relative motion of the rail and sleeper.

- $f \approx 150$ Hz: the combined mass of the rail and sleeper moves on the ballast stiffness,
- $f \approx 500$ Hz: the mass of the sleeper moves on the stiffness of the pad and ballast giving an anti-resonance,
- $f \approx 800$ Hz: the rail moves on the pad stiffness (out of phase with the sleeper).

Table 2.3 Values of TWINS parameters used for the track.

	Vertical	Lateral
rail bending stiffness, Nm^2	6.49×10^6	1.08×10^6
rail shear coefficient	0.4	0.4
rail loss factor	0.01	0.01
mass per length, kg/m	60	
cross receptance level, dB	-12	
pad stiffness, N/m	7.0×10^8	8.5×10^7
pad loss factor	0.25	0.25
sleeper mass (1/2 sleeper), kg	80	
distance between sleepers, m	0.625 (0.6-0.65)	
ballast stiffness, N/m	6.7×10^7	3.4×10^7
ballast loss factor	2.0	2.0

As the support in the *rodel* model is continuous, this model cannot predict the behaviour associated with the pinned-pinned effects (where sleeper separation equals half a bending wavelength, about 1000 Hz). On the other hand, the *tinf* model predicts the pinned-pinned resonances and a difference in frequency response between the two measured positions (above a sleeper and at mid-span). However, the phenomena associated with the pinned-pinned resonance cannot be seen clearly in the measurements, possibly due to randomness in the periodicity [33]. The *rodel* model appears to give better agreement with the measurements.

Figure 2.8 shows the predicted and measured accelerances in the lateral direction. For the lateral accelerance, it can be seen that the predictions of both models are lower than the measurements. This is explained by the omission of torsion in the TWINS model [9, 10].

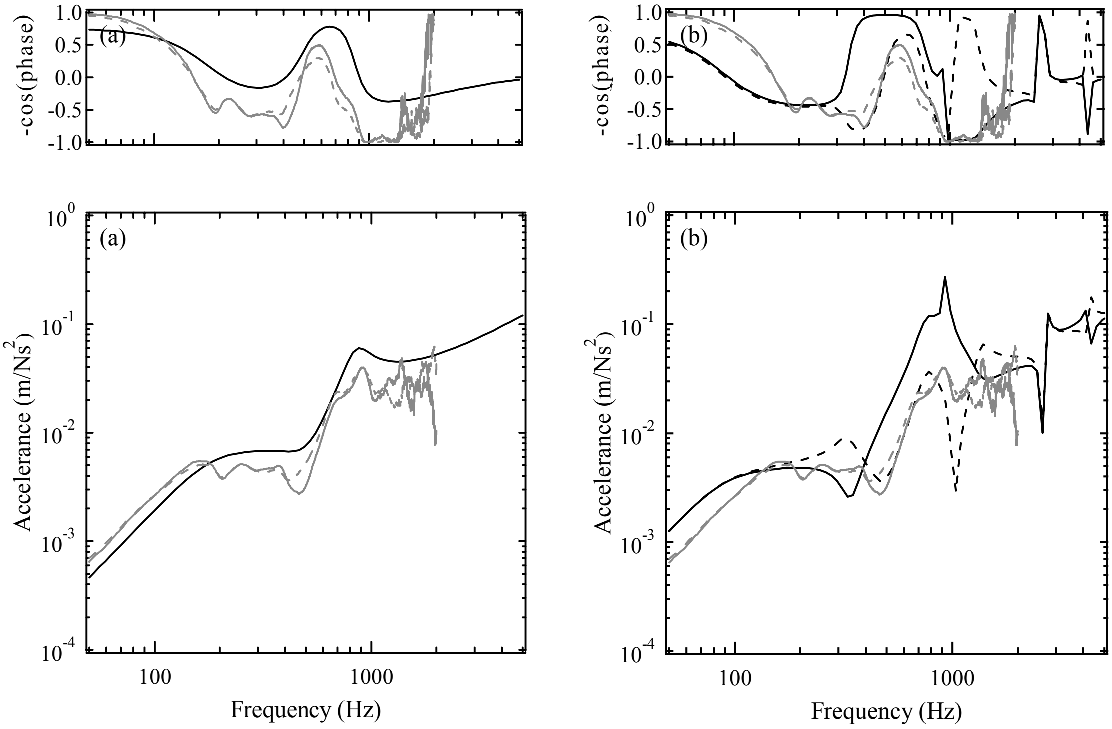

Figure 2.7 Vertical point accelerance. Measured results, —, above sleeper; - - -, between sleepers. (a) Predicted results —, *rodel* model; (b) Predicted results —, *tinf* model, between sleepers; – – –, *tinf* model, above a sleeper.

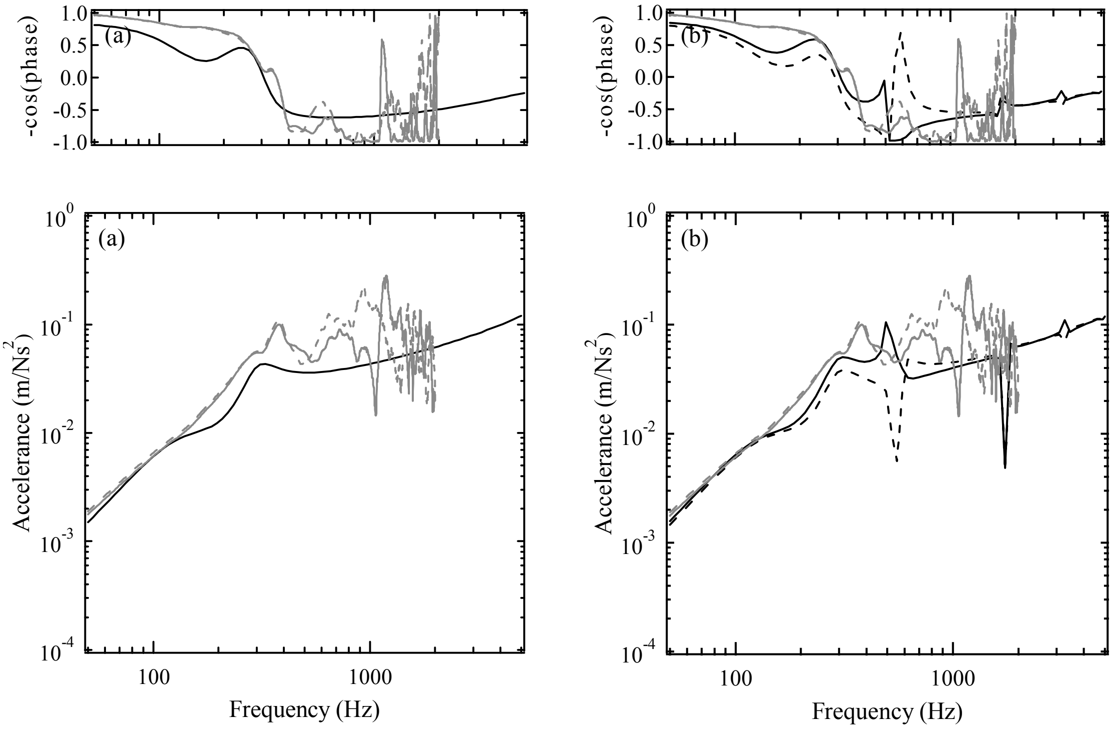

Figure 2.8 Lateral point accelerance. Measured results, —, above sleeper; - - -, between sleepers. (a) Predicted results —, *rodel* model; (b) Predicted results —, *tinf* model, between sleepers; – – –, *tinf* model, above a sleeper.

2.2.2 Track decay rates

The decay rates of vertical and lateral vibrations along the rail have been obtained from the transfer accelerance, measured at regular intervals away from the excitation position. The measurements for the decay rates have also been performed at the Hino test site [59]. However, the total length measured is limited to 1.6 m, since the same conditions of the rail support system (e.g. rail-pad, track support) are set up only within a few metres at the site [59].

The measured decay rate is estimated from an integral of squared vibration over the length of the rail [60]. If the transfer accelerance from x=0 to position x is $A(x)$, its amplitude can be approximated by

$$|A(x)| \approx |A(0)| e^{-\beta x} \tag{2.1}$$

where β is the imaginary (decaying) part of the wave number. Then the integral

$$\int_0^\infty |A(x)|^2 dx \approx |A(0)|^2 \int_0^\infty e^{-2\beta x} dx = |A(0)|^2 \frac{1}{2\beta} \tag{2.2}$$

from which the decay rate, Δ (dB/m), can be estimated:

$$\Delta = 8.686\beta \approx \frac{4.343}{\displaystyle\int_0^\infty \frac{|A(x)|^2}{|A(0)|^2} dx} \approx \frac{4.343}{\displaystyle\sum_{i=1}^{N} \frac{|A(x_i)|^2}{|A(0)|^2} \Delta x_i} \tag{2.3}$$

where N measurement positions are used and Δx_i is the distance between adjacent measurement positions. This method gives more reliable results than fitting a straight line to the curves of amplitude versus distance, although it is sensitive to the value of the point accelerance, $A(0)$. The effect of the near-field waves is also included in $A(0)$ but these are neglected in equation (2.1). This may lead to a slight systematic error in which Δ is over-predicted. (The use of equation (2.3) is compared with another method in Section 6.2.)

Figure 2.9 shows the transfer function $|A(x)/A(0)|$ at various distances from the force point to the response position. Figure 2.10 shows the decay rates of rail vibrations in vertical and lateral directions predicted using the *rodel* model and from measurements. (The decay rate from the *tinf* model is not shown since the damping of the rail is neglected in this model.) The decay rate of the vertical vibration is well predicted. Above 1000 Hz, the decay rates are not lower than 4 dB/m. This is due to the fact that the integral of the measured vibration is carried out over a short length, and the decay rate is not estimated correctly. From equation (2.3), if $A(x_i)$ is always equal to $A(0)$, a decay rate would be found of 2.7 dB/m which represents the minimum that can be observed [61]. For the lateral decay rate, the predicted curve shows a good agreement with the measured results below 400 Hz. Above 500 Hz, the measured decay rate is much higher than the predicted results. This may also be because the decay rate measurements are performed over a short length.

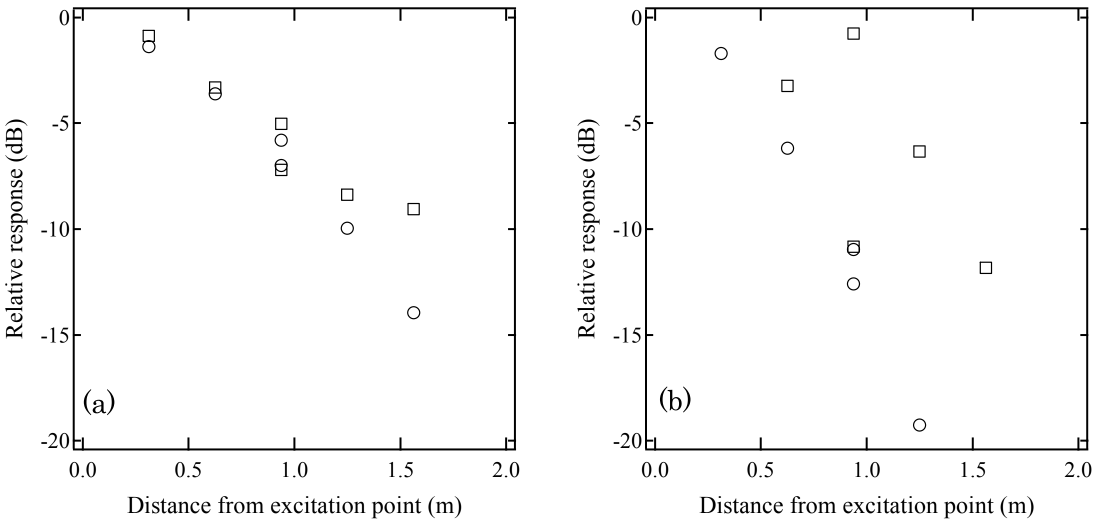

Figure 2.9 Measured transfer function at various distances. ○, 100 Hz; □, 1000 Hz; (a) vertical direction, (b) lateral direction. Results are normalised to 0 dB at 0 m.

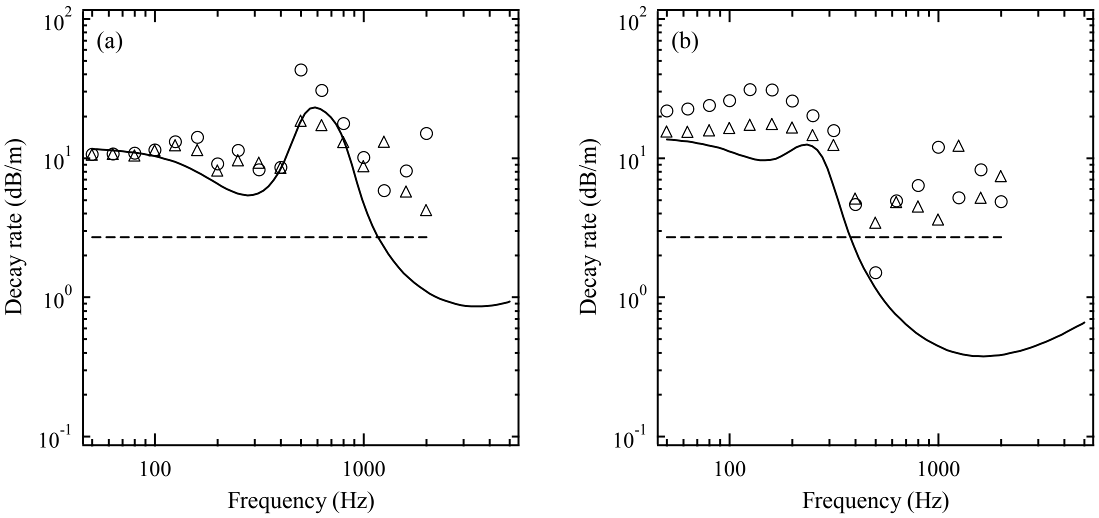

Figure 2.10 Decay rate of vertical and lateral rail vibration with distance. ○ and Δ, Measured (equation (2.3)) ; —, *rodel* model; - - -, minimum measured value; (a) vertical direction, (b) lateral direction.

2.2.3 Tuning of the wheel parameters

For the six types of wheel described in Section 2.2.1, the modal bases (natural frequencies and mode shape data) have been predicted using the finite element software ANSYS, and the frequency responses of the wheel are predicted in TWINS by using the modal superposition method. Use is made of the symmetry of the wheel structure, so that the modal bases have been calculated by modelling a quarter wheel with appropriate boundary conditions (the wheel is clamped at the inner edge of the hub, and symmetric/anti-symmetric boundary conditions are applied to the cross-section of the wheel). Principal wheel modes of vibration are categorized by the number of nodal diameters (n) and the number of nodal circles (m). Predicted natural frequencies for wheel F are listed in Table 2.4. Also listed are measured natural frequencies, obtained from a worn wheel [62]. For worn wheels, the natural frequencies can be modified by up to 10 % compared with new wheels. From Table 2.4, it can be seen that, allowing for the effects of worn wheels on the natural frequencies, reasonable agreement has been achieved, especially for $n \geq 2$. Slightly worse agreement is found for the predicted and measured (again worn) results of wheel A, whose natural frequencies are listed in Table 2.5. However, for the other wheels, measurements have not been taken. For the modal damping ratio, typical values from a similar wheel are used [2, 19], which are in the range 10^{-2}-10^{-4}. This is because no measured data were available from the measurement campaign.

Table 2.4 Natural frequencies for wheel F.

n	Zero-nodal-circle		Radial		One-nodal-circle	
	Pred.	Meas.	Pred.	Meas	Pred.	Meas.
0	313	316	2266	2510	1627	1180
1	163	173	744	809	1912	1480
2	418	442	1072	1270	2475	1850
3	1086	1130	1679	1900	2847	---
4	1922	2000	2354	2600	3921	2710

n, number of nodal diameters; Pred., predicted natural frequency; Meas., measured natural frequency (Hz) (from [62]).

Table 2.5 Natural frequencies for wheel A.

n	Zero-nodal-circle		Radial		One-nodal-circle	
	Pred.	Meas.	Pred.	Meas	Pred.	Meas.
0	466	316	2740	2830	1802	1650
1	246	173	1082	808	2190	1900
2	498	430	1554	1770	2934	2480
3	1279	1130	2199	2420	3822	3200
4	2274	2020	3044	3170	4686	3920

n, number of nodal diameters; Pred., predicted natural frequency; Meas., measured natural frequency (Hz) (from [62]).

Figure 2.11 shows the predicted accelerances of wheel F. In Figure 2.11, it can be seen that the radial accelerance has the behaviour of a mass at low frequencies (constant accelerance), a dip at around 300 Hz, and then above 1000 Hz a series of peaks which are the one-nodal circle modes and the radial modes. In the absence of axial-radial coupling only the radial modes would be seen here. As the wheel has a thinner web the radial modes of the wheel occur at lower frequencies than for a thicker web (see Tables

2.4 and 2.5) [62]. For the axial accelerance, the strong peaks correspond to the zero-nodal-circle modes.

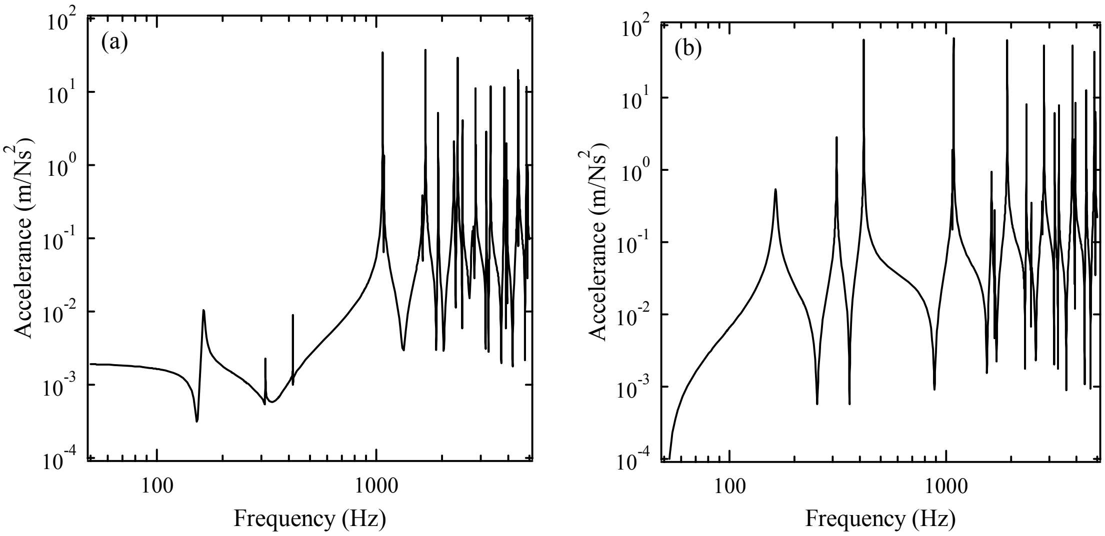

Figure 2.11 Point accelerance of wheel F with no rotation, (a) radial direction (b) axial direction.

2.2.4 Excitation options

In order to evaluate noise and vibration with the TWINS model, a roughness spectrum is required for input to the calculations. As no data were available corresponding to the tests, the TWINS calculations have been carried out by using ‘standard’ roughness spectra from European railway wheels and rails [63]. Figure 2.12 shows these roughness spectra, where wheel and rail roughness spectra are combined, including the contact filtering effect. In the TWINS calculations, a “unit roughness” excitation has been used for each frequency. In the excitation, the responses and sound radiation are calculated relative to this unit roughness amplitude (1 m). This means that all calculated parameters have the form of transfer functions. The roughness is then added in a post-processing step. The wheel/rail roughness spectra used in the TWINS calculation depend on braking system. For tread braked wheels with cast iron blocks, the block braked wheel spectrum is used in the TWINS calculation. Tread braked wheels with sinter iron or resin blocks are assumed to have the same wheel/rail roughness spectra as disc braked wheels.

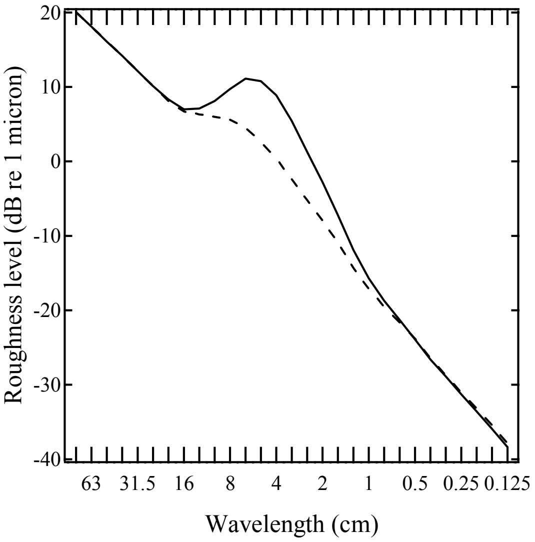

Figure 2.12 Combined wheel/rail roughness spectra after contact filtering. —, Block braked wheel + rail; – – –, disc braked wheel + rail [63].

In order to determine the contact positions on the wheel and rail surfaces, their transverse profiles are needed. However, the contact positions have also not been measured for the measurement campaign, so that the exact contact position is unknown. The nominal contact position on the wheel is therefore chosen as 70 mm from the flange-back. For the rail, the centreline might be selected as the nominal contact position. However, it is not necessary that the contact position on the rail should be specified for the *rodel* and *tinf* models, since the parameter *X* (see equation (1.1)) is used in the TWINS calculations to determine the degree of cross coupling.

2.2.5 Wheel and rail vibration options

The wheel responses are calculated including the wheel rotation effects. As mentioned in Section 2.2.3, the modal bases are predicted using the finite element software ANSYS.

The rail vibrations are predicted with only the *rodel* model. In this model, the rail vibration from each wheel/rail contact point is integrated over the range -/+ infinity, and then the track response is expressed as an average over 20 m. The distance of 20 m corresponds to twice the length of half a coach, and the sound and vibration generated by two adjacent bogies with the same type of wheels are analysed.

2.2.6 Radiation options

The radiation from each noise component is predicted in terms of sound pressure at one microphone point, corresponding to the position used in the measurements (Figure 2.3).

For the wheel, the sound radiation is calculated using separate radiation efficiencies according to the number of nodal diameters in the modes [28]. The rail radiation is predicted using the *proluf* model [3]. The radiation model is a two-dimensional approach based on replacing the vibrating rail by a series of equivalent line monopoles and dipoles within the surface [29]. For the sleeper, the "baffled plate" option is used.

In TWINS, ground reflections can be included in the radiation models with account of interference between direct and reflected sound. Here, however, the reflection effect is neglected, since the sound measurements were made close to the track (see Figures 2.3 and 2.4), and the direct sound has much greater contribution at the microphone point.

2.3 Overall Comparisons

In this section the results of the overall and spectral predictions of noise and vibration are compared with the measurements.

For the TWINS predictions, the track is represented by the continuously supported Timoshenko beam model (*rodel*) using calculated decay rates. In addition, the “mono-bloc” sleeper model is used [3, 26]. In the mono-bloc sleeper model, the sleeper is considered as a beam. This sleeper model introduces modal sleeper behaviour and frequency dependent ballast properties. Use of this model should improve the prediction at low frequencies (where the sleeper vibration is the dominant source of noise).

2.3.1 Distribution of overall measured results

The measured results will generally vary in a certain range, even if the train speed is constant. Before presenting predictions, it is useful to check the variations in the measurement data, which should be borne in mind when discussing the accuracy of the predictions.

Table 2.6 shows the standard deviations of the measured results for each wheel type and train speed. It can be considered that the TWINS model gives adequate predictions as long as the differences between measured and predicted levels fall within a range of plus/minus one standard deviation of the measured results. From Table 2.6 this is generally about ±2.0 dB for the noise and ±2.5 dB for the rail vibration.

In Table 2.6, wheels A, C, D and F are installed on trailer vehicles, and trailer vehicles radiate mainly rolling noise. Therefore, both noise and rail vibration measurements for the four wheel types are suitable for the TWINS validation. Wheels B and E are installed on motor vehicles. The noise radiated from motor vehicles consists of rolling noise and traction-motor fan noise. The traction-motor fan noise generally has a much greater contribution to the total noise of these vehicles than the rolling noise has (see Figure 1.1).

Therefore, for the wheels B and E, only rail vibration measurements are considered for the validation.

As a test train equipped with wheels E and F ran during the measurement campaign, the measured results for wheels E and F are available at the train speed range of 70-120 km/h. However, not all train speeds were measured for the other wheel types, as indicated in Table 2.6. This is because these measurements were carried out mainly using service vehicles which operated at speeds of 100-110 km/h.

Table 2.6 Standard deviations of measured results in dB
(overall A-weighted level).

Velocity (km/h)	Rail vibration [a]					Noise				
	70	100	110	120	Δ[c] (total)	70	100	110	120	Δ (total)
A	---	2.4 (9)[b]	2.5 (20)	---	2.5 (29)	---	1.9 (8)	2.0 (17)	---	2.0 (25)
B	---	2.1 (7)	3.4 (12)	---	2.9 (19)	---	---	---	---	---
C	---	2.0 (13)	3.2 (7)	---	2.4 (20)	---	1.7 (13)	1.4 (7)	---	1.6 (20)
D	---	0.2 (5)	0.7 (5)	---	0.4 (10)	---	0.4 (5)	0.4 (5)	---	0.4 (10)
E	1.4 (6)	1.4 (12)	2.0 (50)	2.0 (22)	1.9 (90)	---	---	---	---	---
F	0.9 (10)	2.0 (13)	2.2 (42)	2.2 (37)	2.2 (102)	1.1 (9)	1.7 (16)	2.0 (48)	1.0 (46)	1.9 (119)

a) The rail vibration is presented in the form of A-weighted velocity levels in the vertical direction.

b) Numerical value in brackets stands for the number of sampled data.

c) Δ is derived from the following equation,

$$\Delta = \sum_i \frac{N_i \Delta_i}{N},$$

where N_i is the number of the sampled data for each train speed, Δ_i is the standard deviation corresponding to N_i and N is the total of the sampled data.

2.3.2 Noise prediction

2.3.2.1 Comparison of overall sound levels

Figure 2.13(a) shows the predicted noise levels plotted against the measured levels in terms of A-weighted levels. The individual points represent the average measurement for one of the ten wheel/speed combinations available. The solid line corresponds to the mean difference between predictions and measurements (+0.3 dB). The dashed lines show a range of +/- one standard deviation, considering all measurements as listed in Table 2.6 (the standard deviation is 2.4 dB). The mean value can be seen to be close to zero, and the overall trends are well predicted.

Figure 2.13(b) shows the total noise predicted minus measured noise in dB(A) for each wheel/track combination, with error bars representing the range of +/- one standard deviation. It can be seen that most of the mean results for the ten wheel/speed combinations are in the range +/-1.5 dB. The overall predictions show good agreement with the measured results.

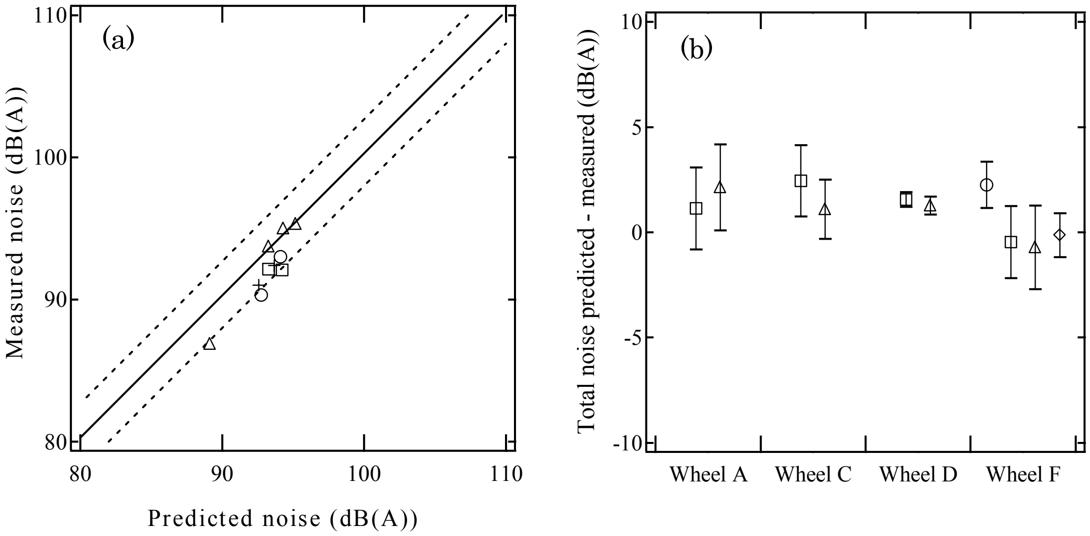

Figure 2.13 (a) Predicted noise plotted against measured noise for all case. □, Wheel A; ○, wheel C; ＋, wheel D; Δ, wheel F; (b) Total predicted noise minus measured noise in dB(A). ○, 70 km/h; □, 100 km/h; Δ, 110 km/h; ◊, 120 km/h.

2.3.2.2 Comparison of spectral results

In order to consider the spectral variation, the difference between predicted and measured noise spectra is constructed for each of seven wheel/speed combinations in 55 measurements. Figure 2.14 shows the spectral differences as the mean and a range of +/- one standard deviation for all cases. The results can be seen to be close to zero above 250 Hz. The average difference is -0.8 dB in the whole frequency range 250-8000 Hz, while the average standard deviation of the results is 3.5 dB. The results show a slight under-prediction below 1000 Hz. This may be because the rail vibration is not predicted correctly, due to omission of torsional motion. Below 250 Hz, the agreement is poor, since the measured results were contaminated by wind noise.

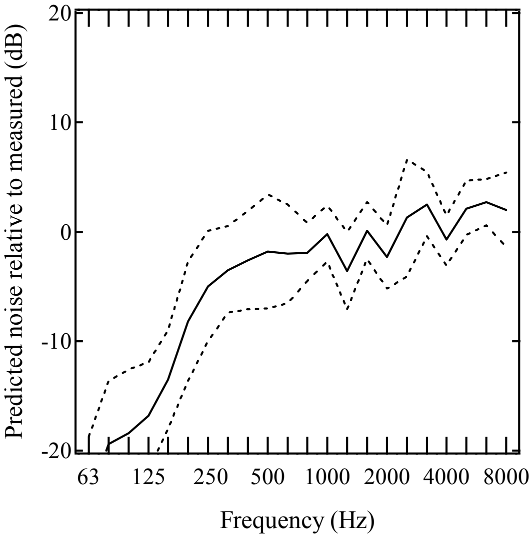

Figure 2.14 Average differences between predicted and measured noise spectra for all cases. ——, Mean; - - -, mean ± standard deviation.

Figure 2.15 shows the total predicted sound pressure level minus measured level for each wheel/track combination and each train speed. The spectral results for wheels A and D are shown only at the speed of 110 km/h. This is because most of the measured results were obtained at the speed of 110 km/h (see Table 2.6). For wheel C, as some of the results at 110 km/h include aberrant values, only the results at 100 km/h are shown.

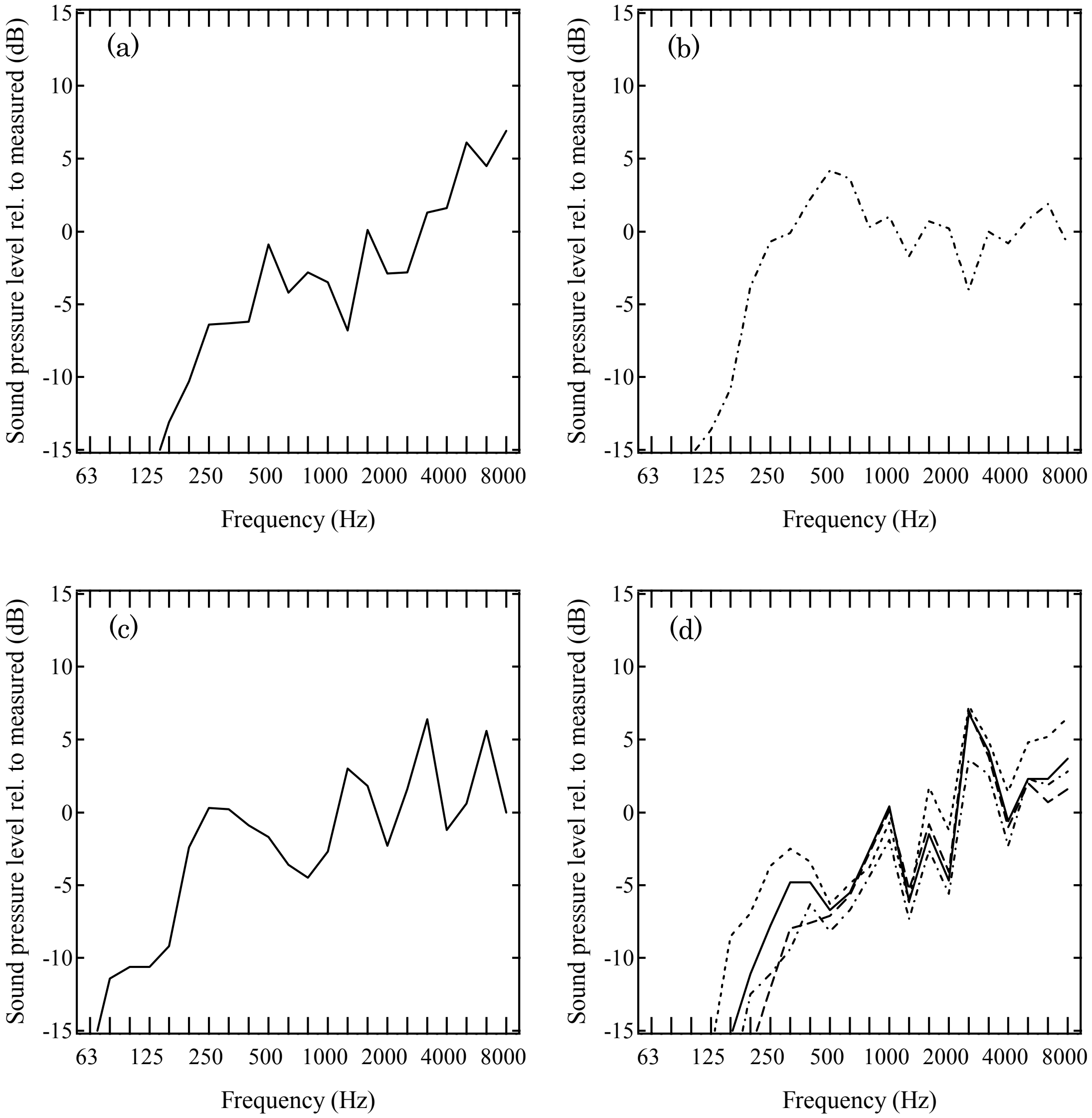

Figure 2.15 Predicted noise minus measured noise for each wheel. ······, 70 km/h; — · —, 100 km/h; ——, 110 km/h; - - -, 120 km/h. (a) Wheel A, (b) wheel C, (c) wheel D, (d) wheel F.

It can be seen that there are some differences between the results for the different wheels below 1000 Hz. The results for wheels C and D can be seen to be closer to 0 dB in the frequency range above 250 Hz, whereas the results of the other wheels show an under-prediction below 1000 Hz. At high frequencies, above 1000 Hz, the results corresponding to wheel D vary significantly. This is probably related to the fact that the predicted wheel resonances do not necessarily lie in the correct one-third octave band. The results of wheels A, D and F are over-predicted above 2500 Hz, whilst the predictions of wheel C show good agreement with the measurements. These differences are not significant considering that assumed roughness spectra have been used, which may differ from the actual ones. From Figure 2.15(d), it can be noted that the difference does not depend strongly on train speed.

2.3.2.3 Contributions of rail, wheel and sleeper

Figure 2.16 shows the separate contributions of noise from rail, wheel and sleeper to the total prediction in the form of A-weighted absolute spectra. The average measured spectra are also shown for comparison.

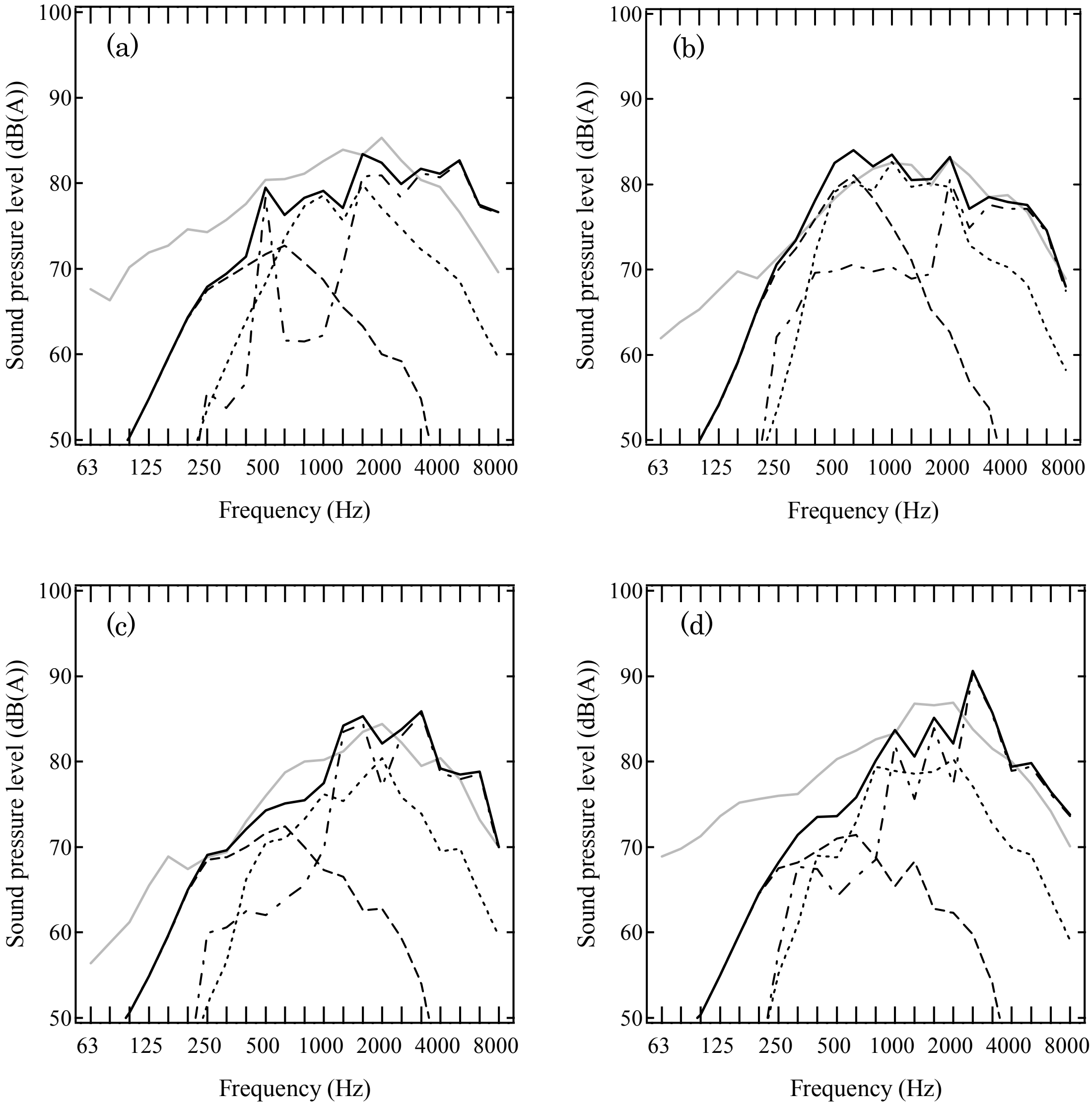

Figure 2.16 Predicted and measured noises for each wheel. ——, Measured noise; ——, predicted noise; - - -, sleeper; ······, rail; — · —, wheel. (a) Wheel A, 110 km/h, (b) wheel C, 100 km/h, (c) wheel D, 110 km/h, (d) wheel F, 110 km/h.

It can be seen that the sleeper is the most important source below around 400 Hz, whilst the wheel is the predominant source above 2000 Hz. In the middle frequencies, the dominant component in the total noise depends on the wheel type. For wheels A and C, the rail becomes dominant in the middle frequencies. On the other hand, for wheels D and F, the wheel has almost the same contribution to the total noise as the rail has between 1000 and 2000 Hz. It can be seen from Tables 2.4 and 2.5 that the radial modes of wheel F commence from 1000 Hz due to the thin web; the same is true for wheel D.

Figure 2.17 shows the relative contributions of wheel, rail and sleeper for each wheel type compared with the results corresponding to wheel A. The relative contribution of each noise component can be seen to be independent of train speed. For the rail, the relative contributions are in the range +/-1 dB(A), and this means that the noise components of the rail are comparable for the three wheel types considered here. For the wheel, the sound generated by wheel F is greater than those of the other wheels.

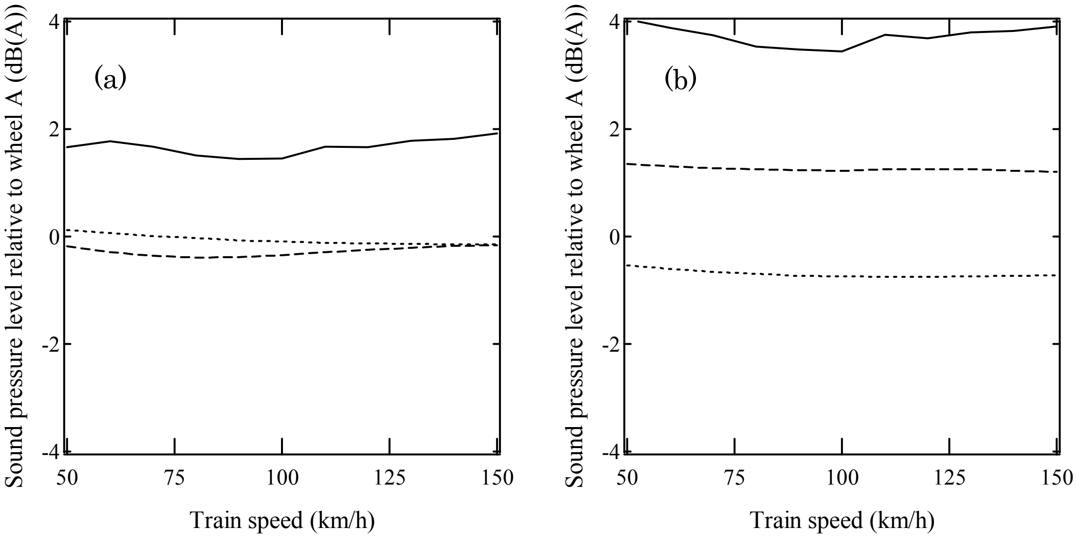

Figure 2.17 Predicted noise components from rail, wheel and sleeper relative to wheel A. ······, Rail; ——, wheel; - - -, sleeper; (a) wheel D, (b) wheel F.

Figure 2.18 shows the overall A-weighted wheel noise component of each wheel relative to the results of wheel A. Results are shown for two different roughness spectra, as shown in Figure 2.12. The changes in relative noise levels of each wheel do not depend strongly on train speed. Wheel C is quieter than the others; it is about 4 dB quieter than wheel A. It can be seen that the noise of wheels D and F is greater than the other wheels. This is due to the fact that these wheels have thinner curved webs. Wheel C has the lowest wheel noise component as it has a straight web.

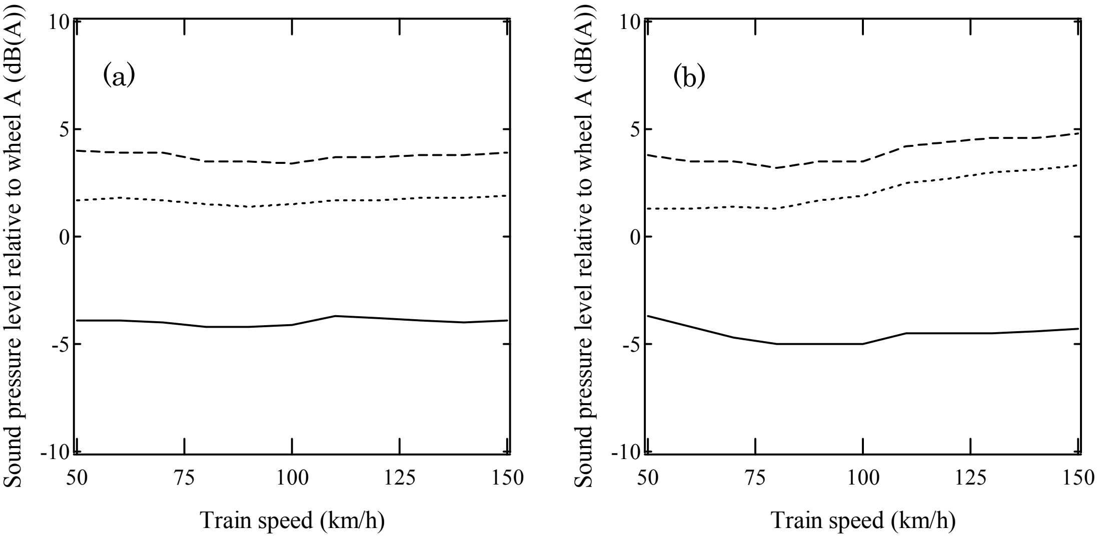

Figure 2.18 Predicted wheel noise relative to wheel A. ——, Wheel C; ⋯⋯, wheel D; - - -, wheel F. (a) Disc braked wheel roughness, (b) tread braked wheel roughness.

Figure 2.19 shows the relative noise levels of each wheel compared with the results of wheel A in the form of the transfer function from roughness to noise. These relative noise levels therefore do not include roughness effects. It is clear that wheel C is quieter than the other wheels. The results of wheels D and F have similar trends, whereas these trends are not found in the results of wheel A. This suggests that the noise radiation of the wheel depends on the wheel web geometry. Above 2500 Hz, it is seen that, for wheels D and F, the variations of the relative noise levels are large (up to 10 dB). This is also because the radial modes of wheels D and F occur from 1000 Hz due to the thin web. For wheel C, the variations of the relative levels are about -5 dB lower than wheel A above 2500 Hz.

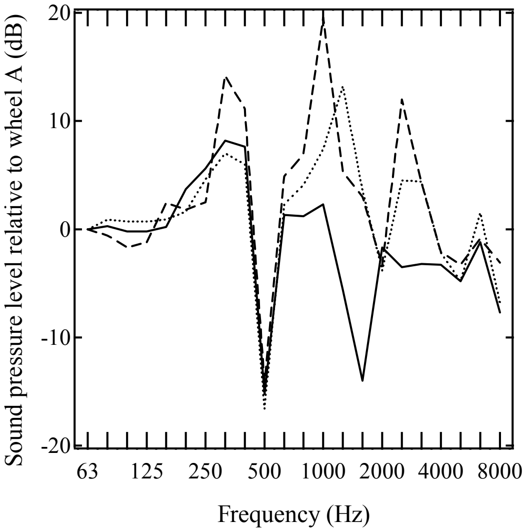

Figure 2.19 Relative noise of each wheel compared with the results of wheel A at 110 km/h. ——, Wheel C; ·····, wheel D; - - -, wheel F.

2.3.3 Rail vibration prediction

2.3.3.1 Comparison of overall levels

Figure 2.20 shows predicted vertical rail vibration velocity level plotted against measured level in terms of overall A-weighted levels. The individual points represent one of the 16 wheel/speed combinations available. The solid line corresponds to the mean difference between predictions and measurements (-0.5 dB). The dashed lines show a range of +/- one standard deviation including all the runs listed in Table 2.6 (the standard deviation is 2.8 dB). The overall trends can be seen to be well predicted.

Figure 2.21 shows a comparison of the predicted and measured rail vibration velocity level for each wheel/track combination, with error bars representing the range of +/- one standard deviation. It can be seen that for most of the results for the 16 wheel/speed combinations the mean is in the range +/-1.5 dB. The overall predictions show good agreement with the measured results.

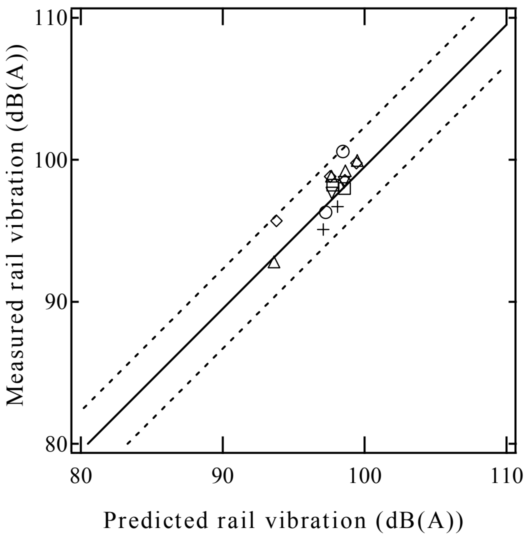

Figure 2.20 Predicted rail vibration velocity in the vertical direction plotted against measured rail vibration velocity for all case. □, Wheel A; ∇, wheel B; ○, wheel C; +, wheel D; ◊, wheel E; Δ, wheel F.

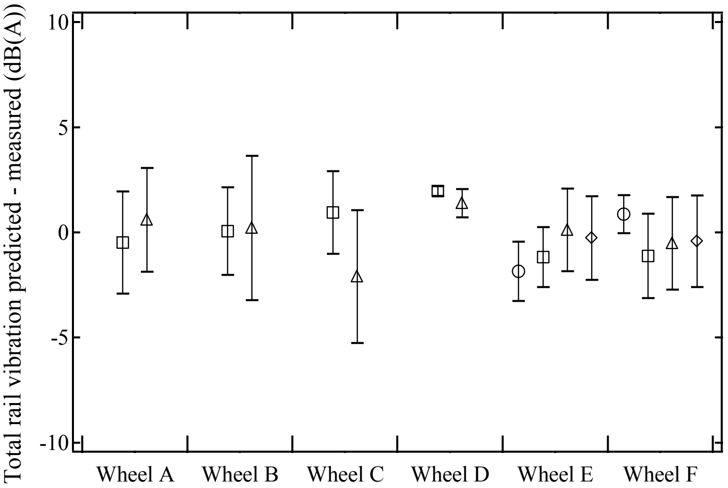

Figure 2.21 Total predicted rail vibration velocity in the vertical direction minus measured rail vibration velocity. ○, 70 km/h; □, 100 km/h; Δ, 110 km/h; ◊, 120 km/h.

2.3.3.2 Comparison of spectral results

Figure 2.22 shows the spectral differences as the mean and a range of +/- one standard deviation for all 85 cases available. The overall trends can be seen to be over-predicted. However, an under-prediction appears in the frequency region 800-1250 Hz. This under-prediction is probably related to the phenomena associated with the pinned-pinned resonance around 1000 Hz. The *rodel* model cannot predict the pinned-pinned resonance correctly, since the foundation is taken as a continuous support in the *rodel* model. It may be noted that the accelerometer is placed at midspan and so does not measure the spatial average rail vibration. Moreover, since it is located on the rail foot it may detect some torsional or foot rocking motion as well as vertical motion.

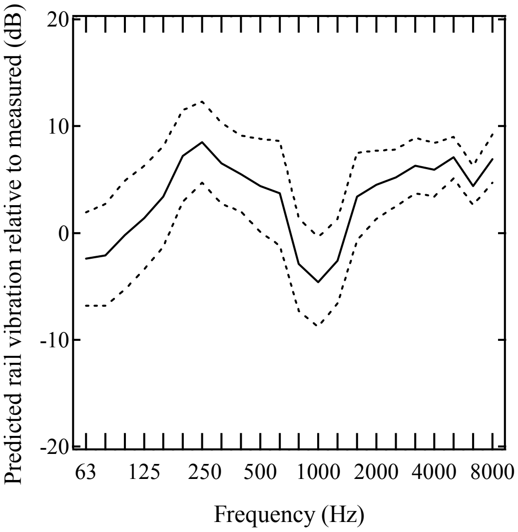

Figure 2.22 Average differences between predicted and measured rail vibration spectra for all cases. ——, Mean; - - -, mean ± standard deviation.

The overall results show a slight under-prediction in Figure 2.20, although, in Figure 2.22, the spectral results are over-predicted in most one-third octave bands. The measured spectra in velocity levels have trends with a peak around 1000 Hz. This means that the vibration components in the range of 800-1250 Hz have greater contribution to the overall levels. Therefore, as an under-prediction appears in the frequency range 800-1250 Hz, the overall levels show an under-prediction.

2.4 Summary

In order to validate the TWINS model for rolling noise prediction, a comparison in terms of noise and rail vibration has been carried out for six wheel types on a typical track of Japanese railways. The main results are summarized as follows.

(1) Overall, the TWINS model gives reliable noise predictions. A linear relationship between the predictions and measurements appears in the train speed range considered,

70-120 km/h. It is found that the mean differences in noise between the predictions and measurements are in the range +/-1.5 dB.

(2) In terms of noise spectra, the average difference between the predictions and measurements in one-third octave bands is about 1 dB above 250 Hz, while the standard deviation is about 2-4 dB. The spectra are somewhat under-predicted below 1000 Hz and show an over-prediction above 2000 Hz. The over-prediction above 2000 Hz may be caused by the inadequacy due to the roughness spectra and contact filter used. Below 250 Hz, there is a significant under-prediction, since the measurements are contaminated by wind noise.

(3) The overall trends of the rail vibration are well predicted. However, the spectra are somewhat over-predicted. This may be due to the roughness used being higher than applicable for Japanese situations or due to the influence of the measurement location on the edge of the rail foot.

Through this validation work of the TWINS model, the predictions are found to be in good agreement with the measurements. Therefore, it is confirmed that the TWINS model gives reliable predictions. It is also found that the rail has greater contribution to rolling noise than the wheel in much of the frequency range.

Subsequent to the work described here, further measurements have been made of decay rates and wheel/rail roughnesses. These are shown in Appendix D.

3 EFFECT OF WHEEL LOAD

The validity of the TWINS model for the Japanese situation has been confirmed throughout Chapter 2. One aspect that has not been validated previously is the effect of vertical load on rolling noise. In this chapter, an attempt to estimate the effect of wheel load on noise and rail vibration will be made by using the TWINS model and compared with measurements.

3.1 Measurement description

Running measurements were carried out for a single track type [64-65], as listed in Table 3.1. The track conditions are nominally the same as in Chapter 2. The site is located on a narrow-gauge line, with track gauge 1.067 m. The measurements were made for two types of freight vehicles with wheels of type A, in loaded and unloaded conditions. The wheel load conditions are listed in Table 3.2.

Table 3.1 Track conditions in Tokaido line (53K150M)

Track	Rail type	Rail-pad	Sleeper	Sleeper spacing (m)	Foundation
B	60	High stiffness “5N-type”	Concrete monobloc	0.6-0.65	Ballast

Table 3.2 Freight vehicles which have been included in the measurements

Freight vehicle	Wheel	Type of braking	Length (m)	Load condition 1 (N)	Load condition 2 (N)
I	A	Tread (sinter iron)	20	23500 N	64000 N
II	A	Tread (sinter iron)	16	21500 N	81500 N

For this track, the measurements were made at two positions:

- 1 accelerometer on the rail (vertically on the rail foot),
- 1 microphone at 2.53 m from the centre of the track (i.e. 1.96 m from the near rail)

These measurement locations are shown in Figure 3.1. As before, no measurements of wheel and rail roughnesses were made during the campaign.

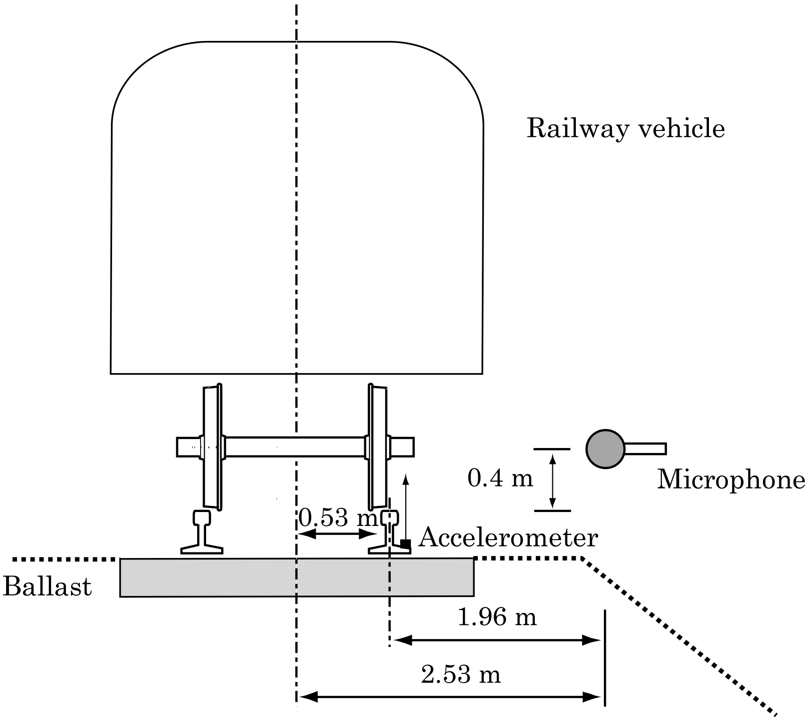

Figure 3.1 Diagram of measuring points.

3.2 Calculation description

The TWINS calculations of noise are carried out using the same track and wheel models used in Chapter 2 and the same assumed roughness spectrum. In order to estimate the effect of the wheel load, two aspects should be considered: the effect on the contact stiffness and the change in contact filter. The wheel load determines the size of the contact zone between the wheel and rail. Roughness with wavelengths that are small in comparison with the contact patch length is attenuated, and does not excite the wheel/track system as well as long wavelength roughness. The contact patch length determines the wavelength at which the contact filter rolls off. Therefore, it is necessary that the contact filter effect corresponding to each wheel load should be determined.

Figure 3.2 shows the contact filter effect due to various loads calculated using the DPRS model [23, 66]. As the wheel load is increased, the whole contact filter curve is shifted to the left. The effective frequency at which the contact filter rolls off reduces as the wheel load is increased.

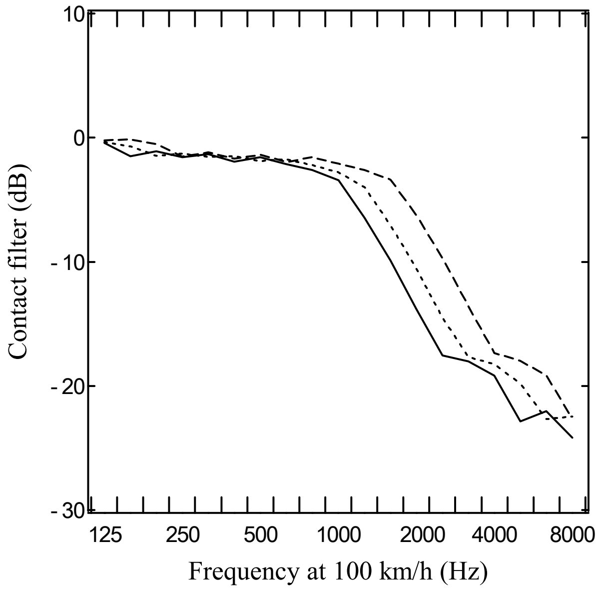

Figure 3.2 Contact filter effect due to various loads. ——, 100 kN; ······, 50 kN; - - -, 25 kN [23, 66].

Figure 3.3 shows the predicted difference in contact filter and contact stiffness effects between the two wheel load conditions. Below 800 Hz, the contact stiffness effect has no significant influence on the noise components. Above 1000 Hz, it is clear that the contact filter effect has greater influence than the contact stiffness. Therefore, the wheel/rail system is significantly influenced due to the contact filtering effect above 1000 Hz, and the increase of the wheel load could lead to some noise reduction.

3.3 Comparison of overall levels

Figure 3.4 shows the overall A-weighted noise level plotted against train speed. It can be seen that in both predictions and measurements the noise reduces as the wheel load increases. The difference between the two wheel load conditions appears to be constant, and independent of train speed. Compared with the measurements, the overall trends are predicted well. However, the predictions are all somewhat too high. This may be because the standard roughness spectrum used here differs from the actual case.

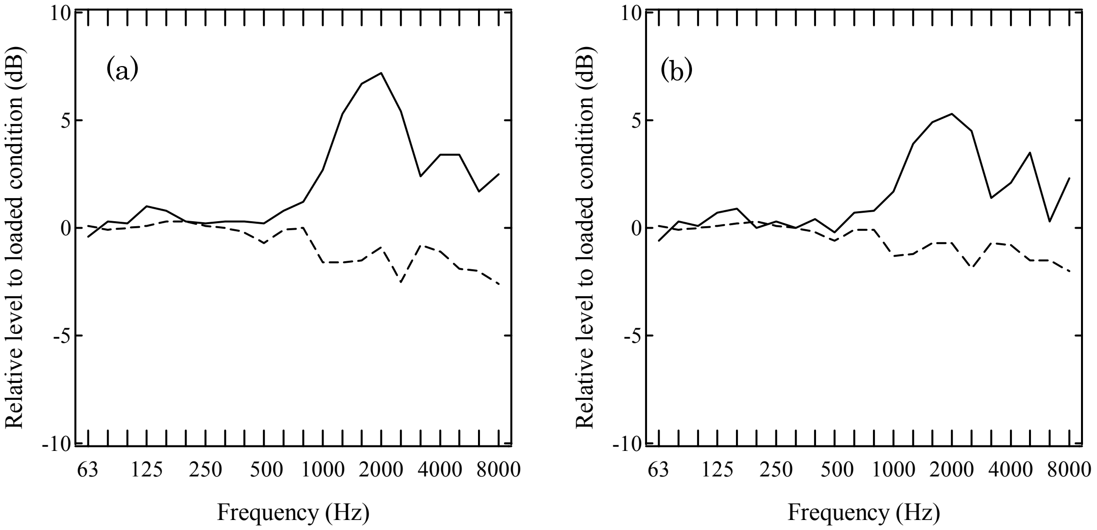

Figure 3.3 Predicted difference in contact filter and normal load effects, 100 km/h, unloaded case relative to loaded. —, Contact filter; ·····, contact stiffness. (a) Freight vehicle I, (b) Freight vehicle II.

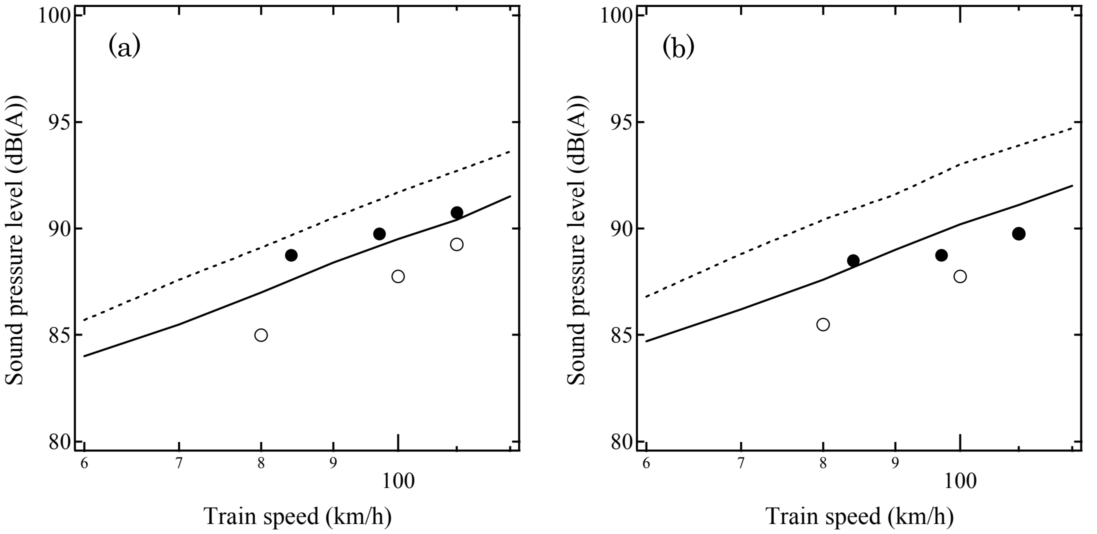

Figure 3.4 Overall levels plotted against train speed. (a) freight vehicle I, ·····, predicted, 23500 N; —, predicted, 64000 N; ●, measured, 23500 N; ○, measured, 64000 N, (b) freight vehicle II, ·····, predicted, 21500 N; —, predicted, 81500 N; ●, measured, 21500 N; ○, measured, 81500 N.

Figure 3.5 shows the differences in A-weighted level between the two wheel load conditions. The predicted difference between the two wheel load conditions is independent of train speed, whilst the measured difference appears to depend slightly on train speed. This may be due to the fact that the noise radiated from other vehicle components (e.g. rattling noise from bogies and goods on cars) may have changed in the measurements.

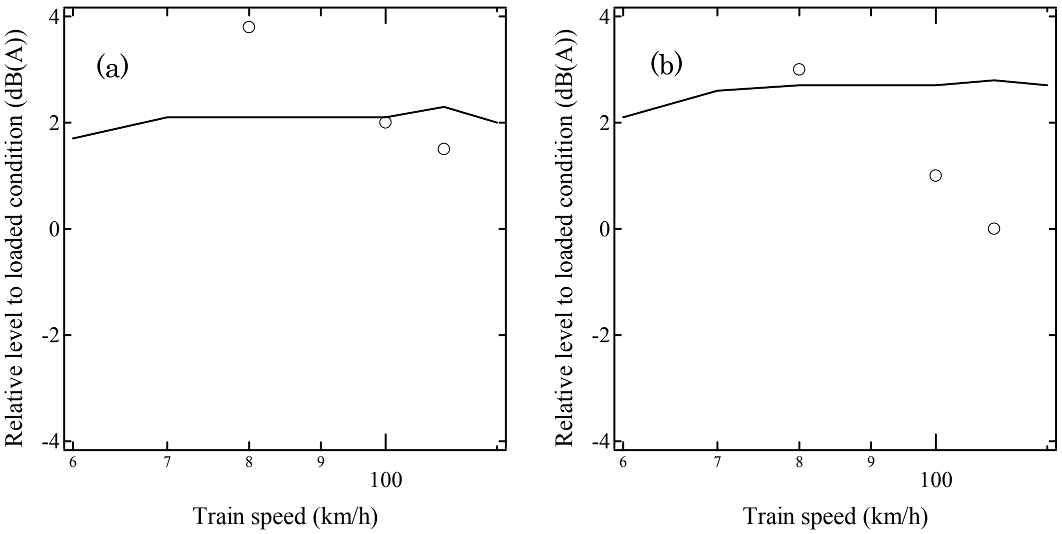

Figure 3.5 Difference in dB(A) between two wheel load conditions. —, predicted; ○, measured results; (a) freight vehicle I, (b) freight vehicle II.

3.4 Comparison of spectral results

Figure 3.6 shows the measured differences between the two wheel load conditions for freight vehicle I at a speed of 100 km/h. The corresponding predictions are also shown for comparison. It is clear that the overall trends are well predicted above 1000 Hz. However, below 1000 Hz, the predictions in noise are poor. This may also due to the fact that the noise radiated from other vehicle components may have changed, as there is much less difference in the rail vibration.

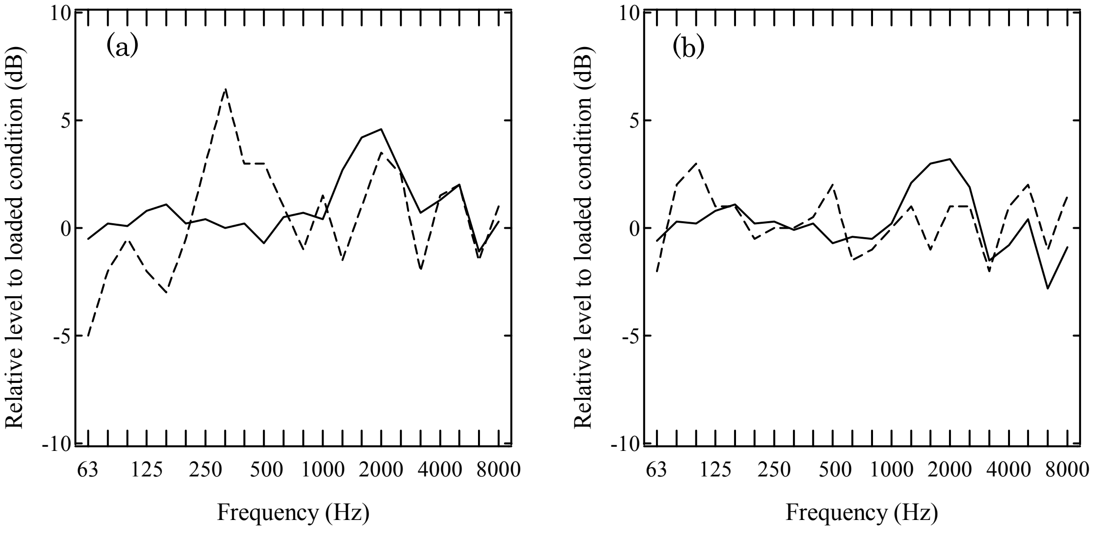

Figure 3.6 Difference in frequency spectra between two wheel load conditions, freight vehicle I, 100 km/h, —, prediction; ·····, measurement; (a) noise, (b) rail vibration.

3.5 Summary

An attempt to estimate the effect of wheel load on noise and rail vibration has been made by using the TWINS model. The results from the TWINS model show similar trends to the measurements. For the predictions and measurements, the overall levels are about 1-2 dB(A) lower in the loaded conditions. The spectral results show that, above 1000 Hz, the predictions are in quite good agreement with the measurements. This indicates that the effect of load on the contact filter is predicted correctly, since the contact filter effect has a significant effect on wheel/rail system above 1000 Hz.

4 SOUND SOURCES MEASURED WITH A MICROPHONE ARRAY

As discussed in Section 1.3, microphone arrays have been widely used in order to identify sound sources on moving trains. For aerodynamic sources this is the main means available to locate sources. However, studies to determine the source distribution of rolling noise have also been widely carried out by microphone array measurements [4, 14, 15, 16, 38, 50, 52, 57]. A common feature of these studies is that they tend to show that the wheel is the dominant source of rolling noise, whereas it is found from theoretical analyses based on TWINS models, such as in Chapter 2 and e.g. in [8, 25], that the rail can be the dominant source in much of the frequency range.

A particular question to be investigated is whether a microphone array gives a correct estimate of the sound power radiated by a rail. A rail vibrates as a structural waveguide, transmitting bending waves along its length. These waves generally have a wavelength that is longer than the acoustic wavelength and a relatively low rate of decay with distance. These features are not consistent with the assumptions used to derive sound power from array measurements, and may affect results obtained using a microphone array. In Chapter 5, the nature of the sound radiation from the rail is investigated to determine whether there is a fundamental problem in measuring it using a microphone array. This chapter sets out the background to measurements with a microphone array.

In Chapter 5, the radiation from a rail will be modelled with using an array of monopole sources, as in [29]. Here, the sound pressure at a single microphone is first determined for single and multiple sources. Then, the response of a microphone array designed for a plane wave will be simulated. Consideration is given of the situations where the multiple sources are incoherent (as assumed in determining sound power from microphone array measurement) as well as where they are coherent, which is more representative of the radiation from the rail.

In Chapters 4 and 5, the Doppler effect will not be taken into account. This can be acceptable if sources run at low speeds, say below 150 km/h. When the noise generated by the sources running at speeds in the range of 70-120 km/h (typical speed of the conventional narrow-gauge trains) are subject to one-third octave band analysis, the results are not significantly blurred due to the Doppler frequency shift. However, it should be noted that, at high source speeds, the measured results are contaminated by the Doppler effect. When the sources move at 300 km/h, the frequency shifts observed are greater than one bandwidth in one-third octave bands. In this case, it is effective to remove the Doppler effect by sweeping the array axis of the microphone array so as to track the sound sources, since the results are equivalent to those that would be measured by an observer moving at the same speed as the sources [38, 49].

4.1 Single microphone

4.1.1 Single source

A point monopole is represented as a pulsating sphere, whose radius, a, is considerably smaller than the wavelength of sound, i.e. $ka \ll 1$, where k is the wavenumber [67]. In a free field, the complex amplitude of pressure, $p(k,r)$, measured with a single microphone can be given by

$$p(k,r) = \rho c_0 \frac{jk}{1+jka} \frac{Q}{4\pi r} e^{-jk(r-a)} \approx \rho c_0 \frac{jkQ}{4\pi r} e^{-jkr} \tag{4.1}$$

where Q is the volume velocity amplitude of the source, ρ is the density of air, c_0 is the speed of sound in air, r is the distance between the source and the microphone, and a time factor of $e^{j\omega t}$ is assumed implicitly. In equation (4.1), the magnitude, $|p|$, depends on the wavenumber. This suggests that the sound power radiated by the monopole would also depend on the wavenumber. In order to make comparisons of the results obtained at any frequency, it is convenient to normalize equation (4.1) by using the time-averaged sound power, W_{mono}. From equation (4.1), the sound pressure amplitude, $p(a)$, and surface normal vibration velocity, $U(a)$, measured on the surface of the sphere, due to a harmonic volume velocity, Q, are [68]:

$$p(a) = \rho c_0 \frac{jk}{1+jka} \frac{Q}{4\pi a} \tag{4.2}$$

$$U(a) = \frac{Q}{4\pi a^2} \tag{4.3}$$

The normal intensity on the surface, $I(a)$, is given by

$$I(a) = \frac{1}{2}\mathrm{Re}\left(Up^*\right) = \frac{1}{2}\rho c_0 \left|\frac{Q}{4\pi a}\right|^2 k^2 \tag{4.4}$$

where * indicates complex conjugate. The sound power radiated, W_{mono}, is given by the integral of $I(a)$ over the surface of the sphere,

$$W_{mono} = 4\pi a^2 I(a) = \frac{\rho c_0}{8\pi}|Q|^2 k^2 \tag{4.5}$$

Equation (4.5) indicates that W_{mono} depends on the square of the wavenumber. Hence, the normalized pressure, $\tilde{p}(k,r)$, is given by

$$\tilde{p}(k,r) \simeq \frac{1}{W_{mono}^{\frac{1}{2}}} \frac{j\rho c_0 kQ}{4\pi r} e^{-jkr} \tag{4.6}$$

The sound pressure radiated by a point dipole is discussed in Appendix A1.1.

4.1.2 A line array of sources

Suppose that there are N monopoles arranged in a line with equal spacing, D (see Figure 4.1). For the estimation of the sound pressure measured with a single microphone, two cases are considered: in the first the monopoles are assumed to be incoherent, and in the second they are assumed to be coherent sources with fixed mutual phase. Provided that the sources are mutually incoherent, by using equation (4.1), the pressure, $p_{inc,mono}$, measured with the single microphone would be given by the sum of the squared amplitudes:

$$p_{inc,mono}(k) = \left\{\sum_{n=1}^{N}\left|\rho c_0 \frac{jkQ_n}{4\pi r_n} e^{-jkr_n}\right|^2\right\}^{\frac{1}{2}} = \left\{\sum_{n=1}^{N}\left|\rho c_0 \frac{kQ_n}{4\pi r_n}\right|^2\right\}^{\frac{1}{2}} \tag{4.7}$$

where Q_n is the amplitude of the n^{th} monopole, and r_n is the distance between the n^{th} monopole and the microphone. In the case of coherent sources, the pressure, $p_{coh,mono}$, is given by the sum of the complex contributions

$$p_{coh,mono}(k) = \sum_{n=1}^{N} \rho c_0 \frac{jkQ_n}{4\pi r_n} e^{-jkr_n} \tag{4.8}$$

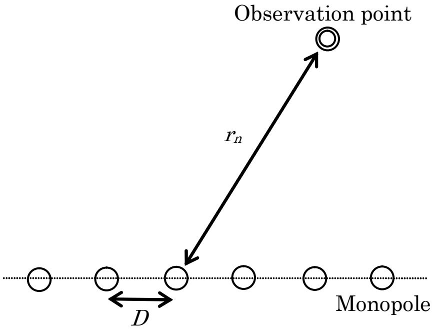

Figure 4.1 Illustration of a line array of monopole sources.

It is again convenient to normalize these equations by using the time-averaged sound power, $W_{inc,mono}$ and $W_{coh,mono}$ which can be determined as follows.

For N incoherent sources with radius a, in a free field, the sound power is simply the sum of the powers from the individual sources. Therefore, the total sound power radiated, $W_{inc,mono}$, is given by

$$W_{inc,mono} = \sum_{n=1}^{N} \frac{\rho c_0}{8\pi} |Q_n|^2 k^2 \tag{4.9}$$

For the case of N coherent sources, the pressure, $p_{n,coh,mono}(a)$, and surface normal velocity, $U_{n,coh,mono}(a)$, on the n^{th} monopole are given by

$$p_{n,coh,mono}(a) = \sum_{i=1}^{N} \rho c_0 \frac{jk}{1+jka} \frac{Q_i}{4\pi r_{ni}} e^{-jkr_{ni}} \tag{4.10}$$

$$U_{n,coh,mono}(a) = \frac{Q_n}{4\pi a^2} \tag{4.11}$$

where r_{ni} is the distance between the i^{th} monopole and the surface of the n^{th} monopole. Thus,

$$r_{ni} = \begin{cases} (n-i)D & (n \neq i) \\ a & (n=i) \end{cases} \tag{4.12}$$

The normal intensity, $I_{n,coh.mono}(a)$, on the n^{th} monopole is given by

$$I_{n,coh,mono}\left(a\right) = \frac{1}{2}\mathrm{Re}\left(U_{n,coh,mono}(a)\,p_{n,coh,mono}(a)^{*}\right) \tag{4.13}$$

and the total sound power radiated, $W_{coh,mono}$, is given by

$$W_{coh,mono} = \sum_{n=1}^{N} 4\pi a^{2} I_{n,coh,mono}\left(a\right) = 2\pi a^{2}\sum_{n=1}^{N}\mathrm{Re}\left(U_{n,coh,mono}\,p_{n,coh,mono}(a)^{*}\right) \tag{4.14}$$

Hence, the normalized pressures, $\tilde{p}_{inc,mono}\left(k,r\right)$ and $\tilde{p}_{coh,mono}\left(k,r\right)$, are given by

$$\tilde{p}_{inc,mono}\left(k,r\right) = \frac{1}{W_{inc,mono}^{\frac{1}{2}}}\left\{\sum_{n=1}^{N}\left|\rho c_{0}\frac{kQ_{n}}{4\pi r_{n}}\right|^{2}\right\}^{\frac{1}{2}} \tag{4.15}$$

$$\tilde{p}_{coh,mono}\left(k,r\right) = \frac{1}{W_{coh,mono}^{\frac{1}{2}}}\sum_{n=1}^{N}\rho c_{0}\frac{jkQ_{n}}{4\pi r_{n}}e^{-jkr_{n}} \tag{4.16}$$

Appendix A1.2 similarly gives the response of a single microphone for a line array of dipoles.

4.2 Sound sources measured with a one-dimensional microphone array

4.2.1 Array description

The methods of the conventional array are based on following two assumptions [13, 38, 40, 45, 48, 53]:

(a) the source propagates a coherent wavefront to the microphones,

(b) the wavefront shape is known as a function of source position.

Suppose that there is a planar array of 2M+1 microphones at locations $\overrightarrow{r_m}$ (m=-M,…,M) in the x-y plane of the coordinate system (see Figure 4.2) [53]. By making the measured pressure signals, p_m, of the microphone array be individually delayed by Δ_m and summed using weighting factors, w_m, the output, s, of the microphone array is given by

$$s(\overrightarrow{e_\phi},t) = \sum_{m=-M}^{M} w_m p_m(t - \Delta_m(\overrightarrow{e_\phi})) \tag{4.17}$$

where t is the time, and $\sum_{m=-M}^{M} w_m = 1$. The individual time delays, Δ_m, are determined to achieve selective directional sensitivity in a specific direction, which is characterized by a unit vector, $\overrightarrow{e_\phi}$.

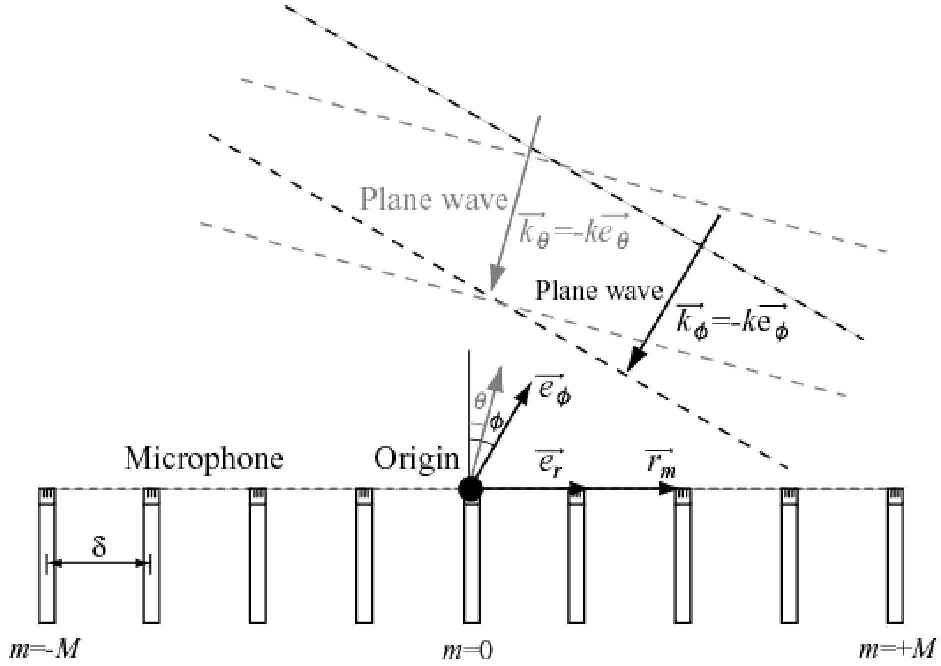

Figure 4.2 Illustration of a one-dimensional microphone array [53].

4.2.2 Beam pattern for a plane wave

For a one-dimensional microphone array with regular spacing δ (see Figure 4.3) [54], the position vector, $\overrightarrow{r_m}$, of the m^{th} microphone (m = –M,…,+M) is,

$$\overrightarrow{r_m} = m\delta\overrightarrow{e_r} \tag{4.18}$$

where $\overrightarrow{e_r}$ is the unit vector along the array axis. In order to avoid spatial aliasing, it is required that the microphone spacing is less than half the wavelength corresponding to each frequency operated by the microphone array ($\delta \le \lambda/2$).

By arranging the time delays, Δ_m, to be $\Delta_m = -\dfrac{m\delta \sin\phi}{c_0}$, the microphone array can preferentially measure signals from the preferred direction, $\overrightarrow{e_\phi}$. However, in reality, leakage from plane waves which are incident from other directions is included in the signals measured. Suppose that a plane wave of amplitude, P_0, and angular frequency, ω, is incident with a wavenumber vector, $\overrightarrow{k_\theta}$, which may be different from the preferred direction, $\overrightarrow{k_\phi}$. Then, the amplitude of the pressure measured with the microphones will be,

$$P_m(\omega) = P_0 e^{-j\overrightarrow{k_\theta}\cdot\overrightarrow{r_m}} \tag{4.19}$$

By using equation (4.19), the output, S, of the microphone array at angular frequency, ω, will be given by

$$S(\overrightarrow{e_\phi}, \omega) = \sum_{m=-M}^{M} w_m P_0 e^{-j\overrightarrow{k_\theta}\cdot\overrightarrow{r_m}} e^{-j\omega\Delta_m} = P_0 \sum_{m=-M}^{M} w_m e^{jkm\delta(\sin\phi - \sin\theta)} = P_0 W \tag{4.20}$$

In equation (4.20), the function, W, gives the beam pattern of the microphone array, which is related to a spatial resolution of the array.

Figure 4.3 shows the beam patterns of a one-dimensional microphone array for the case of an incident plane wave arriving at angle θ. Figure 4.3(a) shows the dependence of the sensitivity on the number of microphones when ϕ=0°. It can be seen that, by increasing the number of microphones, the microphone array has a higher spatial resolution. It is also found that a microphone array with a longer length has a more selective sensitivity. Figure 4.3(b) shows the beam patterns for different ratios of the microphone spacing to the wavelength. It can be seen that, as the ratio is reduced, the microphone array has a wider spatial resolution. This means that, if the microphone spacing is fixed, the microphone array will have a better resolution at higher frequencies and that if the source frequency is constant, the microphone spacing should be as wide as possible (within the limit $\delta/\lambda \leq 0.5$), since a microphone array of a longer length can have a higher spatial resolution. Therefore, Figures 4.3(a) and (b) suggests that the spatial resolution of the array is higher as the number of microphones increases or as the microphone spacing increases. This supports the characteristics of the spatial resolution of the array given by Equation (1.3). Figures 4.3(c) and (d) show the results for $\phi=30^\circ$. This shows that, by steering the array axis, the array is directed to the designed angle. However, the beam patterns are no longer symmetric.

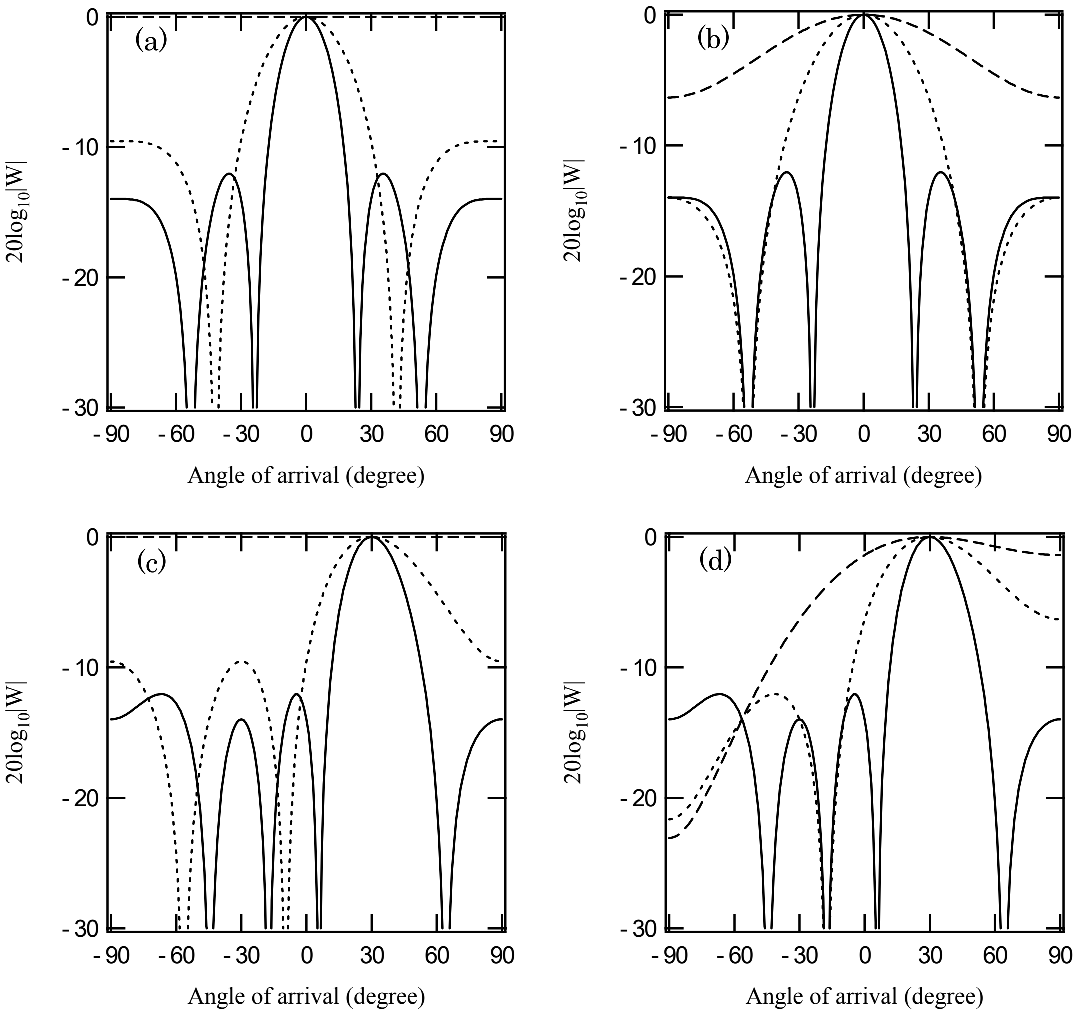

Figure 4.3 Beam patterns of a one-dimensional microphone array for a plane wave by using rectangular window. *M* is number of microphones. (a) Dependence on number of microphones, ϕ=0°. - - -, *M*=1; ········, *M*=3; ——, *M*=5, (b) dependence of δ/λ, ϕ=0°. *M*=5. - - -, δ/λ=0.125; ········,δ/λ=0.25; ——, δ/λ=0.5, (c) dependence on number of microphones, ϕ=30°. - - -, *M*=1; ········, *M*=3; ——, *M*=5, (d) dependence of δ/λ, ϕ=30°. *M*=5. - - -, δ/λ=0.125; ········, δ/λ=0.25; ——, δ/λ=0.5.

The weighting factors can be arranged in order to design the beam pattern of a microphone array. The Hanning window and rectangular window functions are commonly used [45]. The Dolph-Tschebyscheff method is also applied to determine the weighting factors of the microphones, allowing the weighting factors to be arranged to give a desirable beam pattern in terms of ratio of the main beam to side lobe height [38, 39]. Figure 4.4 shows the beam patterns resulting from several windows. In all cases, an 11-microphone line array with a spacing of 0.5λ has been used. The beam pattern for the rectangular window (i.e. the case where all the weighting factors are equal) has the narrowest main lobe, compared with the results of the other windows. However, large side lobes appear in this beam pattern. The side lobes could lead to the leakage of the signals away from the main lobe. The beam patterns for the Hanning window and the Dolph-Tschebyscheff method have a broader main lobe, but reduce the amplitudes of the side lobes.

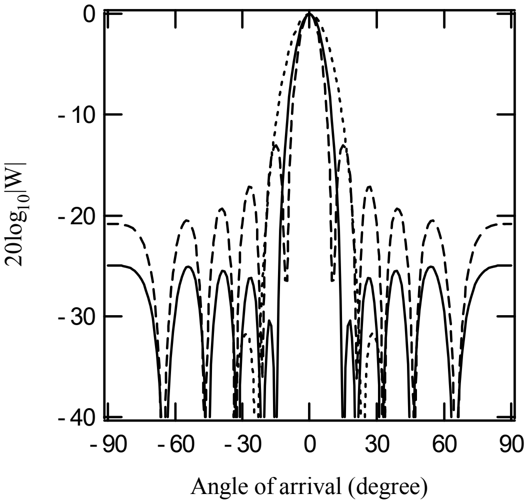

Figure 4.4 Beam patterns of a one-dimensional microphone array for a plane wave by using several weighting factors. Number of microphones is 11. Microphone spacing is half of sound wavelength. ϕ=0°. - - -, Rectangular window; ·······, Hanning window; ——, Dolph-Tschebyscheff method.

4.2.3 Single source

In the previous section, the incident field was assumed to consist of plane waves, which is appropriate for sources at large distances. However, if a one-dimensional array is located close to the sources, the microphone array should be designed to have a directional character appropriate for a spherical wave. Then, the outputs of the microphone array should depend on the distance of a measuring point to the track, as the wavefront of the incident wave would depend on the distance. Therefore, the microphone array designed for a plane wave might not give appropriate spatial distributions when the microphone array is positioned close to the sources [38, 40, 48]. Here, the dependence of the outputs of the one-dimensional microphone array on the incident wavefront from a monopole or dipole is investigated.

Suppose that a monopole source moves along a track, and that there is a line array of $2M+1$ microphones at positions $\overrightarrow{r_m}$ ($m=-M,\ldots,+M$) in the x-y plane of the coordinate system which are installed parallel to the track at a distance, r_0, from the track (see Figure 4.5).

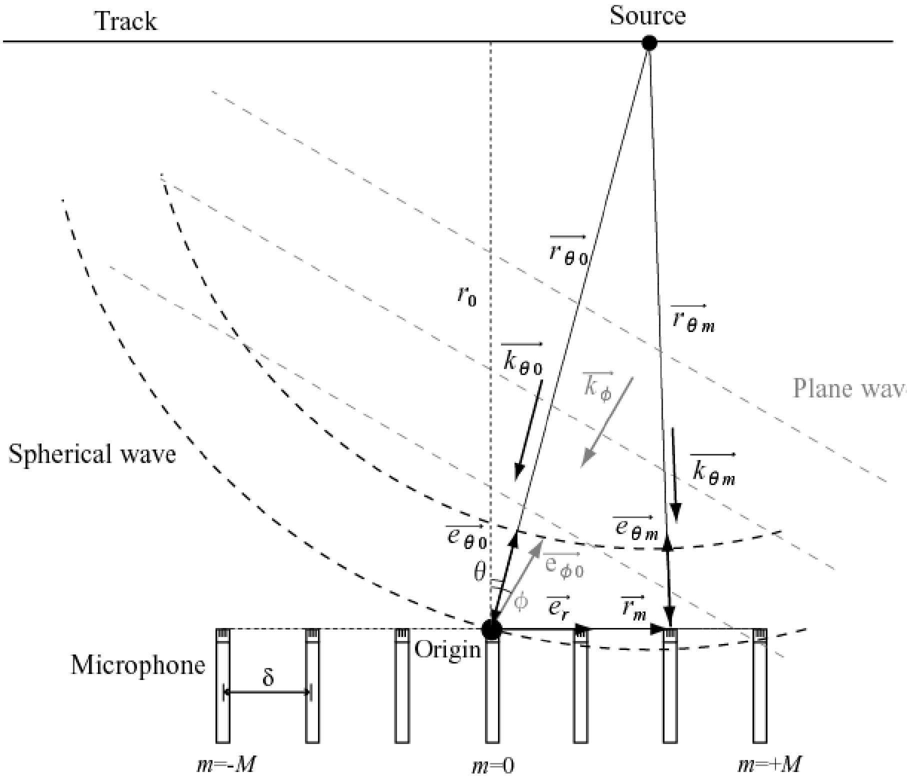

Figure 4.5 Illustration of a one-dimensional microphone array and spherical waves [48].

Here, suppose that the microphone array has been designed to be suitable for a plane wave in the direction, $\overrightarrow{e_\phi}$. It is assumed that a single spherical wave of a point monopole arrives from an angle θ relative to the centre of the array, and impinges on the m^{th} microphone with a wavenumber vector, $\overrightarrow{k_{\theta m}}(\neq \overrightarrow{k_\phi})$. Then, by referring to the procedure used in Section 4.1.1, the amplitude of the pressure, $P_m(\omega)$ measured with the m^{th} microphone will be,

$$P_m(\omega) = \rho c_0 \frac{jkQ}{4\pi\left|\overrightarrow{r_{\theta m}}\right|} e^{-j\overrightarrow{k_{\theta m}}\cdot\overrightarrow{r_{\theta m}}} = \rho c_0 \frac{jkQ}{4\pi\left|\overrightarrow{r_{\theta m}}\right|} e^{-jk\left|\overrightarrow{r_{\theta m}}\right|} \tag{4.21}$$

$$(\because \overrightarrow{k_{\theta m}} \cdot \overrightarrow{r_{\theta m}} = \left|\overrightarrow{k_{\theta m}}\right|\left|\overrightarrow{r_{\theta m}}\right| \cos 0 = k\left|\overrightarrow{r_{\theta m}}\right|)$$

where $\overrightarrow{r_{\theta m}} = \overrightarrow{r_m} + \overrightarrow{r_{\theta 0}}$. Then, the output, $S_{mono,pl}$, of the array at angular frequency ω will be given by

$$S_{mono,pl}(\overrightarrow{e_{\phi 0}}, \omega) = \sum_{m=-M}^{M} w_m P_m(\omega) e^{-j\omega\Delta_m}$$

$$= \sum_{m=-M}^{M} w_m \rho c_0 \frac{jkQ}{4\pi\left|\overrightarrow{r_{\theta m}}\right|} e^{-j\overrightarrow{k_{\theta m}}\cdot\overrightarrow{r_{\theta m}}} e^{-j\omega\Delta_m}$$

$$= \sum_{m=-M}^{M} w_m \rho c_0 \frac{jkQ}{4\pi\left|\overrightarrow{r_{\theta m}}\right|} e^{-jk\left|\overrightarrow{r_{\theta m}}\right|} e^{jkm\delta\sin\phi}$$

$$= \rho c_0 \frac{jkQ}{4\pi r_0} \sum_{m=-M}^{M} w_m \frac{r_0}{\left|\overrightarrow{r_{\theta m}}\right|} e^{-jk\left|\overrightarrow{r_{\theta m}}\right|} e^{jkm\delta\sin\phi} = \rho c_0 \frac{jkQ}{4\pi r_0} W' \tag{4.22}$$

In equation (4.22), the function, *W'*, gives the beam pattern of the microphone array.

It is again useful to normalize equation (4.22) by using the time-averaged sound power, W_{mono}, given by equation (4.5). Then, the normalized output, $\tilde{S}_{mono,pl}\left(\overrightarrow{e_{\phi 0}}, \omega\right)$, is

$$\tilde{S}_{mono,pl}\left(\overrightarrow{e_{\phi 0}}, \omega\right) = \frac{1}{W_{mono}^{\frac{1}{2}}} \sum_{m=-M}^{M} w_m \rho c_0 \frac{jkQ}{4\pi\left|\overrightarrow{r_{\theta m}}\right|} e^{-jk\left|\overrightarrow{r_{\theta m}}\right|} e^{jkm\delta\sin\phi} \tag{4.23}$$

For a point dipole, the responses of the microphone array are formulated in Appendix A2.1.

Figure 4.6 shows the beam patterns of a one-dimensional microphone array tuned for a plane wave when the incident wavefront is spherical. In Figure 4.6(a), the spatial resolution of the microphone array can be seen to depend on the ratio of the distance, r_0, to the wavelength of sound. When the ratio of the distance to the wavelength is smaller (i.e. the distance measured in wavelengths is shorter), the microphone array has a broader spatial resolution, and the maximum array gain of the microphone array at 0° is lower than 0 dB. When the distance measured in wavelengths is larger (the distance is twenty times as large as the wavelength), the incident wave is close to a plane wave, and the microphone array has a higher spatial resolution. Figure 4.6(b) shows the same effect for specific frequencies at constant distance. The distance chosen here corresponds to that used in previous measurements [58] (see also Chapter 5).

In Appendix B1, the beam patterns of a one-dimensional microphone array are demonstrated, when the array is designed for a spherical wave. The spatial resolution of the microphone array does not present the dependence upon the ratio of the distance, r_0, to the wavelength of sound or on frequency, as contrasted to the results of the array designed for a plane wave,

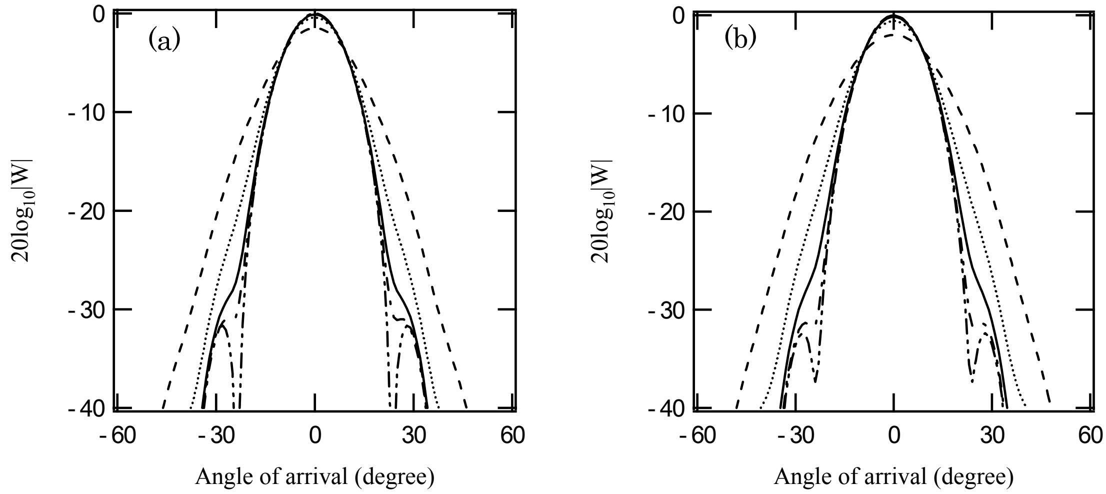

Figure 4.6 Beam patterns of a one-dimensional microphone array due to an incident spherical wave. Hanning window is used for the weighting factors. The array is tuned for a plane wave at ϕ=0°. Number of microphones is 11. Microphone spacing is half of wavelength. (a) - - -, $r_0/\lambda=5$; ········, $r_0/\lambda=10$; ——, $r_0/\lambda=20$; – · –, $r_0/\lambda=30$; – ·· –, plane wave, (b) r_0=5.72 m. - - -, 250 Hz; ········, 500 Hz; ——, 1000 Hz; – · –, 2000 Hz; – ·· –, 4000 Hz.

Figure 4.7 shows the dependence of the beam patterns on the tuned directions of the array. It can be seen that, by manipulating the array axis, the main lobe in the beam patterns is properly directed to the tuned angle. However, the maximum array gain is reduced by up to 1 dB. The drop of the array gain at ϕ=30° is mainly due to the attenuation with distance (i.e. $20\log_{10}\left(\sqrt{3}/2\right) \simeq$-1.3 dB). It is also found that, at this higher tuned angle, the main lobe is slightly wider and is not symmetric in shape.

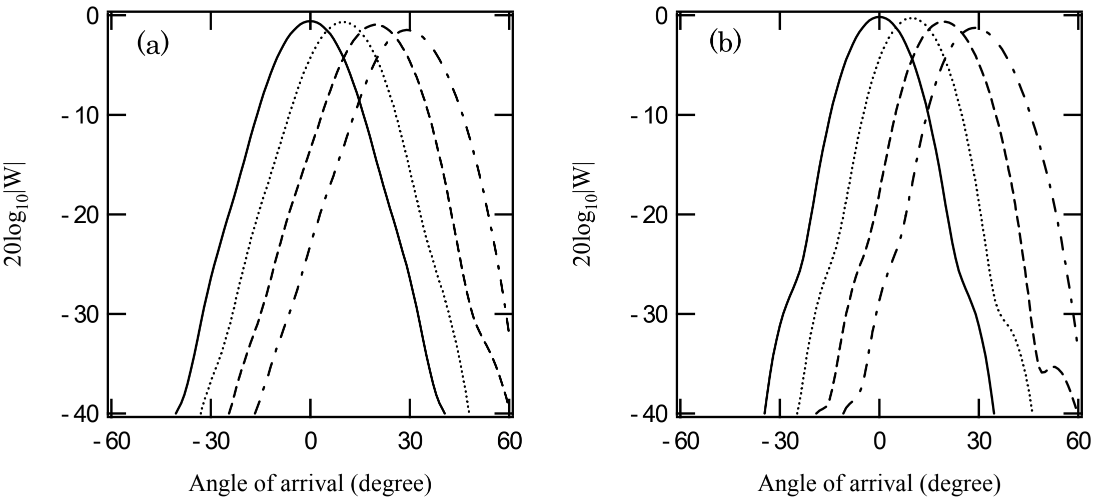

Figure 4.7 Beam patterns of a one-dimensional microphone array due to an incident spherical wave by using Hanning window. The array is tuned for a plane wave. Number of microphones is 11. Microphone spacing is half of wavelength. r_0=5.72 m. ——, ϕ=0°; ·······, ϕ=10°; - - -, ϕ=20°; – · –, ϕ=30°. (a) 500 Hz, (b) 1000 Hz.

4.2.4 A line array of sources

In this section, equations are derived for the sound pressure due to a line array of monopole sources as measured by a microphone array designed for a plane wave. These sources will be used in the next chapter to represent a rail. For a line array of dipole sources, the response of the microphone array is given in Appendix A4.

Suppose that, for the microphone array tuned for a plane wave, there are N sources arranged in a line with equal spacing. By referring to equation (4.22), the output, $S_{n,mono,pl}$, of the microphone array for the n^{th} monopole will be

$$S_{n,mono,pl}(\overrightarrow{e_{\phi 0}},\omega) = \sum_{m=-M}^{M} w_m \rho c_0 \frac{jkQ_n}{4\pi\left|\overrightarrow{r_{\theta mn}}\right|} e^{-jk\left|\overrightarrow{r_{\theta mn}}\right|} e^{jkm\delta\sin\phi} \tag{4.24}$$

where $\overrightarrow{r_{\theta mn}} = \overrightarrow{r_m} + \overrightarrow{r_{\theta 0n}}$.

The total output, $S_{inc,mono,pl}$, of the microphone array for the line array of *incoherent* monopoles will be simply given by

$$S_{inc,mono,pl}(\overrightarrow{e_{\phi 0}},\omega)=\left\{\sum_{n=1}^{N}\left|S_{n,mono}\right|^{2}\right\}^{\frac{1}{2}}$$

$$=\left\{\sum_{n=1}^{N}\left|\sum_{m=-M}^{M}w_m\rho c_0\frac{jkQ_n}{4\pi\left|\overrightarrow{r_{\theta mn}}\right|}e^{-jk\left|\overrightarrow{r_{\theta mn}}\right|}e^{jkm\delta\sin\phi}\right|^{2}\right\}^{\frac{1}{2}} \qquad (4.25)$$

By using equation (4.24), the total output of $S_{coh,mono,pl}$, of the microphone array for the line array of *coherent* monopoles will be

$$S_{coh,mono,pl}(\overrightarrow{e_{\phi 0}},\omega)=\sum_{n=1}^{N}S_{n,mono}$$

$$=\sum_{n=1}^{N}\sum_{m=-M}^{M}w_m\rho c_0\frac{jkQ_n}{4\pi\left|\overrightarrow{r_{\theta mn}}\right|}e^{-jk\left|\overrightarrow{r_{\theta mn}}\right|}e^{jkm\delta\sin\phi} \qquad (4.26)$$

These equations can be normalized by using the time-averaged sound power given by equations (4.9) and (4.14). Then, the normalized outputs, $\tilde{S}_{inc,mono,pl}$ and $\tilde{S}_{coh,mono,pl}$, are

$$\tilde{S}_{inc,mono,pl}=\frac{1}{W_{inc,mono}^{\frac{1}{2}}}\left\{\sum_{n=1}^{N}\left|\sum_{m=-M}^{M}w_m\rho c_0\frac{jkQ_n}{4\pi\left|\overrightarrow{r_{\theta mn}}\right|}e^{-jk\left|\overrightarrow{r_{\theta mn}}\right|}e^{jkm\delta\sin\phi}\right|^{2}\right\}^{\frac{1}{2}} \qquad (4.27)$$

$$\tilde{S}_{coh,mono,pl}=\frac{1}{W_{coh,mono}^{\frac{1}{2}}}\sum_{n=1}^{N}\sum_{m=-M}^{M}w_m\rho c_0\frac{jkQ_n}{4\pi\left|\overrightarrow{r_{\theta mn}}\right|}e^{-jk\left|\overrightarrow{r_{\theta mn}}\right|}e^{jkm\delta\sin\phi} \qquad (4.28)$$

In Appendix B2, the sound pressure of a line array of monopoles or dipoles as measured with a microphone array tuned for a spherical wave is similarly derived.

These equations will be used with source strengths derived from rail vibration in the next chapter to simulate the microphone array measurement of rail noise.

5 RADIATION FROM THE RAIL

In this chapter, an attempt is made to investigate the characteristics of the noise radiated by the rail and in particular the results that are measured with a one-dimensional microphone array. Simulations are given for two situations:

(a) the multiple sources are incoherent, which is assumed in determining sound power from microphone array measurements,

(b) the sources are coherent, which is more representative of the rail radiation.

5.1 Outline of MY13 array

The microphone array considered represents an MY13 array as used by RTRI [69]. A photograph of the MY13 array is given in Figure 5.1. This is a one-dimensional array composed of 119 microphones, used horizontally. The number of microphones used for each one-third octave band is shown in Table 5.1. A different set of up to 17 microphones is selected to give an optimal resolution for each band. In each case the microphones are arranged in a line with an equal spacing, which is set to one half wavelength at each one-third octave band centre frequency [69]. The weighting factors are also listed in Table 5.1, which are determined by using the Dolph-Tschebyscheff method [38]. The delay-and-sum process is implemented in the analogue circuits. The array can be used with different time delays to determine the radiation in different directions. However, the array is designed for a plane wave only.

Sound pressure measurements for the conventional narrow-gauge railway lines with the MY13 array are most commonly carried out at a distance of 6.25 m from the centre of the track (i.e. the distance between the near rail and the array is 5.72 m). This is because, due to the spatial resolution of the array, the sound distribution of an individual bogie in a running train can be separated with the array, if the array is set up at this position.

Figure 5.1 Microphone array in wayside horizontal position (MY13)

Table 5.1 Number of microphones and weighting factors (MY13)

Frequency (Hz)	500 - 5000	400	315	250	200	125 - 160
Number of Microphones	17	13	11	9	7	5
w_{-8}, w_8	0.0269	---	---	---	---	---
w_{-7}, w_7	0.0277	---	---	---	---	---
w_{-6}, w_6	0.0392	0.0509	---	---	---	---
w_{-5}, w_5	0.0515	0.0536	0.0489	---	---	---
w_{-4}, w_4	0.0636	0.0690	0.0558	0.0864	---	---
w_{-3}, w_3	0.0744	0.0825	0.0847	0.0884	0.102	---
w_{-2}, w_2	0.0830	0.0931	0.1110	0.1170	0.131	0.140
w_{-1}, w_1	0.0885	0.0998	0.1300	0.1370	0.173	0.225
w_0	0.0904	0.1020	0.1370	0.1440	0.188	0.270

Figure 5.2 shows the beam patterns of the MY13 array tuned at ϕ=0° for the case of an incident plane wave. It can be seen that, as the number of microphones is increased, the microphone array has a higher spatial resolution.

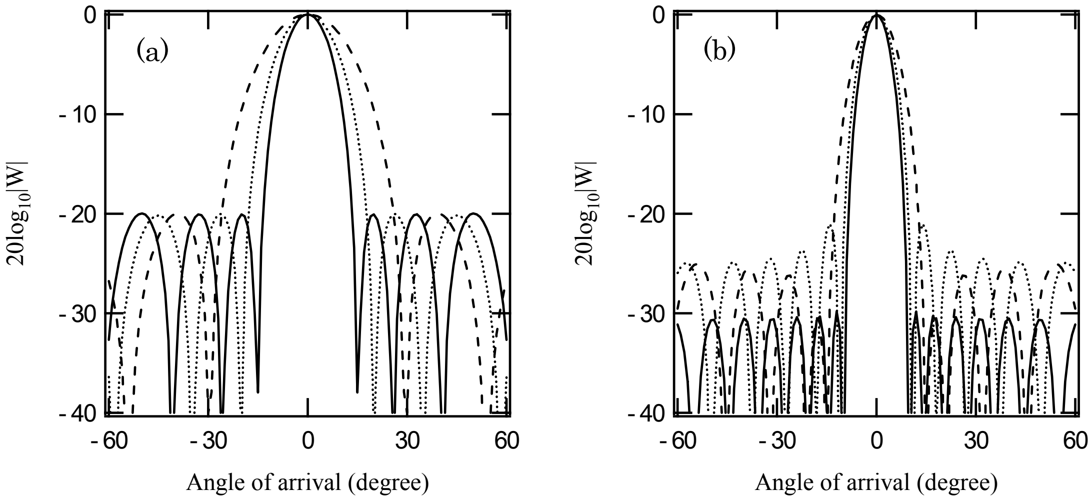

Figure 5.2 Beam patterns of an MY13 array for a plane wave at ϕ=0°. M is number of microphones. (a) - - -, M=5; ········, M=7; ——, M=9. (b) - - -, M=11; ········, M=13; ——, M=17.

Figure 5.3 shows the beam patterns of the MY13 array tuned at ϕ=0° when the incident wave front is spherical. It can be seen that, below 1000 Hz, the microphone array has a broader spatial resolution, and the maximum array gain at 0° is lower than 0 dB. This indicates that, in the case of a spherical wave from a monopole, the MY13 does not give appropriate sound distributions below 1000 Hz. Figure 5.4 shows the beam patterns of the MY13 array in the case of an incident wave from a dipole. It is found that the beam patterns have the same trends as seen in the results of a monopole (see Figure 5.3). This indicates that, for a single source, the beam patterns of the array tuned at ϕ=0° are not much affected by the type of source.

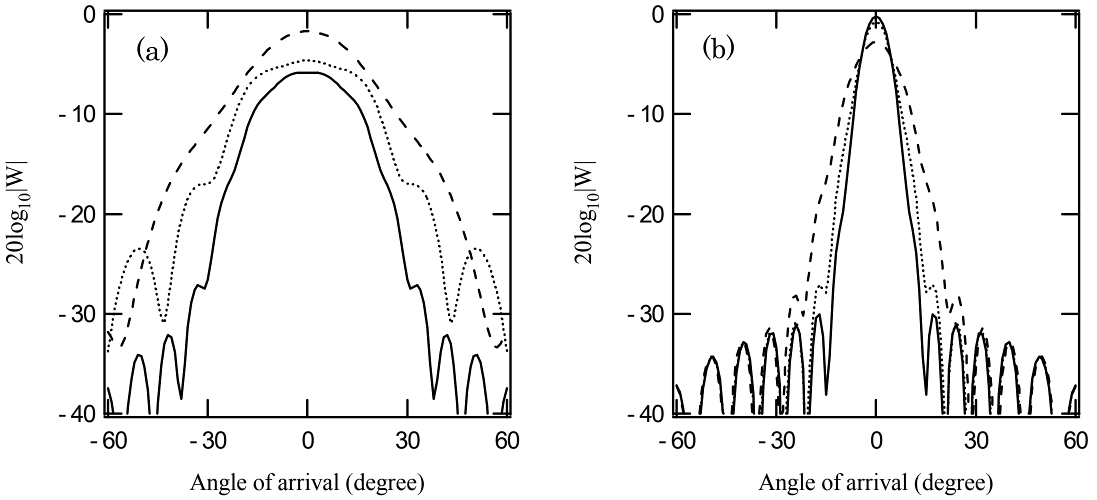

Figure 5.3 Beam patterns of an MY13 array due to an incident spherical wave at (=0°. MY13 is installed at a distance of 5.72 m from the rail. (a) - - -, 125 Hz; ········, 250 Hz; ——, 500 Hz, (b) - - -, 1000 Hz; ········, 2000 Hz; ——, 4000 Hz.

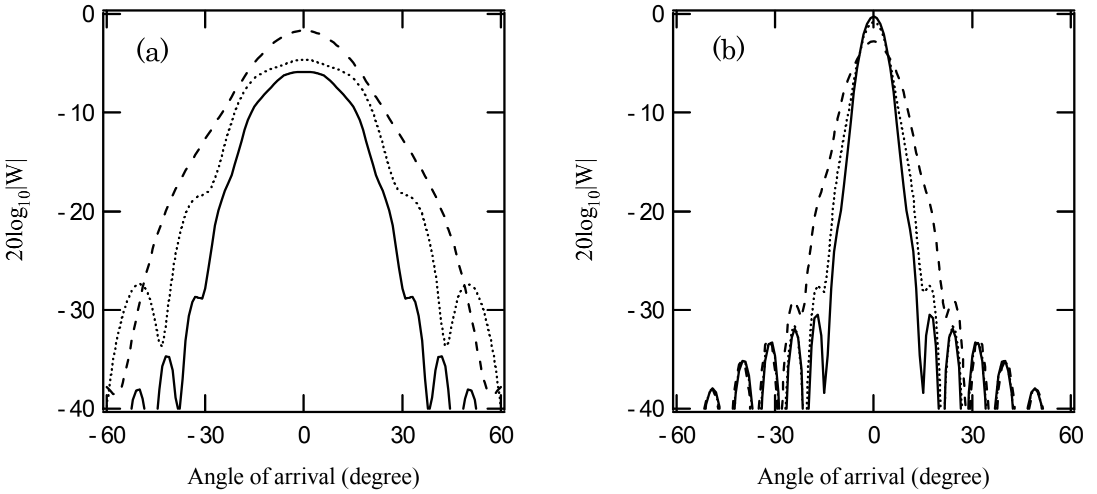

Figure 5.4 Beam patterns of an MY13 array due to an incident wave of a dipole at (=0°. MY13 is installed at a distance of 5.72 m from the rail. (a) - - -, 125 Hz; ········, 250 Hz; ——, 500 Hz, (b) - - -, 1000 Hz; ········, 2000 Hz; ——, 4000 Hz.

Table 5.2 shows the spatial resolution of the MY13 array, both as an angle and as a length. These results correspond to the beam width at 10 dB below the peak. Also listed is spatial resolution given by equation (1.3). It can be seen that the spatial resolution of the MY13 array has similar trends to those given by equation (1.3). As discussed in Section 4.2.2, it can be seen that the beam width of the array is narrower as the number of microphones is greater (see Table 5.1). For the plane wave, the ratio of the microphone spacing to the wavelength at each one-third octave band centre frequency is constant above 500 Hz, the spatial resolution of the MY13 array shows similar trends above 500

Hz. As the frequency increases, the MY13 array has a higher spatial resolution for an incident wave of a monopole or dipole. This is again due to the fact that, as the distance measured in wavelengths becomes larger, the incident wave becomes closer to a plane wave. It is again found that the spatial resolutions of the MY13 array for a monopole are similar to those for a dipole.

Table 5.2 Beam width of the MY13 array at 10 dB below peak. The MY13 array is set up at a distance of 5.72 m from the centre of the near rail (i.e. d_{-10dB}=5.72tanθ_{-10dB}).

(Hz)	$\Delta\theta$= ±$\sin^{-1}(\lambda/D)$ (Eq. (1.3))	Plane wave		Monopole		Dipole	
		θ_{-10dB} (°)	d_{-10dB} (m)	θ_{-10dB} (°)	d_{-10dB} (m)	θ_{-10dB} (°)	d_{-10dB} (m)
125	±30	±20	±2.1	±30	±3.3	±28	±3.0
160	±30	±20	±2.1	±25	±2.7	±24	±2.5
200	±19	±14	±1.4	±28	±3.0	±26	±2.8
250	±14	±10	±1.0	±25	±2.7	±25	±2.7
315	±12	±9	±0.9	±24	±2.5	±23	±2.4
400	±10	±7	±0.7	±25	±2.7	±24	±2.5
500	±7	±6	±0.6	±22	±2.3	±21	±2.2
630	±7	±6	±0.6	±18	±1.9	±18	±1.9
800	±7	±6	±0.6	±15	±1.5	±15	±1.5
1000	±7	±6	±0.6	±12	±1.2	±12	±1.2
1250	±7	±6	±0.6	±10	±1.0	±10	±1.0
1600	±7	±6	±0.6	±9	±0.9	±9	±0.9
2000	±7	±6	±0.6	±8	±0.8	±8	±0.8
2500	±7	±6	±0.6	±7	±0.7	±7	±0.7
3150	±7	±6	±0.6	±7	±0.7	±7	±0.7
4000	±7	±6	±0.6	±6	±0.6	±6	±0.6
5000	±7	±6	±0.6	±6	±0.6	±6	±0.6

5.2 Simulation procedure

5.2.1 Rail vibration

The rail vibration is determined first using the *rodel* model, as in Chapter 2, using the parameters given in Table 2.3. Using the *rodel* model, the rail response is obtained at many points along the rail due to a force at $x = 0$. The rail response due to a force can be evaluated in terms of the propagating/decaying waves in the rail. Their complex propagation constants are expressed as $s_i=\beta_i+jk_i$ (i=1 (near-field wave), 2 (bending wave)), where k_i represents the propagating part of the wavenumber and β_i represents the decay with distance. Then, the response u in wave i at a position x along the rail is given by

$$u_i(x)=u_i(0)e^{-s_i|x|}=u_i(0)e^{-(\beta_i+jk_i)|x|} \tag{5.1}$$

where $u_i(0)$ represents the point response in wave i at x=0. The total response, u, at x in one direction (vertical or lateral) consists of a sum of these two waves (near-field and bending waves), as given by

$$u(x)=\sum_{i=1}^{2}u_i(0)e^{-s_i|x|}=\sum_{i=1}^{2}u_i(0)e^{-(\beta_i+jk_i)|x|} \tag{5.2}$$

Figure 5.5 shows the wave propagation constants of a rail, predicted using the *rodel* model. The real part of the propagation constant, β_i, is directly related to the decay with distance. For the vertical rail vibration, it can be seen that the real part for the bending wave decreases considerably above 1000 Hz. This suggests that free wave propagation occurs above 1000 Hz. Similar trends are seen for the horizontal rail vibration but free wave propagation occurs above 400 Hz.

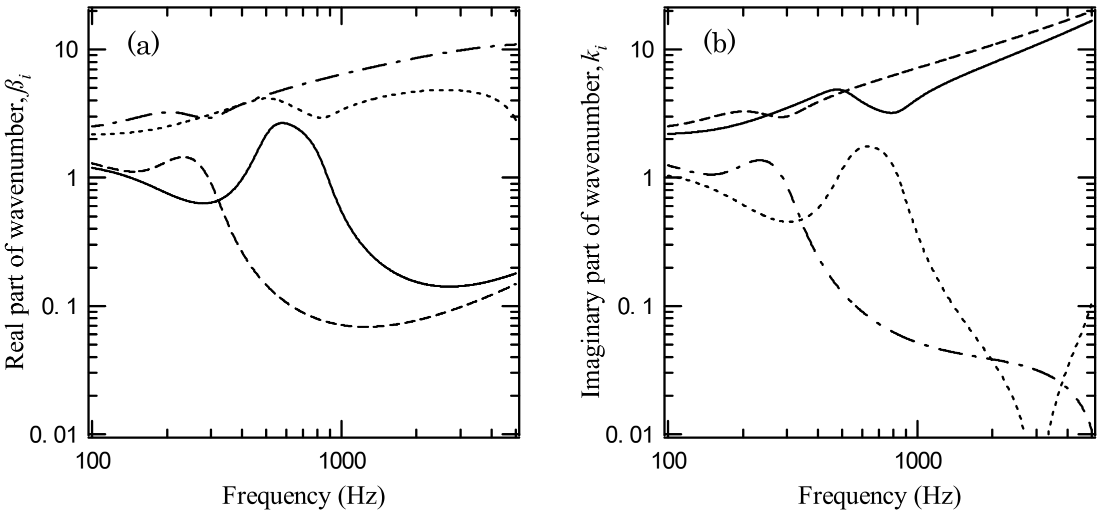

Figure 5.5 Wavenumber propagating in a rail, parameters as in Table 2.3. ——, Vertical bending wave; ·······, vertical near-field wave; - - -, horizontal bending wave; – · –, horizontal near-field wave. (a) real part, (b) imaginary part.

Figure 5.6 shows the vertical and horizontal accelerance as a function of frequency at 0, 5 and 10 m from the forcing position. For the vertical accelerance, it is found that, above 1000 Hz, the results for the three points are closer. This again indicates that free wave propagation commences above 1000 Hz. The same trends can be seen for the horizontal accelerance.

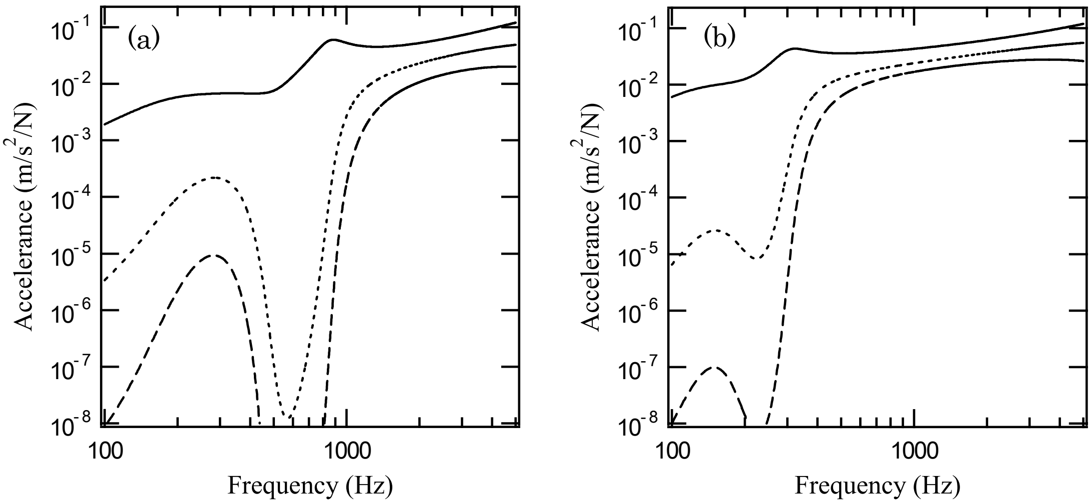

Figure 5.6 Accelerance, parameters as in Table 2.3. ——, x=0; ·······, x=5; - - -, x=10. (a) Vertical direction, (b) horizontal direction.

Figure 5.7 shows the amplitude of the vertical and horizontal accelerance as a function of the distance from the forcing position at 125 Hz, 500 Hz, 1000 Hz and 1600 Hz. It can be seen that a near-field wave appears close to the forcing position beyond which a constant decay occurs. For the vertical rail vibration, as the frequency increases, the slope can be seen to be more gradual. This is again due to free wave propagation in the rail with lower decay rates.

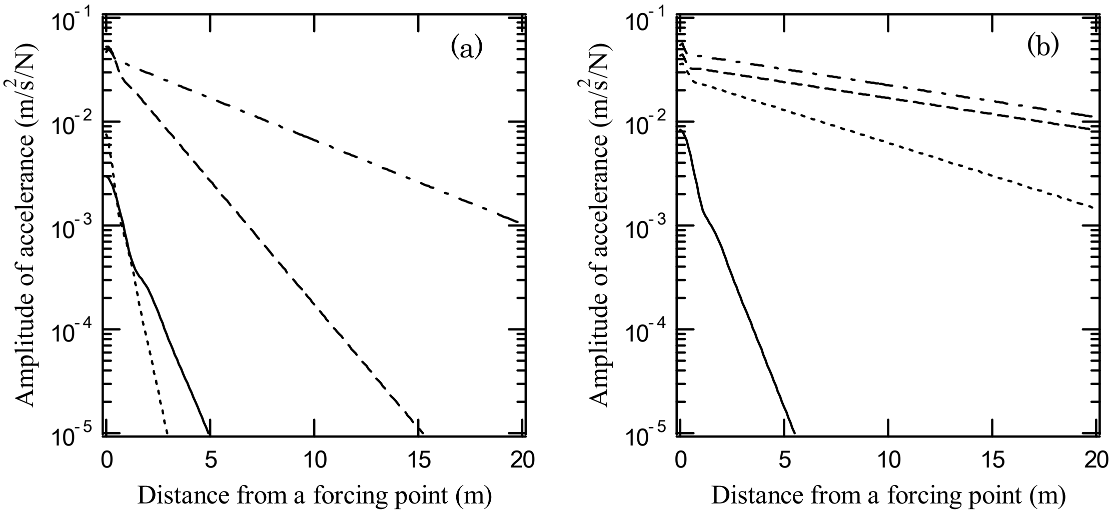

Figure 5.7 Amplitude of accelerance, parameters as in Table 2.3. ——, 125 Hz; ·······, 500 Hz; - - -, 1000 Hz; – · –, 1600 Hz. (a) Vertical direction, (b) horizontal direction.

5.2.2 Sound radiation of rail

For the sound radiation of a rail, a modelling approach similar to that used in [29] has been used. The vibrating rail is replaced by a line array of acoustic point sources of suitable source strength arranged along the centreline of the rail, as indicated in Figure 5.8. Here, both monopole and dipole point sources are considered.

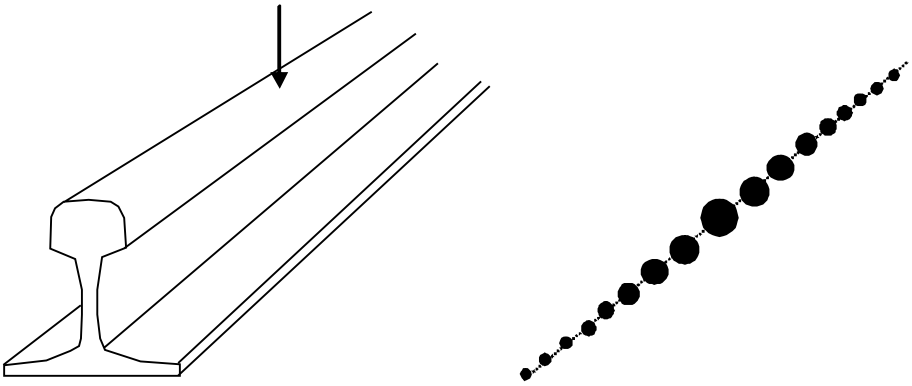

rail section

array of point sources

Figure 5.8 Modelling methods. Vibration on the rail is assigned to the source strengths of an array of point sources.

In order that the model might be equivalent to the rail, it is necessary to determine a source separation distance that is small compared with both the wavelength in air and the wavelength in the structure. On the other hand, the number of sources should not be too large, due to computational limitations. Figure 5.9 shows the wavenumbers in the rail and air. It can be seen that, although the results are comparable below 200 Hz, in the frequency range above 200 Hz the wavelength in the structure is longer than that in air. Hence, the source spacing is taken as one-quarter acoustic wavelength.

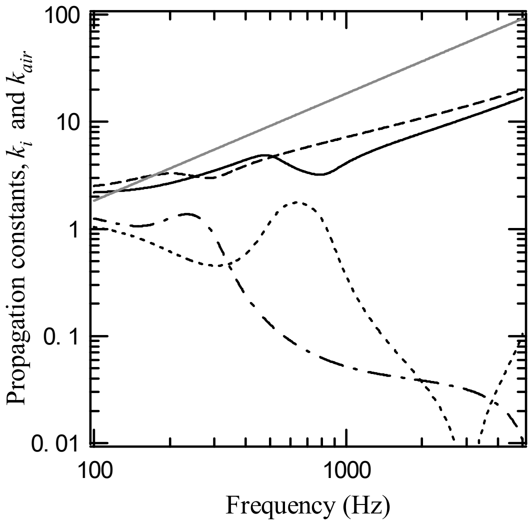

Figure 5.9 Propagation constants, parameters as in Table 2.3. k_i is the propagating part of the wavenumber in the rail. k_{air} is the wavenumber in air. ——, vertical bending wave; ·······, vertical near-field wave; - - -, horizontal bending wave; – · –, horizontal near-field wave; ——, air.

For an absolute prediction of sound radiation, the source strengths should be determined allowing for the spacing of the sources, the size of the rail section, and the velocity amplitude and phase on the surface of the rail [29]. Here, however, only the relative magnitude and phase of the source strengths are important. These are estimated by using the *rodel* model (see Appendix C), and are assigned according to equation (5.2) to represent the radiation from the two combined waves. This suggests that the sources arranged along the rail are coherent with fixed mutual phase. Meanwhile, in the microphone array measurements, the sources are assumed to be incoherent.

The length of the source region depends on the real part of the complex propagating constant, s_i. Here, the length is taken to be at least $6.5/\beta_i$, which leads to 56 dB reductions in amplitude at the end of the source region [29]. However, since at higher frequencies the decay rate is small, the source region tends to be longer, and then the number of sources becomes very large. Therefore, in order to avoid computational difficulties, if the number of total sources on one side is larger than 1000, the length has been truncated so that only half of the total number sources are used in the calculation. Table 5.3 shows the number of total sources on one side and the corresponding source length (again on one side) used to yield 56 dB reduction in the simulation. It can be seen that, for the vertical rail vibration, the total number of sources on one side is larger than 1000 above 2000 Hz. Therefore, the source length is truncated above 2000 Hz in the simulation and set to be $3.25/\beta_i$, which corresponds to 28 dB reduction in amplitude. (An investigation of the effect of source length will be given in Section 5.3.1.)

Table 5.3 Total number of sources on one side and the corresponding source length required in the simulation of the rail radiation to give 56 dB reduction in amplitude at the end of the source region.

	Vertical vibration		Horizontal vibration	
Frequency (Hz)	Number of sources	Source length (m)	Number of sources	Source length (m)
125	8	5.44	8	5.44
160	13	6.91	10	5.31
200	20	8.50	11	4.68
250	29	9.86	13	4.42
315	36	9.71	33	8.90
400	31	6.59	120	25.5
500	17	2.89	284	48.3
630	18	2.43	557	75.2
800	38	4.04	974	103.5
1000	141	12.0	1480 (720) a)	125.8 (62.9)
1250	361	24.6	2080 (1040)	141.4 (70.7)
1600	736	39.1	2792 (1396)	148.3 (74.2)
2000	1198 (599)	50.9 (25.5)	3412 (1706)	145.0 (72.5)
2500	1758 (879)	59.8 (29.9)	3958 (1979)	134.6 (67.3)
3150	2390 (1195)	64.5 (32.3)	4418 (2209)	119.2 (59.6)
4000	3024 (1512)	64.3 (32.1)	4766 (2383)	101.3 (50.6)
5000	3540 (1770)	60.2 (30.1)	4982 (2491)	84.7 (42.4)

a) Numerical value in brackets stands for the number of sources on one side and the corresponding source length used in the simulation to avoid computational difficulties. The source length is truncated and set to be $3.25/\beta_i$, which leads to 28 dB reduction in amplitude at the end of the source region.

5.2.3 Sound pressure estimation

The sound pressure generated by an array of monopole or dipole sources is estimated for a single microphone and a microphone array, which are set up at a distance of 5.72 m from the rail, as shown in Figure 5.10. By using the method derived in Section 4.2.4, the sound pressure generated by the source array is calculated at a series of receiver locations along the rail, and summed to give the total pressure at these locations. The excitation point on the rail is allowed to vary relative to the location of the microphone array. This can be seen to represent the sound pressure at a microphone as the rail vibration (due to a single wheel) passes the microphone, apart from the Doppler effect. Here, the Doppler effect is ignored. This is justified because the sources move at speeds in the range of 70-120 km/h (typical speed of the conventional narrow-gauge trains), so that the frequency shifts due to the Doppler effect have only a small contribution on estimations of the measurements shown in terms of one-third octave bands. The total length that the source region is allowed to move past the microphones is set to the length of the source region plus 6*d*, where $d = 5.72$ m is the distance from the track to the microphones.

To simulate the microphone array, it is mostly used with no time delays in order to extract the sound radiated from the sources directly in front of the array. This is because the MY13 array is mainly used for a plane wave only at ϕ=0˚. Even in cases where microphone arrays are used with a swept focus [38], the range of angles considered is generally only a few degrees.

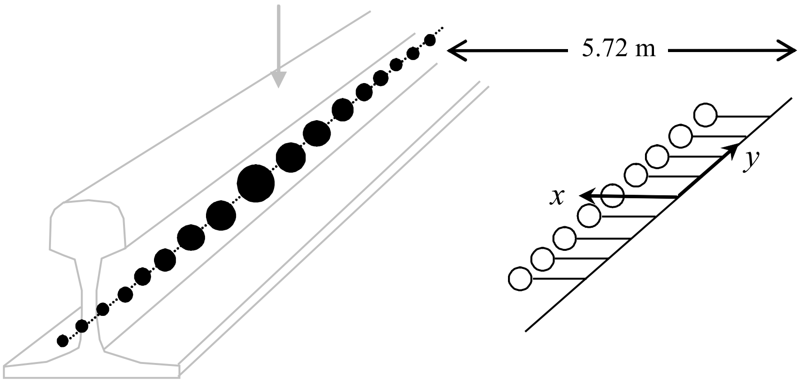

Figure 5.10 Modelling methods. The sound pressure is calculated at the microphone positions due to each point source.

5.3 Sound distribution of a rail

In this section, the estimations for an array of monopole sources are performed with the MY13 array tuned for a plane wave at ϕ=0˚. In this calculation, equations (4.27) and (4.28) are used, which give the results for the incoherent and coherent monopole sources. For the MY13 array hypothetically tuned for a spherical wave, the equivalent estimations are given in Appendix B3.

5.3.1 Source distribution

Figure 5.11 shows the distribution of vertical rail vibration amplitude along the rail, the output from a single microphone and the output from a microphone array for 125 Hz. Also shown are the results that are obtained if the same source distribution is used but the sources are assumed to be incoherent (with the same total output power). Figure 5.11(b) shows that the rail vibration is localised to a region of about 1 m from the forcing point, due to high decay rate of about 10 dB/m at 125 Hz. This effectively forms a point source. The results at the single microphone decay gradually with distance. This indicates that the single microphone measures spherical spreading from the point source. For the microphone array measurements (5 microphones at a spacing of 1.36 m), the result gives better localisation of the source. This suggests that the microphone array can locate the point source fairly well. For the wave with a high decay rate, the rail acts as a point source, hence the sound distributions measured with the single microphone and microphone array do not depend on the phase relationship between the sources.

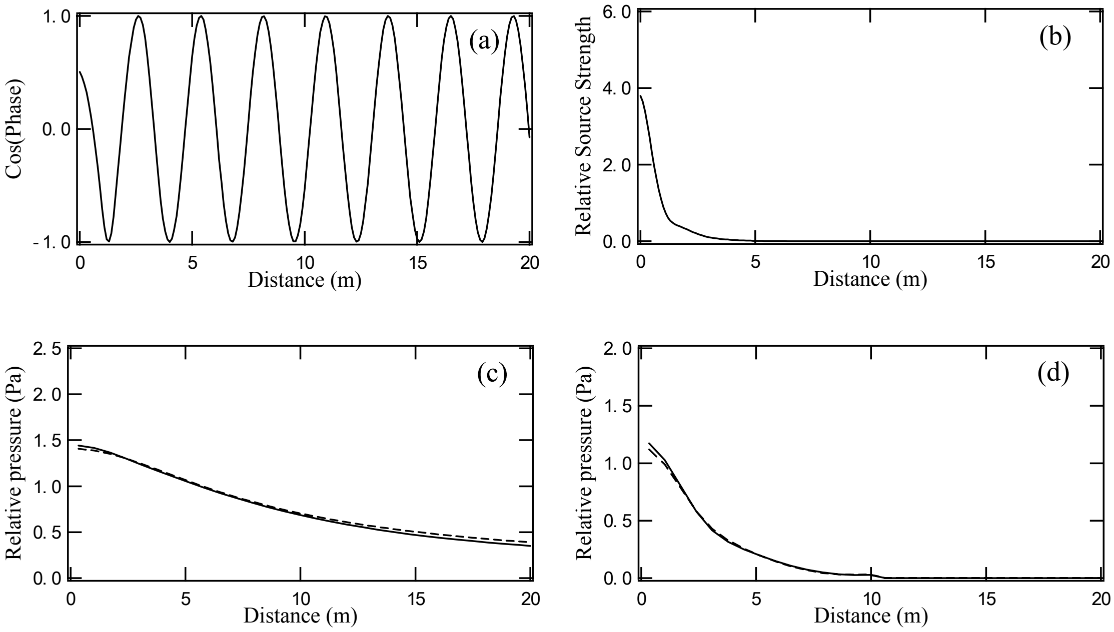

Figure 5.11 Simulation results for vertical rail vibration at 125 Hz. (a) Relative phase obtained from rail vibration, (b) relative source strength obtained from rail vibration (arbitrary scale), (c) magnitude of sound pressure at single microphone versus distance along the track from the forcing position, (d) output from microphone array. — Sources accounting for phase; - - - incoherent sources.

Similar trends are seen for 500 Hz in Figure 5.12, where the decay rate reaches its maximum value of over 20 dB/m. In this case, the array has 17 microphones with a spacing of 0.34 m.

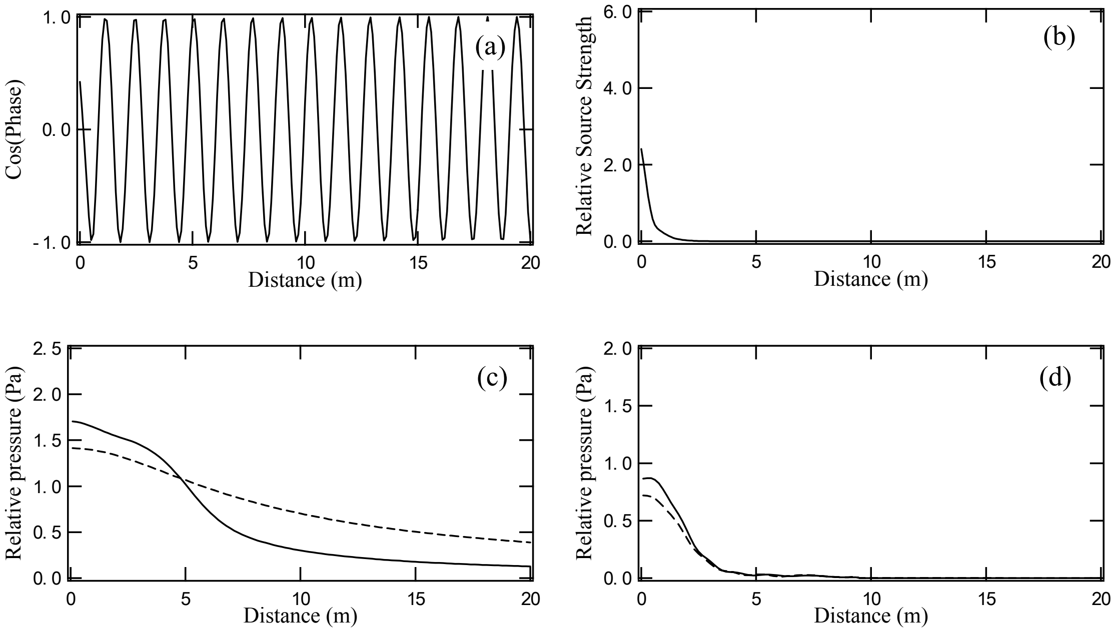

Figure 5.12 Simulation results for vertical rail vibration at 500 Hz. (a) Relative phase obtained from rail vibration, (b) relative source strength obtained from rail vibration (arbitrary scale), (c) magnitude of sound pressure at single microphone versus distance along the track from the forcing position, (d) output from microphone array. — Sources accounting for phase; - - - incoherent sources.

Figures 5.13 and 5.14 show the corresponding results for 1000 and 1600 Hz. At these frequencies, the distribution of the vertical rail vibration amplitude shows an extended source on the rail, here with a decay rate of 4.8 and 1.6 dB/m. The structural wavelengths are 1.5 and 0.96 m at the two frequencies, whereas the acoustic wavelengths are 0.34 and 0.21 m. Close to the excitation point, the presence of a near-field wave can also be seen in Figure 5.14(b). For the single microphone, a peak is found at about 2 m for both 1000 and 1600 Hz which does not exist in the rail vibration. This indicates that, as the rail is an extended line source, the rail radiates sound at an angle to the normal. This is closely related to typical supersonic structural radiation [67, 70], whose radiation direction is determined by the ratio of the structural and acoustic wavelengths.

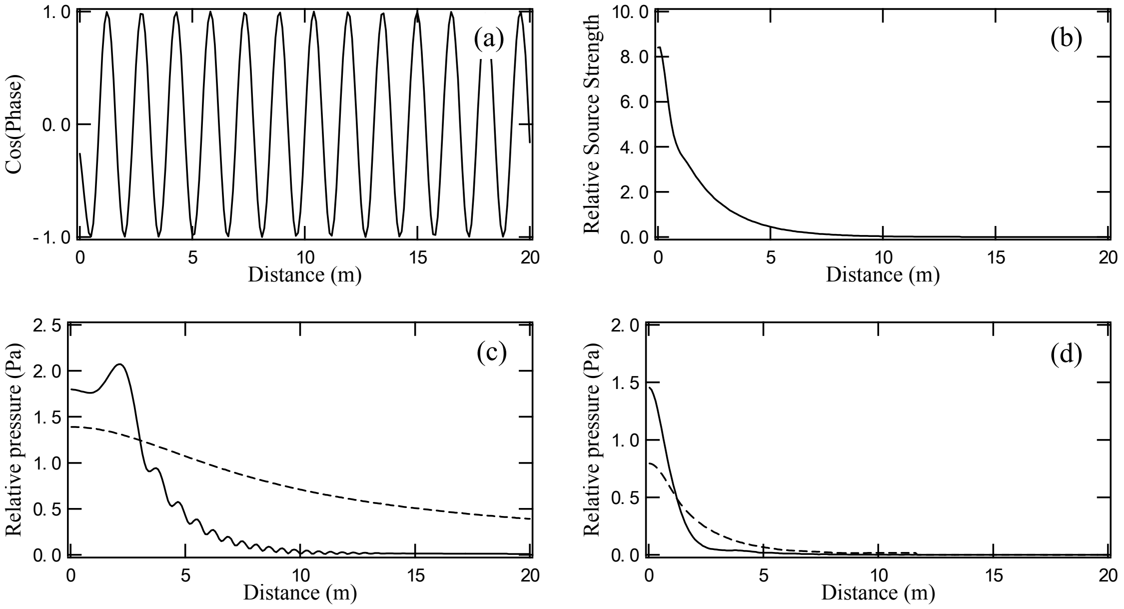

Figure 5.13 Simulation results for vertical rail vibration at 1000 Hz. (a) Relative phase obtained from rail vibration, (b) relative source strength obtained from rail vibration (arbitrary scale), (c) magnitude of sound pressure at single microphone versus distance along the track from the forcing position, (d) output from microphone array. — Sources accounting for phase; - - - incoherent sources.

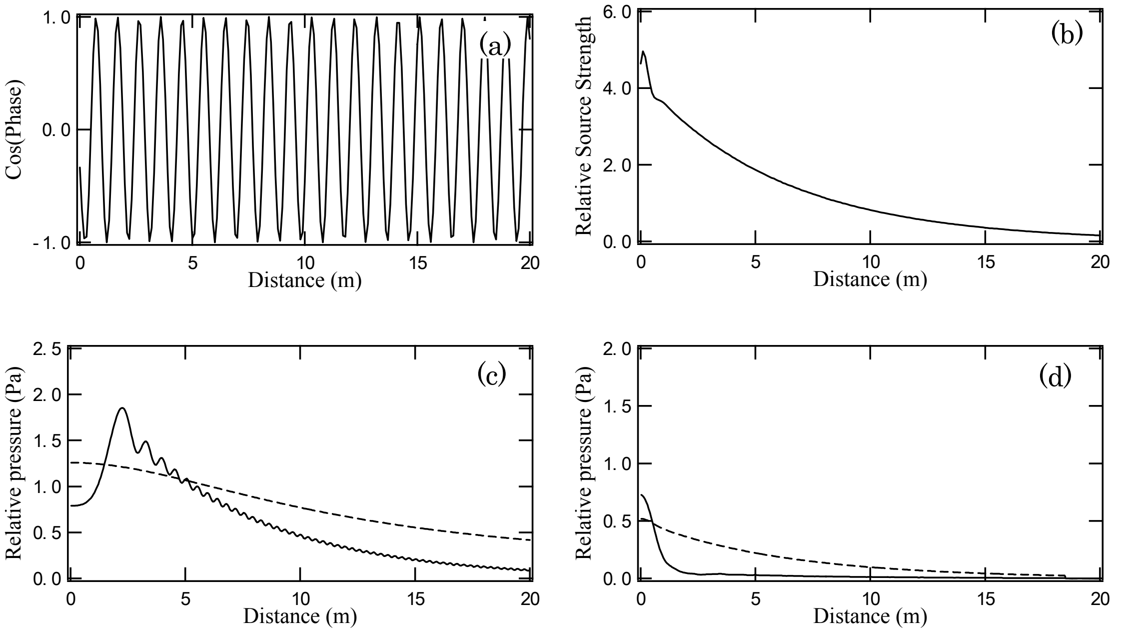

Figure 5.14 Simulation results for vertical rail vibration at 1600 Hz. (a) Relative phase obtained from rail vibration, (b) relative source strength obtained from rail vibration (arbitrary scale), (c) magnitude of sound pressure at single microphone versus distance along the track from the forcing position, (d) output from microphone array. — Sources accounting for phase; - - - incoherent sources.

At 1600 Hz, a free wave in the rail radiates at 13° ($\approx\sin^{-1}(0.21/0.96)$) to the normal. At a distance of 5.72 m from the line source, this means that the maximum pressure is expected to occur at about 1.5 m from the forcing point, which roughly corresponds with the main peak in Figure 5.14(c). These characteristics of the rail radiation are found when the rail is represented as an array of coherent sources, not the incoherent sources.

Figure 5.15 shows the angles between the *x*-axis and a line joining the origin to the positions corresponding to local maximum values in the sound distribution obtained from a single microphone. Also shown are the angles, ψ, that are obtained by

$$\psi = \sin^{-1}\left(\frac{\lambda_{air}}{\lambda_{rail}}\right) \tag{5.3}$$

where λ_{air} is the acoustic wavelength and λ_{rail} is the structural wavelength. Equation (5.3) shows the radiation direction due to the supersonic structural radiation. It is found that, above 1000 Hz, the global trends of these two angles show good agreement. This indicates that, at low decay rate, the rail is an extended line source, and radiates sound at an angle determined by the supersonic structural radiation.

In Figure 5.14, the microphone array for 1600 Hz has 17 microphones with a spacing of 0.11 m. The distributed nature of the source is reflected in the microphone array results when the sources are incoherent. However, for the case when the sources have the correct phase according to the rail vibration, the source distribution is not appropriately detected with the microphone array. In the case of the coherent sources, the microphone array only sees the radiation from the region close to the forcing point. This means that, although the rail radiates sound at an angle to the rail, the microphone array can only see the part corresponding to the vibrational near-field, and the travelling wave part of the field is suppressed.

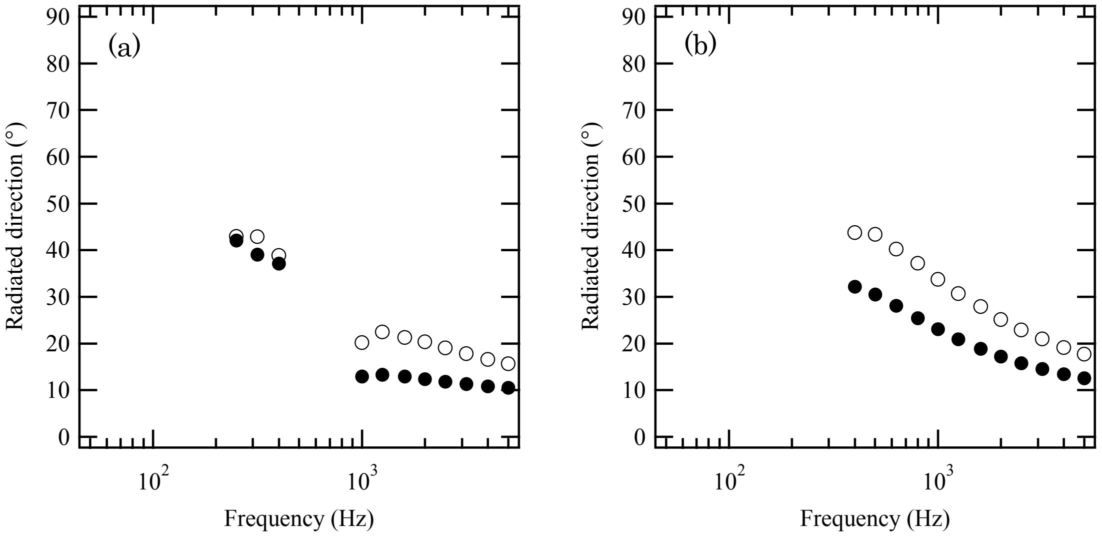

Figure 5.15 Simulated radiation directions for vertical rail vibration. ○, angle between the x-axis and a line joining the origin to the positions corresponding to local maximum values in sound distribution measured with a single microphone; ●, angle determined by the supersonic structural radiation. (a) Vertical rail vibration, (b) horizontal rail vibration.

Figures 5.16 and 5.17 show the corresponding results for the horizontal rail vibration for two different frequencies. It is found that the same trends as seen in Figures 5.11-5.14 are obtained for the horizontal rail vibration.

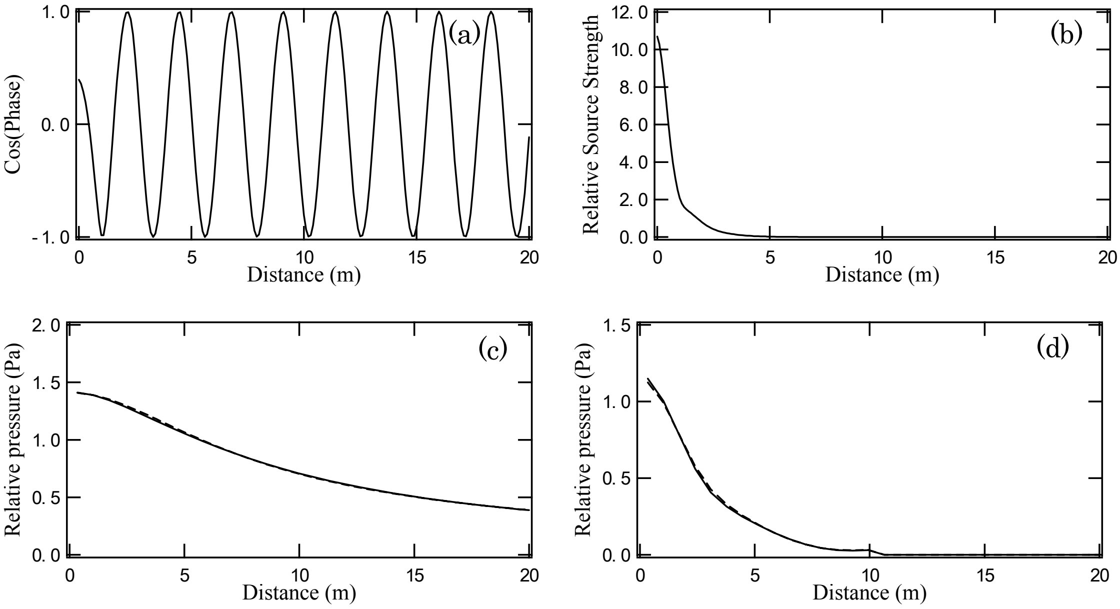

Figure 5.16 Simulation results for horizontal rail vibration at 125 Hz. (a) Relative phase obtained from rail vibration, (b) relative source strength obtained from rail vibration (arbitrary scale), (c) magnitude of sound pressure at single microphone versus distance along the track from the forcing position, (d) output from microphone array. — Sources accounting for phase; - - - incoherent sources.

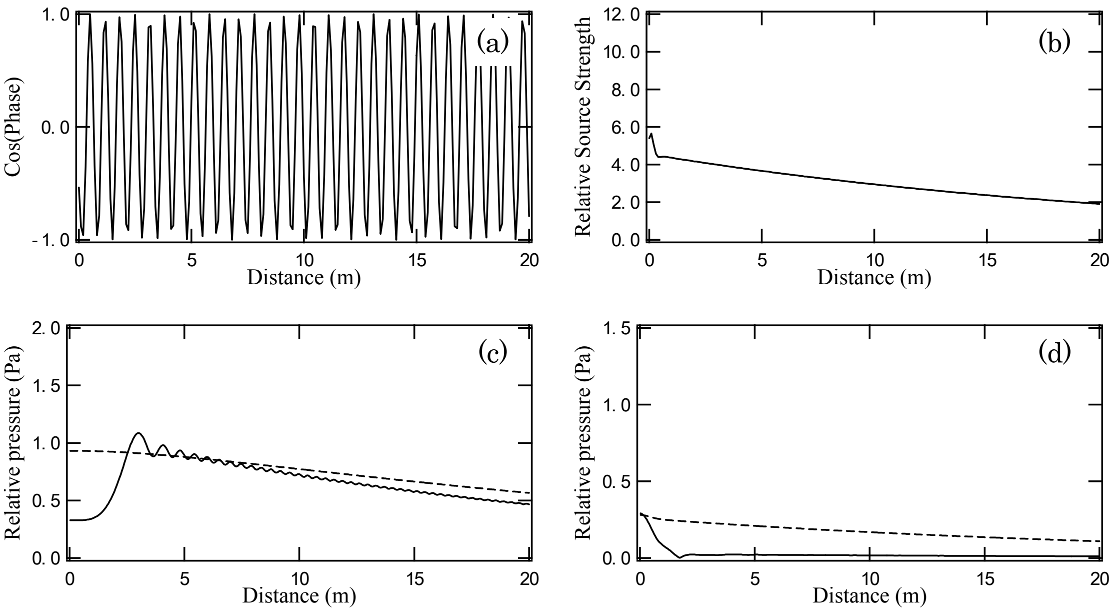

Figure 5.17 Simulation results for horizontal rail vibration at 1600 Hz. (a) Relative phase obtained from rail vibration, (b) relative source strength obtained from rail vibration (arbitrary scale), (c) magnitude of sound pressure at single microphone versus distance along the track from the forcing position, (d) output from microphone array. — Sources accounting for phase; - - - incoherent sources.

5.3.2 Overall result

To quantify the effect of measuring with a microphone array, the squared pressure obtained by using the microphone array is integrated along a sufficient length. The equivalent result is also obtained for the set of incoherent sources with the same overall power. The level difference between these two results is used as a measure of the extent to which the microphone array can measure the noise from the rail.

Figure 5.18(a) shows the overall effects of using microphone array to measure noise from rail vibration. The corresponding track decay rates are shown in Figure 5.18(b). For the track studied in Chapter 2, with a pad stiffness of 700 MN/m, free propagation of vertical waves only occurs above about 1 kHz. Results are also shown for a reduced pad stiffness of 200 MN/m, for which free wave propagation occurs above about 500 Hz. It can be seen that the microphone array underestimates the rail source in the region where free wave propagation occurs. Differences of up to about 13 dB are found here. In the region around 800 Hz (400 Hz for the softer pad) the microphone array over-estimates the rail noise. However, this corresponds to a region of very high decay rate associated with the sleeper vibrating as a vibration absorber where the rail contribution is small. Results are also shown for horizontal rail vibration; here the wave propagation commences at a lower frequency but similar trends are found.

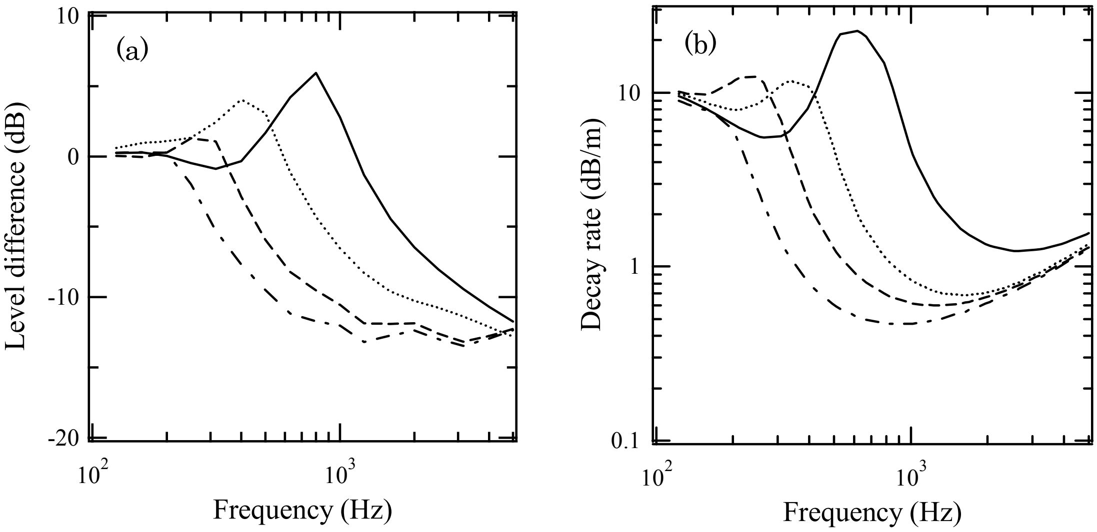

Figure 5.18 (a) Overall effect of using microphone array to measure noise from rail vibration. (b) Track decay rates. ——, Vertical vibration, rail pad stiffness 700 MN/m; - - - - - , horizontal vibration, rail pad stiffness 85 MN/m; ········, vertical vibration, rail pad stiffness 200 MN/m; – · –, horizontal vibration, rail pad stiffness 40 MN/m.

In order to examine the effect of the source length used in the simulation, the calculations have been performed with different source lengths. Figure 5.19 shows the overall effects of using microphone array to measure noise from horizontal rail vibration for five source lengths. In these simulations, the source length is not truncated. It can be seen that, if the source length is set to be at least $3.25/\beta_i$, which corresponds to 28 dB reduction in amplitude at the end of the source region, the results are not affected by the length of the source region. It is clear that the source region considered in the above results is sufficient to quantify the effect of measuring with a microphone array in the simulations.

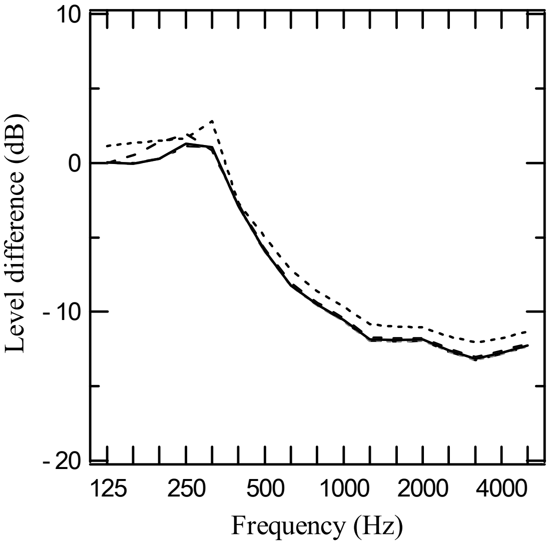

Figure 5.19 Overall effect of using microphone array to measure noise from horizontal rail vibration for different source lengths. The rail pad stiffness is 85 MN/m. ——, the method used in the simulation (see Section 5.2.2); ·······, $0.8125/\beta_i$, which corresponds to 7 dB reduction; - - - - -, $1.625/\beta_i$, which corresponds to 14 dB reduction; – · –, $3.25/\beta_i$, which corresponds to 28 dB reduction; ——, $6.5/\beta_i$, which corresponds to 56 dB reduction; ·······, $9.75/\beta_i$, which corresponds to 84 dB reduction.

5.4 Estimation of rail component of noise

To find the overall effect of using a microphone array on the rail component of noise, the differences shown in Figure 5.18(a) are applied to the vertical and horizontal components of the sound power from the rail obtained by using the TWINS model, as in Chapter 2. The parameters used in the calculation of the sound power generated by the rail vibration are given in Table 2.3.

Figure 5.20 gives an estimate of the rail component of noise and that which would be inferred from a microphone array measurement. Clearly, at frequencies above 1 kHz the microphone array tends to underestimate the rail contribution considerably. For the softer rail pad considered above, large differences are present from 630 Hz upwards. The results for dipoles are similar to those seen for monopoles (see Appendix A3).

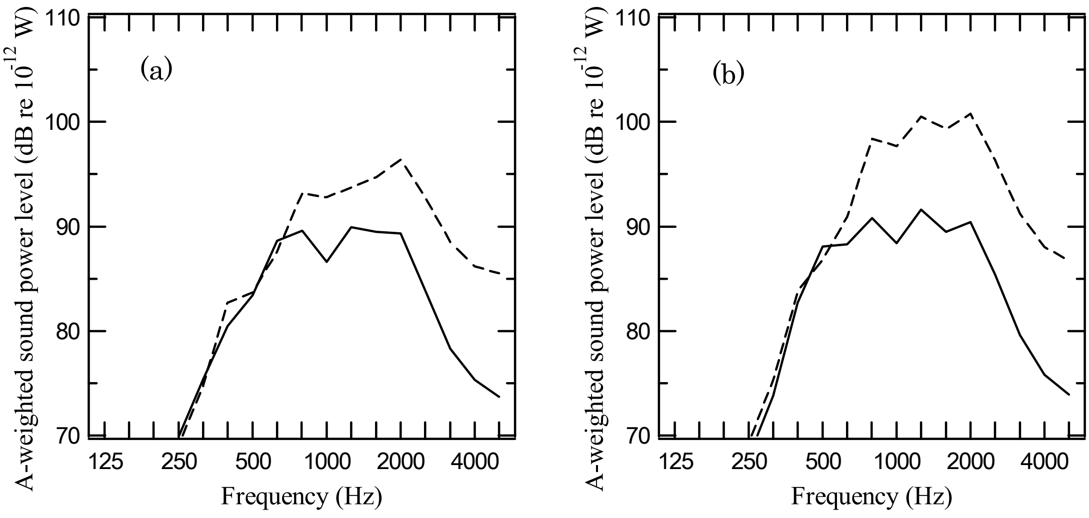

Figure 5.20 Effect on rail component of noise of using a microphone array tuned for a plane wave. The modification factor is derived from the results for an array of monopole sources. – – –, Actual rail noise; ——, rail noise inferred from microphone array. (a) Track with 700 MN/m pads; (b) track with 200 MN/m pads.

Figure 5.21 shows the effect of the microphone array measurements on each noise component using wheel F. The modifications estimated here due to the array measurements are applied for only the rail component. This is because, as the wheel acts as a localised source, it is not necessary to modify the wheel component for the effect of the array. The sleeper also acts as a localised source as it is significant only when the decay rate is high. It is clear that the wheel component mainly determines the total noise above 1-2 kHz, especially for the harder rail pad. Consequently, the effect estimated here may be masked by the presence of the wheel, which means that the overall spectra do not differ greatly. Table 5.4 gives the overall contribution of each noise component. Clearly, the wheel is seen as the dominant source by the microphone array measurement whereas in fact its contribution is similar to that of the rail. The results of dipole sources show similar overall trends as seen for monopoles (see Appendix A4).

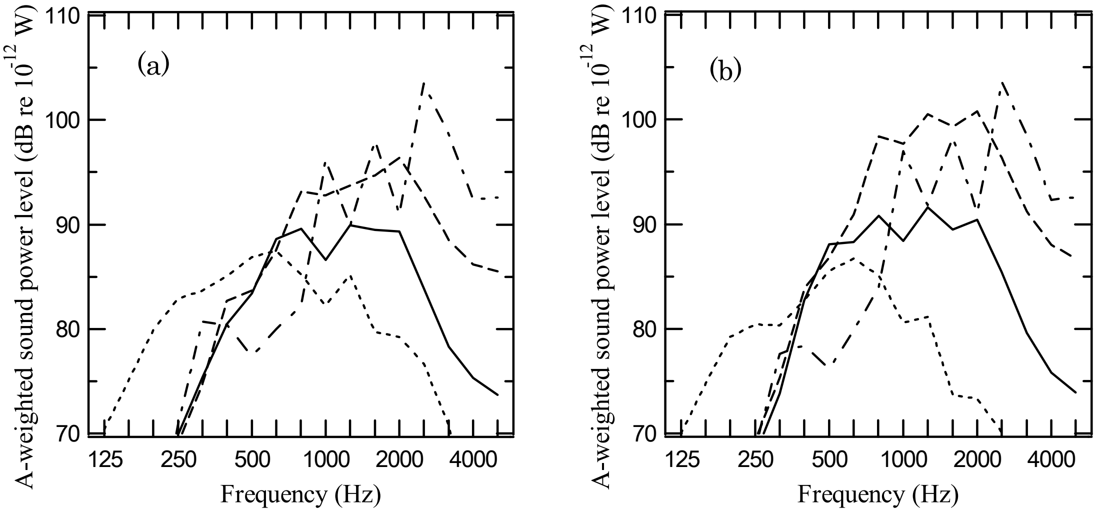

Figure 5.21 Comparison of the contribution of each noise component by measuring with a microphone array tuned for a plane wave. The modification factor is derived from the results for an array of monopole sources. – – –, Actual rail noise; ——, rail noise inferred from microphone array; ········, sleeper noise; – · –, wheel noise. (a) Track with 700 MN/m pads; (b) track with 200 MN/m pads.

Table 5.4 Contribution of each noise component by using a microphone array tuned for a plane wave. The modification factor is derived from the results for an array of monopole sources. Wheel F is used in the calculation, and other parameters are given in Table 2.3.

	Track with 700MN/m pads		Track with 200MN/m pads	
	TWINS	Microphone array	TWINS	Microphone array
Wheel	106.6	106.6	106.6	106.6
Rail	102.6	97.7	107.3	98.7
Sleeper	94.8	94.8	94.8	94.8
Total	108.3	107.4	110.2	107.7

5.5 Tuned angle for the microphone array

In this section, the evaluations of the sound pressure for an array of monopole sources are carried out by turning the array axis of the MY13 array hypothetically. Here, equations (4.27) and (4.28) are used. The rail vibration is again calculated by using the parameters given in Table 2.3.

5.5.1 Sound distribution

Figure 5.22 shows the output from a single microphone and the output from a microphone array for 125 Hz and 1600 Hz. For the wave with a high decay rate at 125 Hz, the results measured with a single microphone and microphone array show the same overall trends for the incoherent and coherent sources.

For the wave with a low decay rate at 1600 Hz, it can be seen that, by turning the array axis, the maximum array gains obtained from the incoherent sources are only slightly changed. This is because the rail is an extended line source, and the region where the array detects is larger. In the case of the coherent sources, by directing the array axis at 10° a much larger response is found by the microphone array than for 0° due to the extended nature of the source. At 20° the increase is more modest and at 30° it is negligible. Thus, depending on the angle of the array axis, an over-estimation or under-estimation of the rail source could be reflected in the microphone array results.

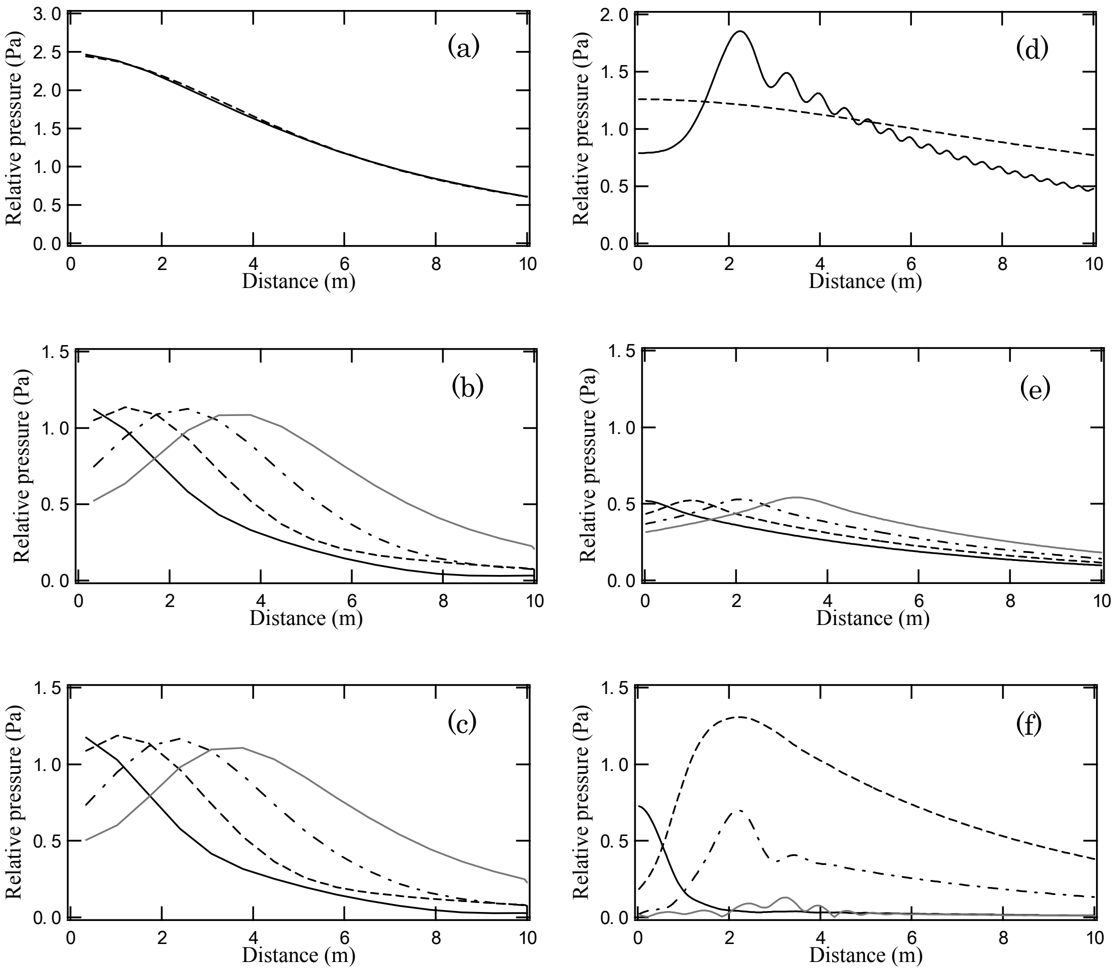

Figure 5.22 Simulation results for vertical rail vibration for 125 Hz (left) and 1600 Hz (right). The microphone array is designed for a plane wave. (a, d) magnitude of sound pressure at single microphone versus distance along the track from the forcing position; ——, coherent sources; - - - - -, incoherent sources, (b, e) output from microphone array for a line array of incoherent sources, (c, f) output from microphone array for a line array of coherent sources. ——, ϕ=0°; - - - - -, ϕ=10°; – · –, ϕ=20°; ——, ϕ=30°.

5.5.2 Overall effect

Figure 5.23 shows the overall effects of using the microphone array to measure noise from rail vibration for different tuned angles of the array. For the wave with a high decay rate, it can be seen that the level difference between incoherent and coherent sources does not depend on the tuned angle. In the frequency region where free wave propagation occurs, however, the microphone array makes incorrect estimates of the rail source. At ϕ=10°, the array over-estimates the rail source. This is close to the angle at which the rail radiates most strongly (see Figure 5.15). As this angle is the maximum of the directivity, the microphone array will measure a strong signal which will be interpreted as a source strength that is greater than the actual one, due to the coherent nature of the source. At

ϕ=20°, the result from the microphone array gives a smaller difference, while at ϕ=30°, the microphone array cannot measure the rail source, since the array axis is not aligned with the radiation angle. It would appear to be difficult to direct the array at an appropriate angle to identify correctly the rail contribution.

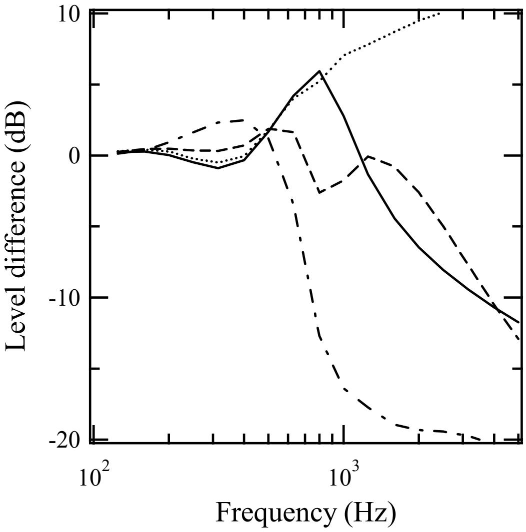

Figure 5.23 Overall effect of using microphone array for monopole sources to measure noise from rail vibration. The microphone array tuned for a plane wave. ——, ϕ=0°; ··········, ϕ=10°; - - - - - , ϕ=20°; – · –, ϕ=30°.

Figure 5.24 shows the overall effect of using a microphone array with different tuned angles for selected frequencies. For waves with a high decay rate, it is again found that the tuned angle does not have influence on the level difference between incoherent and coherent sources. However, for waves with a low decay rate, the level difference depends strongly on the tuned angle. It can be seen that, if the microphone array is directed at the angle of maximum structural radiation (about 13°, see Figure 5.15), the over-prediction reaches its maximum. To obtain the correct sound power, account would have to be taken of the coherent nature of the source.

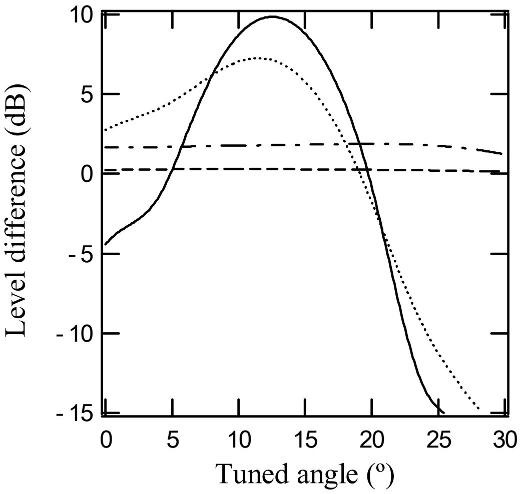

Figure 5.24 Overall effect of using a microphone array with different tuned angles for monopole sources. - - - - - , 125 Hz; – · –, 500 Hz; ·······, 1000 Hz; ——, 1600 Hz. The microphone array is designed for a plane wave.

5.6 Summary

Through the analysis of the performance of a microphone array, it is found that a horizontal array cannot detect a large part of the noise from the rail at high frequencies where free wave propagation occurs in the rail. Differences of up to 15 dB are found. This is mainly due to the fact that the multiple sources, which represent the rail, are assumed to be incoherent when measuring the sound radiation with a microphone array. This leads to the underestimation of the noise from the rail. This explains why measurements using microphone arrays tend to emphasise the wheel as the dominant source, whereas using the TWINS model the rail is also found to be an important source in many situations. It is noted that, by directing the array axis to the angle determined by the supersonic structural radiation, the microphone array could measure the distributed character of the source in the region where wave propagation occurs. However, a modified method of obtaining the sound power would be required to account for the coherent nature of the source. Moreover, it appears difficult to select an appropriate angle at which to direct the array as this is frequency-dependent.

6 MEASUREMENTS ON A RAILWAY TRACK EXCITED BY A SHAKER

6.1 Introduction

Through the simulation of the performance of a horizontal microphone array, it has been found that the results measured with the microphone array do not necessarily reflect the radiation characteristics of the noise from a rail. This is mainly because the microphone array, focused normal to the rail, cannot detect a large part of the noise from the rail at high frequencies where free wave propagation occurs in the rail. In this chapter, an attempt is made to examine the vibration and radiation properties of a rail experimentally using shaker excitation. The vibratory behaviour of the rail is first investigated, and the appropriate parameters used in the model for the sound radiation of the rail are determined. Then, in order to validate the radiation model described in Chapter 5, the directivities of the sound radiated from the rail are verified by steering the array axis of a one-dimensional microphone array.

The measurements were carried out for a single track type at the Hino test site. Figure 6.1 shows a photograph of the test section at the Hino site. The test section is 25 m long and is laid with new 60-type rails. The track is of ballasted construction, and concrete monobloc sleepers are used with a nominal spacing of 0.625 m. The rail pad is different from those used in Chapter 2, and has a somewhat lower stiffness. This has been chosen for these measurements as the decay rates of the track are lower over a wider frequency range allowing the investigation of the effect of propagating waves in the rail for more frequency bands.

In Section 6.2, the measurements for the vibratory behaviour of the rail are described, and an attempt is made to investigate the characteristics of the noise generated by the rail on the same track through the acoustic measurements in Sections 6.3-6.5.

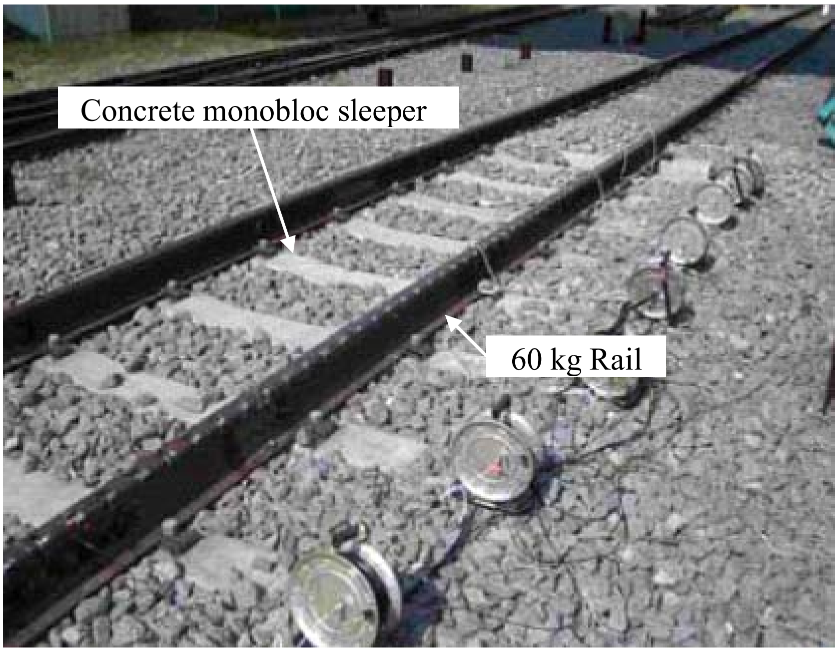

Figure 6.1 Photograph of the test section

6.2 Description of the vibration measurements

The vibratory behaviour of the rail was investigated by using shaker excitation. The following were determined:

(1) vertical and horizontal point accelerances,

(2) vibration decay rates along the rail for vertical and horizontal directions.

By comparing the results from the measurements with the predictions from the *rodel* model, the values of the stiffness and damping of the rail-pad and ballast are chosen to obtain a good tuning for the track resonances in both directions. This tuned *rodel* model will be used in later for comparison with the microphone array measurements.

Figure 6.2 shows a schematic diagram of the vibration measurements. The measurements were performed with the track in the unloaded condition. The shaker was installed at the mid-point between two neighbouring sleepers. Valid measurements were possible over a frequency band up to 3000 Hz, limited by the specifications of the shaker used. The rail was excited by a continuous signal produced by a pseudorandom signal generator up to 3000 Hz. Force measurements were made using an internal force gauge built into the shaker. A mesh of 8 accelerometers was arranged on the rail and arranged at various locations with an equal spacing of 0.1 m, up to a position 5.6 m from the forcing point.

For both vertical and horizontal shaker excitations, signals were transformed directly into the frequency domain by using a multi-channel digital Fourier analyser over the frequency range 0-3000 Hz. For each measurement, the frequency response functions were obtained by averaging 16 measured samples.

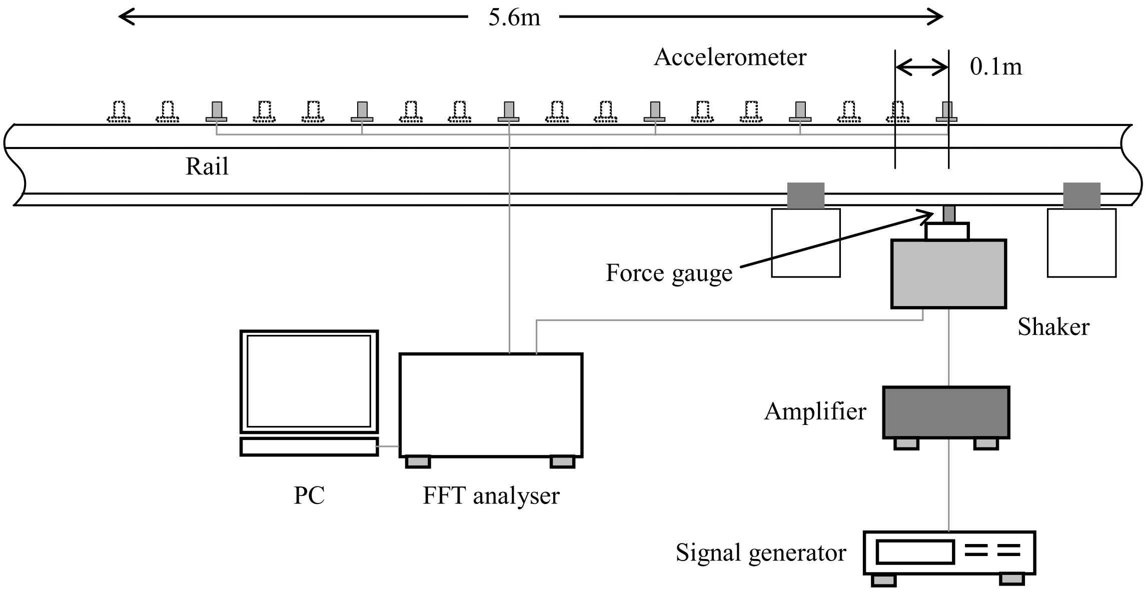

Figure 6.2 Schematic diagram for the vibration measurements

Figure 6.3 shows photographs of the measurements of the rail vibration. For the vertical excitation, the shaker was installed under the rail and the measurements of acceleration were performed by using accelerometers on the railhead. For the horizontal excitation, the shaker and accelerometers were both mounted on the sides of the railhead.

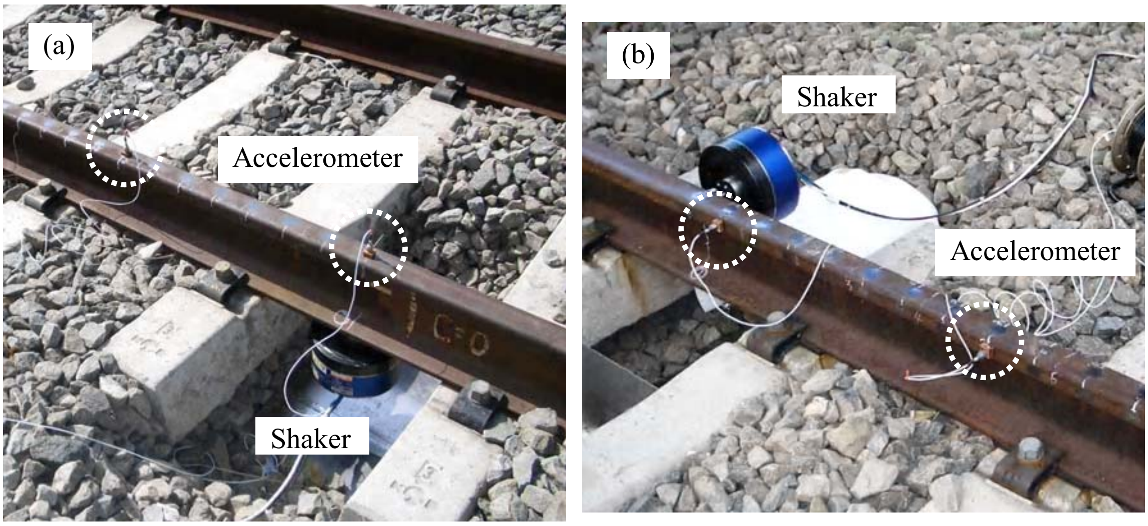

Figure 6.3 Examples of measurement locations for the rail vibration. (a) Vertical excitation, (b) horizontal excitation

Figure 6.4 shows the accelerance in the vertical and horizontal directions. The results obtained by hitting the railhead with an instrumented impact hammer are also included for comparison. The results predicted with the *rodel* model are also shown. The properties used in the *rodel* model are listed in Table 6.1. The rail-pad is softer than those used in Chapter 2. For the vertical accelerance, it can be seen that the results are predicted reasonably well. At about 1000 Hz, the resonance behaviour associated with the pinned-pinned effect can be seen in the measured results. However, the predictions do not show the periodicity effect due to the pinned-pinned resonance, because the support in the *rodel* model is continuous. For the horizontal accelerance of the track, it is found that the overall trends are predicted reasonably well, although the predictions are somewhat lower than the measurements. This is due to the fact that torsion of the rail is neglected in the *rodel* model. The pinned-pinned mode can be seen in the measured accelerance at around 500 Hz for the horizontal direction.

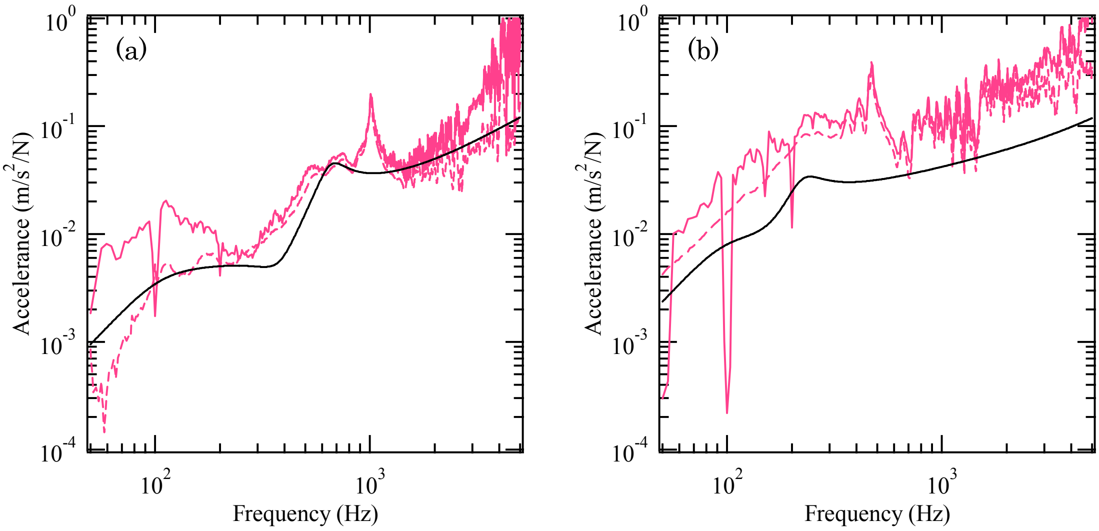

Figure 6.4 Vertical and horizontal point accelerance. Measured results between sleepers, —, by shaker excitation; - - -, by hammer excitation; predicted results, —, *rodel* model. (a) Vertical point accelerance; (b) horizontal point accelerance.

Table 6.1 Values of parameters used for the *rodel* model

	Vertical	Horizontal
rail bending stiffness, Nm^2	6.49×10^6	1.08×10^6
rail shear coefficient	0.4	0.4
rail loss factor	0.02	0.02
mass per length, kg/m	60	
cross receptance level, dB	-12	
pad stiffness, N/m	4.1×10^8	4.5×10^7
pad loss factor	0.3	0.3
sleeper mass (1/2 sleeper), kg	80	
distance between sleepers, m	0.625 (0.6-0.65)	
ballast stiffness, N/m	2.3×10^7	2.0×10^7
ballast loss factor	2.0	2.0

Figure 6.5 shows the imaginary parts of propagation coefficients (wavenumbers) for the waves propagating along the rail. It is again noted that the rail-pad is different from those used in Chapter 2. The predictions obtained using the *rodel* model are also shown. The measurement results have been obtained using two calculation approaches. The

first approach is based on the Prony method [71, 72, 73, 74]. In the Prony method, the technique can be only applied to discretely sampled, equispaced data point. The Prony method is a two stage process. In the first stage, the wavenumbers are found and, in the second stage, the amplitudes for theses wavenumbers are found from a linear least square fit of the model to the data. The Prony method seems to offer the most accurate estimation but is very sensitive to noise in the data [70, 71]. This means that any noise will corrupt the wavenumber estimation in the Prony method. Therefore, it is important to examine the effects of noise and type of contributing wavenumbers for the measured data. In the second approach, wavelengths are directly estimated by using the change in phase of transfer functions measured at response positions with an equal spacing. Unlike the Prony method, it only allows the wavenumber to be obtained, not the decay rate. It can be seen that, for the rail vibration measured in the vertical direction, the global trends estimated by the two approaches are similar. Above 200 Hz, it is found that the *rodel* model gives good predictions. For the horizontal rail vibration, the predicted wavenumbers can be seen to be greater than those found from the measurements below 300 Hz, but the agreement is again good above 300 Hz.

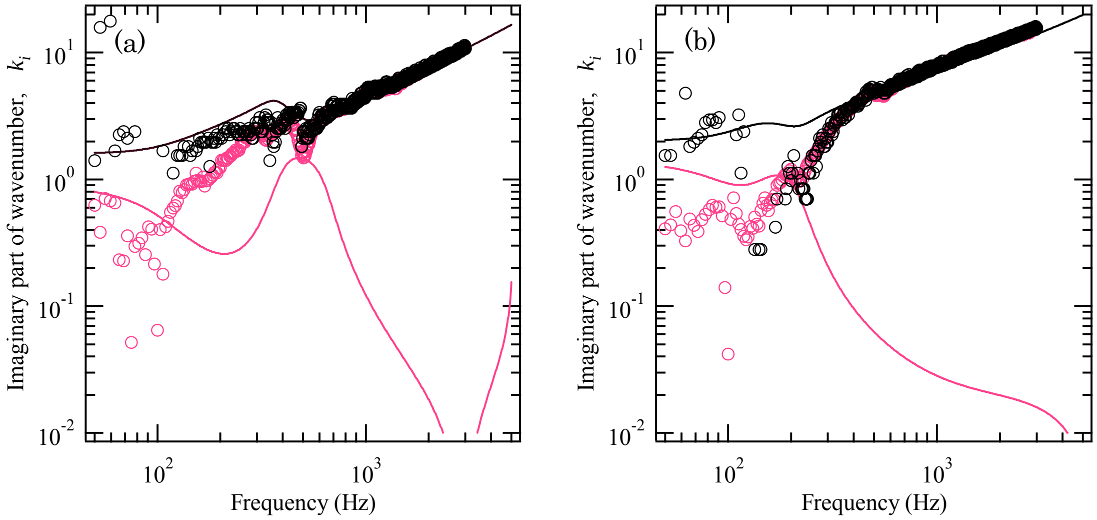

Figure 6.5 Imaginary parts of wave propagation coefficients of a rail, parameters as in Table 6.1. —, Vertical bending wave; —, vertical near-field wave; ○, Prony method; ○, values calculated by using phase relation. (a) Vertical vibration, (b) horizontal vibration.

Figure 6.6 shows the decay rates of the vertical and horizontal rail vibration. The measured decay rates are again obtained using two methods: the Prony method and from an integral of squared vibration over the length of the rail (using Equation (2.3)). For the vertical rail vibration, it can be seen that predicted curves show good agreement with the measured results estimated by the two approaches, although there is significant under-prediction in the frequency range 1000-1500 Hz. This is due to the vibratory behaviour associated with the pinned-pinned resonance. For the horizontal decay rate, the overall trends are well predicted, although the predictions are somewhat lower than the measurements above 300 Hz. The effect of the pinned-pinned resonance on the horizontal decay rates can be seen at around 630 Hz.

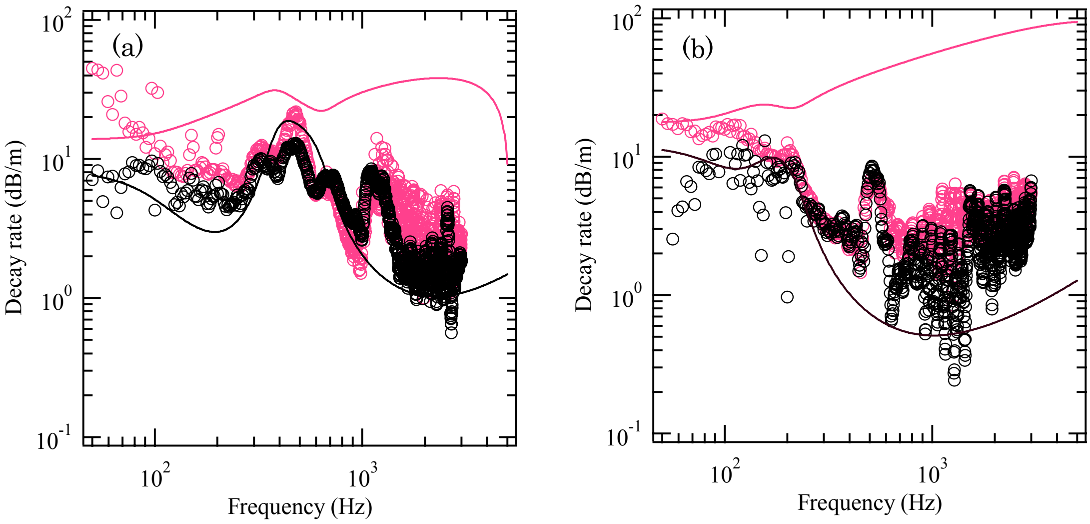

Figure 6.6 Decay rate of vertical and horizontal rail vibration, parameters as in Table 6.1. —, Propagating wave; —, near-field wave; ○, Prony method; ○, measured values (equation (2.3)). (a) Vertical vibration, (b) horizontal vibration.

Figure 6.7 shows the vertical and horizontal accelerances as a function of frequency at 0, 1.2, 2.5 and 5 m from the forcing position. It is clear that the predictions show good agreement with the measurements for both directions. For the vertical accelerance, it can be seen that the results obtained at the four points are closer together above 800 Hz. This indicates that free wave propagation occurs above 800 Hz corresponding to the fall in decay rate seen in Figure 6.6. For the horizontal accelerance, the same trends can be seen above 300 Hz.

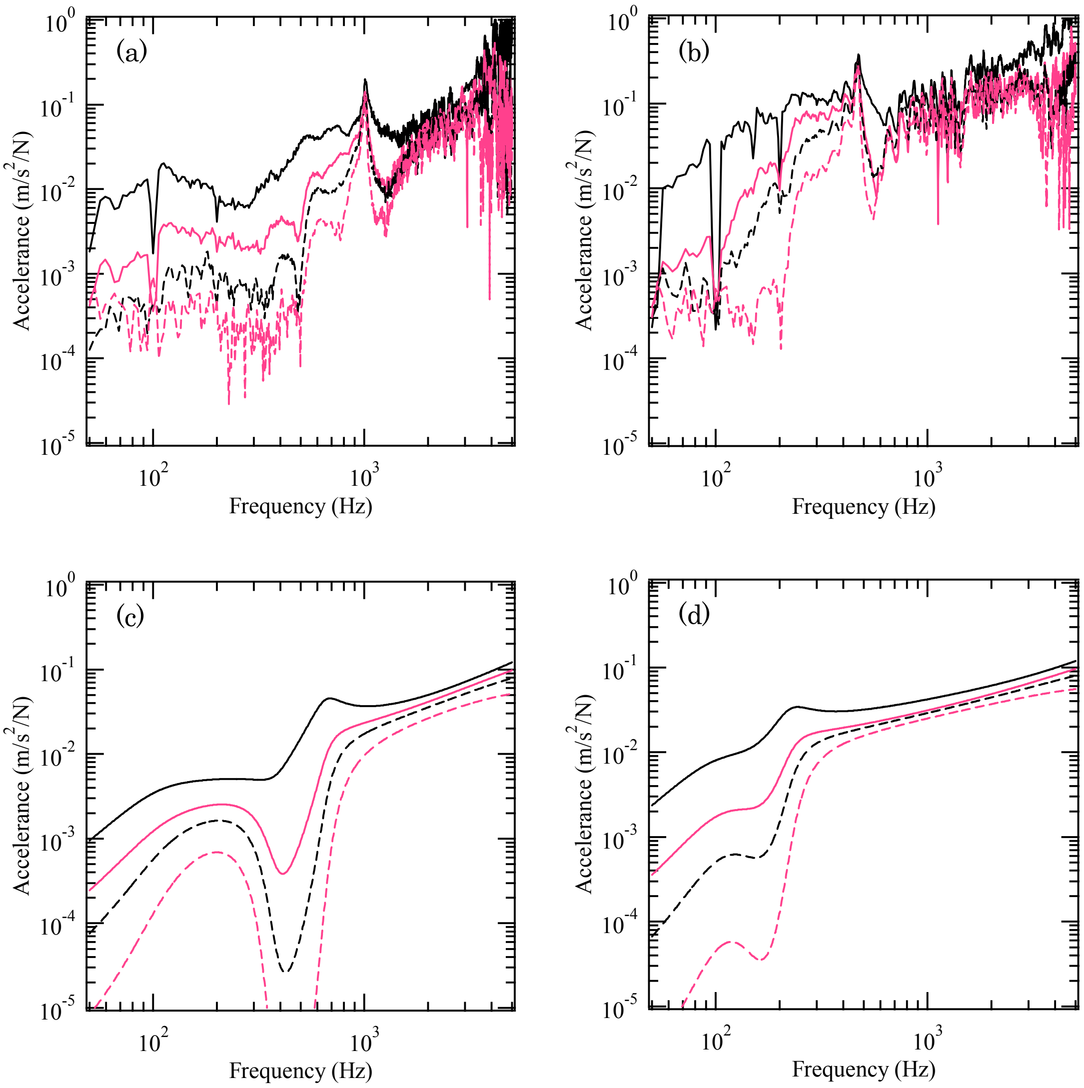

Figure 6.7 Accelerance for vertical (left) and horizontal (right) rail vibrations. The parameters used in the *rodel* model are listed in Table 6.1. —, z=0; —, z=1.2; - - -, z=2.5; - - -, z=5. (a, b) Predicted, (b, d) measured.

Figures 6.8 and 6.9 show the amplitude of the vertical accelerance as a function of the distance from the forcing position at 8 frequencies (500 Hz, 630 Hz, 800 Hz, 1000 Hz, 1250 Hz, 1600 Hz, 2000 Hz and 2500 Hz). For the vertical vibration, it can be seen that the overall trends are predicted reasonably well. As the frequency increases, the slope can be seen to become more gradual. This corresponds to the occurrence of free wave propagation. At 1000 Hz and 1250 Hz, the measured results can be seen to contain significant undulations due to the pinned-pinned resonance. For the horizontal accelerance, similar trends can be seen but the undulation associated with the pinned-pinned resonance occurs at 500 Hz.

These various results give confidence in the reliability of the *rodel* model with the parameters identified to represent the track vibration. This model will be used to predict sound radiation for comparison with the microphone array measurements in the next section.

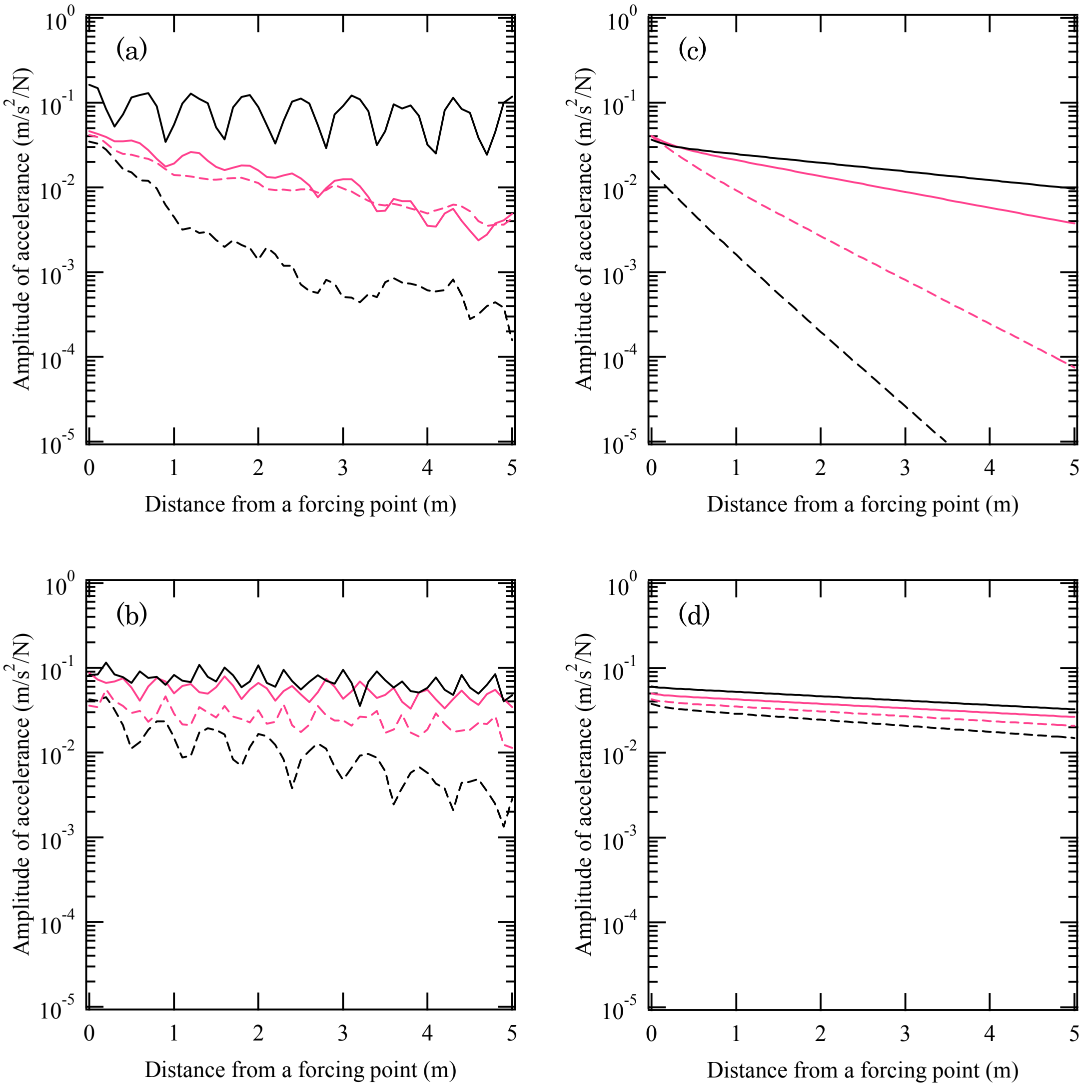

Figure 6.8 Amplitude of accelerance for measured (left) and predicted (right) rail vibration in vertical direction. The parameters used in the *rodel* model are listed in Table 6.1. (a, c) - - -, 500 Hz; - - -, 630 Hz; ——, 800 Hz; ——, 1000 Hz. (b, d) - - -, 1250 Hz; - - -, 1600 Hz; ——, 2000 Hz; ——, 2500 Hz.

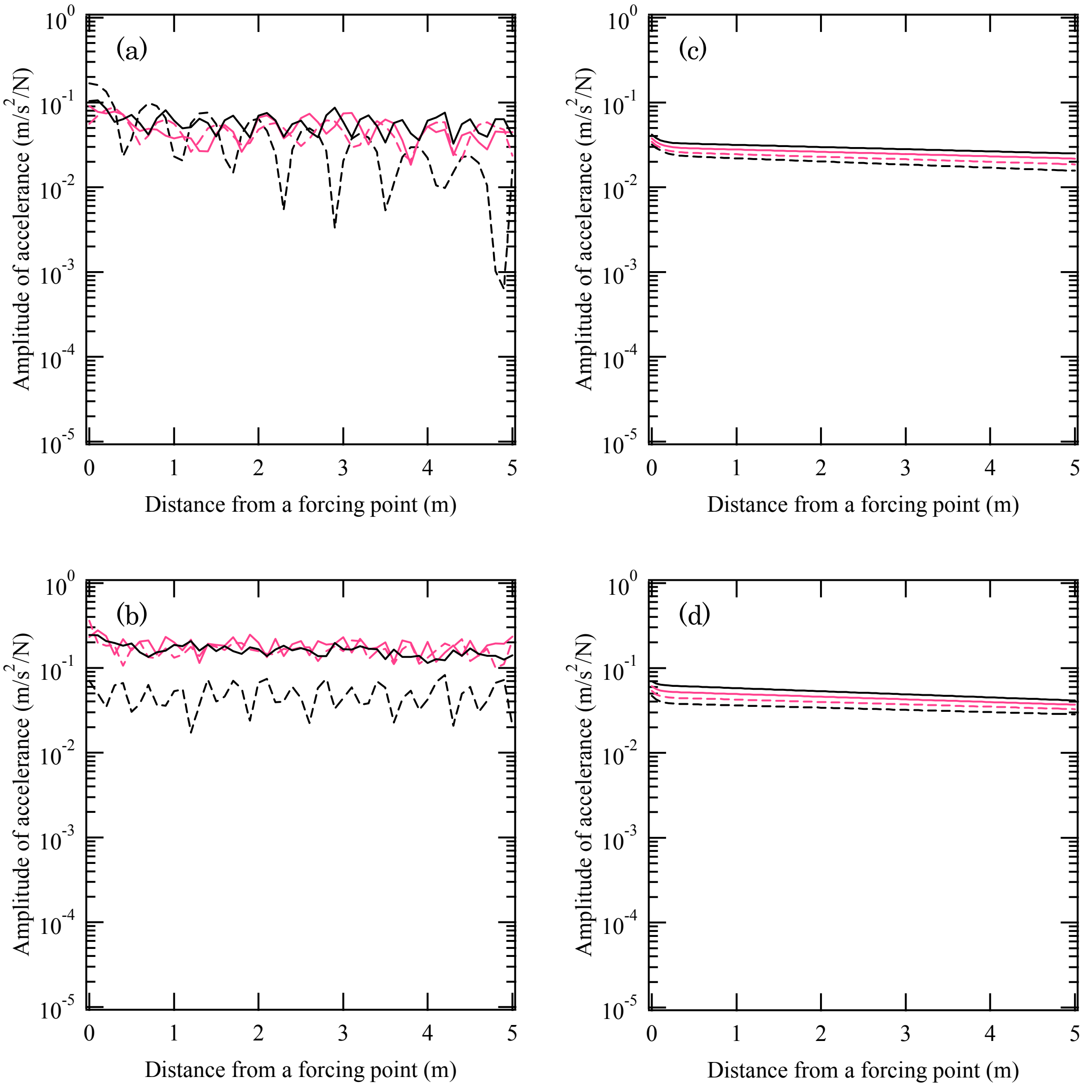

Figure 6.9 Amplitude of accelerance for measured (left) and predicted (right) rail vibration in horizontal direction. The parameters used in the *rodel* model are listed in Table 6.1. (a, c) - - -, 500 Hz; - - -, 630 Hz; —, 800 Hz; —, 1000 Hz. (b, d) - - -, 1250 Hz; - - -, 1600 Hz; —, 2000 Hz; —, 2500 Hz.

6.3 Description of the sound measurement

The sound measurements were carried out using a one-dimensional horizontal microphone array. The main aim is to examine the radiation behaviour of the rail by steering the microphone array at different angles. Figure 6.10 shows a schematic diagram of the sound measurements. The rail was excited by using a shaker driven by a signal generator with 8 pure tone signals (500, 630, 800, 1000, 1250, 1600, 2000 and 2500 Hz). The force applied to the rail was measured using a force gauge built into the shaker. The axis of the microphone array was parallel to the rail, and the sound measurements were carried out at several receiver positions along the rail with the centre of the array between 1.5 and 5 m from the forcing point. The raw data measured with the microphones of the array were recorded simultaneously. The delay-and-sum process is carried out subsequently in a PC, and the time delay is arranged in order that the microphone array might be directed at an appropriate angle to detect the rail radiation.

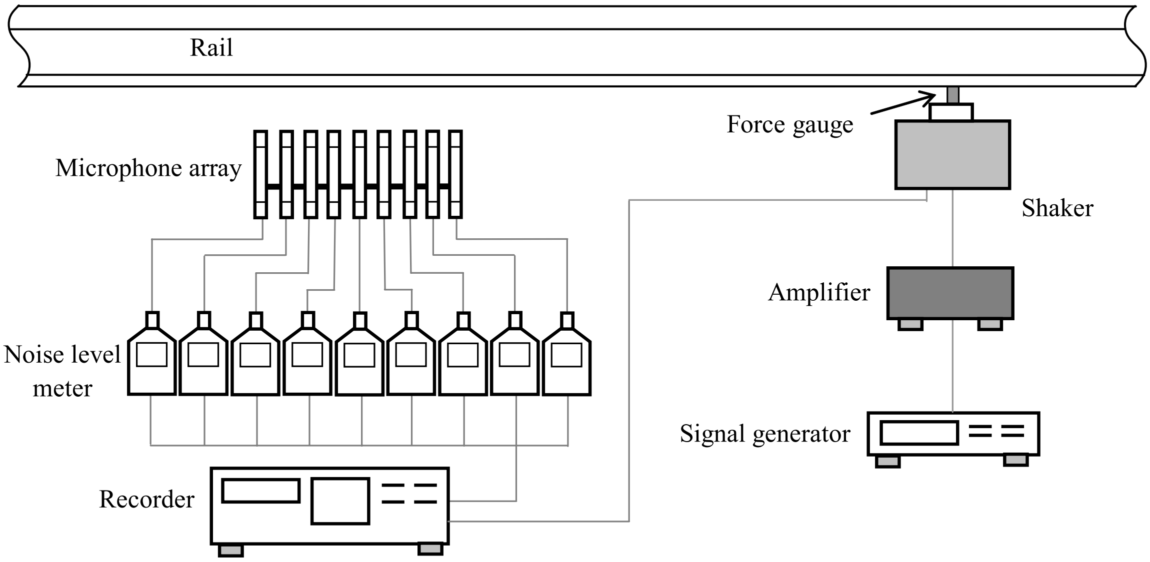

Figure 6.10 Schematic diagram for the sound measurements

When the rail was excited by the shaker, the rail itself radiated sound but the sound from the shaker was found to be louder. Therefore, in order to investigate the acoustic properties of the rail properly, a simple device to reduce the noise of the shaker was introduced during the acoustic test. Figure 6.11 shows the steel box used to reduce the noise of the shaker for the sound measurements. The shaker was enclosed by the steel box, the interior of which was covered with sound absorbing materials.

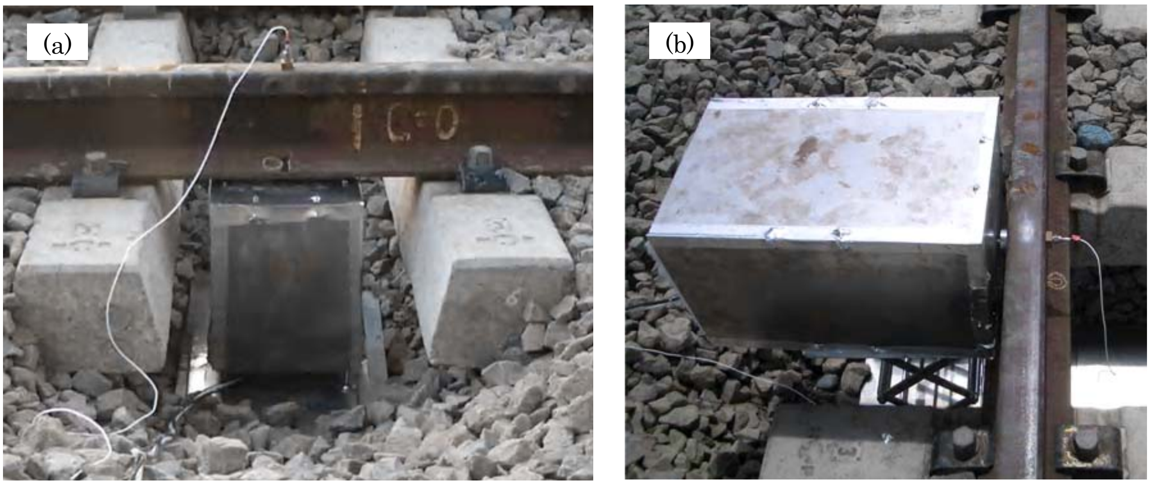

Figure 6.11 Box to screen the noise generated from the shaker. (a) Vertical vibration, (b) horizontal vibration.

Figures 6.12-6.13 show diagrams and photographs of the measurement locations used during the measurement campaign.

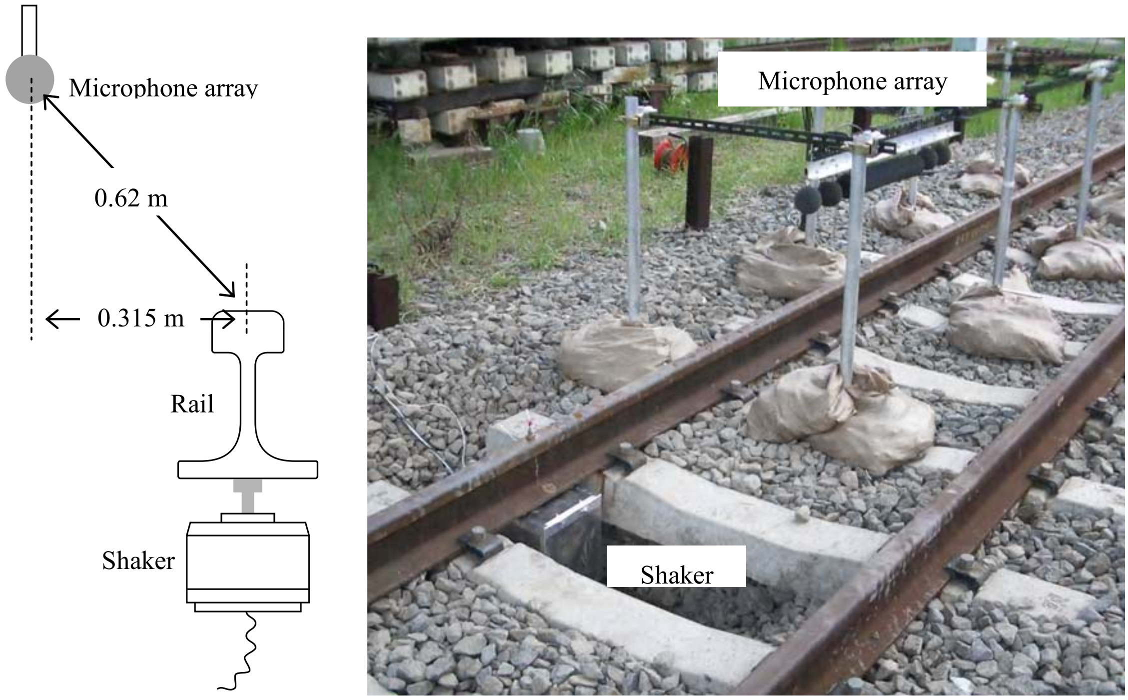

Figure 6.12 Setup for the sound measurements of the vertical excitation

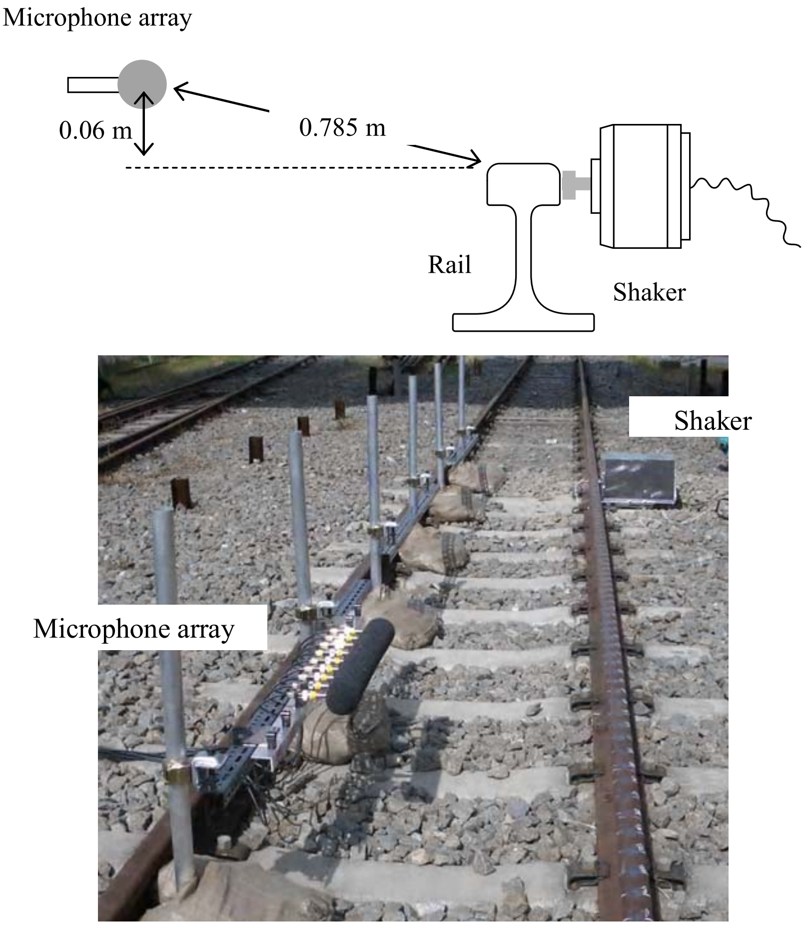

Figure 6.13 Setup for the sound measurements of the horizontal excitation

6.4 Outline of one-dimensional microphone array

The microphone array used for the shaker excitation measurement is a one-dimensional array composed of 13 microphones. Figure 6.14 shows a photograph of the array. The specification of the array is given in Table 6.2. The array is designed to give appropriate sound distributions below 2500 Hz. The number of microphones used for each one-third octave band is 9. These are arranged in a line with an equal spacing, which is chosen to give optimal spatial resolution at 1250 Hz and 2500 Hz. The weighting factors are determined by using the Dolph-Tschebyscheff method [38], as listed in Table 6.2.

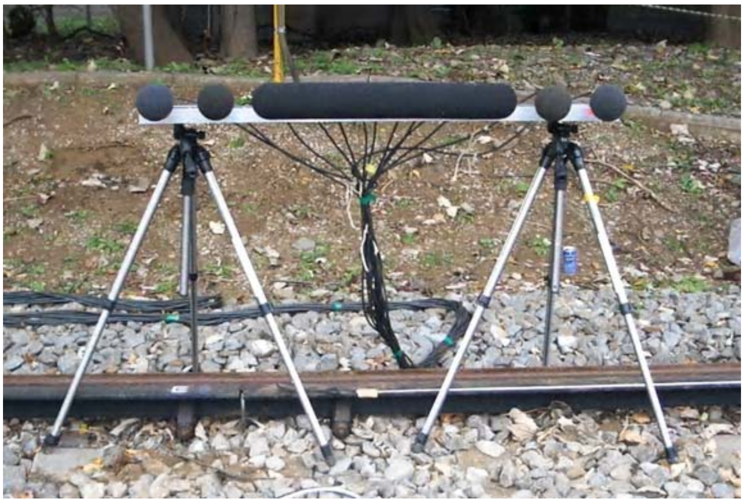

Figure 6.14 Microphone array used for the sound measurements

Table 6.2 Number of microphone and weighting factors

Frequency (Hz)	500-1250	1600-2500
Number of microphones	9	
Microphone spacing (m)	0.136	0.068
w_{-4}, w_{+4}	0.0864	
w_{-3}, w_{+3}	0.0884	
w_{-2}, w_{+2}	0.1170	
w_{-1}, w_{+1}	0.1370	
w_0	0.1440	

Before the evaluating of the radiation behaviour of the rail, the sensitivity of this particular microphone array is investigated for an incident wave. In particular, the purpose is to see whether plane wave or spherical wave focussing should be used. Here, by following the same procedures as in Chapter 5.2, the estimations for an array of monopole sources are performed with the microphone array at 0.62 m from the rail. It was previously shown that the global trends obtained for the dipole sources are similar to those seen for the monopole sources. The rail vibration is again estimated by the *rodel* model using the parameters given in Table 6.1. The microphone array is situated parallel to the rail at various distances from the shaker. The estimations of the sound pressure are carried out by steering the array axis of the microphone array.

Figure 6.15 shows the simulated outputs for the vertical rail vibration from the microphone arrays designed for both incident plane and spherical waves at 500 Hz. As the propagating wave has a high decay rate at this frequency, the results obtained with the microphone array show the same overall trends for the incoherent and coherent sources. There is also not much difference between plane and spherical wave steering.

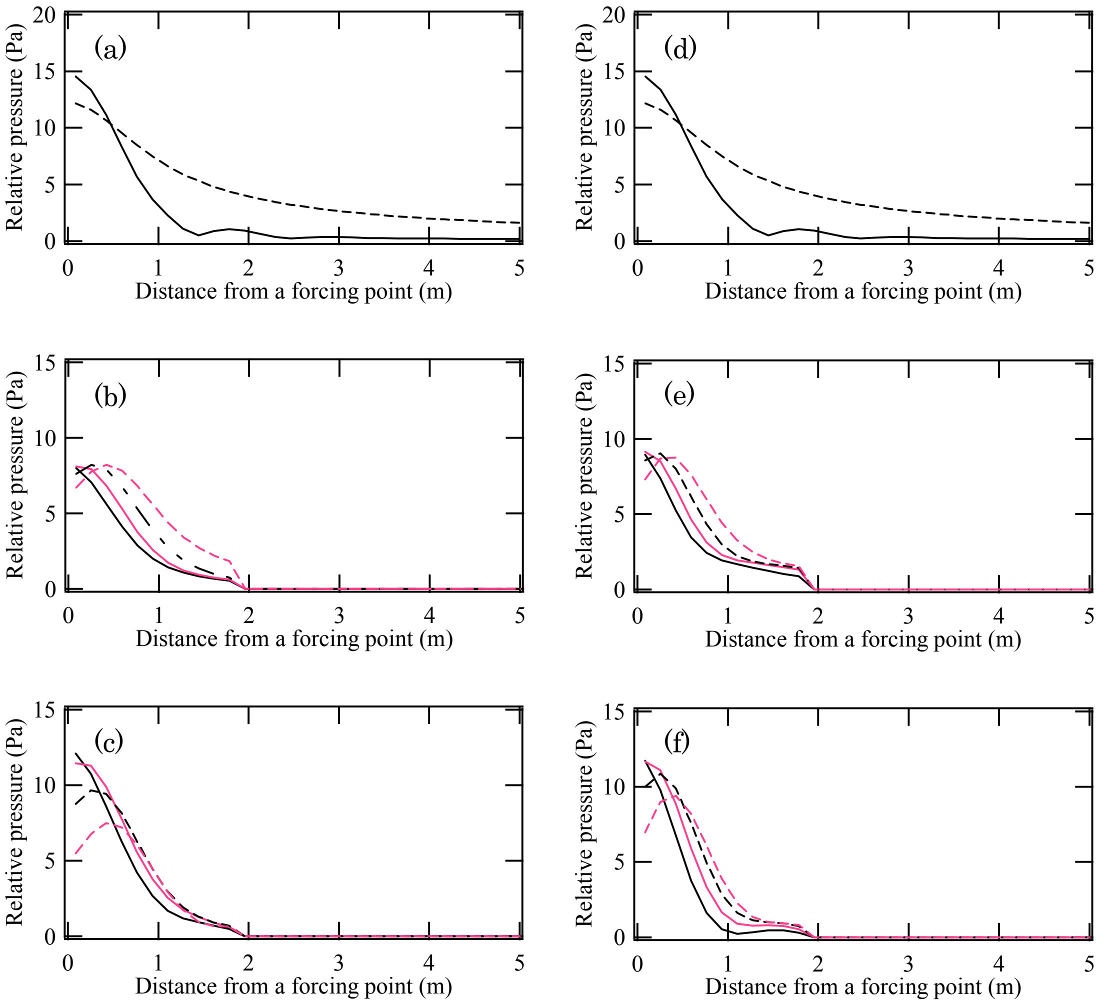

Figure 6.15 Simulation results for vertical rail vibration for 500 Hz. The microphone array is designed for two types of incident wave: a plane wave (left) and spherical wave (right). (a, d) Magnitude of sound pressure at single microphone versus distance along the track from the forcing position; —, coherent sources; - - -, incoherent sources. (b, e) output from microphone array for a line array of incoherent sources, (c, f) Output from microphone array for a line array of coherent sources. —, ϕ=0°; —, ϕ=10°; - - -, ϕ=20°; - - -, ϕ=30°.

Figure 6.16 shows the outputs for the vertical rail vibration from the microphone array designed for plane or spherical waves at 2500 Hz. The overall trends of the results measured with two microphone arrays are similar for the incoherent sources. However, for the coherent sources, it can be seen that, by turning the array axis, a larger change in sensitivity response is obtained by the microphone array designed for a plane wave. Also, the difference in sensitivity gain between incoherent and coherent sources is apparently larger in the results of the microphone array tuned for a plane wave. This is because the rail is an extended line source, and the incident wave is close to a plane wave due to its low decay rate. Thus, in order to examine the radiation characteristics of the rail properly, the arrangement for the measured data should be made by using the microphone array designed for a plane wave rather than for spherical waves, even though the microphone array is located quite close to the rail.

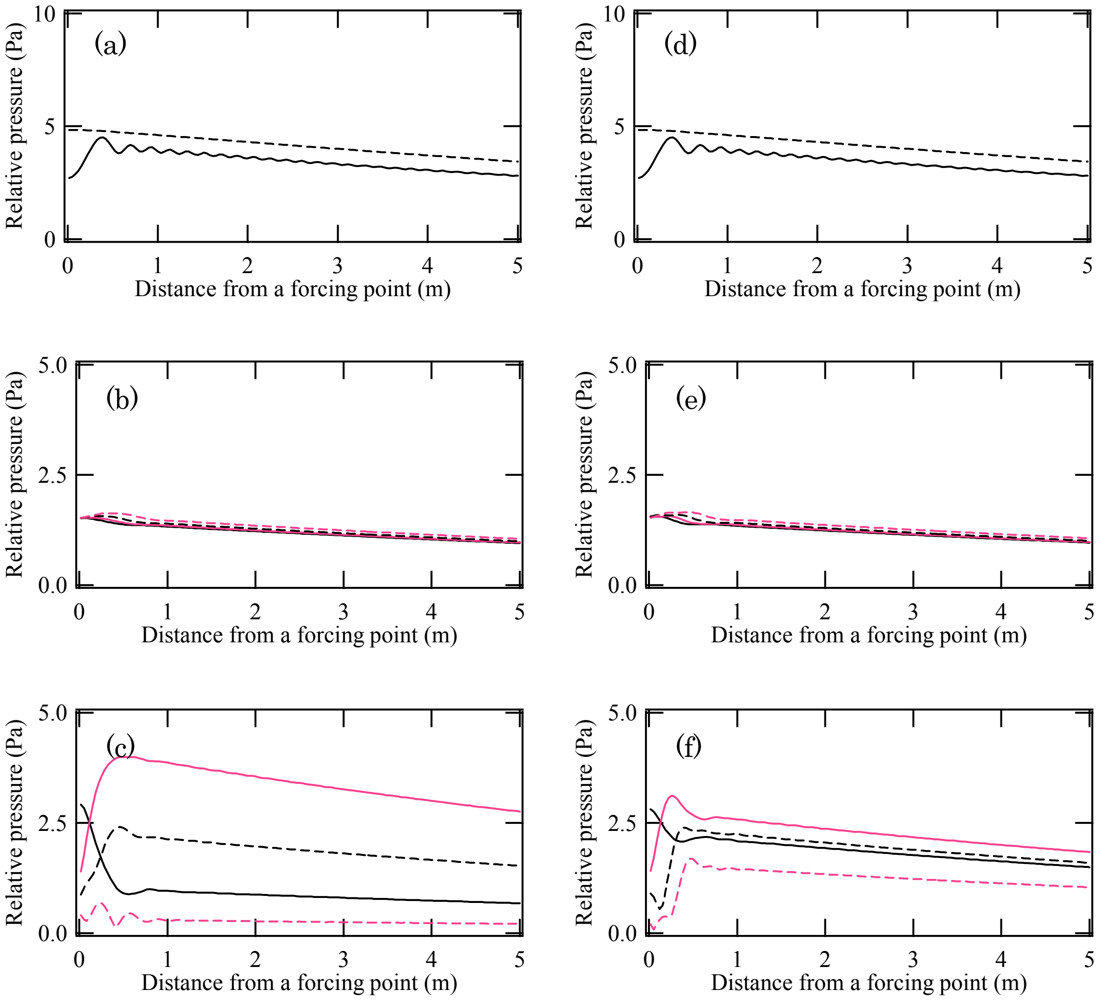

Figure 6.16 Simulation results for vertical rail vibration for 2500 Hz. The microphone array is designed for two types of incident wave: a plane wave (left) and spherical wave (right). (a, d) Magnitude of sound pressure at single microphone versus distance along the track from the forcing position; —, coherent sources; - - -, incoherent sources. (b, e) output from microphone array for a line array of incoherent sources, (c, f) Output from microphone array for a line array of coherent sources. —, ϕ=0°; —, ϕ=10°; - - -, ϕ=20°; - - -, ϕ=30°.

6.5 Radiation behaviour of a rail

In this section, the investigation of the measured radiation behaviour of the rail is carried out for different tuned angles, ϕ=-60° to +60° of the microphone array designed for a plane wave (see Figure 6.17). Measured results are compared with predictions based on both the coherent and incoherent monopole sources with the same sound distribution derived from the *rodel* model.

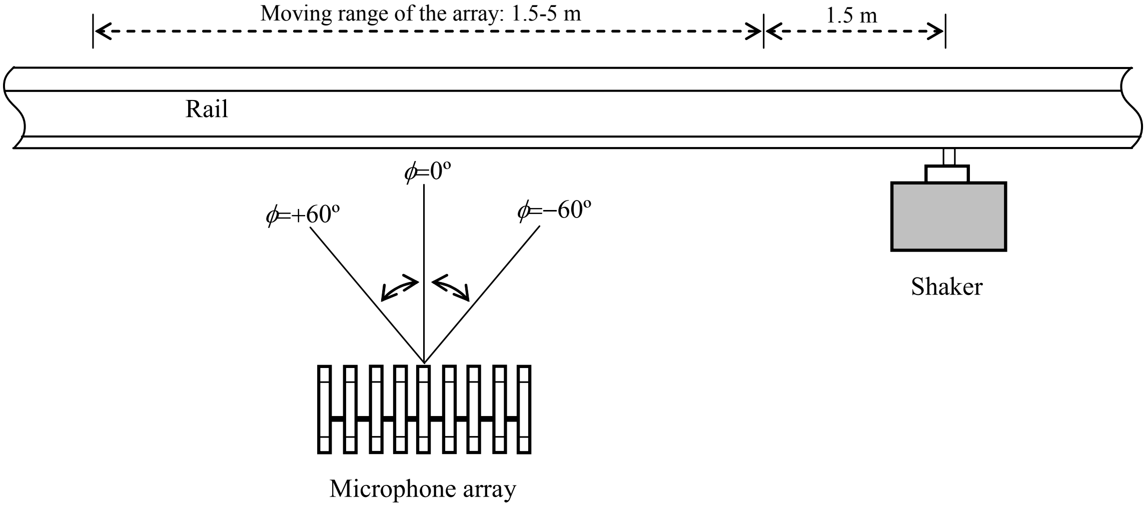

Figure 6.17 Illustration of the microphone array measurements

6.5.1 Sound distribution for vertical excitation

Figure 6.18(a) shows the distribution of vertical rail vibration along the rail, and Figure 6.18(b) the radiation characteristics of the rail obtained by turning the axis of the microphone array for 500 Hz at one location. Also shown are the outputs measured with the microphone array if the predicted source distribution is used and the sources are assumed to be a line array of coherent or incoherent monopoles. In Figure 6.18(b), ‘relative level’ means the difference in dB between the output of the microphone array and the average of the 9 microphones used for this frequency. From Figure 6.18(a), it can be seen the decay rate of vibration is high at this frequency (see also Figure 6.6). This effectively leads to the radiation behaviour of a point source localised in a region around the forcing point. For the array measurements, the overall trends in the measured results are well predicted by both the coherent and incoherent sources, and the maximum gain can be seen at -60°. This again indicates that the microphone array detects spherical spreading from the point source localised at the force point. Figure 6.18(c) shows the directed angle and Figure 6.18(d) shows the level at the main lobe in the radiation pattern as a function of distance from the forcing point. These measurements show similar overall trends to the predictions for the coherent sources. Therefore, it is confirmed that the sound radiation model for the rail is effective for a propagating wave with a high decay rate.

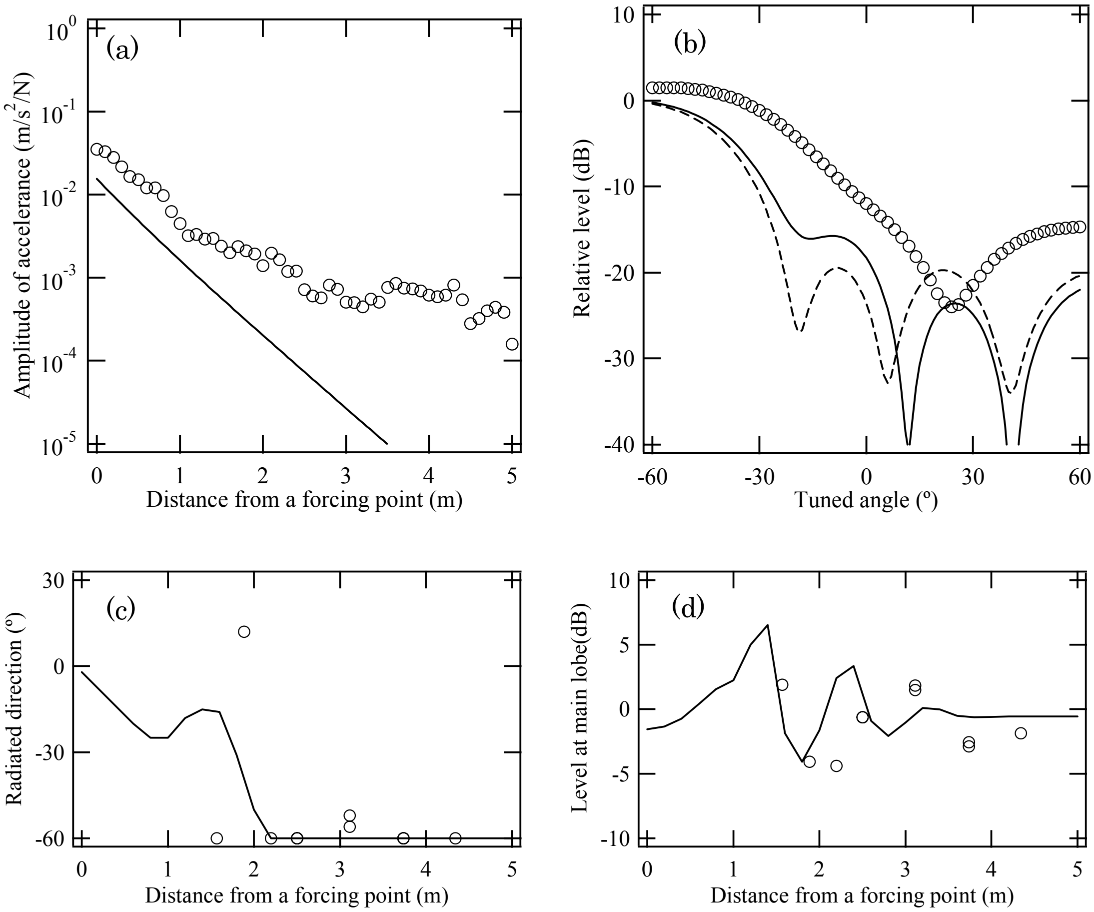

Figure 6.18 Measured and predicted results for vertical shaker excitation at 500 Hz. The microphone array is designed for a plane wave. (a) Rail transfer accelerance; ○, measured results; ——, *rodel* model, (b) radiation pattern measured at a distance of 3.115 m from the forcing point. ○, Measured results; ——, predictions for coherent sources; ······, predictions for incoherent sources. (c) Direction of main lobe in the radiation pattern. ○, Measured results; ——, predictions for coherent sources. (d) Maximum level at main lobe. ○, Measured results; ——, predictions for coherent sources.

Figure 6.19 shows the corresponding results for 1000 Hz. At this frequency, the amplitudes of the rail vibration measured along the rail contain strong undulations due to the pinned-pinned resonance; the amplitudes also decay gradually with distance. Results are shown in Figures 6.19(b) and (c) for two different distances. The predictions give similar overall trends to the measurements. However, in the predictions, the amplitudes of the rail vibration do not contain undulations, since, in the *rodel* model, the rail is supported continuously and no pinned-pinned resonance is present. For the array measurements, it can be seen that the measured results do not show very good agreement with the predictions, and the main lobe in the radiation patterns is not so clear in the measurements. This is because the vibratory behaviour induced by the pinned-pinned resonance has a significant influence on the radiation characteristics of the rail. In Figures 6.19(b) and (b), instead of a single main lobe at 15° seen in the predictions, the measured results indicate peaks at ±10° and ±20° respectively, caused by reflections at the sleepers leading to positive and negative going waves. The level at the main lobe is associated with the presence of significant radiation energy in the negative going direction.

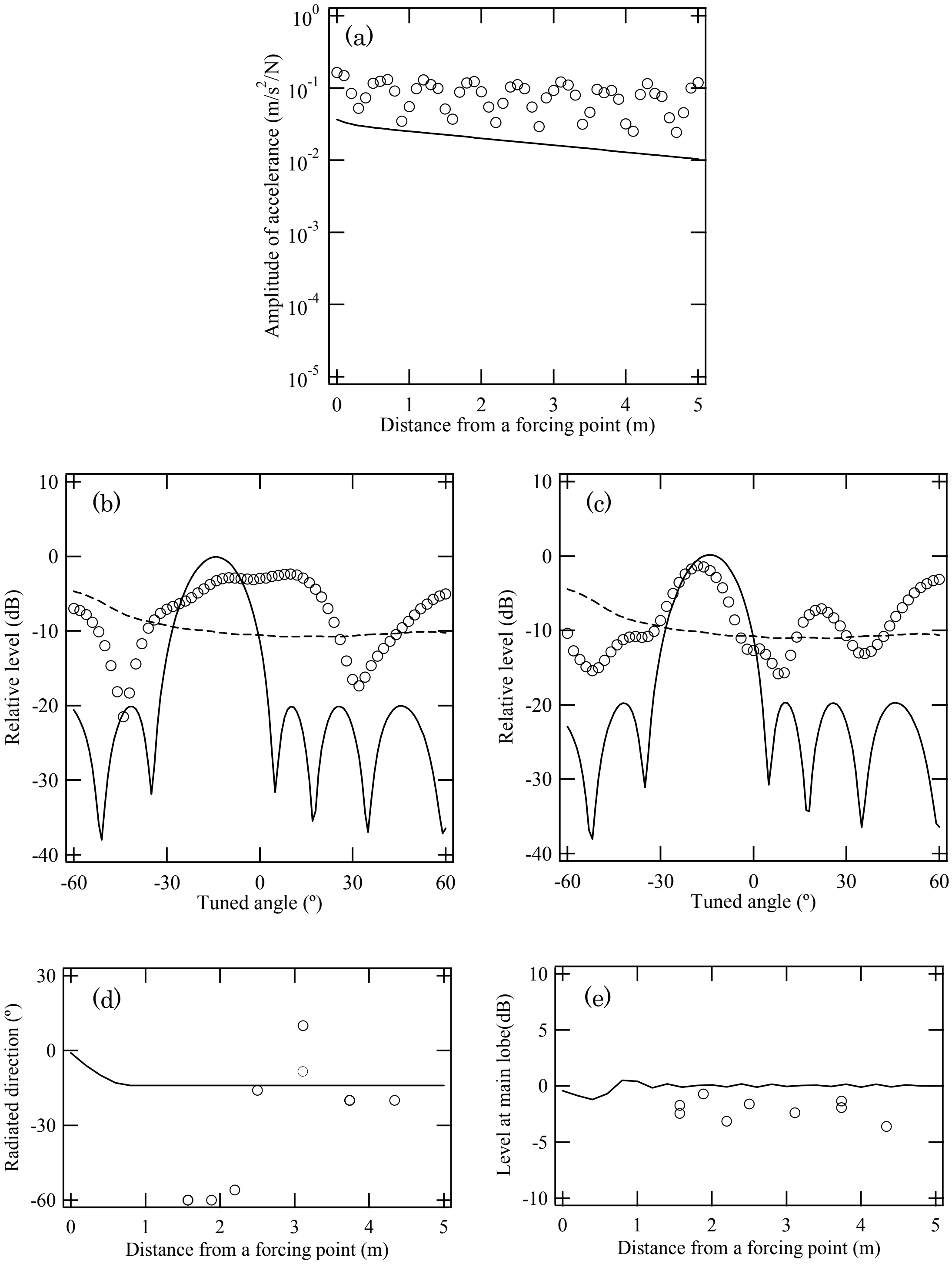

Figure 6.19 Measured and predicted results for vertical shaker excitation at 1000 Hz. The microphone array is designed for a plane wave. (a) Rail transfer accelerance; ○, measured results; —–, *rodel* model, (b) radiation pattern measured at a distance of 3.115 m from the forcing point. ○, Measured results; ——, predictions for coherent sources; ······, predictions for incoherent sources. (c) radiation pattern measured at a distance of 3.74 m from the forcing point. ○, Measured results; ——, predictions for coherent sources; ······, predictions for incoherent sources. (d) Direction of main lobe in the radiation pattern. ○, Measured results; ——, predictions for coherent sources. (e) Maximum level at main lobe. ○, Measured results; ——, predictions for coherent sources.

Figures 6.20 and 6.21 show the corresponding results for 2000 Hz and 2500 Hz. It is found that the slope of the amplitude of the rail vibration is more gradual, corresponding to free wave propagation in the rail, and the rail effectively represents an extended line source. For the array measurements, by steering the array axis, a clear peak can be seen at about 10° for 2000 Hz and 2500 Hz in the measured results. This is related to typical supersonic structural radiation, and the rail radiates sound at an angle to the normal. The measured results show excellent agreement with the prediction for the coherent sources. This confirms that it is appropriate to replace the vibrating rail as a line array of coherent sources. For the directed angle and level at the main lobe in the radiation pattern, it can be seen that the predictions for the coherent sources also show very good agreement with the measurements. Therefore, it is confirmed that, through the array measurements, the radiation characteristics of the rail are investigated properly when the rail is represented as a line array of coherent sources, not incoherent sources.

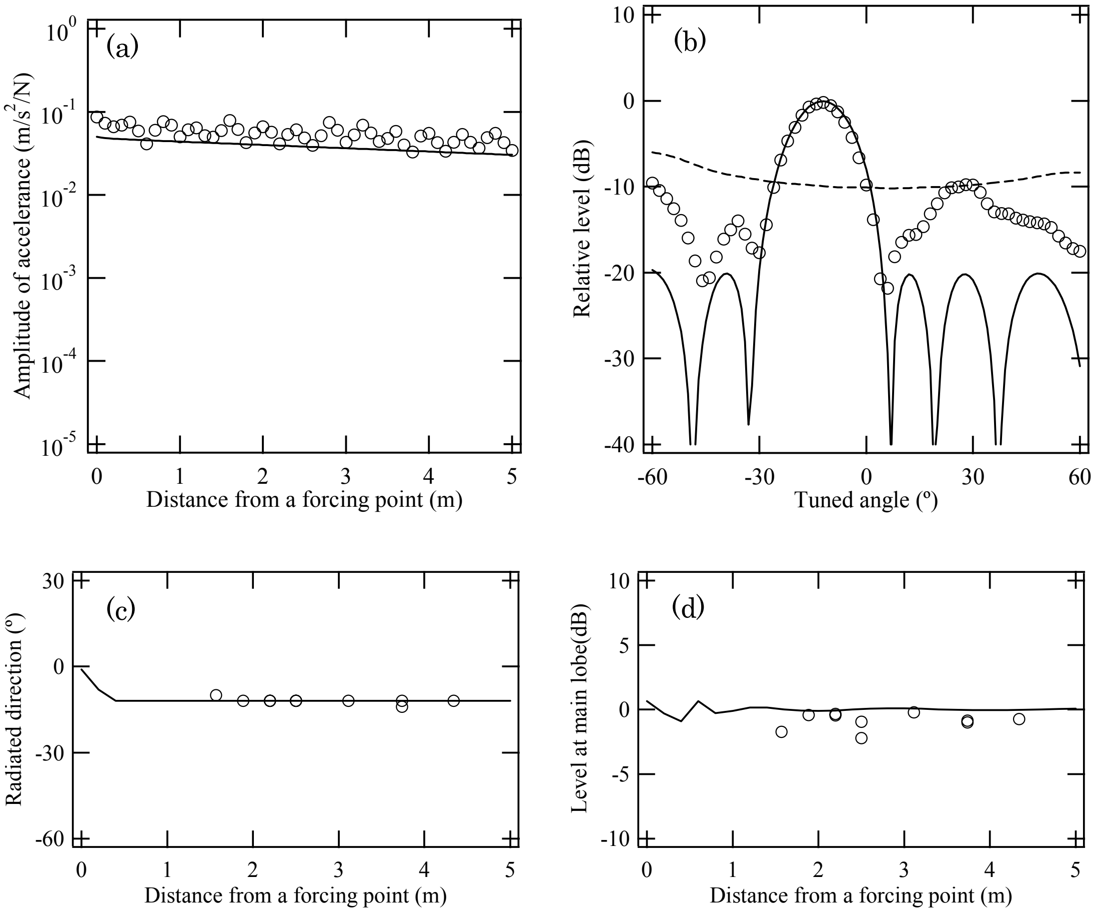

Figure 6.20 Measured and predicted results for vertical shaker excitation at 2000 Hz. The microphone array is designed for a plane wave. (a) Rail transfer accelerance; ○, measured results; —, *rodel* model, (b) radiation pattern measured at a distance of 3.115 m from the forcing point. ○, Measured results; ——, predictions for coherent sources; ······, predictions for incoherent sources. (c) Direction of main lobe in the radiation pattern. ○, Measured results; ——, predictions for coherent sources. (d) Maximum level at main lobe. ○, Measured results; ——, predictions for coherent sources.

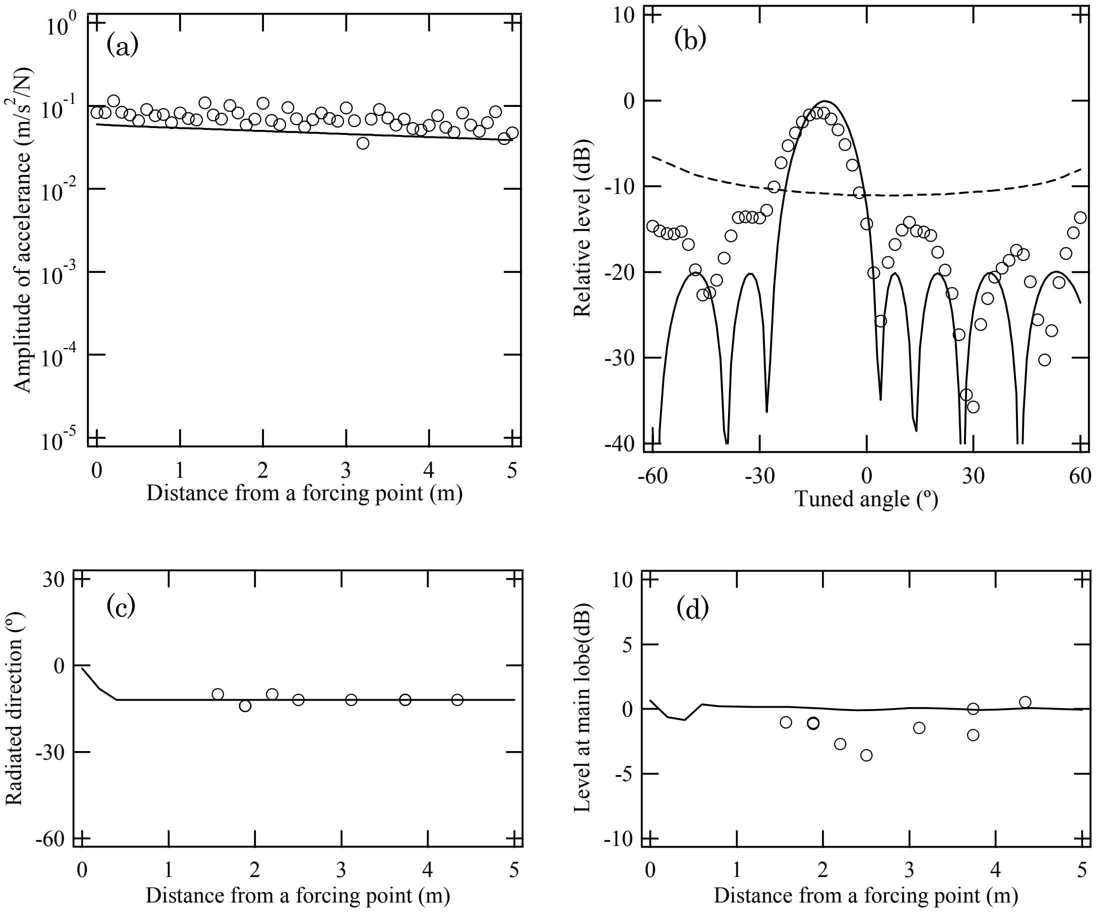

Figure 6.21 Measured and predicted results for vertical shaker excitation at 2500 Hz. The microphone array is designed for a plane wave. (a) Rail transfer accelerance; ○, measured results; ──, *rodel* model, (b) radiation pattern measured at a distance of 3.115 m from the forcing point. ○, Measured results; ——, predictions for coherent sources; ······, predictions for incoherent sources. (c) Direction of main lobe in the radiation pattern. ○, Measured results; ——, predictions for coherent sources. (d) Maximum level at main lobe. ○, Measured results; ——, predictions for coherent sources.

6.5.2 Sound distribution for horizontal excitation

Figures 6.22, 6.23, 6.24 and 6.25 show the corresponding results for the horizontal rail vibration for four different frequencies, 630 Hz, 800 Hz, 1250 Hz and 1600 Hz. It is found that the overall trends of the results for the horizontal vibration are similar to those seen in Figures 6.20 and 6.21. The angle of the main lobe is greater in the present case due to the shorter wavelengths for horizontal vibration, see Figure 6.5. In fact, the *rodel* model slightly underpredicts the wavenumbers for horizontal vibration at high frequencies (see Figure 6.5), and therefore the angle of the main lobe tends to be greater in the measurements than in the predictions.

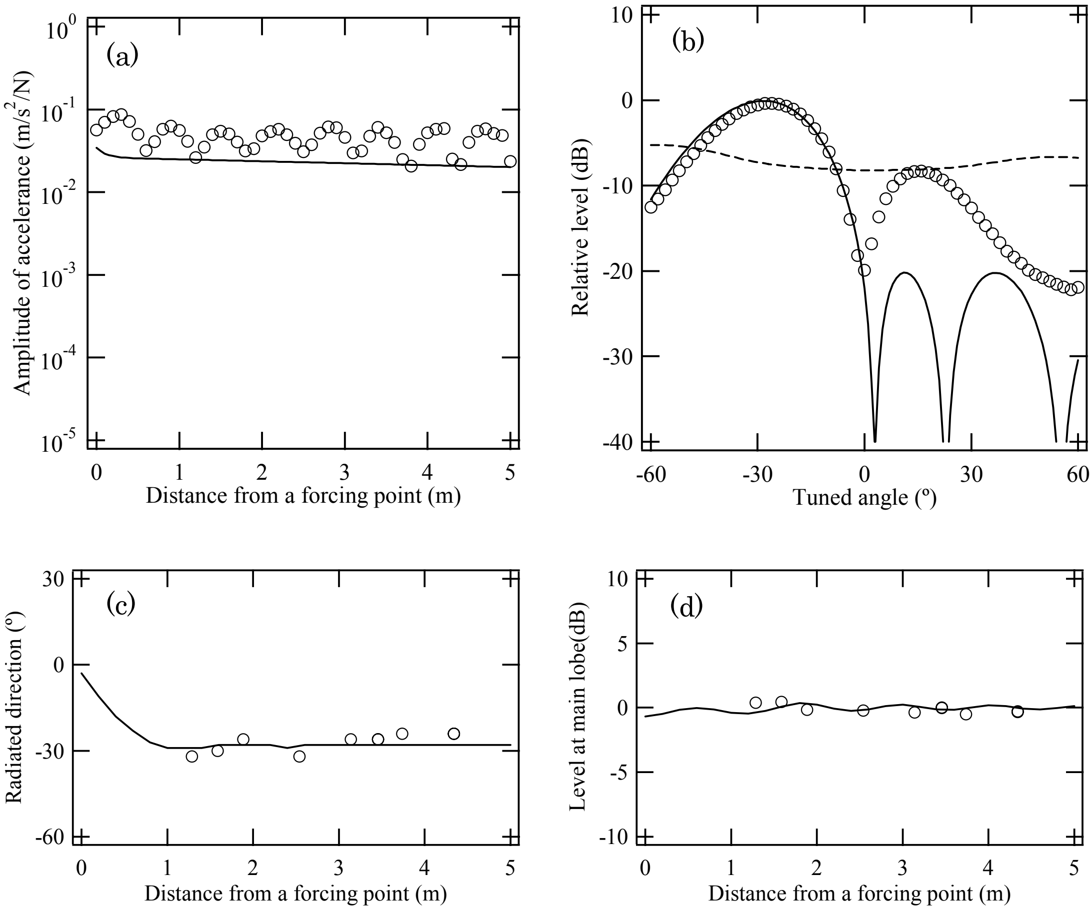

Figure 6.22 Measured and predicted results for horizontal shaker excitation at 630 Hz. The microphone array is designed for a plane wave. (a) Rail transfer accelerance; ○, measured results; ——, *rodel* model, (b) radiation pattern measured at a distance of 3.14 m from the forcing point. ○, Measured results; ——, predictions for coherent sources; ······, predictions for incoherent sources. (c) Direction of main lobe in the radiation pattern. ○, Measured results; ——, predictions for coherent sources. (d) Maximum level at main lobe. ○, Measured results; ——, predictions for coherent sources.

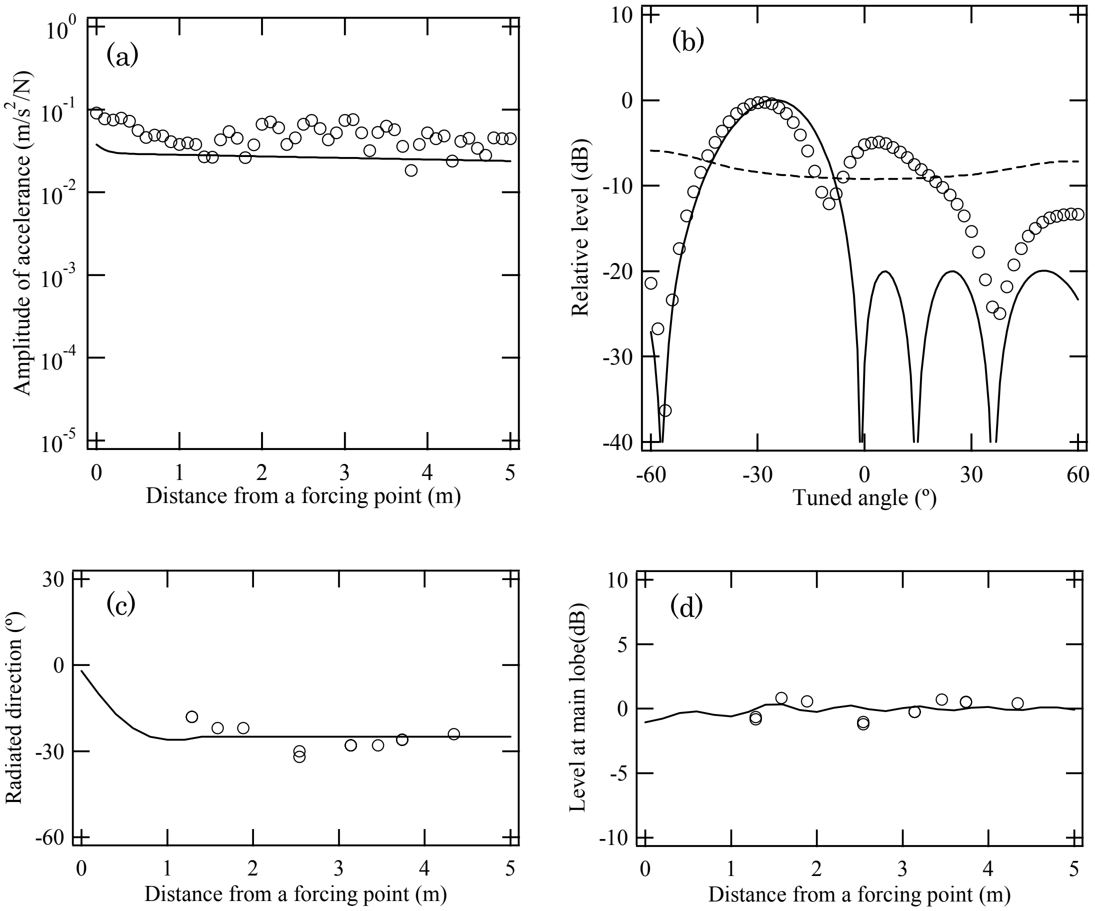

Figure 6.23 Measured and predicted results for horizontal shaker excitation at 800 Hz. The microphone array is designed for a plane wave. (a) Rail transfer accelerance; ○, measured results; —, *rodel* model, (b) radiation pattern measured at a distance of 3.14 m from the forcing point. ○, Measured results; ——, predictions for coherent sources; ······, predictions for incoherent sources. (c) Directivity of main lobe in the radiation pattern. ○, Measured results; ——, predictions for coherent sources. (d) Maximum level at main lobe. ○, Measured results; ——, predictions for coherent sources.

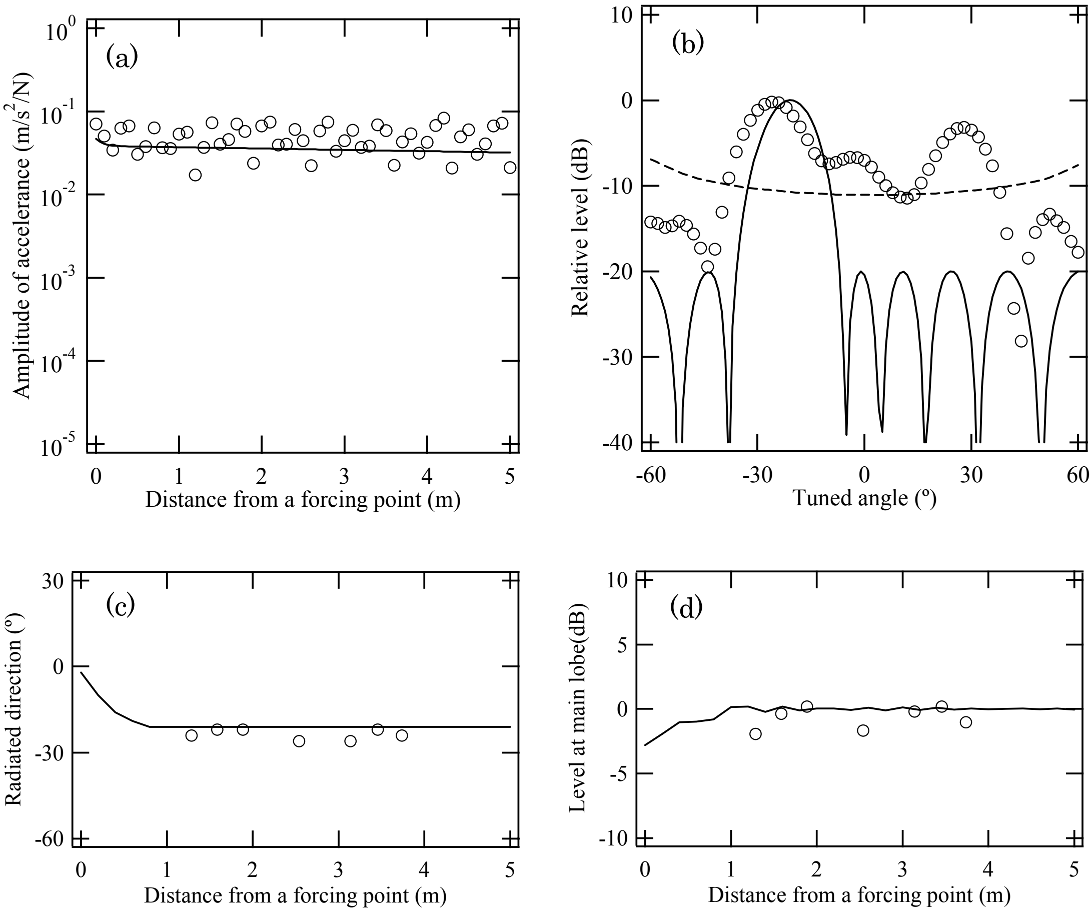

Figure 6.24 Measured and predicted results for horizontal shaker excitation at 1250 Hz. The microphone array is designed for a plane wave. (a) Rail transfer accelerance; ○, measured results; ──, *rodel* model, (b) radiation pattern measured at a distance of 3.14 m from the forcing point. ○, Measured results; ——, predictions for coherent sources; ⋯⋯, predictions for incoherent sources. (c) Directivity of main lobe in the radiation pattern. ○, Measured results; ——, predictions for coherent sources. (d) Maximum level at main lobe. ○, Measured results; ——, predictions for coherent sources.

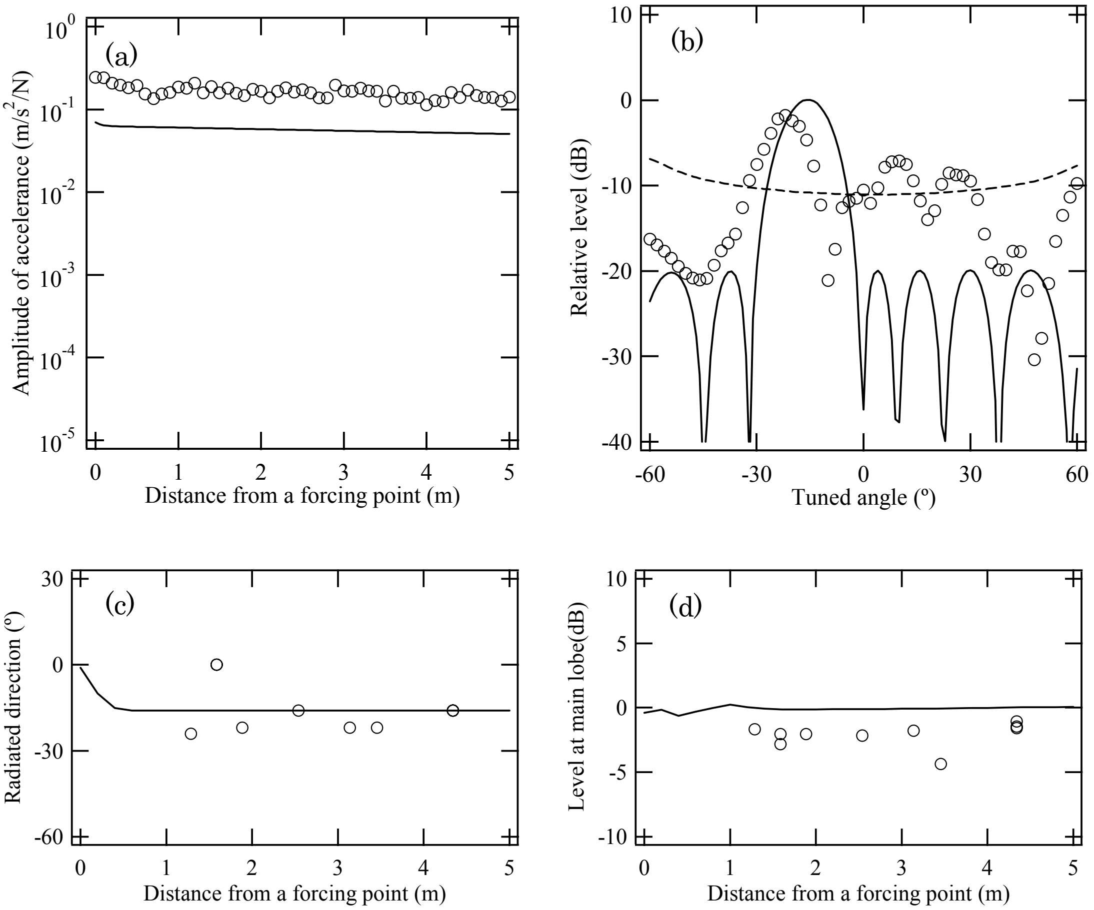

Figure 6.25 Measured and predicted results for horizontal shaker excitation at 2500 Hz. The microphone array is designed for a plane wave. (a) Rail transfer accelerance; ○, measured results; ──, *rodel* model, (b) radiation pattern measured at a distance of 3.14 m from the forcing point. ○, Measured results; ───, predictions for coherent sources; ······, predictions for incoherent sources. (c) Directivity of main lobe in the radiation pattern. ○, Measured results; ───, predictions for coherent sources. (d) Maximum level at main lobe. ○, Measured results; ───, predictions for coherent sources.

6.5.3 Sound radiation characteristics

Figure 6.26 summarises the results by showing the angle of the main lobe and the corresponding level for both vertical and horizontal directions. For the directed angle of the rail, the results can be seen to be predicted reasonably well in the frequency range where free propagating wave motion occurs in both vertical and horizontal directions (results are not shown for 500 Hz for the vertical vibration). At frequencies associated with the pinned-pinned resonance, especially 1000 Hz for the vertical vibration, the predictions show less good agreement with the measurements. This is because, at these frequencies, the vibratory behaviour is more complex than assumed in the model and this has significant influence on the radiation characteristics of the rail. However, for 1600 Hz and above in the vertical direction and for most frequencies in the lateral direction, agreement is excellent. For the level at the main lobe in the radiation patterns, it can be seen that the overall trends are predicted fairly well, although the measurements for the vertical rail vibration are slightly lower than the predictions.

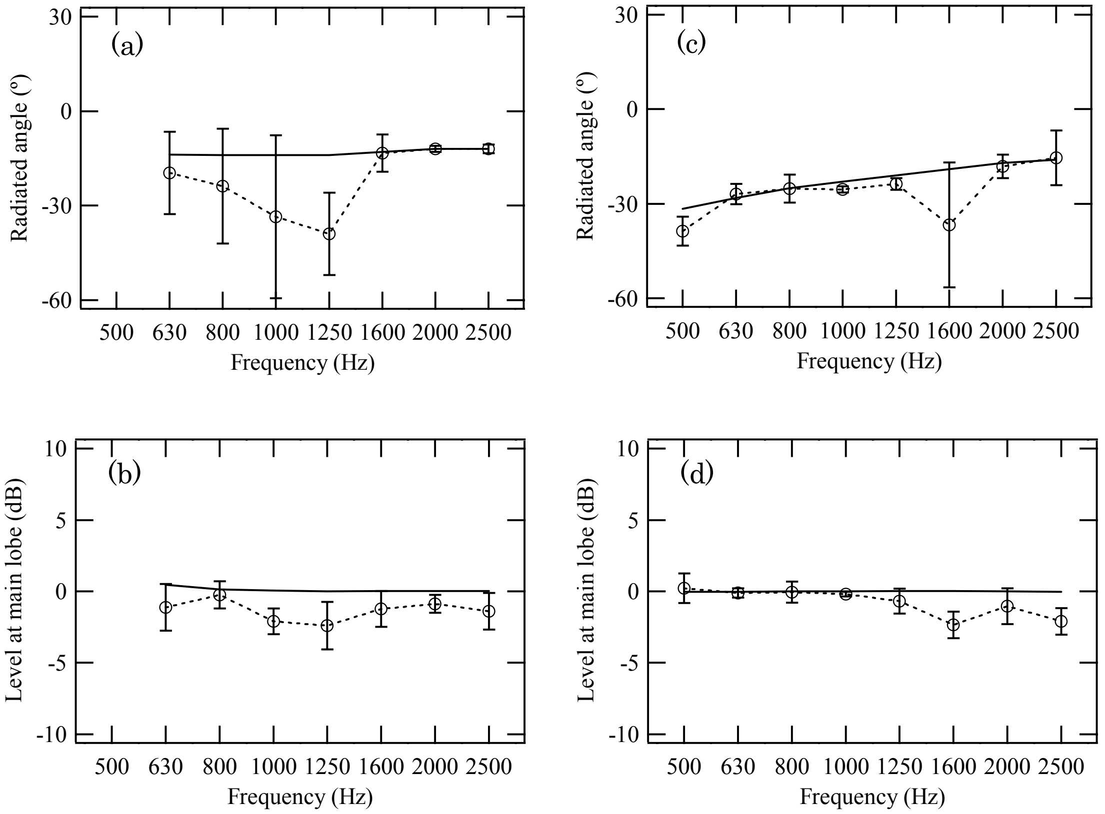

Figure 6.26 Sound characteristics radiated from the rail by the vertical (left) and horizontal (right) shaker excitation. The microphone array is designed for a plane wave. Error bars are ± standard deviation. ○, Measured results; ——, predictions for coherent sources. (a, c) Directivity of main lobe in the radiation pattern, (b, d) maximum level at main lobe.

6.6 Summary

Through the measurements obtained using shaker excitation of the track, the radiation properties of the rail have been verified by a one-dimensional microphone array. It is found that, by directing the array, the rail radiates at an angle to the normal in the frequency range where free wave propagation occurs. The measured results show good agreement with the predictions for the coherent sources in both vertical and horizontal directions. This means that the radiation behaviour of the rail is investigated appropriately by replacing the rail as a line array of coherent sources, not incoherent sources. Therefore, it is confirmed that the prediction model in Chapter 5 is suitable to represent the characteristics of the rail radiation.

7 MEASUREMENTS FOR A MOVING TRAIN

7.1 Introduction

Through the experiments using shaker excitation, the radiation properties of the rail have been investigated by steering the axis of the microphone array. It has been confirmed that the sound is radiated from the rail at an angle to the normal in the frequency range where free propagation wave occurs, and, by comparing the predictions with the measurements, the radiation behaviour of the rail is suitably modelled as a line array of coherent monopoles (or dipoles). In this chapter, an attempt to investigate the sound generated by the rail during a train pass-by is made by using a horizontal microphone array. The main purpose is to make a qualitative examination of the radiation properties of the rail through measurements of moving trains. The microphone array is positioned close to the rail, and the radiation behaviour of the rail is examined by steering the array axis. The situation is more complex than in the previous chapter due to the presence of the wheels as sources of noise as well as the track.

The sound measurements were carried out for a single track type in the Kosei line. Figures 7.1 and 7.2 show photographs of the measurement section. The section is laid with 50N-type rails, which are continuously welded. The track is of ballasted construction, and concrete monobloc sleepers are used with a nominal spacing of 0.62 m. The measurements were performed for trailer cars with three types of wheel; wheels A, D and F. Trailer cars are used as they do not have driving devices (i.e. traction motors), and so they radiate mainly rolling noise. The details of the three wheels were shown in Table 2.2.

Figure 7.1 Photograph of the measurement section

Figure 7.2 Photograph of the track and vehicles

7.2 Description of the sound measurements

In order to estimate the vibratory and acoustic behaviour of the rail, appropriate parameters associated with the vibratory properties of the track are required. However, no static tests were performed to characterize the vibration of the track prior to the sound measurements, since the track was of a similar type to Track A (see Table 2.1). Therefore, the calculations of the rail vibration with the *rodel* model have been performed by using the parameters given in Table 2.3.

The sound measurements were carried out with the same horizontal microphone array used in the shaker excitation experiments in Chapter 6. Figure 7.3 shows the setup and Figure 7.4 a schematic diagram of the sound measurements. The specifications of the microphone array are given in Table 6.2. The microphone array was composed of 13 microphones with two sets of 9 microphones arranged in a line with an equal spacing. The microphone array was situated parallel to the rail at a distance of 2.88 m from the rail. A single microphone was located at the centre of the array for comparison. An axle detector was mounted on one side of the railhead close to the position of the array. The axle detector is a device to produce a pulse when a train wheel passes over it. During the measurements, the pulse occurs just before the wheel runs in front of the array (see Figure 7.5). The raw data measured with the 13 microphones of the array were recorded simultaneously using a tape recorder. Subsequent to the field measurements, the data were analysed by using the delay-and-sum process in a PC. In the analysis process, the array was designed for a plane wave. This is because a larger change in sensitivity response is obtained by the microphone array designed for a plane wave (see Figures 6.15 and 6.16).

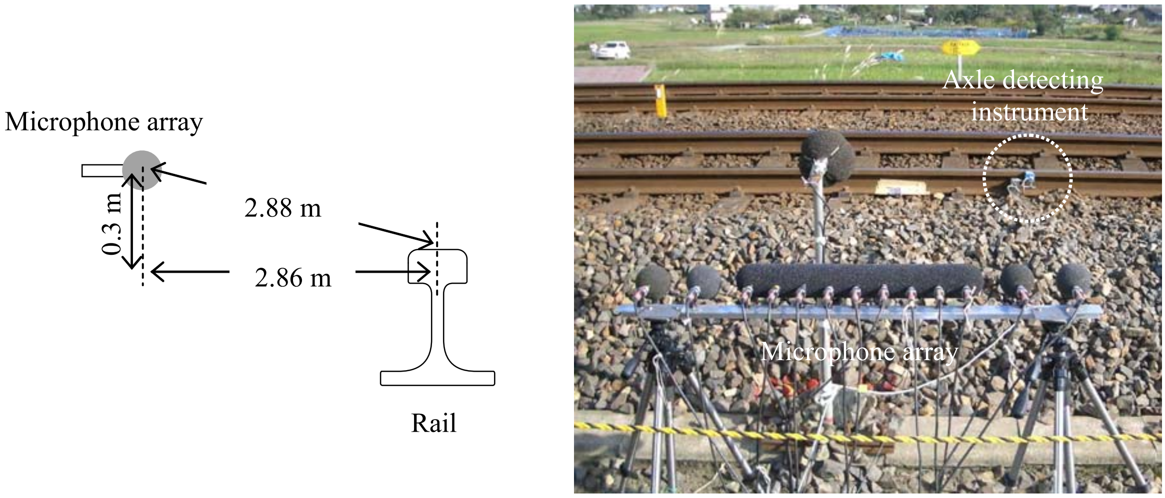

Figure 7.3 Setup for the sound measurements

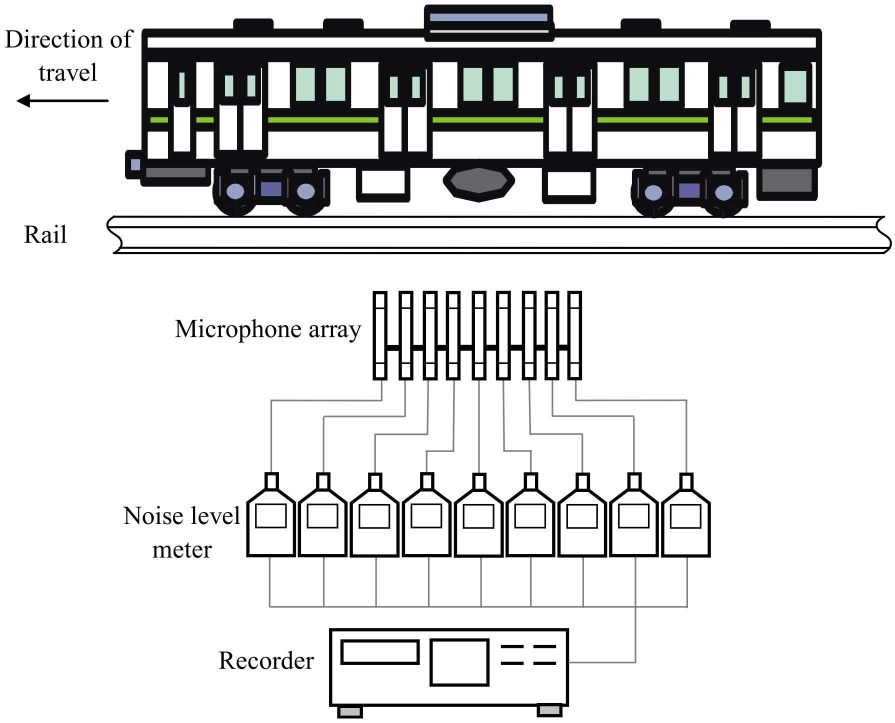

Figure 7.4 Schematic diagram for the sound measurements

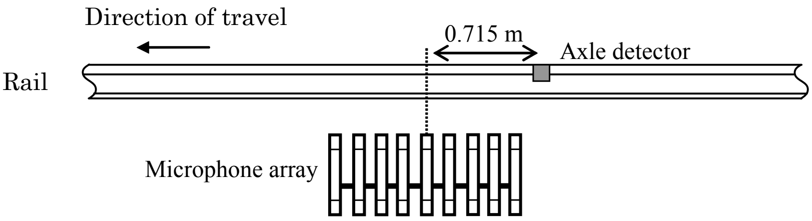

Figure 7.5 Setup of the axle detector

Before studying the sound measurements, it is important to see which wheel type is most suitable for the investigation of the rail radiation. This is because it is better that the contribution of the rail is greater than that of the wheel, especially in the frequency range where free wave propagation occurs. Here, the examinations for the rail component of noise are carried out by using the TWINS predictions from Section 2.3.2.3. From Figure 2.16, in the frequency range 500 Hz to 1250 Hz, the dominant noise source depends on the wheel type. It can be seen that, for wheel A, the rail has a greater contribution to the total noise than the wheel below 1600 Hz. In contrast, wheels D and F have a large wheel contribution in the 1250 Hz band. Thus, in order to investigate the radiation behaviour of the rail, it is more appropriate to use wheel A for the sound measurements, and only results for this wheel type will be shown.

7.3 Rail radiation for a moving train

In this section, the qualitative examination of the radiation behaviour of the rail is performed for different tuned angles, ϕ=-30° to +30°, of the microphone array designed for a plane wave.

Figures 7.6 and 7.7 show the time histories filtered in one-third octave bands of the sound pressure level measured with the single microphone and microphone array directed at 0º.

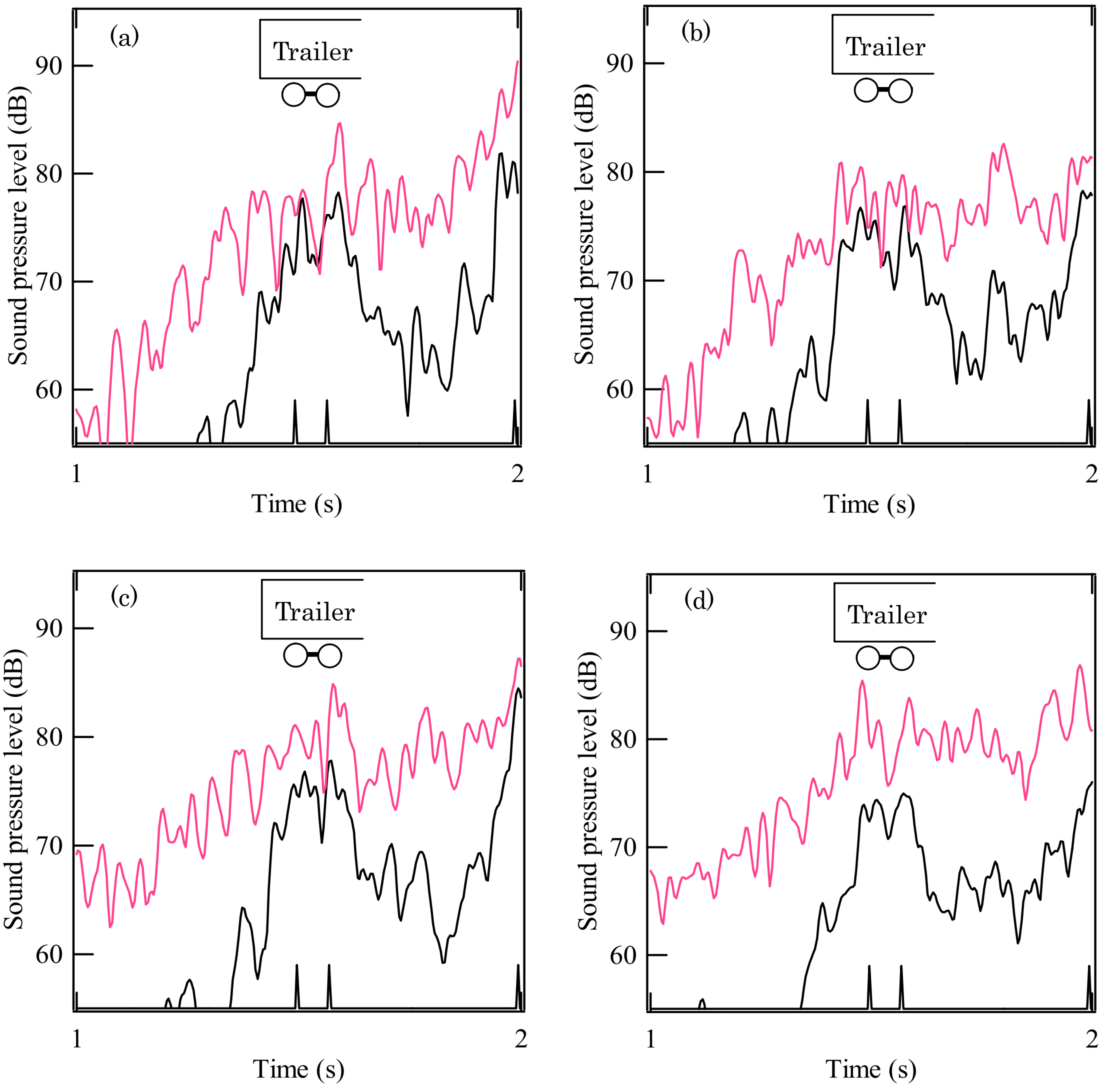

Figure 7.6 Time histories filtered in one-third octave bands of a trailer bogie running at 102 km/h measured with the single microphone and microphone array filtered in one-third octave bands. The array is designed for a plane wave with a tuned angle, ϕ=0º. —, Microphone array; —, single microphone. The positions of the wheels are indicated by the pulses at the bottom of the graph. (a) 500 Hz, (b) 630Hz, (c) 800 Hz, (d) 1000 Hz.

A trailer bogie runs at 102 km/h (=28.3 m/s); this is the first bogie of the train. The positions of the wheels are indicated by the pulses at the bottom of the graph. It can be seen that the sources appear to be at the wheels, and that the sound levels measured with the array do not reach the corresponding levels measured with the single microphone. The single microphone measures the overall sound generated from the rail and wheel. Therefore, this indicates that the microphone array might see only the sound radiation from the region localised around the wheel, and miss the sound radiation generated by the propagating wave part of the rail vibration.

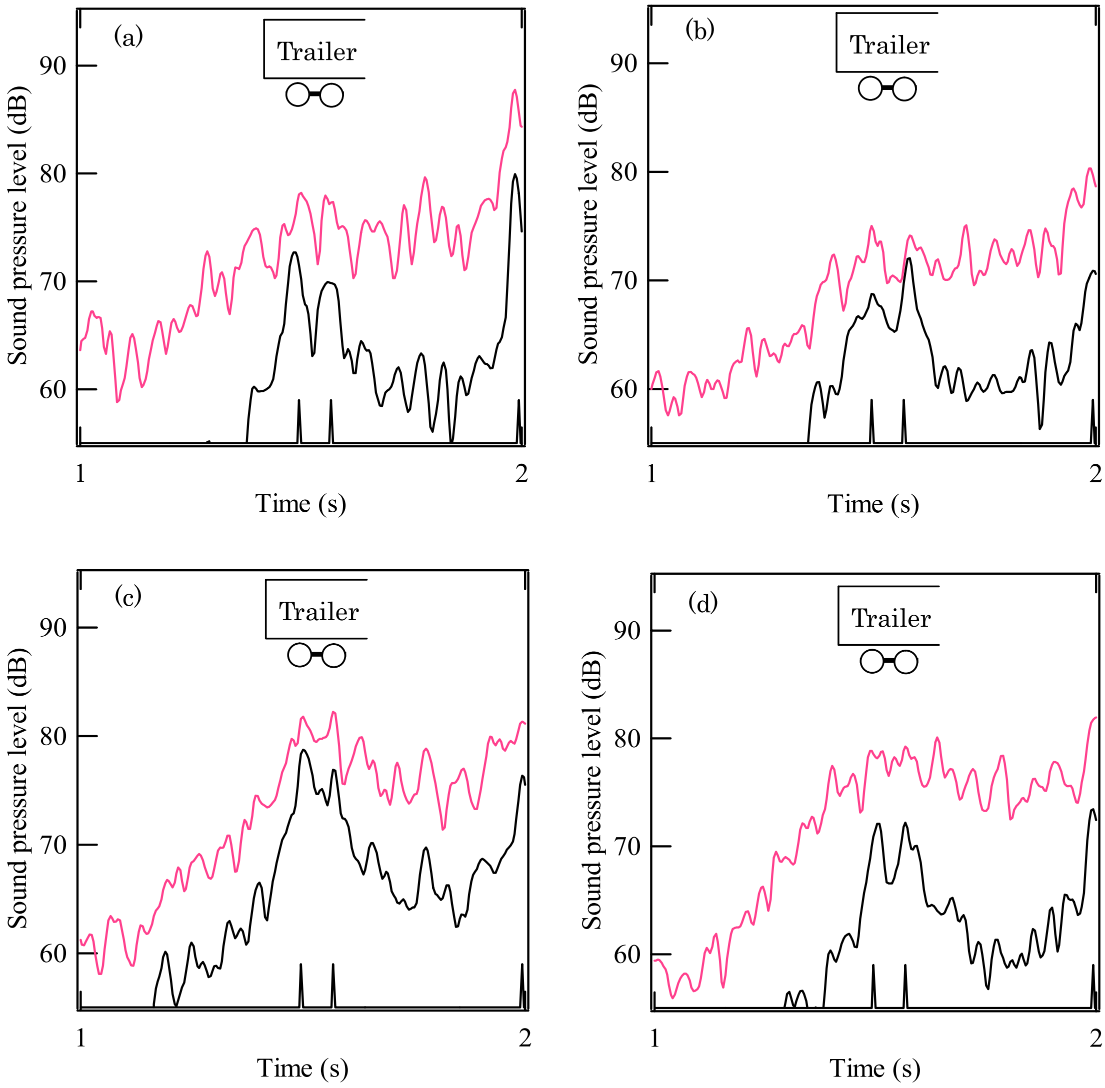

Figure 7.7 Time histories filtered in one-third octave bands of a trailer bogie running at 102 km/h measured with the single microphone and microphone array filtered in one-third octave bands. The array is designed for a plane wave with a tuned angle, ϕ=0º. —, Microphone array; —, single microphone. The positions of the wheels are indicated by the pulses at the bottom of the graph. (a) 1250 Hz, (b) 1600Hz, (c) 2000 Hz, (d) 2500 Hz.

Figures 7.8-7.15 show the time histories of the sound pressure level generated by the trailer bogie running at 102 km/h obtained by steering the microphone array at angles of -30º to +30º for each one-third octave band.

From Figure 7.8, for 500 Hz, it can be seen that there is an apparent shift in the location of the sound levels in the time histories towards the left as the array axis is turned with a larger angle and towards the right for negative tuned angles. As, below 1600 Hz, the rail is the dominant noise source in the total noise, the sound levels in the time history are mainly composed of the rail noise. In this frequency band, the decay rate of vertical vibration is high, but for horizontal vibration it is lower (see Figure 5.5(a)). This suggests that the rail acts not only as a point source localised in a region around the wheels, but also as a line source caused by horizontal travelling waves.

The lateral shift in the time histories does not correspond to the point source at the wheel position. This is because the tuned angle of the array is much less than that obtained from the shift in the location of the sound levels (e.g. when the microphone array is directed at 20º, the lateral shift is about 0.1 sec. This shift corresponds to an angle of 45º ($\approx \tan^{-1}(28.3(\mathrm{m/s})\times 0.1(\mathrm{s})/2.88(\mathrm{m}))$.). It also can be seen that, by directing the array at an angle close to ±30º, the response of the sound levels induced before or after the trailer bogie passes in front of the array is greater than for 0º. This is because the array is tuned at the angle closely related to the supersonic structural radiation of horizontal rail vibration (the rail radiates at an angle of about 28º ($\approx \sin^{-1}(\lambda_{air}/\lambda_{rail}) = \sin^{-1}(0.68/1.30)$) in the horizontal direction). Therefore, it may be concluded that the lateral shift occurs due to free wave motion in horizontal direction.

From Figure 7.9, at 630 Hz, it is found that, by turning the array axis, the results show similar overall trends to those seen in Figure 7.8. This also indicates that, at 630 Hz, horizontal rail vibration has a significant influence on the rail component of noise.

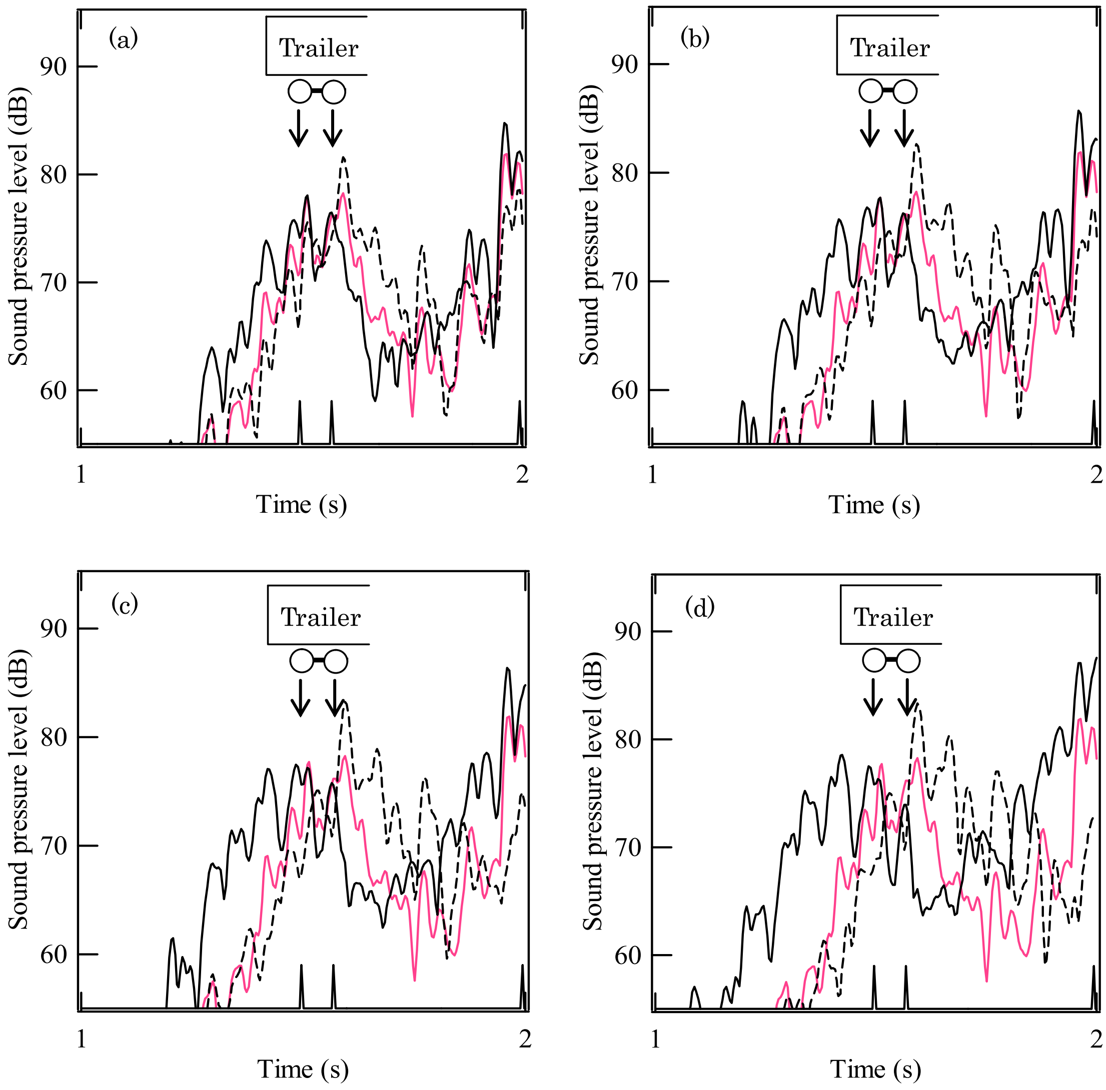

Figure 7.8 Time histories of a trailer bogie running at 102 km/h measured with the microphone array filtered in 500 Hz band. The array is designed for a plane wave with a tuned angle, ϕ. The positions of the wheels are indicated by the pulses at the bottom of the graph. (a) —, ϕ=10º; - - -, ϕ=-10º; —, ϕ=0º. (b) —, ϕ=15º; - - -, ϕ=-15º; —, ϕ=0º. (c) —, ϕ=20º; - - -, ϕ=-20º; —, ϕ=0º. (d) —, ϕ=30º; - - -, ϕ=-30º; —, ϕ=0º.

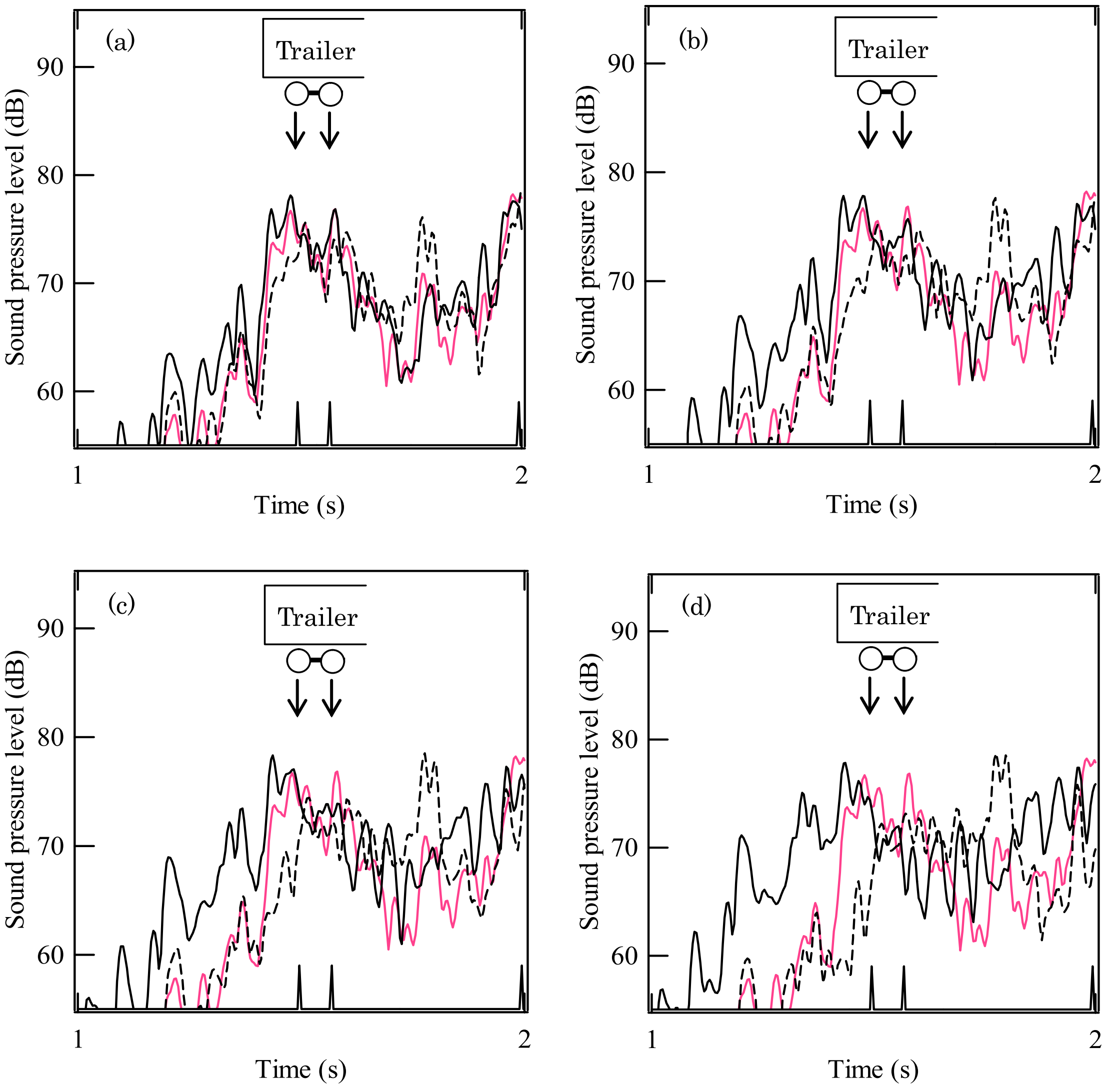

Figure 7.9 Time histories of a trailer bogie running at 102 km/h measured with the microphone array filtered in 630 Hz band. The array is designed for a plane wave with a tuned angle, ϕ. The positions of the wheels are indicated by the pulses at the bottom of the graph. (a) —, ϕ=10°; - - -, ϕ=-10°; —, ϕ=0°. (b) —, ϕ=15°; - - -, ϕ=-15°; —, ϕ=0°. (c) —, ϕ=20°; - - -, ϕ=-20°; —, ϕ=0°. (d) —, ϕ=30°; - - -, ϕ=-30°; —, ϕ=0°.

From Figure 7.10, at 800 Hz, it can be seen that, by steering the array axis at positive angles, there is an apparent increase in the sound levels before the trailer bogie runs in front of the array, although the time histories shift only slightly to the left. Conversely, by directing the array at negative angles, the sound levels in the time history are increased *after* the trailer bogie passes in front of the array. For the waves with a low decay rate, the rail acts as an extended line source, and the rail radiates sound at an angle to the normal due to free wave propagation. Therefore, the increase is caused by the sound radiated from the rail at the tuned angles of the array. It is found that the maximum sound levels in the time histories at 800 Hz are obtained by steering the array at 15º. This is because the array is directed at the angle at which the rail radiates strongly by vertical rail vibration. This also supports the supposed directivity of the rail radiation. A free wave in the rail radiates at the angle determined by the supersonic structural radiation. As the angle is about 14º $(\approx\sin^{-1}(\lambda_{air}/\lambda_{rail})=\sin^{-1}(0.425/1.75))$ for vertical waves in this frequency band, the array directed at 15º yields a greater response than for 0º.

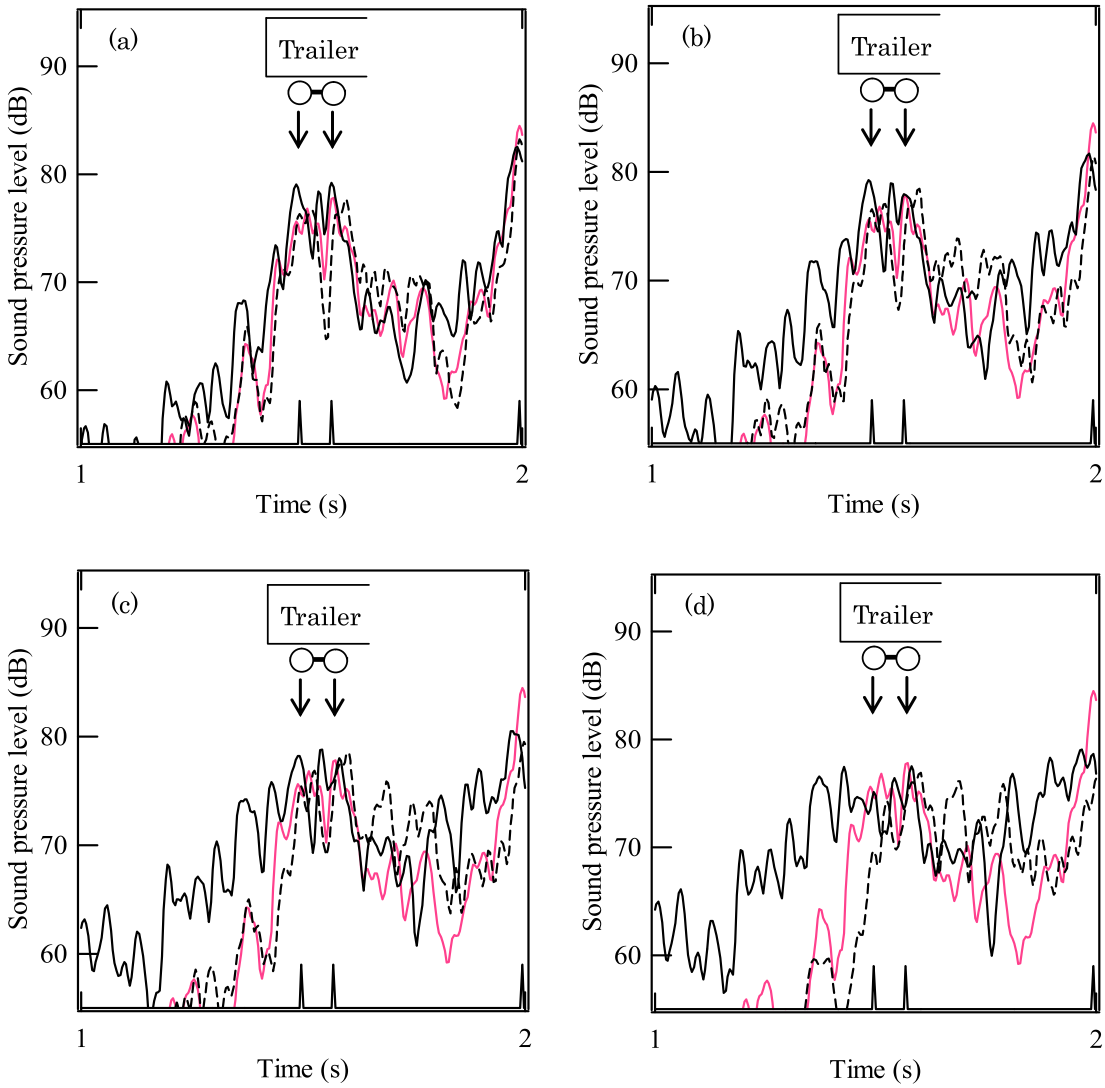

Figure 7.10 Time histories of a trailer bogie running at 102 km/h measured with the microphone array filtered in 800 Hz band. The array is designed for a plane wave with a tuned angle, ϕ. The positions of the wheels are indicated by the pulses at the bottom of the graph. (a) ——, ϕ=10º; - - -, ϕ=-10º; ——, ϕ=0º. (b) ——, ϕ=15º; - - -, ϕ=-15º; ——, ϕ=0º. (c) ——, ϕ=20º; - - -, ϕ=-20º; ——, ϕ=0º. (d) ——, ϕ=30º; - - -, ϕ=-30º; ——, ϕ=0º.

It can be seen that, by steering the array at larger angles, the sound levels in the time histories are greater before or after the passage of the trailer bogie in front of the array. This again may be closely related to the supersonic structural radiation in horizontal direction; the sound due to horizontal rail vibration is radiated strongly at 24^{o} ($\approx \sin^{-1}(\lambda_{air}/\lambda_{rail})=\sin^{-1}(0.425/0.949)$) in this frequency band. From Figure 7.11, at 1000 Hz, the overall trends are similar to those seen in Figure 7.10, although the pinned-pinned resonance has a significant influence on the results.

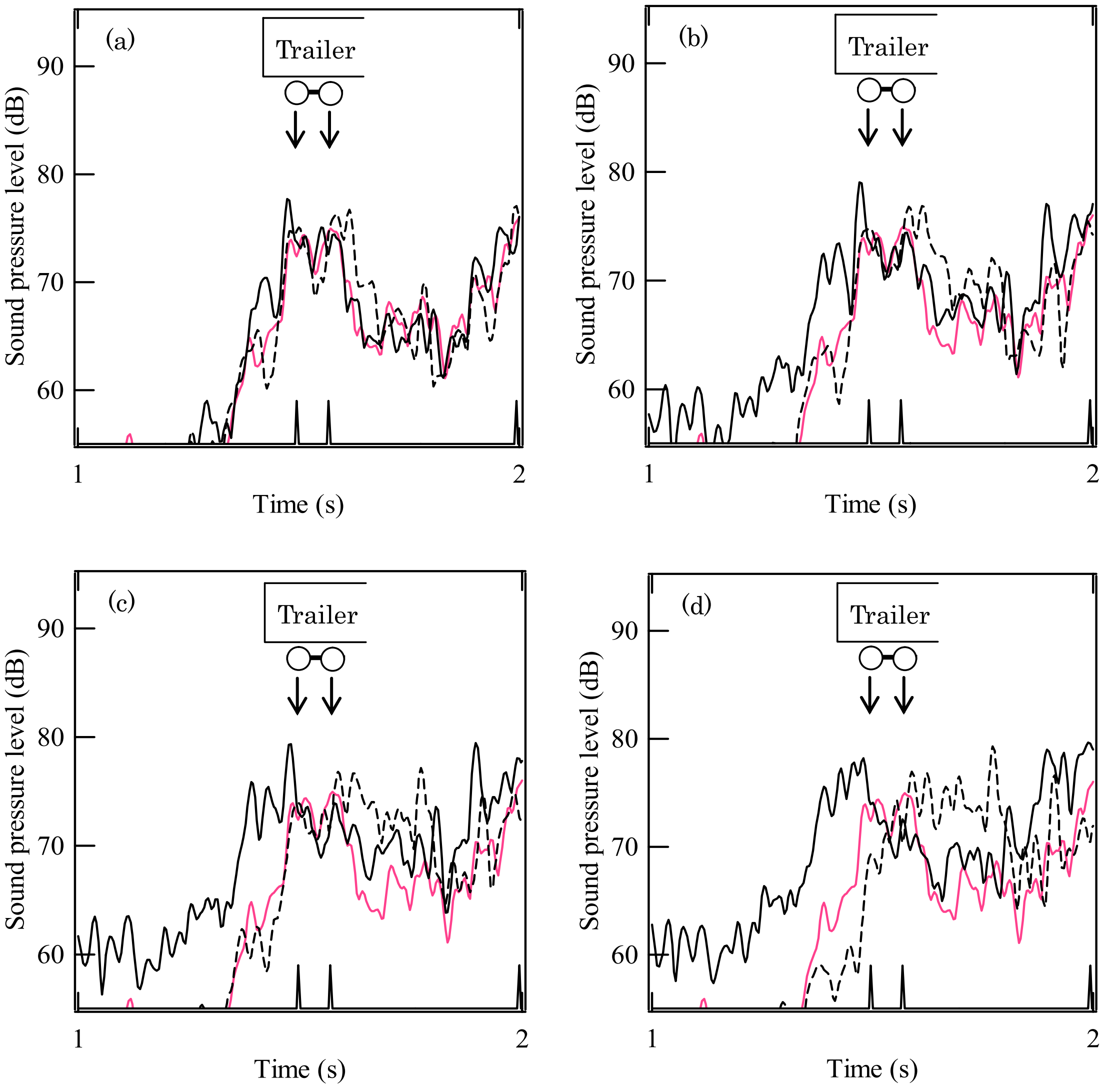

Figure 7.11 Time histories of a trailer bogie running at 102 km/h measured with the microphone array filtered in 1000 Hz band. The array is designed for a plane wave with a tuned angle, ϕ. The positions of the wheels are indicated by the pulses at the bottom of the graph. (a) —, ϕ=10º; - - -, ϕ=-10º; —, ϕ=0º. (b) —, ϕ=15º; - - -, ϕ=-15º; —, ϕ=0º. (c) —, ϕ=20º; - - -, ϕ=-20º; —, ϕ=0º. (d) —, ϕ=30º; - - -, ϕ=-30º; —, ϕ=0º.

From Figure 7.12, at 1250 Hz, it is found that the same trends are obtained as seen at 800 and 1000 Hz in Figures 7.10 and 7.11. There is a larger peak in the sound levels in the time histories obtained by steering the array at 10°, although the peak disappears at the tuned angles larger than 20°. This is due to the fact that the array is well tuned at the angle at which the rail radiates most strongly. The angle related to the supersonic structural radiation of vertical rail vibration is about 12° ($\approx\sin^{-1}(\lambda_{air}/\lambda_{rail})=\sin^{-1}(0.272/1.22)$).

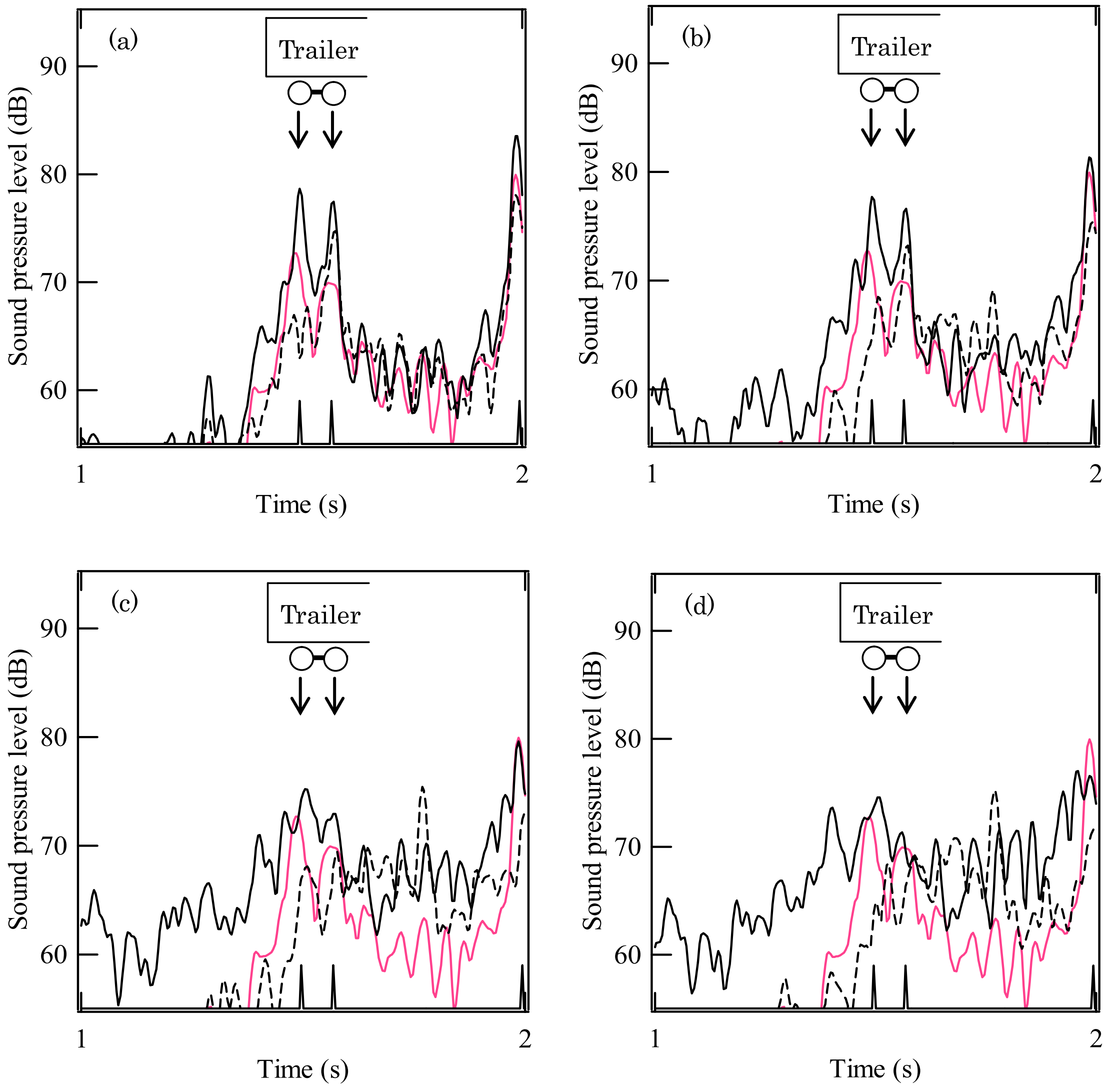

Figure 7.12 Time histories of a trailer bogie running at 102 km/h measured with the microphone array filtered in 1250 Hz band. The array is designed for a plane wave with a tuned angle, ϕ. The positions of the wheels are indicated by the pulses at the bottom of the graph. (a) ——, ϕ=10°; - - -, ϕ=-10°; ——, ϕ=0°. (b) ——, ϕ=15°; - - -, ϕ=-15°; ——, ϕ=0°. (c) ——, ϕ=20°; - - -, ϕ=-20°; ——, ϕ=0°. (d) ——, ϕ=30°; - - -, ϕ=-30°; ——, ϕ=0°.

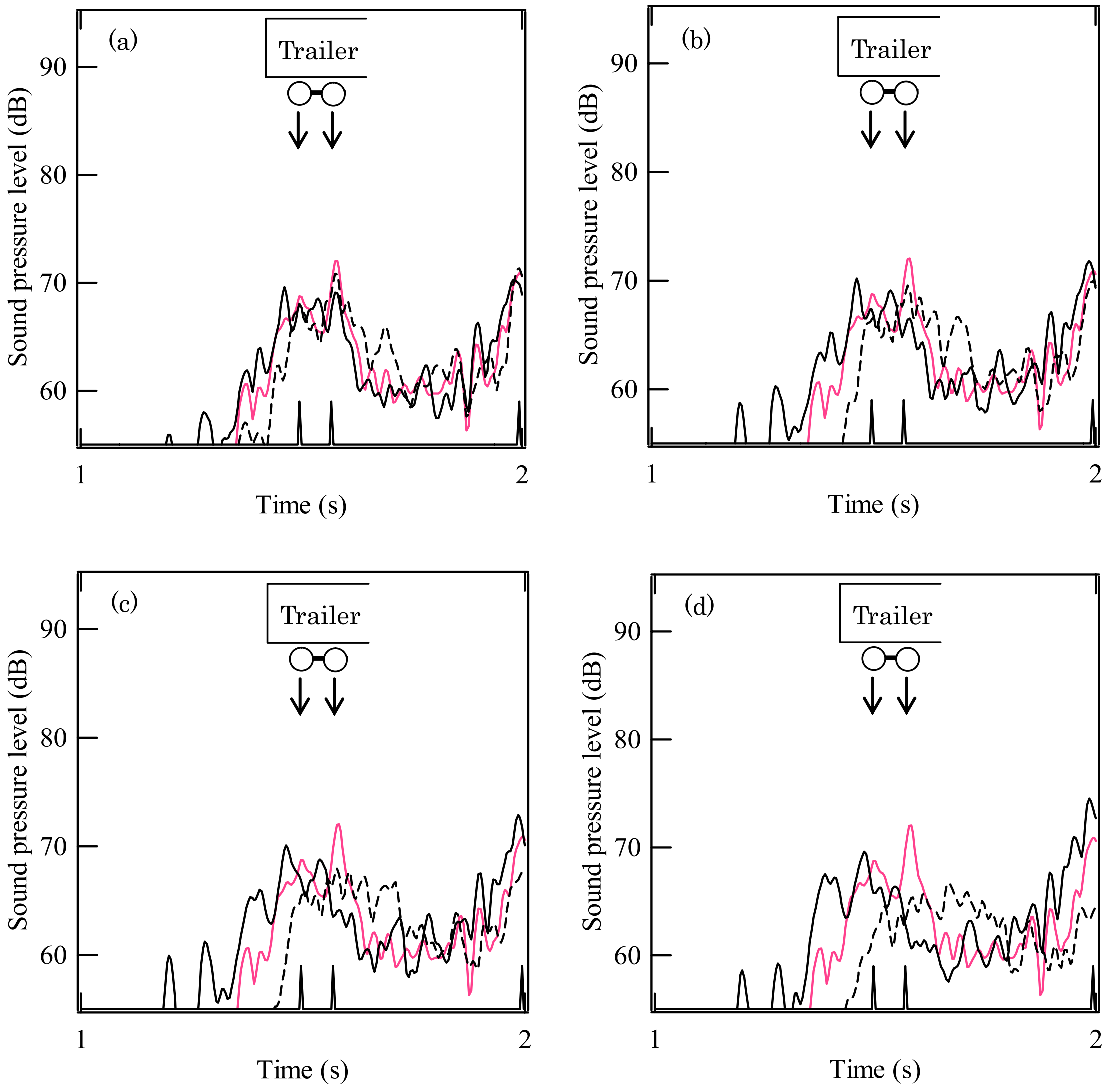

Figure 7.13 Time histories of a trailer bogie running at 102 km/h measured with the microphone array filtered in 1600 Hz band. The array is designed for a plane wave with a tuned angle, ϕ. The positions of the wheels are indicated by the pulses at the bottom of the graph. (a) ——, ϕ=10°; - - -, ϕ=-10°; ——, ϕ=0°. (b) ——, ϕ=15°; - - -, ϕ=-15°; ——, ϕ=0°. (c) ——, ϕ=20°; - - -, ϕ=-20°; ——, ϕ=0°. (d) ——, ϕ=30°; - - -, ϕ=-30°; ——, ϕ=0°.

For 1600 Hz and above (Figures 7.13-7.15), it can be seen that, by turning the array, the increase of the sound levels in the time histories can be seen apparently before or after the trailer bogie passes in front of the array. It is also found that, at higher frequencies, the increase in the sound levels tends to be slightly smaller by turning the array axis at ±30°. This indicates that the array detects the radiation behaviour of the rail even in this frequency range where the wheel has a greater contribution to the total noise than the rail. This is also due to the fact that free wave propagation occurs in the rail above 1600 Hz, and this leads to an underestimation of the contribution of the rail component of noise using only steering at 0º. Therefore, the microphone array does not detect a large part of the noise radiated from the rail, when directed normal to the rail.

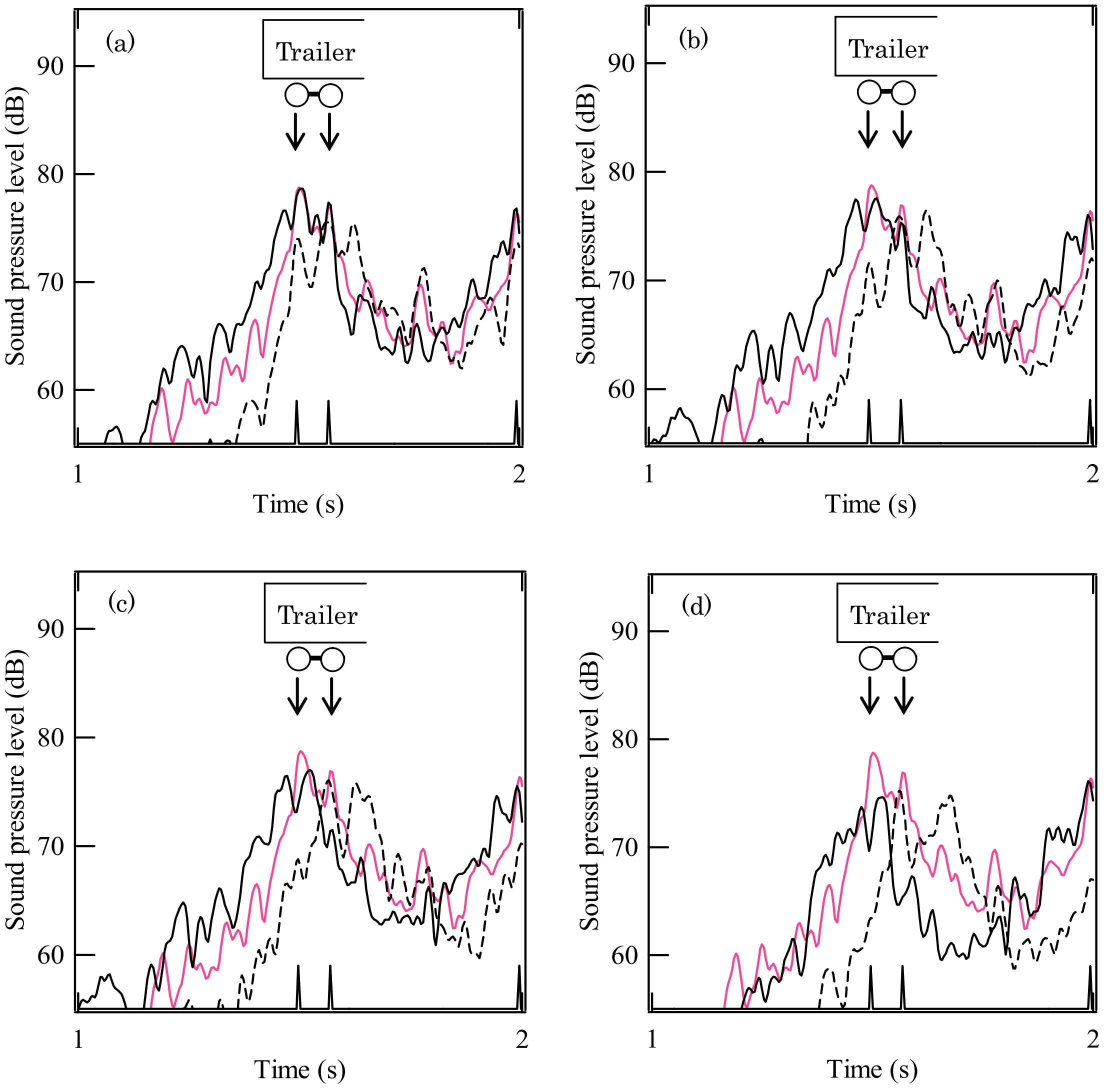

Figure 7.14 Time histories of a trailer bogie running at 102 km/h measured with the microphone array filtered in 2000 Hz band. The array is designed for a plane wave with a tuned angle, ϕ. The positions of the wheels are indicated by the pulses at the bottom of the graph. (a) ——, ϕ=10º; - - -, ϕ=-10º; ——, ϕ=0º. (b) ——, ϕ=15º; - - -, ϕ=-15º; ——, ϕ=0º. (c) ——, ϕ=20º; - - -, ϕ=-20º; ——, ϕ=0º. (d) ——, ϕ=30º; - - -, ϕ=-30º; ——, ϕ=0º.

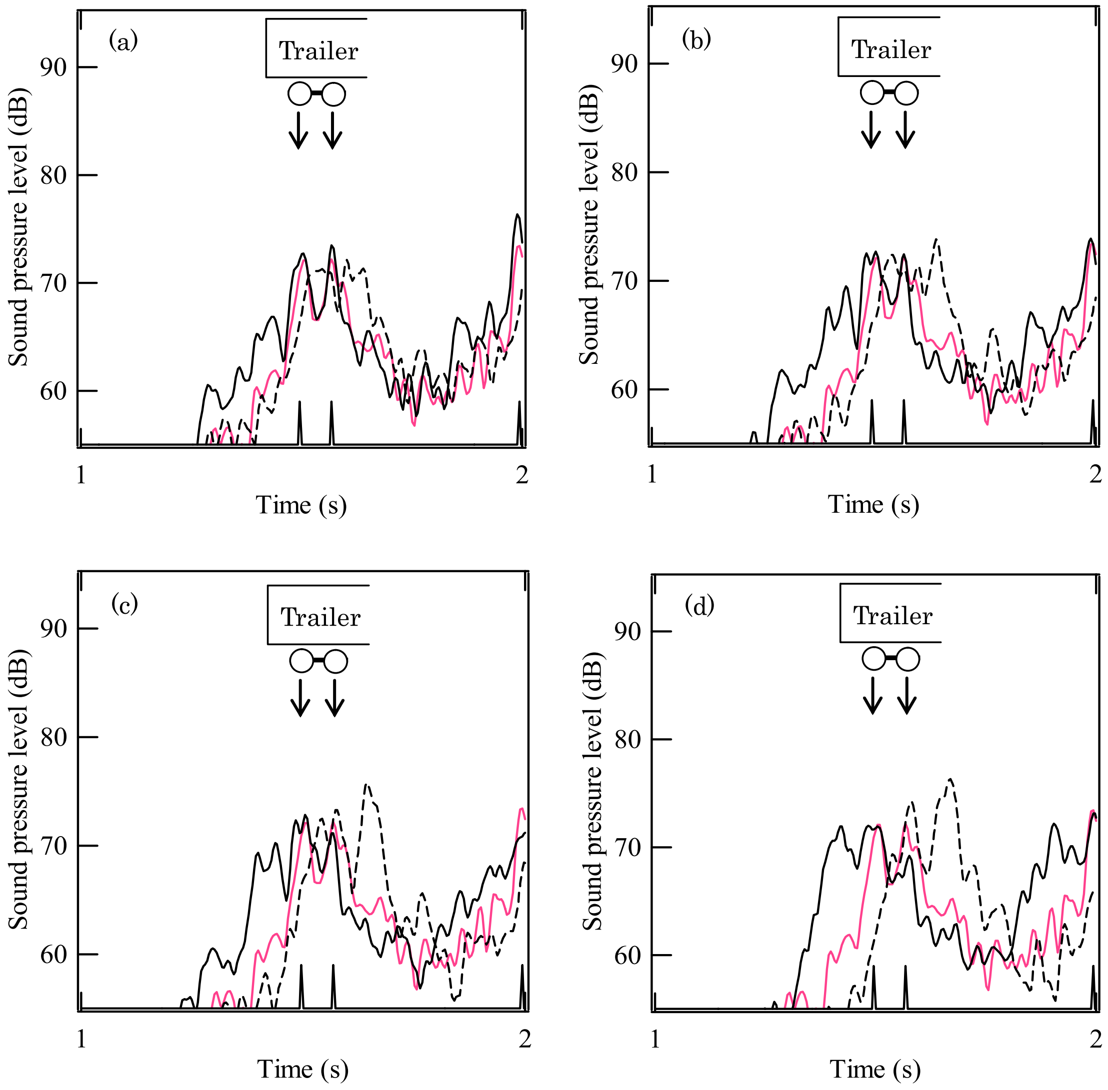

Figure 7.15 Time histories of a trailer bogie running at 102 km/h measured with the microphone array filtered in 2500 Hz band. The array is designed for a plane wave with a tuned angle, ϕ. The positions of the wheels are indicated by the pulses at the bottom of the graph. (a) —, ϕ=10°; - - -, ϕ=-10°; —, ϕ=0°. (b) —, ϕ=15°; - - -, ϕ=-15°; —, ϕ=0°. (c) —, ϕ=20°; - - -, ϕ=-20°; —, ϕ=0°. (d) —, ϕ=30°; - - -, ϕ=-30°; —, ϕ=0°.

7.4 Summary

Through the sound measurements for moving trains, qualitative investigation of the rail radiation has been performed using a one-dimensional microphone array. It is found that the rail is represented as an extended line source in the frequency range where free wave propagation occurs, and that, when directed normal to the rail, the microphone array does not detect a large part of the noise radiated from the rail. This leads to an underestimation of the rail component of noise, and confirms the reason why the microphone array makes the wheel component of noise more noticeable.

8 CONCLUSIONS AND RECOMMENDATIONS

Studies to develop understanding of the noise from both wheel and rail have previously been performed by using both theoretical models and measurements. The theoretical models, such as TWINS, have been validated in terms of noise and vibration [2, 8], and give reliable predictions of rail and wheel contributions to the total noise for conventional and novel designs of wheels and tracks. Meanwhile, in order to determine the source distribution, microphone array measurements have been widely carried out [17, 47]. The array measurements lead to the conclusion that the dominant noise source is located in the wheel region at frequencies from 500 Hz to 2000 Hz, and that the wheel noise has a greater contribution than the rail noise [17]. This result is inconsistent with the conclusions found in the theoretical research on the wheel/rail noise radiation, such as in [2, 8], in which the rail can be the dominant source in much of the frequency range. Therefore, the acoustic character of the rail has been investigated to determine whether there is a fundamental problem in measuring it using a microphone array. In this chapter, the results obtained in the thesis will be summarized.

8.1 Validation of the TWINS model

In order to investigate the characteristics of the wheel/rail rolling noise, the applicability of the TWINS model for Japanese railways has been investigated for six wheel/rail combinations. The calculation parameters associated with the vibratory behaviour of the track have been estimated in the static measurements. The decay rates of the track have been evaluated based on a direct estimate of the summed response [60]. It is found that the overall predictions in terms of noise and vibration show good agreement with the measured results. This suggests that the TWINS model gives reliable predictions. A linear relationship between the predictions and measurements appears at speeds in the available range of 70-120 km/h. In terms of noise spectra, the average difference between the predictions and measurements in one-third octave bands is about 1 dB above 250 Hz, while the standard deviation is about 2-4 dB. The spectra are somewhat under-predicted below 1000 Hz and show an over-prediction above 2000 Hz. The over-prediction above 2000 Hz may be caused by the inadequacy of the assumed roughness spectra and the contact filter used. The rail vibration spectra are somewhat over-predicted. This may be due to the roughness used being higher than applicable for Japanese situations or due to the influence of the measurement location on the edge of the rail foot.

An attempt to estimate the effect of wheel load on noise and rail vibration has been made by using the TWINS model. The TWINS model shows similar trends to the measurements, with a slight reduction in rolling noise as load increases. The spectral results show that, above 1000 Hz, the predictions are in quite good agreement with the measurements. This indicates that the contact filter effect is predicted correctly, since the contact filter effect has a significant effect on wheel/rail system above 1000 Hz.

Through the validation work, it is confirmed that the TWINS model gives reliable predictions, and is constructed on the basis of robust theory. It is also found that the rail is the dominant source of rolling noise in much of the frequency range.

8.2 Microphone array measurements

After verifying the validity of the TWINS model, an attempt to identify the radiation characteristics of the rail has been carried out by comparing predictions for the results of a single microphone and a one-dimensional microphone array. Attention is focused on the basic assumption of using the microphone arrays in order to estimate sound power from the measurements. This assumption is that the sources are composed of a distribution of uncorrelated point sources located in a plane at some known distance from the array. Then, in order to make an examination of the assumption, a simulation of the performance of the microphone array is carried out for two situations: (i) the multiple sources are incoherent, as assumed in determining sound power from microphone array measurement, (ii) the sources are coherent, which is more representative of the rail radiation. In the simulation of the array performance, the rail is replaced by an array of incoherent or coherent sources, and the source strengths are determined according to the vibration of the rail, calculated with the TWINS model.

Through the simulation of the performance of the microphone array, the acoustic properties of a rail have been understood more clearly. For a wave with a high decay rate, the rail vibration forms a point source, and both the single microphone and microphone array locate an incident wave spreading from this source. However, for a wave with a low decay rate, the rail tends to be an extended line source. The rail radiates sound at an angle to its axis, whereas the microphone array only detects the radiation from the region close to a forcing point, not perceiving the sound radiation generated by the travelling wave part of the rail vibration. This indicates that the array cannot see a large part of the noise from the rail at high frequencies, where free wave propagation occurs in the rail. Differences of up to 15 dB are found in some frequency bands, which is definitely due to the assumptions that the multiple sources are incoherent. Therefore, it has been confirmed that the results obtained by using microphone arrays do not reflect the radiation characteristics of the noise from a rail, and this leads to the underestimation of the contribution of the rail component of noise. This explains why measurements using microphone arrays tend to emphasise the wheel as the dominant source, whereas using the TWINS model the rail is also found to be an important source in many situations. By changing the focus of the array so that it is directed at an angle to the normal, large differences in its output are predicted, with a maximum when it coincides with the angle of radiation from the rail.

By using a shaker to excite the rail, the radiation properties of the rail have been examined by steering the array at different angles. Through the experiments using shaker excitation, by directing the array it is demonstrated that, the rail radiates at an angle to the normal in the frequency range where free wave propagation occurs. The measured results show good agreement with the prediction based on the coherent sources for both vertical and horizontal directions. This means that the radiation behaviour of the rail is investigated appropriately by replacing the rail as a line array of coherent sources, not incoherent sources. Therefore, it is confirmed that the prediction model in Chapter 5 is suitable to represent the characteristics of the rail radiation.

Through the sound measurements for a moving train, qualitative investigation of the rail radiation has been performed using a one-dimensional microphone array. It is found that the rail is represented as an extended line source in the frequency range where free wave propagation occurs, and that, by steering the array axis normal to the rail, the microphone array does not perceive a large part of the noise radiated from the rail. This leads to an underestimation of the rail component of noise, and explains why the microphone array makes the wheel component of noise more noticeable.

8.3 Recommendations for further work

8.3.1 Validation of the TWINS model

Further tests and studies are required to cover a wider range of rolling stock and track. In this thesis, the validation of the TWINS model has been confirmed only in some cases of Japanese railway lines as a first step. In particular only one track type has been investigated. In order to make a deeper understanding of rolling noise, more measured data are also needed to characterize the vibratory behaviour of the track and wheel. For the validation works of the TWINS model at other track types, it is necessary that the wheel/rail roughness measurements are carried out, and that the vibratory characteristics of the tracks are confirmed from some experimental investigation.

(1) Roughness measurement

For the roughness, here, the TWINS calculations have been carried out by using a "unit roughness" excitation and reference wheel/rail roughness spectra. This means that the wheel and rail roughness profiles of Japanese railways are not used, since the wheel and rail roughness measurements were not performed during the running tests. It is recommended that the TWINS calculations are carried out directly by using wheel and rail roughness profiles of Japanese railways. However, care should be taken to ensure that these measurements are compatible with the requirements of TWINS.

(2) Track and wheel measurements

It is necessary to obtain a better understanding of the vibratory behaviour of the tracks and wheels by performing characterisation measurements. In this thesis, the vibratory behaviour of the tracks was confirmed only below 2000 Hz (3000 Hz for the measurements in Chapter 6). It is important to make a clear confirmation of the vibratory behaviour of the tracks from some experimental investigation covering the whole frequency range 63-8000 Hz. More extensive measurements of track decay rate are also required as part of these. For the wheel measurements, it is important to find the vibratory behaviour in terms of modal characteristics, particularly natural frequencies and modal damping ratios.

8.3.2 Microphone array measurements

In this thesis, in order to investigate the acoustic properties of wheel/rail noise, equivalent source models of the rail radiation have been arranged, and the radiation characteristics have been studied by using simulations of a one-dimensional microphone array. However, this is not sufficient to analyse the wheel/rail noise completely.

(1) The characteristics of the sleeper noise should also be considered. The sleeper noise can be replaced by a monopole source, but it is complicated to estimate the sleeper radiation, since the sleeper radiates sound only when the train runs over it. It might be better that each sleeper is replaced by a monopole source, which radiates intermittently as the wheel passes.

(2) It is necessary to find the contribution or acoustic power level of each component (the sleeper, wheel and rail) by combining the actual results measured with the microphone array and the modification factors estimated in the thesis, and to compare these with the powers of the sources estimated using the TWINS model.

(3) The Doppler effect is neglected here. This is because the sources move at low speed, below 120 km/h. However, for the case of Shinkansen trains which run above 300 km/h, the Doppler effect will have greater influence on the array measurements. Therefore, the

de-dopplerisation technique should be included in the array processing by tracking the measured position of the sources and taking account of the radiation direction of a rail.

(4) Through the analysis of the microphone array measurements, as the assumption that the sources are incoherent is not appropriate for the rail radiation, the array cannot give a correct estimate of the sound power radiated by the rail. However, if the array axis is adjusted at an appropriate angle based on a source model suitable for the rail radiation in the microphone array processing, the array could detect the distributed character of the source in the region where free wave propagation occurs. This suggests that it is necessary to design the array processing for the coherent nature of the sources for the research on the wheel/rail noise. However, it appears to be difficult to direct the array at an appropriate angle to detect the rail radiation reliably. Although two-dimensional arrays are beyond the scope in the thesis, this will also be true for two-dimensional arrays. Therefore, it is necessary to design new processing methods to measure the radiation character of a rail directly, i.e. to detect distributed sources with a coherent character.

(5) Since the microphone array misses the rail radiation associated with free wave propagation in the rail, it can be expected that the effects of rail dampers on the reduction of the rail component of noise will not be detected by a microphone array. A test could be carried out using a microphone array and a single microphone for a situation with and without rail dampers as an additional check of the main contribution of this thesis.

9 REFERENCES

[1] White Paper on the Environment: Quality of the Environment in Japan 1996, the Environment Agency, 1996.

[2] Thompson, D.J., Jones, C.J.C., A review of the modelling of wheel/rail noise generation. *Journal of Sound and Vibration*, 231(3), 2000, 519-536.

[3] Thompson, D.J., Janssens, M.H.A., de Beer, F.G., TWINS: Track-Wheel Interaction Noise Software. Theoretical manual (version 3.0). *TNO Report.* TPD-HAG-RPT-990211, Nov 1999.

[4] Kitagawa, T., et al., Sound Radiated by Vibration of Railway Wheels. *Proceedings of Inter Noise 2001*, Hague (Netherlands).

[5] Kitagawa, T., Murata, K., Zenda, Y., Analysis about Vibration and Sound Generated by Wheels *RTRI Report* Vol.15 (2001), No.5, 47-52 (in Japanese).

[6] Kitagawa, T., Nagakura, K., Ogata, S., Noise Prediction Method for Conventional Railways. *RTRI Report*, Vol.13 (1998), No.12, 41-46 (in Japanese).

[7] Thompson, D.J., Hemsworth, B., Vincent, N., Experimental Validation of the TWINS Prediction Program for Rolling Noise, Part 1: Description of the Model and Method. *Journal of Sound and Vibration*, 193(3), 1996, 123-135.

[8] Thompson, D.J., Fodiman, P., Mahé, H., Experimental Validation of the TWINS Prediction Program for Rolling Noise, Part 2: Results. *Journal of Sound and Vibration*, 193(3), 1996, 137-147.

[9] Thompson, D.J., Vincent, N., Track Dynamic Behaviour at High Frequencies. Part 1: Theoretical Models and Laboratory Measurements. *Vehicle System Dynamics Supplement*, 24, 1995, 86-99.

[10] Vincent, N., Thompson, D. J., Track Dynamic Behaviour at High Frequencies. Part 2: Experimental Results and Comparisons. *Vehicle System Dynamics Supplement*, 24, 1995, 100-114.

[11] Thompson, D.J., On the relationship between wheel and rail surface roughness and rolling noise. *Journal of Sound and Vibration*, 193(1), 1996, 149-160.

[12] Jones, C.J.C., & Thompson, D.J., Extended validation of a theoretical model for railway rolling noise using novel wheel and track designs. *Journal of Sound and Vibration*, 267(3), 2003, 509-522.

[13] Fahy, F., Noise control 2, *ISVR MSc lecture notes*, 2003.

[14] Johnson, D.H., Dudgeon, D.E., Array signal processing: Concepts and techniques, Prentice-Hall, New Jersey, 1993.

[15] Degen, K.G., Nordborg, A., Martens, A., Wedemann, J. Willenbrink, L. Bianchi, M. Spiral array measurements of high-speed train noise, *Inter-noise'2001*, The Hague (Netherlands), 2001.8, 2071-2074

[16] Nordborg, A., Martens, A., Wedemann, J. Willenbrink, L. Wheel/rail noise separation with microphone array measurements, *Inter-noise'2001*, The Hague (Netherlands), 2001.8, 2083-2088.

[17] Van Der Toorn, J.D., Hendriks, H., and Van Den Dool, T.C., Measuring TGV source strength with SYNTACAN. *Journal of Sound and Vibration*, 193(1), 1996, 113-121.

[18] Thompson, D.J., Wheel-Rail Noise Generation, Part I: Introduction and Interaction Model. *Journal of Sound and Vibration*, 161(3), 1991, 387-400.

[19] Thompson, D.J., Wheel-Rail Noise Generation, Part II: Wheel Vibration. *Journal of Sound and Vibration*, 161(3), 1991, 401-419.

[20] Thompson, D.J., Wheel-Rail Noise Generation, Part III: Rail Vibration. *Journal of Sound and Vibration*, 161(3), 1991, 420-446.

[21] Thompson, D.J., Wheel-Rail Noise Generation, Part IV: Contact Zone and Results. *Journal of Sound and Vibration*, 161(3), 1991, 447-466.

[22] Thompson, D.J., Wheel-Rail Noise Generation, Part V: Inclusion of Wheel Rotation. *Journal of Sound and Vibration*, 161(3), 1991, 467-482.

[23] Remington, P.J., & Webb, J., Estimation of wheel/rail interaction forces in the contact area due to roughness. *Journal of Sound and Vibration*, 193(1), 1996, 83-102.

[24] Thompson, D.J., The influence of the contact zone the excitation of wheel/rail noise. *Journal of Sound and Vibration*, 267(3), 2003, 523-535.

[25]Thompson, D.J., Mace, B.R., High frequency structural vibration, *ISVR lecture notes*, University of Southampton, 2003.

[26] Grassie, S.L., Dynamic modelling of concrete railway sleepers. *Journal of Sound and Vibration*, 187(5), 1995, 799-813.

[27] Jones, C.J.C., Thompson, D.J., Toward M.G.R. The Dynamic Stiffness of the Ballast Layer in Railway Track. *Seventh International Conference on Recent Advances in Structural Dynamics*, 2002, 1037-1048.

[28] Thompson, D.J., & Jones, C.J.C., Sound radiation from vibrating railway wheel. *Journal of Sound and Vibration*, 253(2), 2002, 401-419.

[29] Thompson, D.J., Jones, C.J.C., & Turner, N., Investigation into the validity of two-dimensional models for sound radiation from waves in rails. *Journal of the Acoustical Society of America*, 113(4), Part 1, 2003, 1965-1974.

[30] Wu, T.X., & Thompson, D.J., A double beam Timoshenko beam model for vertical vibration analysis of railway track at high frequencies. *Journal of Sound and Vibration*, 224(2), 1999, 329-348.

[31] Wu, T.X., & Thompson, D.J., Analysis of lateral vibration behavior of railway track at high frequencies using a continuously supported multiple beam model. *Journal of the Acoustical Society of America*, 106(3), Part 1, 1999, 1369-1376.

[32] Wu, T.X., & Thompson, D.J., Application of a multiple-beam model for lateral vibration analysis of a discretely supported rail at high frequencies. *Journal of the Acoustical Society of America*, 108(3), Part 1, 2000, 1341-1344.

[33] Wu, T.X., & Thompson, D.J., The influence of random sleeper spacing and ballast stiffness on the vibration behaviour of railway track. *Acustica*, 84, 2000, 313-321.

[34] Wu, T.X., & Thompson, D.J., The effects of local preload on the foundation stiffness and vertical vibration of railway track. *Journal of Sound and Vibration*, 219(5), 1999, 881-904.

[35] Wu, T.X., & Thompson, D.J., Vibration analysis of railway track with multiple wheels on the rail. *Journal of Sound and Vibration*, 239(1), 2001, 69-97.

[36] Wu, T.X., & Thompson, D.J., The effects on railway rolling noise of wave reflections in the rail and support stiffing sue to the presence of multiple wheels. *Applied Acoustics*, 62, 2001, 1249-1266.

[37] Wu, T.X., & Thompson, D.J., The vibration behaviour of railway track at high frequencies under multiple preloads and wheel interactions. *Journal of the Acoustical Society of America*, 108(3), Part 1, 2000, 1048-1053.

[38] Barsikow, B., King III, W. F., and Pfizenmaier, E., Wheel/rail noise generated by a high-speed train investigated with a line array of microphones. *Journal of Sound and Vibration*, 118(1), 1987, 99-122.

[39] Moritoh, Y., Zenda, Y., and Nagakura, K., Noise control of high speed Shinkansen. *Journal of Sound and Vibration*, 193(1), 1996, 319-334.

[40]Nagakura, K., The method of analyzing Shinkansen noise. *Quarterly Report of RTRI*, 37(4), 1996, 210-215.

[41] Hamet, J.F., et al., DEUFRAKO-1: Microphone array techniques used to locate acoustic sources on ICE, TGV-A and Transrapid-07. *Inter-noise'94*, Yokohama (JAPAN), 1994, 187-192.

[42] Takano, Y., et al., Analysis of sound source characteristics of Shinkansen cars by means of X-shaped microphone array. *Inter-noise'96*, Liverpool (UK), 1996, 399-402.

[43] Boone, M. M., and Berkhout, A. J., Theory and applications of high-resolution synthetic acoustic antenna for industrial noise measurements, *Noise Control Engineering Journal*, September-October 1984, 60-68.

[44] Bongini, E., et al. Synthesis of noise of operating vehicles: development within SILENCE of a tool with listening features. *9th International Workshop on Railway Noise*, Feldafing (Germany), 4-8 September 2007, paper S9.3.

[45] White, P. R., Array signal processing, *ISVR Advanced Course in Acoustics, Noise and Vibration*, 2002.9.

[46] Torii, A., Takano, Y., et al., Shinkansen's sound source measurements using microphone arrays. *Inter-noise’92*, Toronto (Canada), 1992.7, 1171-1174

[47] Nordborg, A., Wedemann, J., Willenbrink, L. Optimum array microphone configuration, *Inter-noise’2000*, Nice (France), 2000, 2474-2478.

[48] Manabe, K., Microphone array technique to localize sound sources with a spherical wave, *RTRI report*, 1994 (in Japanese).

[49] Barsikow, B., and King III, W. F., On removing the Doppler frequency shift from array measurements of railway noise, *Journal of Sound and Vibration*, 120(1), 1988, 190-196.

[50] Barsikow, B., Experiences with various configurations of microphone arrays used to locate sound sources on railway trains operated the DB AG. *Journal of Sound and Vibration*, 193(1), 1996, 283-293.

[51] Hölzl, G., Low noise goods wagons. *Journal of Sound and Vibration*, 193(1), 1996, 359-366.

[52] Hölzl, G., et al., DEUFRAKO-2: Localized Sources on the high-speed vehicles ICE, TGV-A and Transrapid-07. *Inter-noise'94*, Yokohama (Japan), 1994, 192-198.

[53] Hald, J., and Christensen, J.J., A class of optimal broadband phased array geometries designed for easy construction, *Inter-noise’2002*, Dearborn (USA), 2002, N447

[54] Takano, Y., et al., Development of visualization system for high-speed noise source with a microphone array and a visual sensor. *Inter-noise’2003,* Seogwipo (Korea), 2003.8, 2683-2690.

[55] Boone, M.M., Kinneging, N., and Van Den Dool, T.C., Two-dimensional noise source imaging with a T-shaped microphone array. *Journal of the Acoustic Society of America,* 108(6), 2000, 2284-2890.

[56] Nagakura, K., et al., Noise source visualization of rolling noise based on acoustic mirror measurements. *Inter-noise’2003,* Seogwipo (Korea), 2003.8, 2410-2417

[57] Bruhl, S., and Roder, A., Acoustic noise source modelling based on microphone array measurements. *Journal of Sound and Vibration,* 231(3), 2000, 611-617.

[58] Zenda, Y., Kitagawa, T., Ogata, Y., Abe, Y., & Watanabe, K., Noise characterization of 313 series train Part I, *RTRI Report,* 2001 (in Japanese).

[59] Manabe, K., and Takigawa, M., Modal behaviour of a track, *RTRI Report*, 2001 (in Japanese).

[60] Thompson, D.J., Jones, C. J. C., Wu, T. X. & France, G. The influence of the non-linear stiffness behaviour of rail pads on the component of rolling noise, *Proc. Instn. Mech. Enginrs.*, Vol. 213 Part F, 1999, pp233-241.

[61] Jones, C. J. C., Thompson, D. J., Diehl, R. J., The use of decay rates to analyse the performance of railway track in rolling noise generation, *Journal of Sound and Vibration*, 293(1), 2006, 485-495.

[62] Kozuma, Y., Kitagawa, T., Nagakura, K., Analysis on vibratory characters of railway wheels, *Euronoise 2006,* Tampere (Finland), 2006.5.

[63] Thompson, D.J., Definition of the reference roughness. *ISVR contract report*, 1997.

[64] Ogata, Y., et al., Noise characterization of freight cars, *RTRI contract report*, 1998.

[65]Kitagawa, T., et al., Study on Relationship between Axle Load and Noise. *J-RAIL'99*, Kawasaki (Japan), 1999.12, 109-112 (in Japanese).

[66] Kitagawa, T., Thompson, D. J., Application and Validation of the TWINS model for Japanese Railways, *ISVR Technical Memorandum*, No: 919, 2003

[67] Geerlings, A.C., Thompson, D.J., Verheij, J.W., Model-based acoustic substitution source methods for assessing shielding measures applied trains, *Applied Acoustics*, 62, 2001, 979-1000.

[68] RION, MY13-type microphone array, *Technical manual*, 1992 (in Japanese).

[69] Fahy, F.J., Sound and Structural Vibration: Radiation, Transmission and Response, Academic Press, London, 1987.

[70] Thompson, D.J., Noise and vibration control, *ISVR lecture notes*, University of Southampton, 2003.

[71] Ferguson, N.S., Halkyard, C.R. Mace, B.R., Heron, K.H. The estimation of wavenumbers in two-dimensional structures, *Proc. of ISMA 2002*, KUL, Leuven, September 2002, 799-806.

[72] Grosh, K., Williams, E.G., Complex wave-number decomposition of structural vibration, *Journal of the Acoustical Society of America*, 93(2), 1993, 836-848.

[73] McDaniel, J.G., Dupont, P., Salvino, L., A wave approach to estimating frequency-dependent damping under transient loading, *Journal of Sound and Vibration*, 231(2), 2000, 433-449.

[74] Thompson, D.J., Experimental analysis of wave propagation in railway tracks, *Journal of Sound and Vibration*, 203(5), 1997, 867-888.

APPENDIX A

DIPOLE SOURCES MEASURED WITH A MICROPHONE ARRAY

A1 Single microphone

A1.1 Single dipole

By using the same procedure as in section 4.1.1, the pressure, $p(k,r,\theta)$, radiated by a point dipole can be given. However, it is not so straightforward to estimate the pressure of the dipole, since it depends on the angle, θ, between source axis and the radius vector to the measuring point. Here, it is assumed that a point dipole is a combination of two monopoles in a free field, i.e. a doublet, as shown in Figure A1. The two monopoles with volume velocities Q and $-Q$, are separated by a distance, d, with $kd \ll 1$. The complex amplitude of pressure, $p(k,r,\theta)$, measured with a single microphone can be given by

$$p(k,r,\theta) = \rho c_0 \frac{jkQ}{4\pi}\left(\frac{e^{-jkr_1}}{r_1} - \frac{e^{-jkr_2}}{r_2}\right) \tag{A1}$$

where r_1 is the distance between the first monopole and the microphone, and r_2 is the distance between the other monopole and the microphone. A time factor of $e^{j\omega t}$ is assumed implicitly.

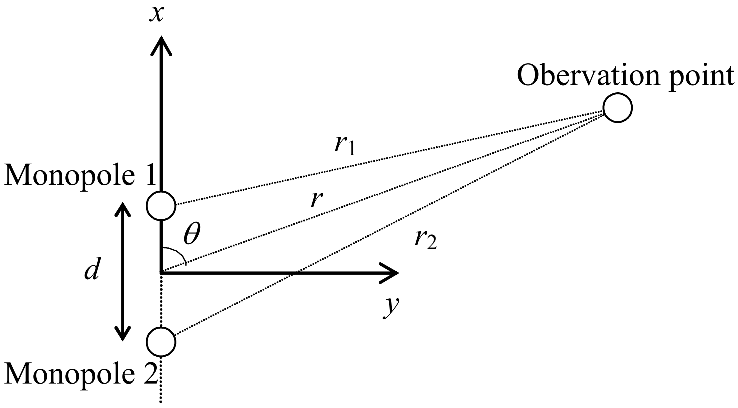

Figure A1 Illustration of a doublet.

It is necessary to confirm that equation (A1) forms a dipole. If d is considerably smaller than the distance, r, from the centre of the dipole to the observation point (i.e. $d \ll r$, see Figure A1), then, distances, r_1 and r_2, can be approximated as

$$r_1 \simeq r - \frac{d}{2}\cos\theta \tag{A2}$$
$$r_2 \simeq r + \frac{d}{2}\cos\theta$$

where θ is the angle between the *x*-axis and a line joining the origin to the observation point.

Then, equation (A1) becomes

$$p(k,r,\theta) \simeq \rho c_0 \frac{jkQ}{4\pi r}\left(e^{-jk\left(r-\frac{d}{2}\cos\theta\right)} - e^{-jk\left(r+\frac{d}{2}\cos\theta\right)} \right)$$

$$\simeq \rho c_0 \frac{jkQ}{4\pi r} 2je^{-jkr}\sin\left(\frac{kd}{2}\cos\theta\right) \tag{A3}$$

If $kd \ll 1$, $\sin\left(\frac{kd}{2}\cos\theta\right) \approx \frac{kd}{2}\cos\theta$. Then, equation (A3) is

$$p(k,r,\theta) \simeq \rho c_0 \frac{jkQ}{4\pi r} e^{-jkr}\left(jkd\cos\theta\right) \tag{A4}$$

Equation (A4) is the familiar result for a dipole. In practice, if $kd<0.5$, equation (A1) gives a quite good approximation to a dipole directivity, but $kd \ll 0.1$ is preferable.

In equation (A1), the magnitude, $|p|$, depends on the wavenumber. It is convenient to normalize equation (A1) by using the time-averaged sound power, W_{dipole}. The sound pressure at the surface of the first sphere of the doublet, assumed to have volume velocity Q, is the sum of the pressure due to that sphere, $p_1(a)$, given by

$$p_1(a) = \rho c_0 \frac{jk}{1+jka}\frac{Q}{4\pi a}, \tag{A5}$$

and the pressure due to the other source with volume velocity $-Q$, given by

$$p_2(d) \approx -j\rho c_0 \frac{Qk}{4\pi d} e^{-jkd} \tag{A6}$$

The surface normal velocity, $U_1(a)$, at the surface of the first sphere is

$$U_1(a) = \frac{Q}{4\pi a^2} \tag{A7}$$

The normal intensity on the surface, $I_{doublet,1}(a)$, is hence given by

$$I_{doublet,1}\left(a\right)=\frac{1}{2}\mathrm{Re}\Big(U_1\left(p_1^*(a)+p_2^*(d)\right)\Big)=\frac{1}{2}\rho c_0\left|\frac{Q}{4\pi a}\right|^2 k^2\left(1-\frac{\sin kd}{kd}\right). \tag{A8}$$

The power radiated by one source of the doublet is therefore

$$W_{doublet,1}=4\pi a^2 I_{doublet,1}\left(a\right)$$

$$=\frac{\rho c_0\left|Q\right|^2 k^2}{8\pi}\left(1-\frac{\sin(kd)}{kd}\right) \tag{A9}$$

If each of the sources would radiate power, W_{mono}, if located separately in the free field, from equation (4.5), the power radiated by the complete doublet is

$$W_{doublet}=2W_{doublet,1}=\frac{\rho c_0\left|Q\right|^2 k^2}{4\pi}\left(1-\frac{\sin(kd)}{kd}\right)=2W_{mono}\left(1-\frac{\sin(kd)}{kd}\right) \tag{A10}$$

If the volume velocity, Q, is given and kd<<1, equation (A10) indicates that $W_{doublet}$ is proportional to k^4, as the term in brackets is proportional to $(kd)^2$.

Hence, the normalized pressure, $\tilde{p}\left(k,r\right)$, is given by

$$\tilde{p}\left(k,r\right)=\frac{1}{W_{doublet}^{\frac{1}{2}}}\rho c_0\frac{jkQ}{4\pi}\left(\frac{e^{-jkr_1}}{r_1}-\frac{e^{-jkr_2}}{r_2}\right) \tag{A11}$$

A1.2 A line array of dipoles

The procedure used in section 4.1.2 can be extended to the case of a line array of dipoles. Again the sources may be considered to be incoherent or coherent. If there are N incoherent dipole sources arranged at equal spacing in a line, by using equation (A1), the pressure, $p_{inc,di}$, measured with the single microphone is given by

$$p_{inc,di}\left(k,r\right)=\left\{\sum_{n=1}^{N}\left|\rho c_0\frac{jkQ_n}{4\pi}\left(\frac{e^{-jkr_{1n}}}{r_{1n}}-\frac{e^{-jkr_{2n}}}{r_{2n}}\right)\right|^2\right\}^{\frac{1}{2}} \tag{A12}$$

where r_{1n} is the distance between the microphone and first monopole of the n^{th} dipole, and r_{2n} is the distance between the microphone and the other monopole of the n^{th} dipole. Similarly, the pressure induced by N coherent dipole sources is given by

$$p_{coh,di}\left(k,r\right)=\sum_{n=1}^{N}\rho c_0\frac{jkQ_n}{4\pi}\left(\frac{e^{-jkr_{1n}}}{r_{1n}}-\frac{e^{-jkr_{2n}}}{r_{2n}}\right) \tag{A13}$$

It is again convenient to normalize these equations by the time-averaged sound power, $W_{inc,di}$ and $W_{coh,di}$.

By referring to equations (A5)-(A10), in the case of a line array of N incoherent dipoles, the sound power is simply the sum of the powers from individual sources. Therefore, the total sound power radiated, $W_{inc,dipole}$, is given by

$$W_{inc,di}=\sum_{n=1}^{N}\frac{\rho c_0\left|Q_n\right|^2k^2}{4\pi}\left(1-\frac{\sin(kd)}{kd}\right) \tag{A14}$$

For the case of N coherent dipoles arranged in a line with equal spacing, the sound pressure at the surface of one of the spheres of the n^{th} dipole is determined by the sum of $2N$ components, as given by

$$p_{1n,coh,di}=\sum_{i=1}^{N}\rho c_0\frac{jk}{1+jka}\frac{Q_i}{4\pi r_{1ni}}e^{-jkr_{1ni}}-\sum_{i=1}^{N}\rho c_0\frac{jk}{1+jka}\frac{Q_i}{4\pi r_{2ni}}e^{-jkr_{2ni}} \tag{A15}$$

where r_{1ni} is the distance between the first monopole of the i^{th} dipole and a point at the surface of the first monopole of the n^{th} dipole, and r_{2ni} is the distance between the other monopole of the i^{th} dipole and the first monopole of the n^{th} dipole. Thus,

$$r_{1ni}=\begin{cases}(n-i)D & (n\neq i)\\ a & (n=i)\end{cases} \tag{A16}$$

$$r_{2ni}=\begin{cases}(n-i)D+d^2/2(n-i)D & (n\neq i)\\ d & (n=i)\end{cases} \tag{A17}$$

The surface normal velocity, $U_{1n,coh,di}(a)$, at the surface of the first sphere of the n^{th} dipole is

$$U_{1n,coh,di}(a)=\frac{Q_n}{4\pi a^2} \tag{A18}$$

The normal intensity on the surface, $I_{1n,inc,di}(a)$, is hence given by

$$I_{1n,coh,di}\left(a\right)=\frac{1}{2}\mathrm{Re}\left(U_{1n,coh,di}\,p_{1n,coh,di}{}^{*}\right) \tag{A19}$$

Therefore, the power radiated by one source of the n^{th} dipole is given by

$$\begin{aligned} W_{1n,coh,di} &= 4\pi a^2 I_{1n,coh,di}\left(a\right) \\ &= 2\pi a^2 \operatorname{Re}\left(U_{1n,coh,di}\, p_{1n,coh,di}{}^{*}\right) \end{aligned} \tag{A20}$$

and, the total power radiated by the complete set of dipoles is

$$W_{coh,di} = 2\sum_{n=1}^{N} W_{1n,coh,di} \tag{A21}$$

Hence, the normalized pressures, $\tilde{p}_{inc,di}\left(k,r\right)$ and $\tilde{p}_{coh,di}\left(k,r\right)$, are given by

$$\tilde{p}_{inc,di}\left(k,r\right) = \frac{1}{W_{inc,di}{}^{\frac{1}{2}}}\left\{\sum_{n=1}^{N}\left|\rho c_0 \frac{jkQ_n}{4\pi}\left(\frac{e^{-jkr_{1n}}}{r_{1n}} - \frac{e^{-jkr_{2n}}}{r_{2n}}\right)\right|^2\right\}^{\frac{1}{2}} \tag{A22}$$

$$\tilde{p}_{coh,di}\left(k,r\right) = \frac{1}{W_{coh,di}{}^{\frac{1}{2}}}\sum_{n=1}^{N}\rho c_0 \frac{jkQ_n}{4\pi}\left(\frac{e^{-jkr_{1n}}}{r_{1n}} - \frac{e^{-jkr_{2n}}}{r_{2n}}\right) \tag{A23}$$

A2 Sound sources measured with a one-dimensional microphone array

A2.1 Single dipole

By using the same procedure as in Section 4.2.3, the outputs, $S_{dipole,pl}$ and $S_{dipole,sp}$ of the microphone array can be estimated for a point dipole. Here, it is again assumed that a point dipole is a combination of two monopoles in a free field, i.e. a doublet [68].

Suppose that a dipole source moves along a track, and that there is a line array of $2M+1$ microphones at positions $\vec{r_m}$ ($m=-M,\ldots,+M$) in the x-y plane of the coordinate system which is installed parallel to the track at a distance, r_0, from the track (see Figure A2).

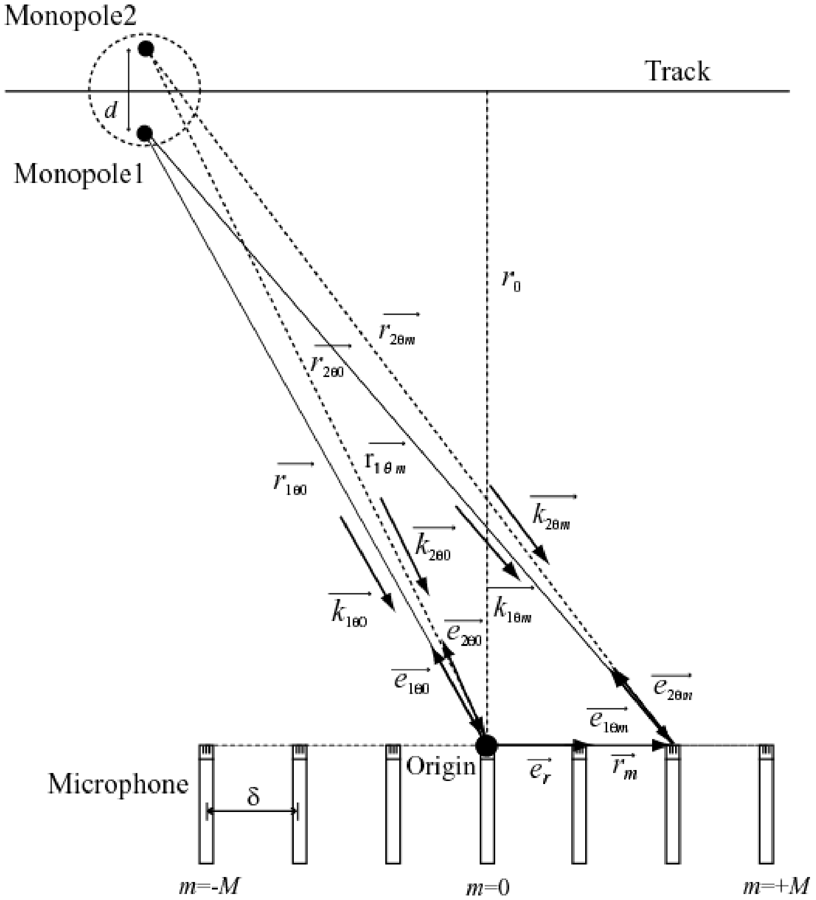

Figure A2 Illustration of a one-dimensional microphone array and dipole.

Here, a microphone array is designed for a plane wave. If two spherical waves arrive from angles, θ_1 and θ_2, and impinge on the m^{th} microphone with wavenumber vectors, $\overrightarrow{k_{1\theta m}}(\neq \overrightarrow{k_\phi})$ and $\overrightarrow{k_{2\theta m}}(\neq \overrightarrow{k_\phi})$, the amplitude of the output, $P_m(\omega)$ measured with the m^{th} microphone will be,

$$\begin{aligned} P_m(\omega) &= \rho c_0 \frac{jkQ}{4\pi\left|\overrightarrow{r_{1\theta m}}\right|} e^{-j\overrightarrow{k_{1\theta m}}\cdot\overrightarrow{r_{1\theta m}}} - \rho c_0 \frac{jkQ}{4\pi\left|\overrightarrow{r_{2\theta m}}\right|} e^{-j\overrightarrow{k_{2\theta m}}\cdot\overrightarrow{r_{2\theta m}}} \\ &= \rho c_0 \frac{jkQ}{4\pi}\left(\frac{e^{-jk\left|\overrightarrow{r_{1\theta m}}\right|}}{\left|\overrightarrow{r_{1\theta m}}\right|} - \frac{e^{-jk\left|\overrightarrow{r_{2\theta m}}\right|}}{\left|\overrightarrow{r_{2\theta m}}\right|} \right) \end{aligned} \tag{A24}$$

where $\overrightarrow{r_{1\theta m}} = \overrightarrow{r_m} + \overrightarrow{r_{1\theta 0}}$ and $\overrightarrow{r_{2\theta m}} = \overrightarrow{r_m} + \overrightarrow{r_{2\theta 0}}$ (see Figure A2). The output, $S_{dipole,pl}$, of the array at angular frequency ω will be given by

$$S_{dipole,pl}(\overrightarrow{e_{\phi 0}},\omega) = \sum_{m=-M}^{M} w_m P_m(\omega) e^{-j\omega\Delta_m}$$

$$= \sum_{m=-M}^{M} w_m \rho c_0 \frac{jkQ}{4\pi}\left(\frac{e^{-jk\left|\overrightarrow{r_{1\theta m}}\right|}}{\left|\overrightarrow{r_{1\theta m}}\right|} - \frac{e^{-jk\left|\overrightarrow{r_{2\theta m}}\right|}}{\left|\overrightarrow{r_{2\theta m}}\right|}\right) e^{jkm\delta\sin\phi}$$

$$\simeq \rho c_0 \frac{jkQ}{4\pi r_0} \sum_{m=-M}^{M} w_m \frac{r_0}{r_m} e^{-jkr_m}\left(jkd\cos\theta_m\right) e^{jkm\delta\sin\phi} \qquad \left(kd \ll 1\right)$$

$$= \rho c_0 \frac{jkQ}{4\pi r_0}\left(jkd\right) \sum_{m=-M}^{M} w_m \frac{r_0}{r_m} e^{-jkr_m} \cos\theta_m e^{jkm\delta\sin\phi}$$

$$= \rho c_0 \frac{jkQ}{4\pi r_0}\left(jkd\right) W''' \tag{A25}$$

In equation (A.25), the function, *W'''*, gives the beam pattern of the microphone array.

The term, $S_{dipole,pl}$, is normalized by the time-averaged sound power, $W_{doublet}$, given by equation (A.10). Then, the normalized output, $\tilde{S}_{dipole,pl}\left(\vec{e}_{\phi 0}, \omega\right)$, is

$$\tilde{S}_{dipole,pl}\left(\vec{e}_{\phi 0}, \omega\right) = \frac{1}{W_{doublet}^{\frac{1}{2}}} \sum_{m=-M}^{M} w_m \rho c_0 \frac{jkQ}{4\pi}\left(\frac{e^{-jk\left|\overrightarrow{r_{1\theta m}}\right|}}{\left|\overrightarrow{r_{1\theta m}}\right|} - \frac{e^{-jk\left|\overrightarrow{r_{2\theta m}}\right|}}{\left|\overrightarrow{r_{2\theta m}}\right|}\right) e^{jkm\delta\sin\phi} \tag{A26}$$

Figure A3 shows the beam patterns of a one-dimensional microphone array suitable for a plane wave in the case of an incident wave of a dipole. It is found that, as the ratio of the distance, r_0, to the wavelength of sound increases, the microphone array has a higher spatial resolution, and the maximum array gain of the microphone array at 0º is close to 0 dB. As for the monopole source, this is because, as the distance measured in wavelengths becomes larger, the incident wave is closer to a plane wave. These trends are similar to those seen in the results for the monopole (see Figure 4.6). This indicates that the type of source does not give great effect on the beam patterns of the array tuned at ϕ=0˚, at least for a single source.

Figure A4 shows the beam patterns for different tuned angles of the array. By steering the array axis, the array enhances the spatial resolution in the designed direction. However, the maximum array gain is decreased by up to 3 dB at ϕ=30°. This reduction is greater than that obtained for the monopole by 2 dB. This is due to the directivity of the dipole.

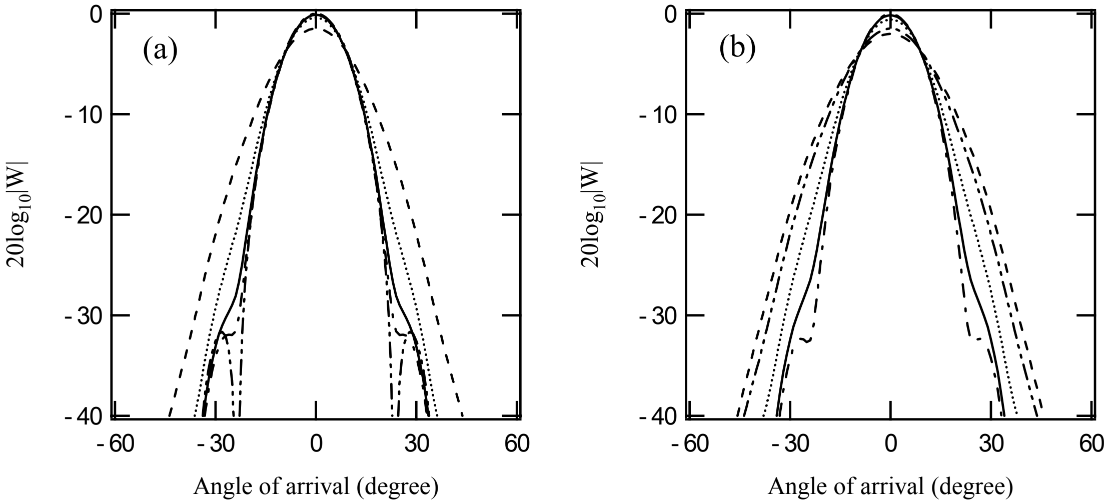

Figure A3 Beam patterns of a one-dimensional microphone array due to an incident wave from a dipole by using Hanning window. The array is tuned for a plane wave at ϕ=0°. Number of microphones is 11. Microphone spacing is half of wavelength. (a) - - -,r_0/λ=5; ·······, r_0/λ=10; ——, r_0/λ=20; – · –, r_0/λ=30; – ·· –, plane wave, (b) r_0=5.72 m. - - -,250 Hz; ·······, 500 Hz; ——, 1000 Hz; – · –, 2000 Hz; – ·· –, 4000 Hz.

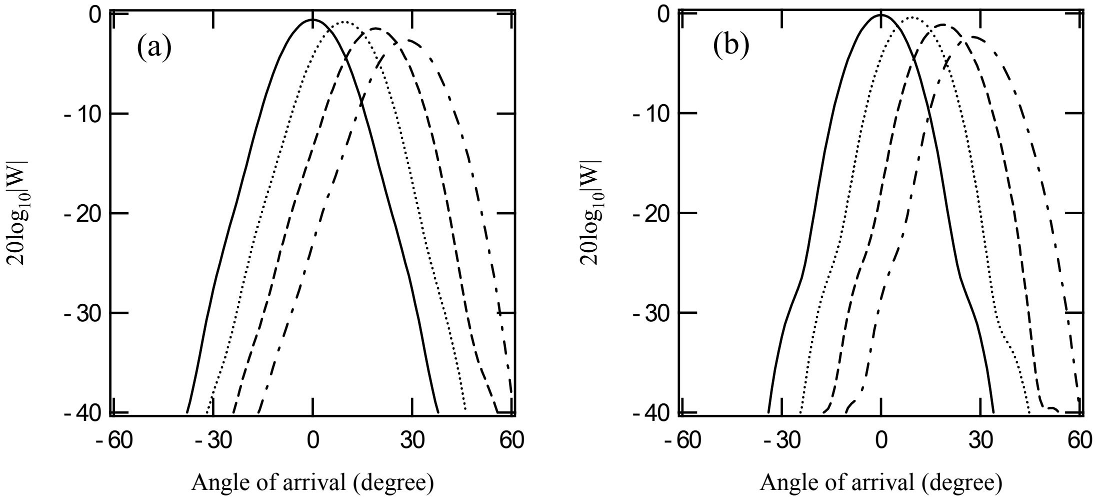

Figure A4 Beam patterns of a one-dimensional microphone array due to an incident wave from a dipole by using Hanning window. The array is tuned for a plane wave. Number of microphones is 11. Microphone spacing is half of wavelength. ——, ϕ=0°; ·······, ϕ=10°; - - -, ϕ=20°; – · –, ϕ=30°. (a) 500 Hz, (b) 1000 Hz.

A2.2 A line array of dipoles

Equations are derived for the sound pressure due to a line array of sources as measured by a microphone array designed for a plane.

As the output of the microphone array for a dipole has been obtained by equation (A26), the output, $S_{n,dipole}$, of the microphone array for the n^{th} dipole will be

$$S_{n,dipole,pl}(\overrightarrow{e_{\phi 0}},\omega)=\sum_{m=-M}^{M} w_m \rho c_0 \frac{jkQ_n}{4\pi}\left(\frac{e^{-jk\left|\overrightarrow{r_{1\theta mn}}\right|}}{\left|\overrightarrow{r_{1\theta mn}}\right|}-\frac{e^{-jk\left|\overrightarrow{r_{2\theta mn}}\right|}}{\left|\overrightarrow{r_{2\theta mn}}\right|}\right)e^{jkm\delta\sin\phi} \tag{A27}$$

where $\overrightarrow{r_{1\theta m}}=\overrightarrow{r_m}+\overrightarrow{r_{1\theta 0n}}$ and $\overrightarrow{r_{2\theta m}}=\overrightarrow{r_m}+\overrightarrow{r_{2\theta 0n}}$. Then, the total output, $S_{inc,di,pl}$ and $S_{coh,di,pl}$ of the microphone array for the line array of *incoherent* and *coherent* dipoles will be

$$S_{inc,di,pl}(\overrightarrow{e_{\phi 0}},\omega)=\left\{\sum_{n=1}^{N}\left|S_{n,dipole,pl}\right|^2\right\}^{\frac{1}{2}}$$

$$=\left\{\sum_{n=1}^{N}\left|\sum_{m=-M}^{M} w_m \rho c_0 \frac{jkQ_n}{4\pi}\left(\frac{e^{-jk\left|\overrightarrow{r_{1\theta mn}}\right|}}{\left|\overrightarrow{r_{1\theta mn}}\right|}-\frac{e^{-jk\left|\overrightarrow{r_{2\theta mn}}\right|}}{\left|\overrightarrow{r_{2\theta mn}}\right|}\right)e^{jkm\delta\sin\phi}\right|^2\right\}^{\frac{1}{2}} \tag{A28}$$

$$S_{coh,di,pl}(\overrightarrow{e_{\phi 0}},\omega)=\sum_{n=1}^{N}S_{n,dipole,pl}$$

$$=\sum_{n=1}^{N}\sum_{m=-M}^{M} w_m \rho c_0 \frac{jkQ_n}{4\pi}\left(\frac{e^{-jk\left|\overrightarrow{r_{1\theta mn}}\right|}}{\left|\overrightarrow{r_{1\theta mn}}\right|}-\frac{e^{-jk\left|\overrightarrow{r_{2\theta mn}}\right|}}{\left|\overrightarrow{r_{2\theta mn}}\right|}\right)e^{jkm\delta\sin\phi} \tag{A29}$$

Hence, by using the time-averaged sound power radiated by the line array of dipoles given by equations (A14) and (A21), $\tilde{S}_{inc,di,pl}$ and $\tilde{S}_{coh,di,pl}$, is normalized. Then,

$$\tilde{S}_{inc,di,pl}(\overrightarrow{e_{\phi 0}},\omega)=\frac{1}{W_{inc,di}^{\frac{1}{2}}}\left\{\sum_{n=1}^{N}\left|\sum_{m=-M}^{M} w_m \rho c_0 \frac{jkQ_n}{4\pi}\left(\frac{e^{-jk\left|\overrightarrow{r_{1\theta mn}}\right|}}{\left|\overrightarrow{r_{1\theta mn}}\right|}-\frac{e^{-jk\left|\overrightarrow{r_{2\theta mn}}\right|}}{\left|\overrightarrow{r_{2\theta mn}}\right|}\right)e^{jkm\delta\sin\phi}\right|^2\right\}^{\frac{1}{2}} \tag{A30}$$

$$\tilde{S}_{coh,di,pl}(\overrightarrow{e_{\phi 0}},\omega)=\frac{1}{W_{coh,di}^{\frac{1}{2}}}\sum_{n=1}^{N}\sum_{m=-M}^{M} w_m \rho c_0 \frac{jkQ_n}{4\pi}\left(\frac{e^{-jk\left|\overrightarrow{r_{1\theta mn}}\right|}}{\left|\overrightarrow{r_{1\theta mn}}\right|}-\frac{e^{-jk\left|\overrightarrow{r_{2\theta mn}}\right|}}{\left|\overrightarrow{r_{2\theta mn}}\right|}\right)e^{jkm\delta\sin\phi} \tag{A31}$$

A3 Radiation from a rail

A3.1 Sound distribution of a rail replaced by a line array of dipole sources

The sound pressure for a line array of dipole sources is evaluated with the MY13 array designed for a plane wave at ϕ=0˚. In this calculation, equations (A30) and (A31) give the results for the incoherent and coherent dipole sources. As the dipoles are orientated horizontally, horizontal rail vibration is used for these simulations.

(a) Source distribution

Figures A5 and A6 show the distribution of horizontal rail vibration amplitude along the rail, the outputs from a single microphone and microphone array for 125 Hz and 1600 Hz. Also shown are the results that are obtained if the same distribution for the coherent sources is used.

For the wave with a high decay rate at 160 Hz, it can be seen that both the single microphone and microphone array locates an incident wave spreading from the dipole sources. This is again due to the fact that the wave with a high decay rate forms a point source. For the wave with a low decay rate above 1000 Hz, the rail radiates sound at an angle to the rail, whereas the microphone array only detects the radiation from the region close to the forcing point, not perceiving the sound radiation generated by the travelling wave part of the rail vibration.

Figure A7 shows the angles between the *x*-axis and a line joining the origin to the positions corresponding to local maximum values in the sound distribution obtained from a single microphone. It can be seen that, above 1000 Hz, the global trends of these two angles show good agreement, as also seen in Figure 5.15. This again indicates that, at low decay rate, the rail taken as an extended line source radiates sound at an angle determined by the supersonic structural radiation.

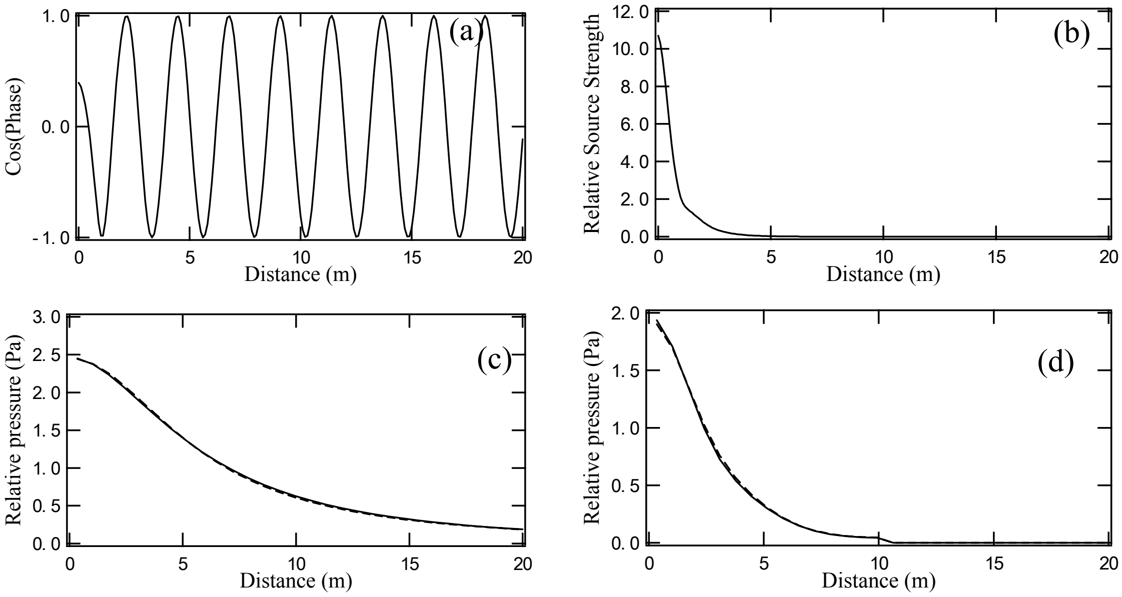

Figure A5 Simulation results for horizontal rail vibration at 125 Hz. (a) Relative phase obtained from rail vibration, (b) relative source strength obtained from rail vibration (arbitrary scale), (c) magnitude of sound pressure at single microphone versus distance along the track from the forcing position, (d) output from microphone array. — Sources accounting for phase; - - - incoherent sources.

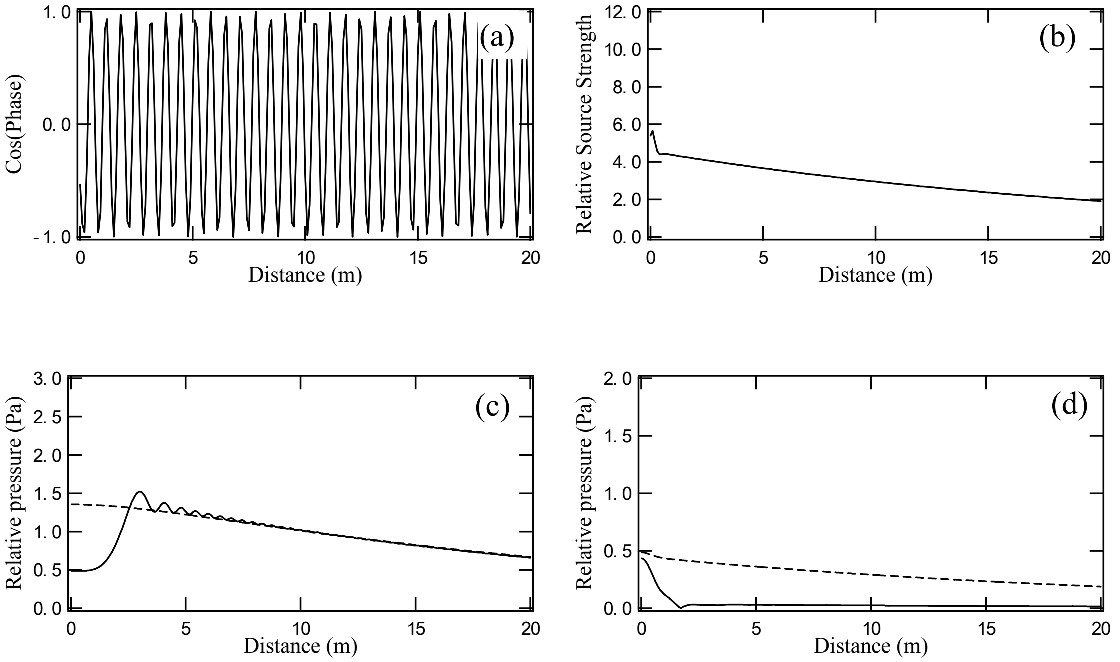

Figure A6 Simulation results for horizontal rail vibration at 1600 Hz. (a) Relative phase obtained from rail vibration, (b) relative source strength obtained from rail vibration (arbitrary scale), (c) magnitude of sound pressure at single microphone versus distance along the track from the forcing position, (d) output from microphone array. — Sources accounting for phase; - - - incoherent sources.

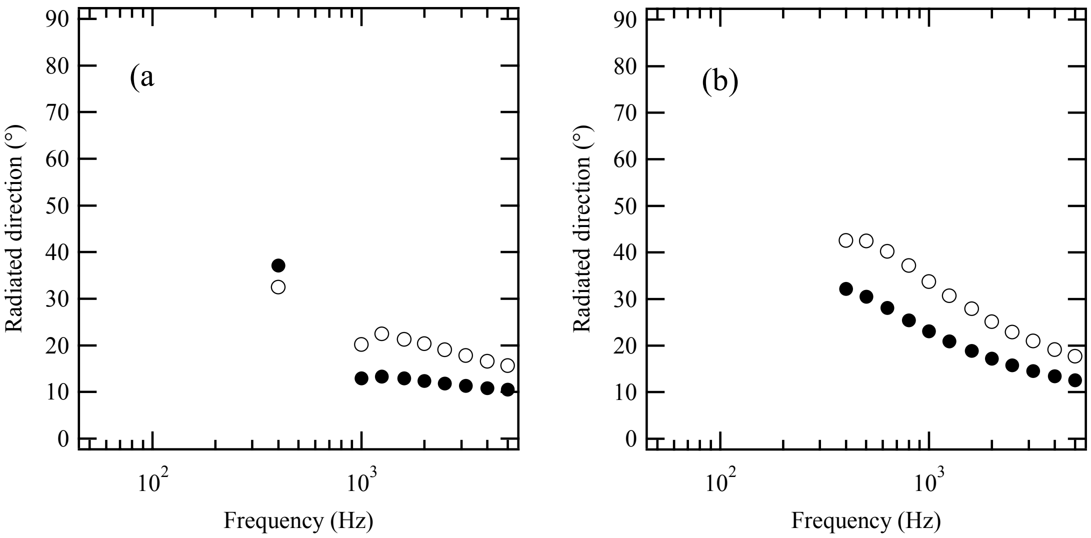

Figure A7 Simulated radiation directions for vertical rail vibration. ○, angles between the *x*-axis and a line joining the origin to the positions corresponding to local maximum values in sound distribution measured with a single microphone; ●, angles determined by the supersonic structural radiation. (a) Vertical rail vibration, (b) horizontal rail vibration.

(b) Overall result

Figure A8 shows the level difference in squared sound pressure between the incoherent and coherent dipole sources. In the frequency region where the free propagation of vertical wave occurs, the microphone array underestimates the rail source up to about 15 dB. Results are also shown for vertical rail vibration.

It is noted that the global trends of the results for the dipole sources are similar to those seen for the monopole sources. This would suggest that, even for a line array of sources, the type of source does not give great influence on the overall effects measured with the array tuned at ϕ=0°.

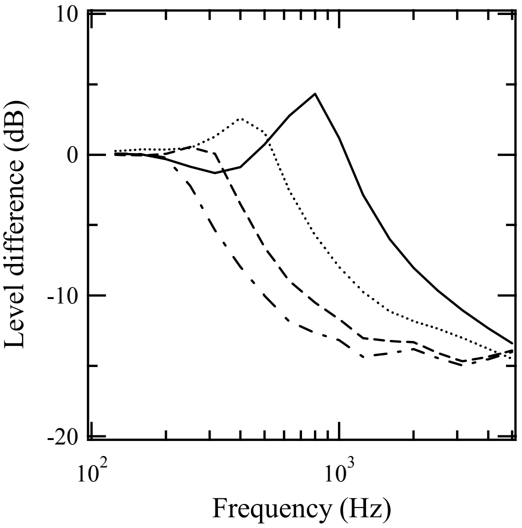

Figure A8 Overall effect of using microphone array for dipole sources to measure noise from rail vibration. ——, Vertical vibration, rail pad stiffness 700 MN/m; - - - - - , horizontal vibration, rail pad stiffness 85 MN/m; ·······, vertical vibration, rail pad stiffness 200 MN/m; – · –, horizontal vibration, rail pad stiffness 40 MN/m.

A3.2 Estimation of rail component of noise

The overall effect of using a microphone array on the rail component of noise is investigated by using the differences shown in Figure A8. The effect is estimated by the same procedure as in Chapter 5.4. The parameters used in the calculation of the sound power generated by the rail vibration are given in Table 2.3.

Figure A9 gives an estimate of the rail component of noise and that which would be obtained from a microphone array measurement. It is found that the overall trends are similar to those seen in Figure 5.20. Above 1 kHz the microphone array tends to make a considerable underestimation of the rail contribution. For the softer rail pad, larger differences are present above 630 Hz.

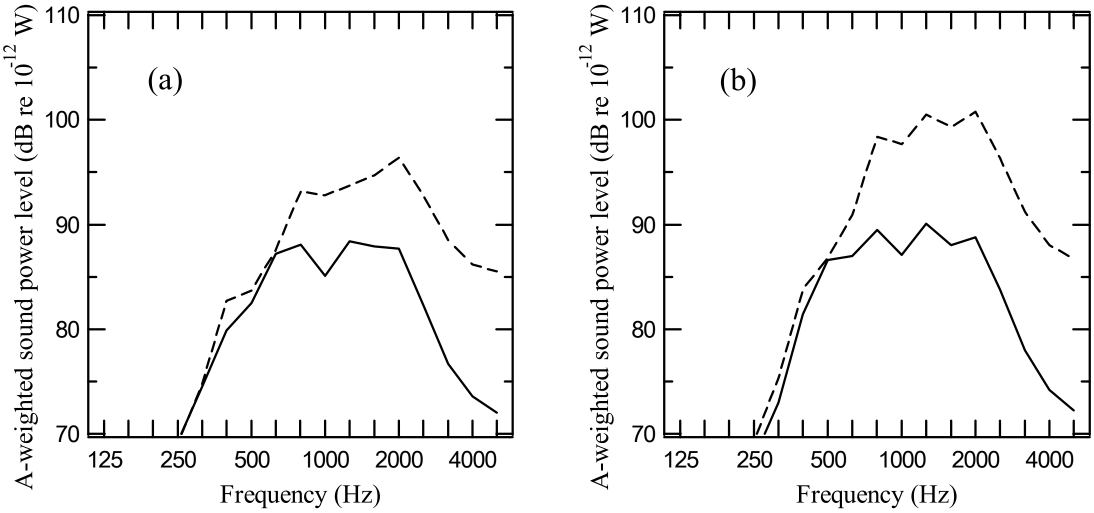

Figure A9 Effect on rail component of noise of using a microphone array tuned for a plane wave. The modification factor is derived from the results for an array of dipole sources. – – –, Actual rail noise; ——, rail noise inferred from microphone array. (a) Track with 700 MN/m pads; (b) Track with 200 MN/m pads.

Figure A10 show the effect of the microphone array measurements on each noise component using wheel F. The results show similar overall trends to those seen for monopoles (Figure 5.21). It is obvious that the wheel component has a greater contribution to the total noise above 1-2 kHz, especially for the stiffer rail pad. This suggests that, for the array measurements, the rail component of noise will not be seen noticeably by the presence of the wheel. Table A1 gives the overall contribution of each noise component. It is clear that the wheel is the dominant source by the microphone array measurement.

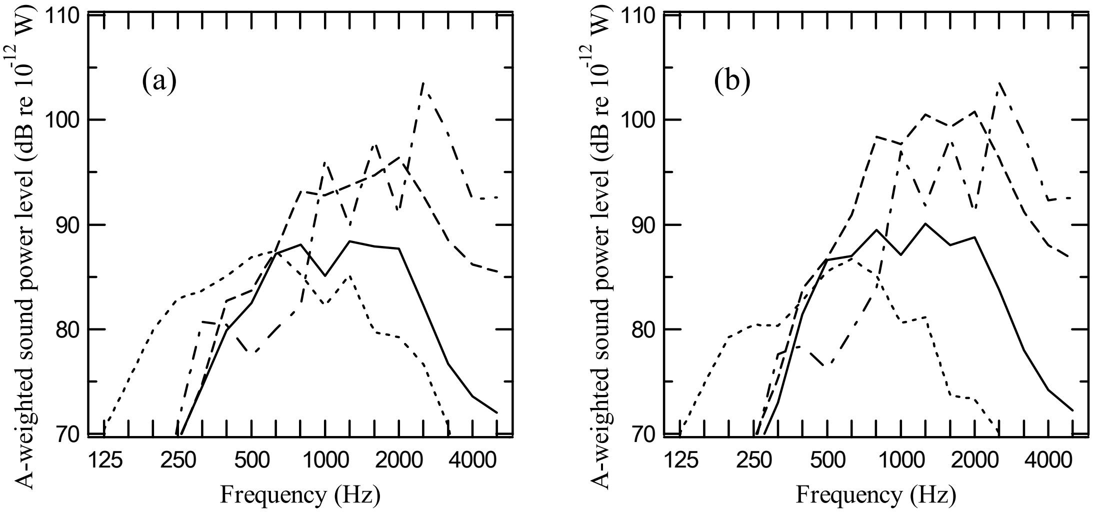

Figure A10 Comparison of the contribution of each noise component by measuring with a microphone array tuned for a plane wave. The modification factor is derived from the results for an array of dipole sources. – – –, Actual rail noise; ——, rail noise inferred from microphone array; ·······, sleeper noise; – · –, wheel noise. (a) Track with 700 MN/m pads; (b) track with 200 MN/m pads.

Table A1 Contribution of each noise component by using a microphone array tuned for a spherical wave. The modification factor is derived from the results for an array of dipole sources. Wheel F is used in the calculation, and other parameters are given in Table 2.3.

	Track with 700MN/m pads		Track with 200MN/m pads	
	TWINS	Microphone array	TWINS	Microphone array
Wheel	106.6	106.6	106.6	106.6
Rail	102.6	96.0	107.3	97.2
Sleeper	94.8	94.8	94.8	94.8
Total	108.3	107.3	110.2	107.5

B. SOUND SOURCES MEASURED WITH A MICROPHONE ARRAY DESIGNED FOR A SPHERICAL WAVE

B1 Single source

B1.1 Single monopole

If the microphone array is designed to be suitable for a spherical wave in the direction $\overrightarrow{e_{\phi}}$ (see Figure B1), the time delays are chosen as $\Delta_m = -\left|\overrightarrow{r_{\phi m}}\right| / c_0$. The output, $S_{mono,sp}$, of the array in the frequency domain will be

$$S_{mono,sp}(\overrightarrow{e_{\phi 0}}, \omega) = \sum_{m=-M}^{M} w_m P_m(\omega) e^{-j\omega\Delta_m}$$

$$= \sum_{m=-M}^{M} w_m \rho c_0 \frac{jkQ}{4\pi\left|\overrightarrow{r_{\theta m}}\right|} e^{-j\overrightarrow{k_{\theta m}}\cdot\overrightarrow{r_{\theta m}}} e^{j\omega\Delta_m}$$

$$= \sum_{m=-M}^{M} w_m \rho c_0 \frac{jkQ}{4\pi\left|\overrightarrow{r_{\theta m}}\right|} e^{-jk\left|\overrightarrow{r_{\theta m}}\right|} e^{jk\left|\overrightarrow{r_{\phi m}}\right|}$$

$$= \rho c_0 \frac{jkQ}{4\pi r_0} \sum_{m=-M}^{M} w_m \frac{r_0}{\left|\overrightarrow{r_{\theta m}}\right|} e^{-jk\left|\overrightarrow{r_{\theta m}}\right|} e^{jk\left|\overrightarrow{r_{\phi m}}\right|} = \rho c_0 \frac{jkQ}{4\pi r_0} W'' \qquad \text{(B1)}$$

In equation (B1), the function, *W”*, gives the beam pattern of the microphone array.

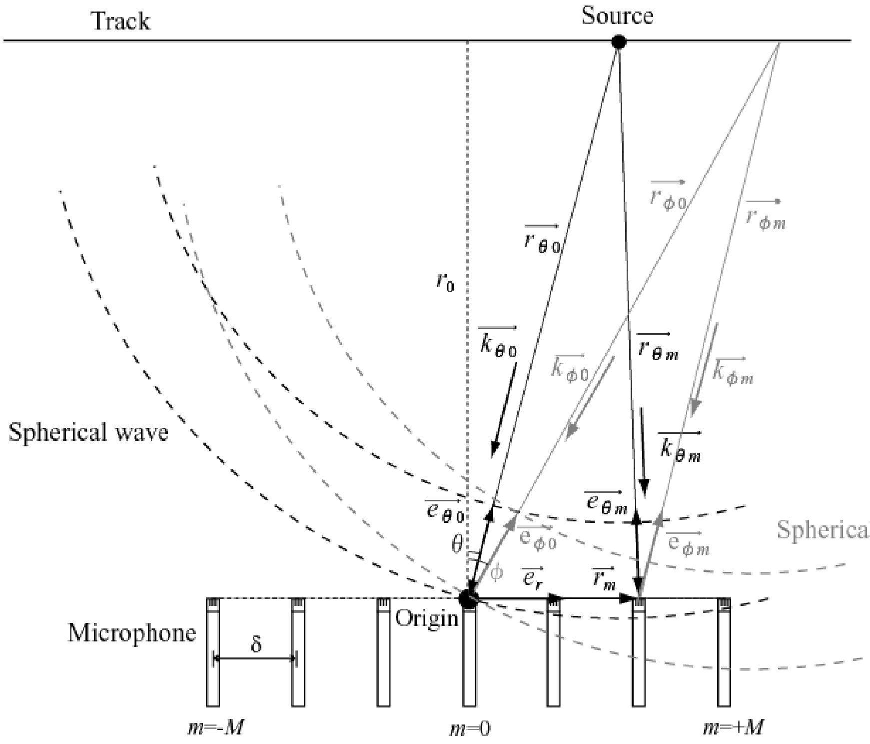

Figure B1 Illustration of a one-dimensional microphone array suitable for a spherical wave and spherical waves.

Figure B2 shows the beam patterns of a one-dimensional microphone array when the incident wavefront is spherical. It can be seen that, in contrast with the results of the array designed for a plane wave (see Figure 4.6), the spatial resolution of the microphone array does not depend on the ratio of the distance, r_0, to the wavelength of sound or on frequency. It is also found that, as the frequency increases, the side lobes are lower.

Figure B3 shows the beam patterns for different tuned angles of the array. By controlling the tuned direction, the main lobe in the beam patterns is directed toward the designed angle. However, the maximum array gain is slightly decreased. This is again due to the attenuation with distance. It is also found that, as the array axis is steered, the main lobes are non-symmetric.

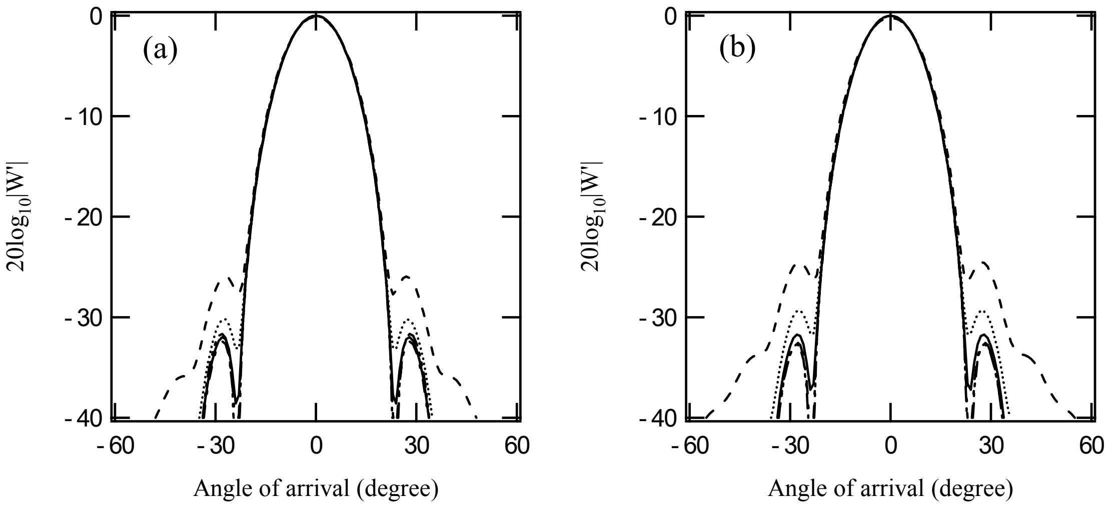

Figure B2 Beam patterns of a one-dimensional microphone array due to an incident spherical wave by using Hanning window. The array is tuned for a spherical wave at ϕ=0°. Number of microphones is 11. Microphone spacing is half of wavelength. (a) - - -, $r_0/\lambda=5$; ········, $r_0/\lambda=10$; ——, $r_0/\lambda=20$; – · –, $r_0/\lambda=30$; – ·· –, plane wave, (b) r_0=5.72 m. - - -, 250 Hz; ········, 500 Hz; ——, 1000 Hz; – · –, 2000 Hz; – ·· –, 4000 Hz.

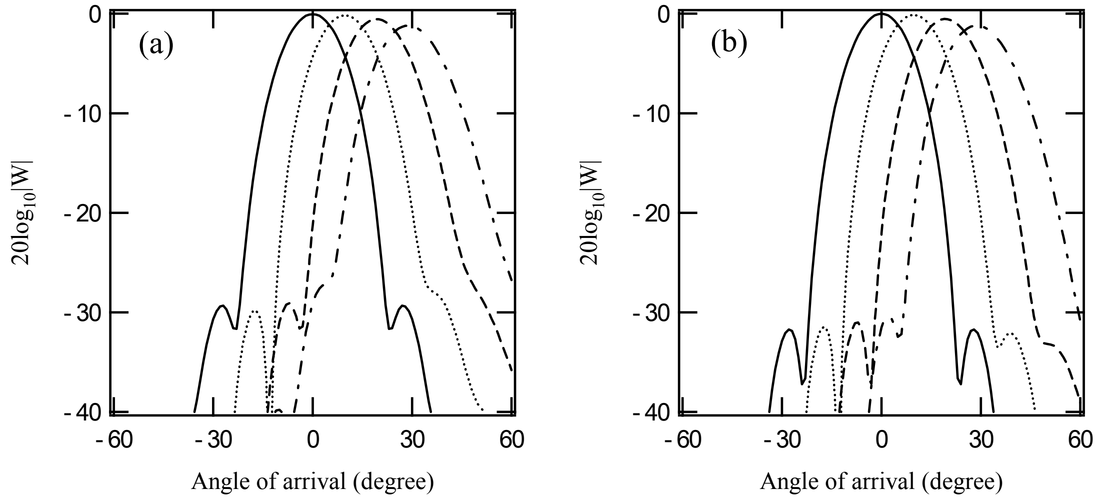

Figure B3 Beam patterns of a one-dimensional microphone array due to an incident spherical wave by using Hanning window. The array is tuned for a spherical wave. Number of microphones is 11. Microphone spacing is half of wavelength. ——, ϕ=0°; ········, ϕ=10°; - - -, ϕ=20°; – · –, ϕ=30°. (a) 500 Hz, (b) 1000 Hz.

Figure B4 shows the beam patterns resulting from several windows. As for a plane wave, the beam patterns for the Hanning window and the Dolph-Tschebyscheff method have a broader main lobe, compared with the results of the rectangular window. However, the amplitudes of the side lobes in the beam patterns of the two windows are reduced.

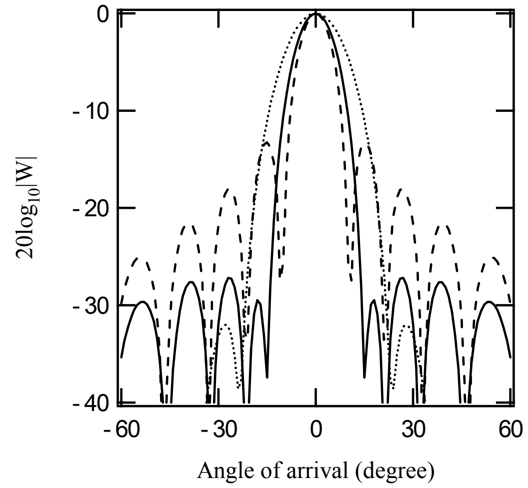

Figure B4 Beam patterns of a one-dimensional microphone array designed for a spherical wave using several weighting factors. Number of microphones is 11. Microphone spacing is half of wavelength. ϕ=0. r_0/λ=20. - - -, Rectangular window; ········, Hanning window; ——, Dolph-Tschebyscheff method.

B1.2 Single dipole

Suppose that a single wave of a dipole arrives from an angle θ, and the microphone array is suitable for a spherical wave from the direction, $\overrightarrow{e_\phi}$. Then, the output, $S_{dipole,sp}$, of the array in the frequency domain will be

$$
\begin{aligned}
S_{dipole,sp}(\overrightarrow{e_{\phi 0}},\omega) &= \sum_{m=-M}^{M} w_m P_m(\omega) e^{-j\omega\Delta_m} \\
&= \sum_{m=-M}^{M} w_m \rho c_0 \frac{jkQ}{4\pi}\left(\frac{e^{-jk\left|\overrightarrow{r_{1\theta m}}\right|}}{\left|\overrightarrow{r_{1\theta m}}\right|} - \frac{e^{-jk\left|\overrightarrow{r_{2\theta m}}\right|}}{\left|\overrightarrow{r_{2\theta m}}\right|}\right) e^{-j\omega\Delta_m} \\
&\simeq \rho c_0 \frac{jkQ}{4\pi r_0} \sum_{m=-M}^{M} w_m \frac{r_0}{r_m} e^{-jkr_m}\left(jkd\cos\theta_m\right) e^{jk\left|\overrightarrow{r_{\phi m}}\right|} \\
&= \rho c_0 \frac{jkQ}{4\pi r_0}\left(jkd\right) \sum_{m=-M}^{M} w_m \frac{r_0}{r_m} e^{-jkr_m}\cos\theta_m e^{jk\left|\overrightarrow{r_{\phi m}}\right|} \\
&= \rho c_0 \frac{jkQ}{4\pi r_0}\left(jkd\right) W'''' \qquad \text{(B2)}
\end{aligned}
$$

In equation (B2), the function, *W””*, gives the beam pattern of the microphone array.

The term, $S_{dipole,sp}$, is normalized by the time-averaged sound power, $W_{doublet}$, given by equation (A10). Then, the normalized output, $\tilde{S}_{dipole,sp}\left(\vec{e}_{\phi 0},\omega\right)$, is

$$\tilde{S}_{dipole,sp}\left(\vec{e}_{\phi 0},\omega\right)=\frac{1}{W_{doublet}^{\frac{1}{2}}}\sum_{m=-M}^{M} w_m \rho c_0 \frac{jkQ}{4\pi}\left(\frac{e^{-jk\left|\overrightarrow{r_{1\theta m}}\right|}}{\left|\overrightarrow{r_{1\theta m}}\right|}-\frac{e^{-jk\left|\overrightarrow{r_{2\theta m}}\right|}}{\left|\overrightarrow{r_{2\theta m}}\right|}\right)e^{jk\left|\overrightarrow{r_{\phi m}}\right|} \qquad \text{(B3)}$$

Figure B5 shows the beam patterns of a one-dimensional microphone array tuned for a spherical wave when the wave from a dipole impinges on the array. It can be seen that the ratio of the distance, r_0, to the wavelength of sound and frequency do not have great influence on the spatial resolution of the microphone array. For the side lobes, at higher frequencies, the gain is reduced. These trends are similar to those seen for monopoles in Figure B2. This again indicates that the type of source does not give great effect on the beam patterns of the array tuned at ϕ=0°, at least for a single source.

Figure B6 shows the beam patterns for different tuned directions of the array. By controlling the tuned angle, the main lobe is directed to the designed direction. However, the maximum array gain of the main lobe is again decreased by up to 3 dB at ϕ=30°, as for the plane wave array.

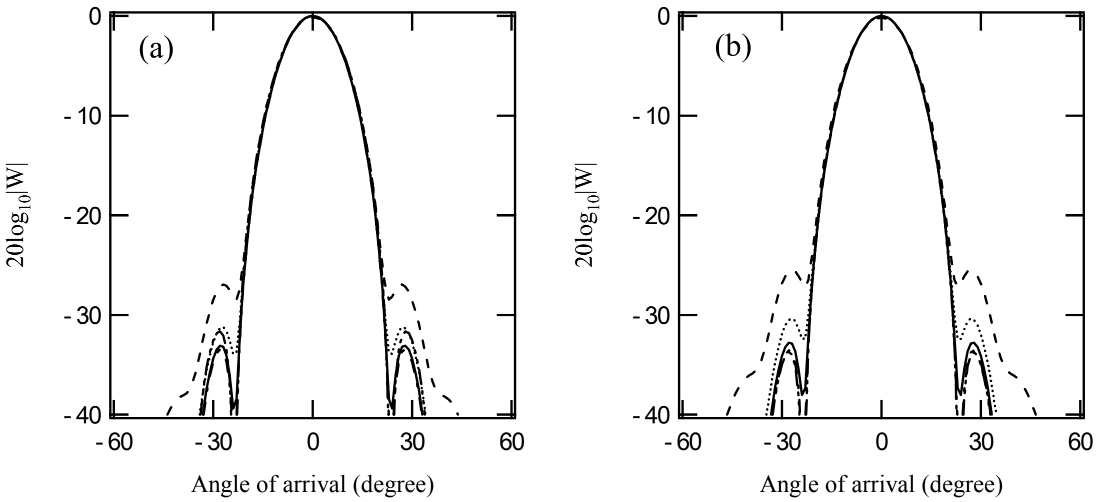

Figure B5 Beam patterns of a one-dimensional microphone array due to an incident wave from a dipole by using Hanning window. The array is tuned for a spherical wave in the preferred angle of 0°. Number of microphones is 11. Microphone spacing is half of wavelength. (a) - - -,r_0/λ=5; ·······, r_0/λ=10; ——, r_0/λ=20; – · –, r_0/λ=30; – ·· –, plane wave, (b) r_0=5.72 m. - - -,250 Hz; ·······, 500 Hz; ——, 1000 Hz; – · –, 2000 Hz; – ·· –, 4000 Hz.

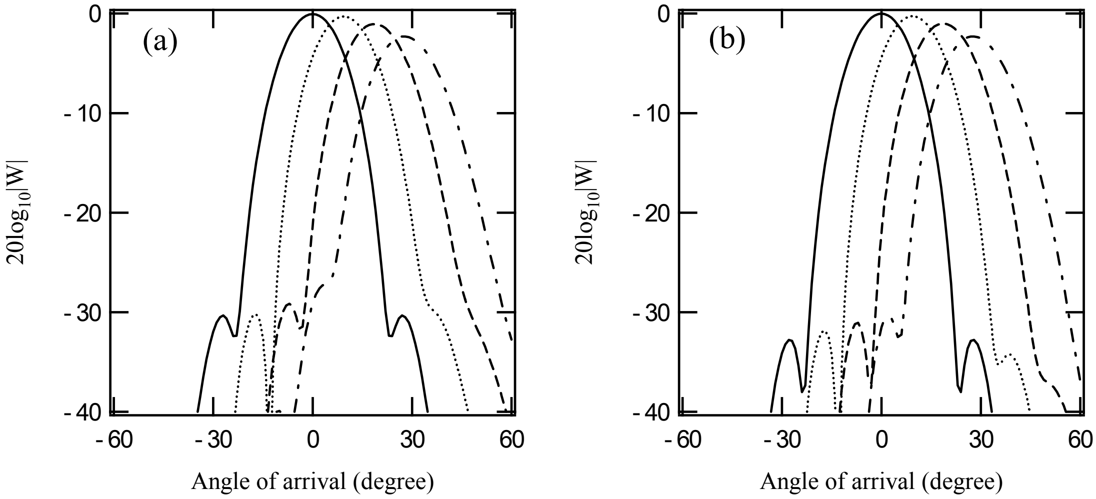

Figure B6 Beam patterns of a one-dimensional microphone array due to an incident wave from a dipole by using Hanning window. The array is tuned for a spherical wave. Number of microphones is 11. Microphone spacing is half of wavelength. ——, ϕ=0°; ·······, ϕ=10°; - - -, ϕ=20°; – · –, ϕ=30°. (a) 500 Hz, (b) 1000 Hz.

B2 A line array of monopoles or dipoles

B2.1 An array of monopole sources

For the microphone array tuned for a spherical wave, it is supposed that there are N sources arranged in a line with equal spacing. By referring to equation (4.25), the total output, $S_{inc,mono,sp}$, of the microphone array for the line array of *incoherent* monopoles will be simply given by

$$S_{inc,mono,sp}(\overrightarrow{e_{\phi 0}},\omega)=\left\{\sum_{n=1}^{N}\left|\sum_{m=-M}^{M} w_m \rho c_0 \frac{jkQ_n}{4\pi\left|\overrightarrow{r_{\theta mn}}\right|} e^{-jk\left|\overrightarrow{r_{\theta mn}}\right|} e^{jk\left|\overrightarrow{r_{\phi mn}}\right|}\right|^2\right\}^{\frac{1}{2}} \qquad \text{(B4)}$$

The total output of $S_{coh,mono,sp}$, of the microphone array for the line array of *coherent* monopoles can be

$$S_{coh,mono,sp}(\overrightarrow{e_{\phi 0}},\omega)=\sum_{n=1}^{N}\sum_{m=-M}^{M} w_m \rho c_0 \frac{jkQ_n}{4\pi\left|\overrightarrow{r_{\theta mn}}\right|} e^{-jk\left|\overrightarrow{r_{\theta mn}}\right|} e^{jk\left|\overrightarrow{r_{\phi mn}}\right|} \qquad \text{(B5)}$$

By using the time-averaged sound power given by equations (4.9) and (4.14), the normalized outputs, $\tilde{S}_{inc,mono,sp}$ and $\tilde{S}_{coh,mono,sp}$, are

$$\tilde{S}_{inc,mono,sp}=\frac{1}{W_{inc,mono}^{\frac{1}{2}}}\left\{\sum_{n=1}^{N}\left|\sum_{m=-M}^{M} w_m \rho c_0 \frac{jkQ_n}{4\pi\left|\overrightarrow{r_{\theta mn}}\right|} e^{-jk\left|\overrightarrow{r_{\theta mn}}\right|} e^{jk\left|\overrightarrow{r_{\phi mn}}\right|}\right|^2\right\}^{\frac{1}{2}} \qquad \text{(B6)}$$

$$\tilde{S}_{coh,mono,sp}=\frac{1}{W_{coh,mono}^{\frac{1}{2}}}\sum_{n=1}^{N}\sum_{m=-M}^{M} w_m \rho c_0 \frac{jkQ_n}{4\pi\left|\overrightarrow{r_{\theta mn}}\right|} e^{-jk\left|\overrightarrow{r_{\theta mn}}\right|} e^{jk\left|\overrightarrow{r_{\phi mn}}\right|} \qquad \text{(B7)}$$

B2.2 An array of dipole sources

As the output of the microphone array for a dipole has been obtained by equation (B.3), the output, $S_{n,dipole,sp}$, of the microphone array for the n^{th} dipole will be

$$S_{n,dipole,sp}(\overrightarrow{e_{\phi 0}},\omega)=\sum_{m=-M}^{M} w_m \rho c_0 \frac{jkQ_n}{4\pi}\left(\frac{e^{-jk\left|\overrightarrow{r_{1\theta mn}}\right|}}{\left|\overrightarrow{r_{1\theta mn}}\right|}-\frac{e^{-jk\left|\overrightarrow{r_{2\theta mn}}\right|}}{\left|\overrightarrow{r_{2\theta mn}}\right|}\right) e^{jk\left|\overrightarrow{r_{\phi mn}}\right|} \qquad \text{(B8)}$$

The total output, $S_{inc,di,sp}$ and $S_{coh,di,sp}$ of the microphone array for the line array of *incoherent* and *coherent* dipoles will be

$$S_{inc,di,sp}(\overrightarrow{e_{\phi 0}},\omega)=\left\{\sum_{n=1}^{N}\left|\sum_{m=-M}^{M} w_m \rho c_0 \frac{jkQ_n}{4\pi}\left(\frac{e^{-jk\left|\overrightarrow{r_{1\theta mn}}\right|}}{\left|\overrightarrow{r_{1\theta mn}}\right|}-\frac{e^{-jk\left|\overrightarrow{r_{2\theta mn}}\right|}}{\left|\overrightarrow{r_{2\theta mn}}\right|}\right) e^{jk\left|\overrightarrow{r_{\phi mn}}\right|}\right|^2\right\}^{\frac{1}{2}} \qquad \text{(B9)}$$

$$S_{coh,di,sp}(\overrightarrow{e_{\phi 0}},\omega)=\sum_{n=1}^{N}\sum_{m=-M}^{M} w_m \rho c_0 \frac{jkQ_n}{4\pi}\left(\frac{e^{-jk\left|\overrightarrow{r_{1\theta mn}}\right|}}{\left|\overrightarrow{r_{1\theta mn}}\right|}-\frac{e^{-jk\left|\overrightarrow{r_{2\theta mn}}\right|}}{\left|\overrightarrow{r_{2\theta mn}}\right|}\right)e^{jk\left|\overrightarrow{r_{\phi mn}}\right|} \qquad \text{(B10)}$$

Hence, by using the time-averaged sound power radiated by the line array of dipoles given by equations (A14) and (A21), $\tilde{S}_{inc,di}$ and $\tilde{S}_{coh,di}$, is normalized. Then,

$$\tilde{S}_{inc,di,sp}(\overrightarrow{e_{\phi 0}},\omega)=\frac{1}{W_{inc,di}^{\frac{1}{2}}}\left\{\sum_{n=1}^{N}\left|\sum_{m=-M}^{M} w_m \rho c_0 \frac{jkQ_n}{4\pi}\left(\frac{e^{-jk\left|\overrightarrow{r_{1\theta mn}}\right|}}{\left|\overrightarrow{r_{1\theta mn}}\right|}-\frac{e^{-jk\left|\overrightarrow{r_{2\theta mn}}\right|}}{\left|\overrightarrow{r_{2\theta mn}}\right|}\right)e^{jk\left|\overrightarrow{r_{\phi mn}}\right|}\right|^2\right\}^{\frac{1}{2}} \qquad \text{(B11)}$$

$$\tilde{S}_{coh,di,sp}(\overrightarrow{e_{\phi 0}},\omega)=\frac{1}{W_{coh,di}^{\frac{1}{2}}}\sum_{n=1}^{N}\sum_{m=-M}^{M} w_m \rho c_0 \frac{jkQ_n}{4\pi}\left(\frac{e^{-jk\left|\overrightarrow{r_{1\theta mn}}\right|}}{\left|\overrightarrow{r_{1\theta mn}}\right|}-\frac{e^{-jk\left|\overrightarrow{r_{2\theta mn}}\right|}}{\left|\overrightarrow{r_{2\theta mn}}\right|}\right)e^{jk\left|\overrightarrow{r_{\phi mn}}\right|} \qquad \text{(B12)}$$

B3 Radiation from a rail

The sound pressure for an array of monopole or dipole sources is evaluated with the MY13 array, which is hypothetically tuned for an incident spherical wave at ϕ=0°. In this calculation, equations (B6), (B7), (B11) and (B12) are used.

B3.1 Sound distribution of monopole and dipole sources

Figures B7 and B8 show the outputs from both a single microphone and the microphone array for 125 Hz and 1600 Hz. These overall trends are similar to those seen for a plane wave array. For the wave with a high decay rate at 125 Hz, it is clear that the local source distributions are reflected in the microphone array measurements for both the monopole and dipole sources. However, for the wave with a low decay rate at 1600 Hz, the rail radiates sound at an angle to the rail, whereas the microphone array still measures only the near-field wave part close to a forcing point.

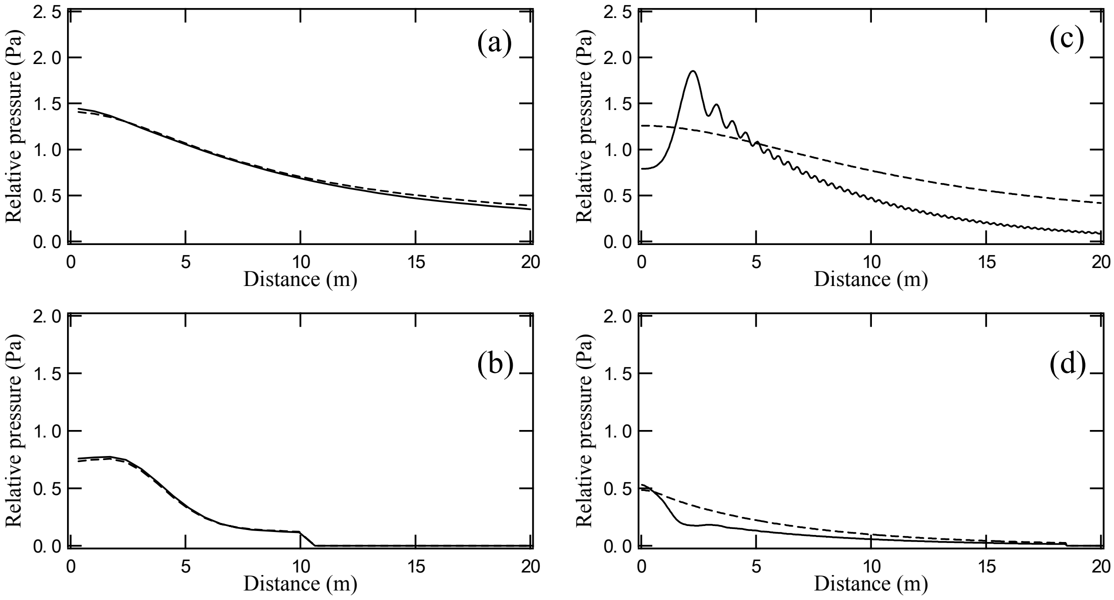

Figure B7 Simulation results for vertical rail vibration for 125 Hz (left) and 1600 Hz (right). The microphone array is designed for a spherical wave. (a, c) Magnitude of sound pressure at single microphone versus distance along the track from the forcing position, (b, d) output from microphone array for a line array of monopole sources. — Sources accounting for phase; - - - incoherent sources.

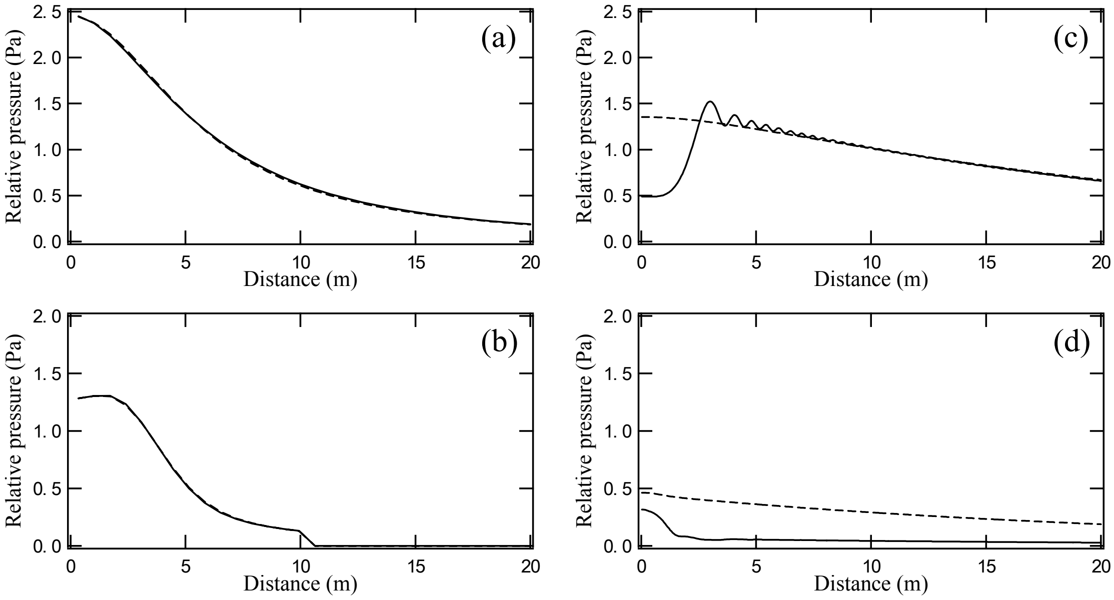

Figure B8 Simulation results for horizontal rail vibration for 125 Hz (left) and 1600 Hz (right). The microphone array is designed for a spherical wave. (a, c) Magnitude of sound pressure at single microphone versus distance along the track from the forcing position, (b, d) output from microphone array for a line array of dipole sources. — Sources accounting for phase; - - - incoherent sources.

B3.2 Overall effect of monopole sources

Figure B9 shows the overall effects of using the microphone array intended for spherical waves to measure noise from rail vibration. In the measurements with the array tuned for a spherical wave, it can be seen that the microphone array again makes under-estimation of the rail source in the frequency region where wave propagation occurs. However, the level difference between the incoherent and coherent sources is smaller than with the array designed for a plane wave. It is again noted that the global trends of the results for the dipole sources are similar to those for the monopole sources.

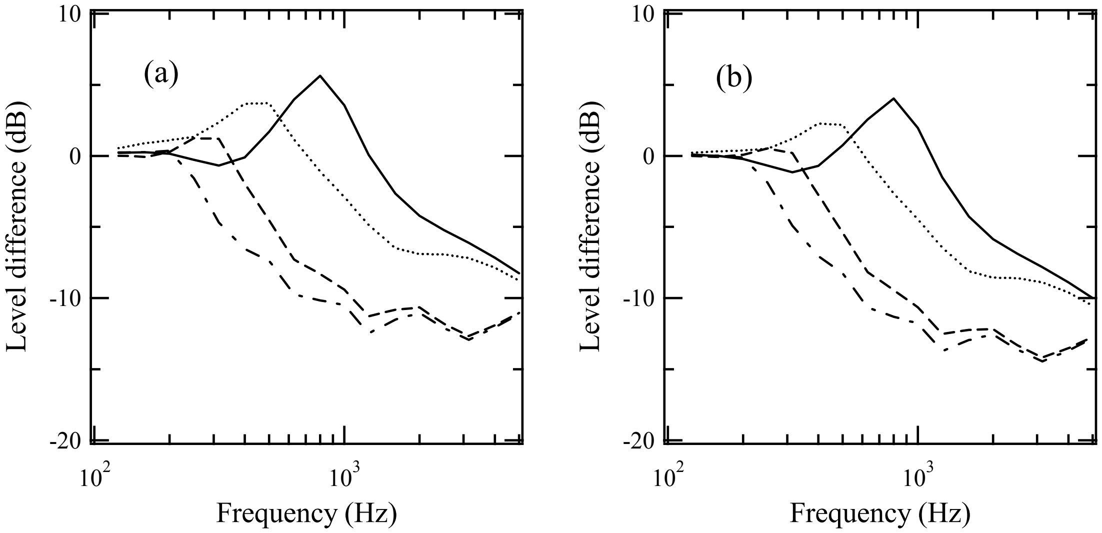

Figure B9 Overall effect of using microphone array for monopole sources to measure noise from rail vibration. The microphone array is designed for a spherical wave. ——, Vertical vibration, rail pad stiffness 700 MN/m; - - - - - , horizontal vibration, rail pad stiffness 85 MN/m; ·······, vertical vibration, rail pad stiffness 200 MN/m; – · –, horizontal vibration, rail pad stiffness 40 MN/m. (a) Monopole, (b) dipole.

B3.3 Tuned angle for the microphone array

The evaluations of the sound pressure for an array of monopole sources are performed by steering the axis of the MY13 array hypothetically. Here, equations (B4), (B5), (B6) and (B7) are used. The parameters associated with the rail vibration are given in Table 2.3.

B3.3.1 Sound distribution

Figure B10 shows the output from a single microphone and the output from a microphone array for 125 Hz and 1600 Hz. At 125 Hz, it can be seen that, when the decay rate of the rail vibration is high, the results measured with a single microphone and microphone array give the same global trends for the incoherent and coherent sources.

For the results at 1600 Hz, by directing the array axis, the maximum array gains obtained from the incoherent sources are only slightly changed. This is because, as the decay rate of the rail vibration is lower, the rail is an extended line source. In the case of the coherent sources, when the array is directed at 10°, a much larger response is obtained by the microphone array due to the extended nature of the source. As tuned angle is larger, the response is more modest. This suggests that the response of the array depends on the angle of the array axis, and this leads to an over-estimation or under-estimation of the rail component of noise in the microphone array results.

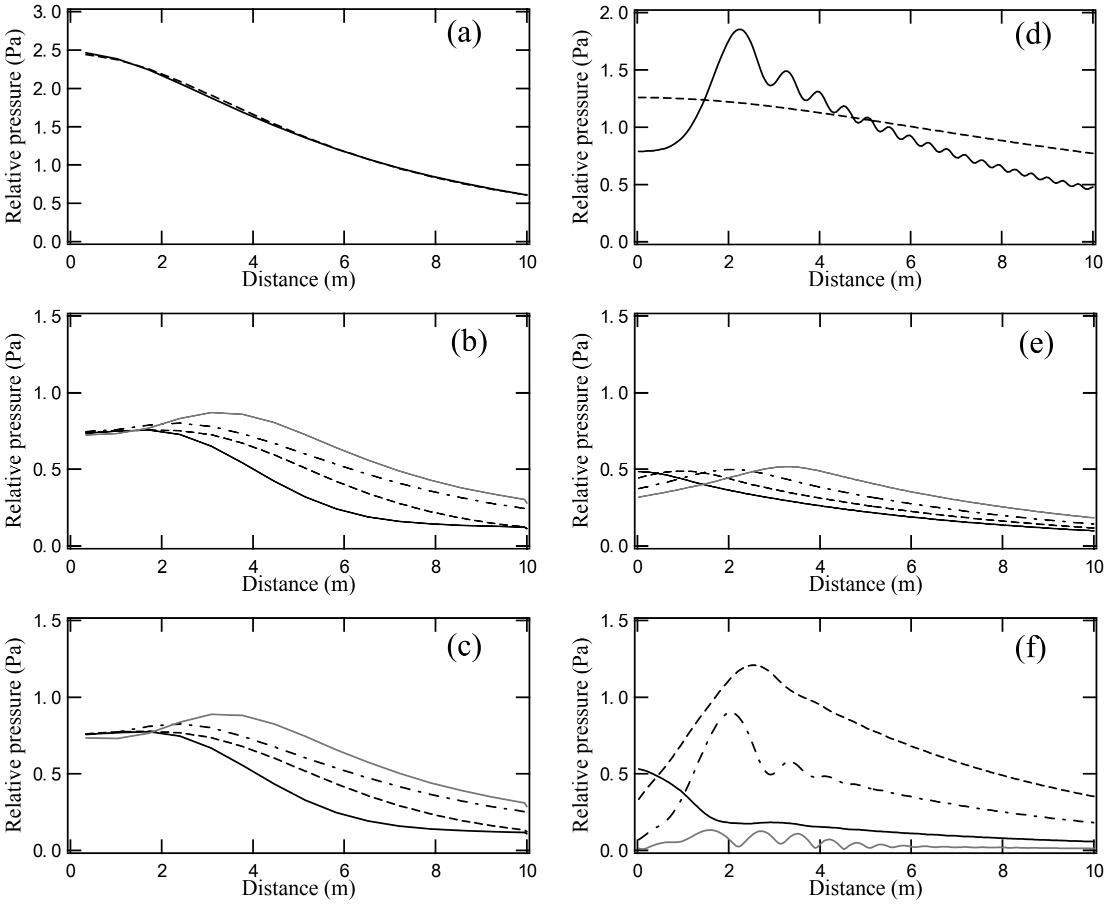

Figure B10 Simulation results for vertical rail vibration for 125 Hz (left) and 1600 Hz (right). The microphone array is designed for a spherical wave. (a, d) magnitude of sound pressure at single microphone versus distance along the track from the forcing position; ——, coherent sources, - - - - -, incoherent sources, (b, e) output from microphone array for a line array of incoherent sources, (c, f) output from microphone array for a line array of coherent sources. ——, ϕ=0°; - - - - -, ϕ=10°; – · –, ϕ=20°; ——, ϕ=30°.

B3.3.2 Overall effect of monopole sources

Figure B11 shows the overall effects of using the microphone array to measure noise from rail vibration for different tuned angles of the array. The results give similar overall trends to those seen for the array designed for a plane wave. It can be seen that, when the decay rate of rail vibration is high, the tuned angle does not affect the level difference between incoherent and coherent sources. In the frequency region where free wave propagation occurs, an overestimation or underestimation of the rail component of noise is made in the microphone array measurements. At the angle closely related to super sonic structural radiation, the microphone array tends to overestimate the rail source. At

ϕ=10°, the array measures a source strength that is greater than the actual one. At ϕ=20°, the result from the microphone array gives a smaller difference. However, at ϕ=30°, the microphone array do not measure the rail source appropriately. This is because the array axis is not arranged with the radiation angle.

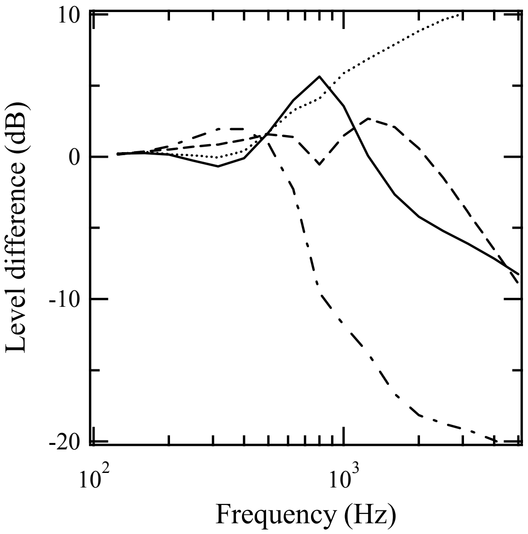

Figure B11 Overall effect of using microphone array for monopole sources to measure noise from rail vibration. The microphone array designed for a spherical wave. ——, ϕ=0°; ··········, ϕ=10°; - - - - - , ϕ=20°; – · –, ϕ=30°.

Figure B12 shows the overall effect of using a microphone array with different tuned angles for selected frequencies. For waves with a high decay rate, it is again found that the tuned angle does not affect the level difference between incoherent and coherent sources. However, for waves with a low decay rate, the level difference depends strongly on the tuned angle. It can be seen that, if the microphone array is directed at the angle close to maximum structural radiation (about 13°, see Figure 5.15), the response is overestimated. In order to obtain the sound power of the rail properly, the coherent nature of the source should be taken into consideration. The results are similar to those seen for the array tuned for a plane wave.

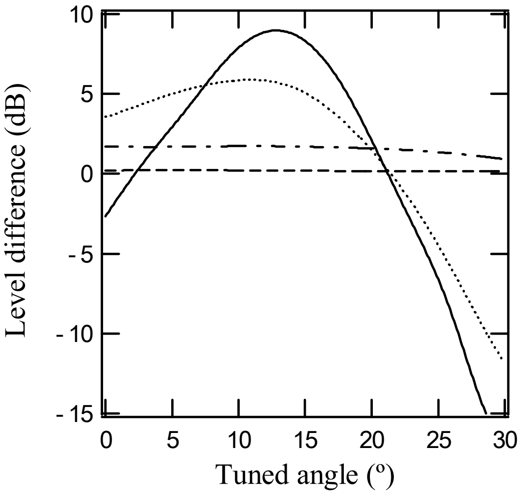

Figure B12 Overall effect of using a microphone array with different tuned angles for monopole sources. The microphone array is designed for a spherical wave. - - - - - , 125 Hz; – · –, 500 Hz; ········, 1000 Hz; ——, 1600 Hz.

APPENDIX C*

CALCULATION OF WAVENUMBERS AND RECEPTANCE USING A CONTINUOUSLY SUPPORTED TIMOSHENKO BEAM (THE *RODEL* MODEL)

It is assumed that a track is modelled as a Timoshenko beam supported on a continuous spring-mass-spring support [3]. The support is formed of damped springs to represent pads, a mass to represent sleeper, and another layer of springs to represent the ballast (see Figure C1). Here, the effect of the discrete nature of the support is neglected.

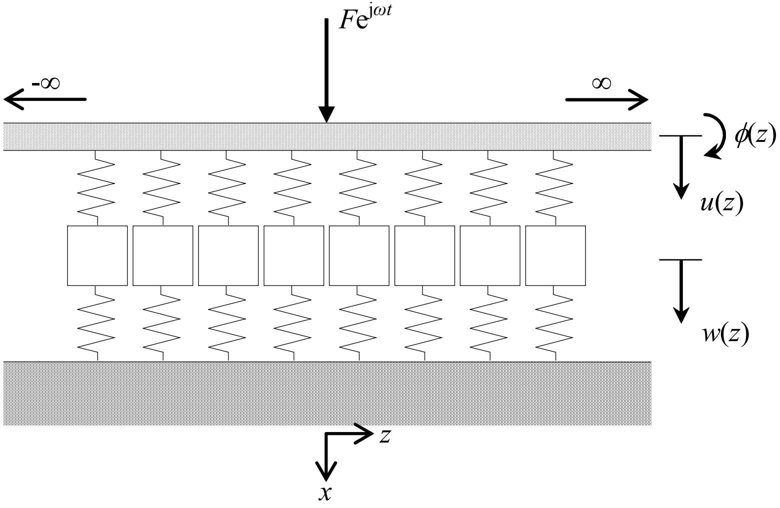

Figure C1 Track modelled as a beam on a continuous support

Consider a harmonic force $Fe^{j\omega t}$ acting at the point z=0. Then, the equations of motion are:

$$\rho A\frac{\partial^2 u}{\partial t^2}+\tilde{G}A\kappa\frac{\partial}{\partial z}\left(\phi-\frac{\partial u}{\partial z}\right)=Fe^{j\omega t}\delta(z)-\tilde{K}_p'(u-w) \tag{C1}$$

$$\rho I\frac{\partial^2 \phi}{\partial t^2}+\tilde{G}A\kappa\left(\phi-\frac{\partial u}{\partial z}\right)-\tilde{E}I\frac{\partial^2 \phi}{\partial z^2}=0 \tag{C2}$$

$$m_s'\frac{\partial^2 w}{\partial t^2}=\tilde{K}_p'(u-w)-\tilde{K}_b'w \tag{C3}$$

where A is the cross-section area, I is the second moment of area of the section and κ is the shear coefficient (proportion of area effective in shear, $0\le\kappa\le1$). The damping of the

---

* This is based on [3].

rail is included by introducing a loss factor η_b into the Young's modulus, E, and the shear modulus, G:

$$\tilde{E} = E\left(1 + j\eta_r\right) \;\; ; \;\; \tilde{G} = G\left(1 + j\eta_r\right) \tag{C4}$$

The pads are represented as the springs with the stiffness per unit length K_p' ($=K_p/d$ where d is the distance between sleepers and K_p is the stiffness of an individual pad) and a damping loss factor η_p). The sleeper is replaced by a mass per unit length m_s' (m_s/d where m_s is the weight of the sleeper). The ballast is also modelled by a stiffness K_b' and a damping loss factor η_b. The damping is also included into the stiffness terms by defining complex stiffness per unit length, $\tilde{K}_p'$ and $\tilde{K}_b'$ for pad and ballast respectively, according to:

$$\tilde{K}_p' = K_p'\left(1 + j\eta_p\right) \;\; ; \;\; \tilde{K}_b' = K_b'\left(1 + j\eta_b\right) \tag{C5}$$

Equations (C1), (C2) and (C3) are solved by introducing solutions of the form as follows,

$$u \sim \hat{u}e^{j\omega t}e^{sz} \, ; \; w \sim \hat{w}e^{j\omega t}e^{sz} \, ; \; \phi \sim \hat{\phi}e^{j\omega t}e^{sz} \tag{C6}$$

Then, the solutions are given by

$$\hat{w} = \hat{u}\frac{\tilde{K}_p'}{\tilde{K}_p' + \tilde{K}_b' - m_s'\omega^2} \tag{C7}$$

$$\hat{\phi} = \hat{u}\frac{\tilde{G}A\kappa s}{\tilde{G}A\kappa - \rho I\omega^2 - \tilde{E}Is^2} \tag{C8}$$

Substituting into equation (C1) and rearranging gives the Laplace transform of the receptance:

$$\hat{\alpha}_{z=0} = \frac{\hat{u}}{F} = -\frac{1}{\tilde{G}A\kappa}\frac{s^2 + C_1(\omega)}{s^4 + C_2(\omega)s^2 + C_3(\omega)} \tag{C9}$$

in which

$$C_1(\omega) = \frac{-\tilde{G}A\kappa + \rho I\omega^2}{\tilde{E}I} \tag{C10}$$

$$C_2(\omega) = \frac{\rho I \omega^2}{\tilde{E}I} - \frac{1}{\tilde{G}A\kappa}\left(\frac{\tilde{K}_p'\left(\tilde{K}_b' - m_s'\omega^2\right)}{\tilde{K}_p' + \tilde{K}_b' - m_s'\omega^2} - \rho A \omega^2 \right) \tag{C11}$$

$$C_3(\omega) = \frac{\tilde{G}A\kappa - \rho I \omega^2}{\tilde{G}A\kappa \tilde{E}I}\left(\frac{\tilde{K}_p'\left(\tilde{K}_b' - m_s'\omega^2\right)}{\tilde{K}_p' + \tilde{K}_b' - m_s'\omega^2} - \rho A \omega^2 \right) \tag{C12}$$

The acceptable complex propagation constants (s_k) of free vibration for a given excitation frequency ω are given by the poles of equation (C9), i.e. the solutions of:

$$s^4 + C_2(\omega)s^2 + C_3(\omega) = 0 \tag{C13}$$

This gives two imaginary (propagating wave) solutions and two real (near-field wave) solutions, in each case one for waves propagating in the left-hand direction and one for right-hand propagating waves. However, at high frequencies, when

$$\rho I \omega^2 \geq \left|\tilde{G}A\kappa\right| \tag{C14}$$

then C_3 changes sign and all four solutions are imaginary. In this frequency range, the Timoshenko bean formulation is strictly no longer valid.

The receptance is found by inverse-transforming equation (C9) using contour integration (the appropriate contour comprises the imaginary axis and a corresponding infinite semi-circle):

$$\alpha^R(\omega) = \frac{1}{2\pi j}\int_{-j\infty}^{j\infty} \hat{\alpha}(s)ds = \sum_{k \text{ with } \mathrm{Re}(s_k) \leq 0} \mathrm{Res}(s_k) \tag{C14}$$

where the residue at the pole s_k are given by

$$\mathrm{Res}(\omega) = -\frac{1}{\tilde{G}A\kappa}\frac{s_k{}^2 + C_1(\omega)}{4s_k{}^3 + 2C_2(\omega)s_k} \tag{C15}$$

APPENDIX D

SUBSEQUENT MEASUREMENTS ON DECAY RATES AND WHEEL/RAIL ROUGHNESSES

D1 Measurements on decay rate

Subsequent to the measurements described in Chapter 2, field tests have been carried out in four test sections for conventional narrow-gauge railway lines during 2005-2007 in order to characterize the vibration decay rates of tracks. The measurements include only one rail-pad type (5N-type rail-pad; the same type investigated in Chapter 2). The rails in the test sections are continuously welded. The track is of ballasted construction and concrete monobloc sleepers are used with a spacing of 0.6-0.65m. The measurements of the decay rates have been performed for each track in both vertical and lateral directions. The data have been obtained on unloaded tracks by hitting the railhead with an instrumented impact hammer, and measuring the response using accelerometers on the railhead. In the measurements, the position of the excitation was moved along the rail up to about 5.0 m, and the responses were measured at the positions of the accelerometers. The measured data were transformed into the frequency domain by a digital analyzer. The decay rates are obtained from an integral of squared vibration over the length of the rail (using equation (2.3)).

Figure D1 shows the measured decay rate of the track. The results show similar trends in both vertical and lateral directions. However, it is found that the decay rates differ between locations within a factor of 2, even though the same type of the rail-pad is used in the track of the four sites. This suggests that, for the validation works of the TWINS model for other test sections, it is better to confirm the vibratory properties of the tracks of the actual sections used through experimental investigation. By comparing Figure D2 with Figure 3.4, it is found that, for the vertical direction, the measured decay rates suitably follow the results predicted with the *rodel* model at higher frequencies. This is due to the longer measured length. However, the predictions are still lower than the measurements for the lateral decay rate.

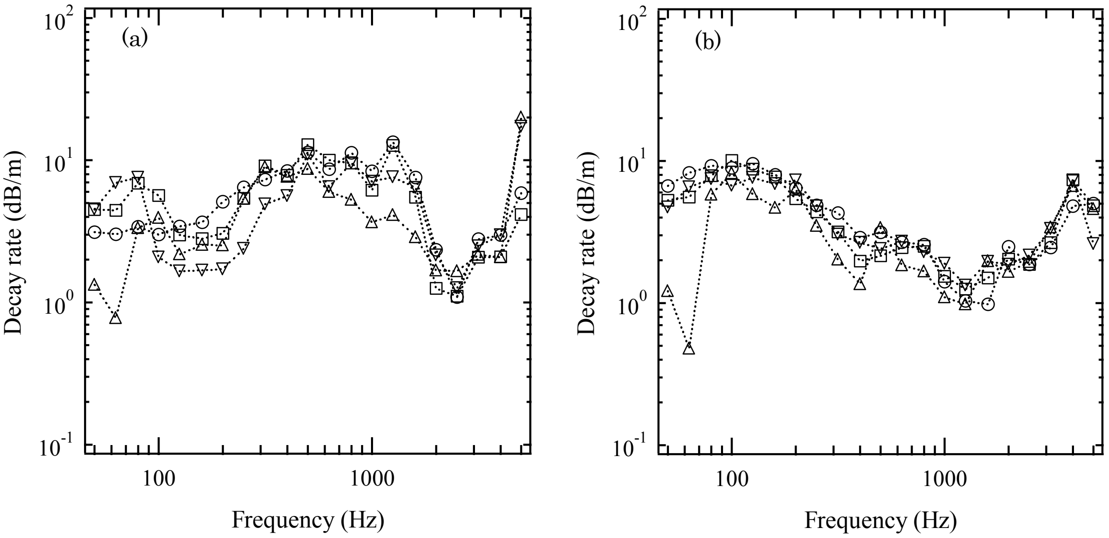

Figure D1 Decay rates of rail vibration for the ballasted, mono-bloc sleeper track with 5N-type rail-pad for four test sections. (a) Vertical direction, (b) lateral direction.

D2 Wheel/rail roughness measurements

In order to evaluate noise and vibration with the TWINS model, a roughness spectrum should be input to the calculations. As wheel and rail roughnesses were not measured for the measurement campaign in Chapter 2, a standard roughness spectrum from European wheels/rails was used instead for the TWINS calculations [63]. The roughness spectra of a number of wheels and rails were measured for the conventional narrow-gauge railway in Japan during 2005-2007. These results are shown in Figure D2. The rail roughnesses are the average levels, which were measured at 14 sites (not including Track A; these can be divided into ground rail: 8 sites and un-ground rail: 6 sites). Two rails were measured at each site. The wheel roughnesses are the average results of 12 tread braked wheels with resin brake blocks, 8 tread braked wheels with sinter blocks and 10 disc braked wheels. For the rail, it is found that the result measured for the sites where the rails have not been ground is similar to the reference roughness spectra used in Chapter 2. It also can be seen that the effect of grinding the rails is a reduction in roughness of about 5 dB. For the wheel, the roughness spectra obtained for Japanese wheels can be seen to be lower than the reference spectra.

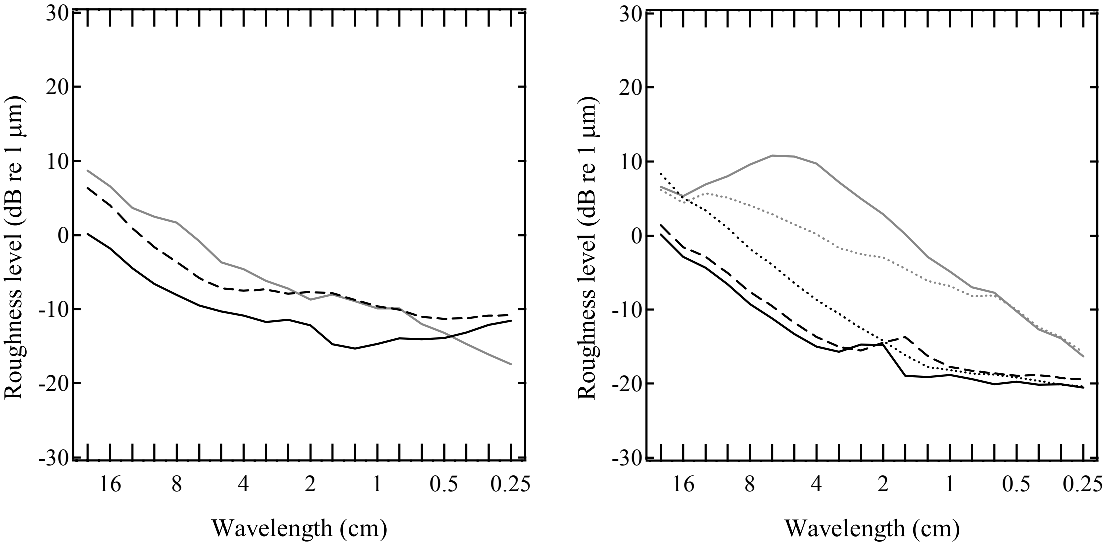

Figure D2 Wheel/rail roughness spectra. (a) Rail roughness, ——, reference rail; ——, rail with rail grinding condition; - - - , rail without rail grinding condition. (b) Wheel roughness, ——, tread braked wheel (cast-iron block, reference); ·········, disk braked wheel (reference); ——, tread braked wheel (resin block); - - - , tread braked wheel (sinter block); ·········, disk braked wheel.